Rik Goudswaard

Characterising emission plumes of individual aircraft operations using low-cost sensor nodes

Thesis Report

TU Delft

This page has intentionally been left blank. Cover picture: own work

Characterising emission plumes of individual aircraft operations using low-cost sensor nodes

By

Rik Goudswaard

in partial fulfilment of the requirements for the degree of

Master of Science
in Aerospace Engineering

at the Delft University of Technology,
to be defended publicly on July 10th 2023 at 13:30.

Report:	MSc thesis
Academic year:	2021-2023
Master track:	Control and Operations
Master profile:	Aircraft Noise and Climate Effects
Student number:	4969855
Thesis committee:	Dr. I.C. Dedoussi (TU Delft, supervisor)
	Prof. dr. D.G. Simons (TU Delft, chairman)
	Dr. ir. C. Borst (TU Delft, examiner)

This thesis is not confidential

An electronic version of this report is available through http://repository.tudelft.nl/.

Keywords: air pollution, air quality, aircraft emissions, jet-engines emissions, low-cost sensors, sensor node network, plume analysis, time-series analysis

This page has intentionally been left blank

Acknowledgements

The research presented in this report was initiated by Delft University of Technology and was conducted to obtain the Master of Science degree in Aerospace Engineering. This therefore marks the end of my student journey, which started nine years ago. Being interested in airplanes from the day I was born, I started studying ‘Aviation’ at the Amsterdam University of Applied Sciences in 2014. After obtaining my Bachelor degree, the desire remained to learn more about airplanes. I therefore enrolled at Delft University of Technology, where I completed my Pre-Master in Aerospace Engineering after two challenging years. This allowed me to enrol for the associated master, of which this thesis is the last milestone to be achieved.

Throughout this journey various people supported me for which I am extremely grateful and would like to use this opportunity to thank them. First of all, I’d like to express my gratitude to my parents (Ariejan and Edith) and brother (Bart) for their continuous support and countless pieces of advice. Furthermore, I owe many thanks to my girlfriend (Valeria) for coming into my life and her constant support and encouragement over the past years. Besides, I would like to thank my friends for being present in my life.

I would also like to express my gratitude to my supervisor I.C. Dedoussi for the countless interesting discussions during which she shared her knowledge with me. This contributed to the results presented in this report, and furthermore challenged me to be always critical towards my own work as well as that of others. Next to I.C Dedoussi, I would like to thank Jeff for his help throughout the thesis and his great company during all the measurements that we performed together. Furthermore, I am grateful for the advice and comments provided by D.G. Simons, which without a doubt contributed to a better end result.

R. Goudswaard
Delft, May 2023

Contents

Abstract I
List of tables J
List of figures K
Abbreviations and Acronyms M
Part I: Introduction and background 1
1 Introduction 2
1.1 Context and relevance 2
1.2 Previous work 3
1.3 Research framework 4
1.4 Outline of the report 7

2 Background 8
2.1 Aircraft exhaust plumes 8
2.2 Influences on aircraft emissions 9
2.2.1 Thrust setting 9
2.2.2 Ambient conditions 9
2.2.3 Aircraft influences 10
2.2.4 Plume rise 10
2.2.5 Engine state 11
2.3 Summary 11

Part II: Materials and methods 12
3 External data sources 13
3.1 Overview of external data sources 13
3.2 Meteorological data 13
3.2.1 CheckWX 13
3.2.2 LiveATC 14
3.3 Aircraft- and engine data 14
3.3.1 The OpenSky Network 14
3.3.2 Supplemental data sources 15
3.3.3 Flight test instrumentation system 16
3.4 Summary 17

4 Experimental set-up 18
4.1 Software and hardware 18
4.1.1 Software description 18
4.1.2 Hardware description 18
4.2 Measurement sites 19
4.2.1 Selected measurement sites 19
4.2.2 Sources of interference 20
4.3 Designed experiments 21
4.3.1 Downwind experiment 21
4.3.2 Upwind experiment 21
4.3.3 Co-location experiment 22
4.3.4 Near engine exit plane experiment 22
4.4 Summary 24

5 Data processing 25
5.1 Method overview 25
5.2 Data preparation 25

5.2.1 Air pollution data 25
5.2.2 Meteorological data 27
5.2.3 Aircraft- and engine data 27
5.3 Estimation of the plume arrival time 28
5.3.1 Estimation approach 28
5.3.2 Caveats of the chosen approach 31
5.4 Plume identification and source appointment 31
5.4.1 Plume identification and source appointment 32
5.4.2 Caveats of the chosen approach 33
5.5 Gaussian representation of plumes 33
5.5.1 Fitting procedure and goodness of fit assessment 33
5.5.2 Gaussian representation of well resolved plumes 35
5.5.3 Gaussian representation of overlapping plumes 35
5.5.4 Caveats of the chosen approach 37
5.6 Plume characterisation 37
5.6.1 Geometrical plume parameters 37
5.6.2 NO to NO_2 ratio 38
5.6.3 SO_2-based emission indices 38
5.7 Quality control 38
5.7.1 Automated data screening 38
5.7.2 Manual verification 39
5.8 Estimation of NO_2 plume characteristics 40
5.9 Summary 40

6 Aircraft emissions estimation method 41
6.1 Model description and implementation 41
6.1.1 Plume radius 41
6.1.2 Emission rate 42
6.2 Summary 43

Part III: Findings, conclusions and recommendations 44
7 Results and discussion 45
7.1 Downwind experiment 45
7.1.1 Analysis based on flight activity 45
7.1.2 Automated screening- and goodness of fit results 47
7.1.3 Aircraft-specific plume characteristics 49
7.1.4 Engine-specific plume characteristics 52
7.1.5 Correlation between area, peak and width 54
7.1.6 Ratio between NO_2 and NO 55
7.1.7 Limitations 56
7.2 Upwind experiment 57
7.3 Co-location experiment 58
7.3.1 Time-series comparison 58
7.3.2 Plume-by-plume comparison 60
7.4 Results and discussion of the near engine exit plane experiment 61
7.4.1 NO_2/NO_x ratios 61
7.4.2 NO_x emission index 62
7.5 Comparison to model results 63
7.6 Summary 65

8 Conclusions and recommendations 66
8.1 Conclusions 66
8.2 Recommendations 68

8.2.1 Sensor node recommendations 68
8.2.2 Recommendations for future experiments and analysis 68
8.2.3 Recommended future work on dispersion modelling 69

Bibliography 70
Appendix A: Supplemental data of the experimental set-up 90
A.1 Specifications of hardware and software 90
A.2 Meteorological conditions during measurements 91

Appendix B: Supplemental data of data processing 96
B.1 Conversion of raw sensor node data 96
B.2 Processing of ATC data 97
B.3 Processing of aircraft- and engine data 97
B.4 Offset in initial estimated plume arrival time 102
B.5 Graphical goodness of fit assessment 102

Appendix C: Supplemental data of the dispersion model 103
C.1 Implementation of dispersion model during previous research 103
C.2 Tables used for the aircraft emissions estimation method 105
C.3 Boeing Fuel Flow Method 2 106

Appendix D: Supplemental data of results 109
D.1 Downwind experiment 109
D.1.1 Certified emission rate 109
D.1.2 Automated screening results 110
D.1.3 Goodness of fit results 114
D.1.3 Aircraft-specific results 117
D.1.4 Engine-specific results 121
D.1.5 Relationship between plume characteristics 123
D.1.6 Sensitivity analysis 123
D.1.7 Internal temperature and relative humidity 125
D.2 Upwind pollutant concentrations 128
D.3 Collocation results 132
D.4 Near engine exit plane experiment results 135
D.5 Dispersion model results 138

Abstract

Aircraft degrade air quality, which has raised concerns about the health of airport personnel and residents living near airports. The aircraft attributable impact on air quality is however currently not well understood, especially in terms of individual aircraft operations. This research aims to increase understanding in the chemical composition of aircraft exhaust plumes using a device (called a sensor node) with commercially available low-cost gas sensors. This is accomplished by carrying out four in-field experiments with these sensor nodes at and near an airport to characterise the captured exhaust plumes in terms of their chemical composition.

In the first experiment a sensor node is deployed downwind of a runway to investigate the possibility of automatically identifying and characterising the pollution footprint of individual aircraft operations using low-cost sensor nodes. To achieve this, a novel tool was developed to identify aircraft attributable pollution (referred to as plume signals) which are coupled to individual aircraft operations and represented by Gaussian curves. The plume signals are screened to filter out plumes that are unlikely to be associated with aircraft. Finally, plumes are characterised in terms of parameters such as the cumulative pollutant concentrations resulting from an aircraft operation. Following this approach, the majority of NO and NO_2 plumes of departing aircraft could be characterised as well as most CO plumes of landing aircraft.

The results showed that significant background-subtracted NO_x concentrations were present for departing aircraft with most NO_x consisting out of NO, while typically no discernible aircraft attributable concentrations could be observed for CO and SO_2. The cumulative NO_x concentrations of large departing aircraft were ~3.5 times higher compared to medium-sized ones with the highest values being observed for the B78X. Landing aircraft typically led to substantial background-subtracted CO concentrations, while typically no discernible aircraft attributable concentrations could be observed for SO_2, NO and NO_2. The cumulative CO concentrations of landing aircraft were independent of aircraft size with the highest values resulting from the B77W. Both for NO_x of departing aircraft and CO of landing aircraft no consistent trend is evident that aircraft with a higher certified emission rate yield higher observed cumulative pollutant concentrations.

In the second experiment sensor nodes were simultaneously deployed upwind and downwind of a runway to investigate whether pollutant concentrations measured upwind can be subtracted from downwind concentrations to obtain the aircraft attributable concentrations. However, as the background-subtracted upwind concentrations were not negligible compared to those obtained downwind, this approach cannot be used.

During the third experiment sensor nodes were collocated downwind of a runway to assess their level of agreement. This revealed that although inter-nodal differences of >100% are present for ambient pollutant concentrations, inter-nodal differences of aircraft attributable cumulative pollutant concentrations differ 26%, 8% and 37% for CO, NO and NO_2 respectively.

The fourth experiment involved measurements taken near a stationary aircraft to investigate whether SO_2 can be used to estimate emission indices. The resulting SO_2-based NO_x emission index was 172% lower compared to the certified emission index. However, measurements were conducted in non-ideal conditions. Nevertheless, by using SO_2 an uncertainty is introduced when the fuel sulphur quantity is unknown as the SO_2 emission index may vary from ~0 – 3 g/kg, although values of 0.3 – 1.3 g/kg are more common.

Based on these four experiments this research demonstrated the potential of low-cost sensor nodes for the analysis of the pollution footprint of individual aircraft operations. The findings of this report can be used by the scientific community, policymakers, and regulatory bodies to further study the air quality impact of individual aircraft and develop mitigation strategies.

List of tables

Table 1.1: Overview of existing research conducted in the past two decades that looked into gas-phase species of aircraft exhaust plumes based on measurements taken with lab grade instruments near airports 4
Table 3.1: Overview of data acquired from CheckWX 14
Table 3.2: Overview of data acquired from the OpenSky Network 15
Table 3.3: Overview of data acquired from sources to supplement OpenSky Network data 16
Table 3.4: Overview of data acquired from the Flight Test Instrumentation System 16
Table 4.1: Measured pollutant species and the name of the incorporated gas sensors 18
Table 7.1: Observed aircraft attributable NO_x peak concentrations (i.e., the maximum background-subtracted concentrations resulting from departing aircraft) by this research and similar existing research 45
Table 7.2: Mean (and standard deviation) of the coefficient of determination (R^2), absolute value of the reduced chi squared ($\chi 2*$), Mean Absolute Error (MAE), Root Mean Square Error (RMSE), percentage difference between the area of the unfiltered plume signal and Gaussian fitting ($A_{difference}$) and percentage difference between the peak pollutant concentration of the filtered plume signal and Gaussian fitting for plumes passing quality control ($P_{difference}$) 48
Table 7.3: Difference in mean NO_x peak concentration observed during this research and similar research of Carslaw et al. for different aircraft types 50
Table 7.4: NO_2/NO ratios of departing aircraft observed during this research and similar existing research 56
Table 7.5: Ratio of NO_2 over NO_x at idle thrust for this research and existing literature 61
Table 7.6: Global mean emission index and ranges between which the SO_2 emission index typically varies according to existing literature reviews whereby N.R. indicates no value was reported 63

List of figures

Figure 1.1: Flow diagram summarising the steps performed during this research 7
Figure 2.1: Simplified representation of combustion emissions of a turbofan engine [3]..... 8
Figure 2.2: Visualisation of the entrainment of an exhaust jet in a wingtip vortex [136] (a) and schematic representation of the main influences on plume formation and evolution [91] (modified by author) (b) 10
Figure 3.1: Overview of external data sources used during this research 13
Figure 4.1: Typical equipment set-up during a field measurement 18
Figure 4.2: Overview of the components of a sensor node employed in this research 19
Figure 4.3: Schematic overview of the measurement sites and weather station (a) and graphical explanation of upwind and downwind (b) 20
Figure 4.4: Equipment set-up of the downwind experiment (a) and a wind rose showing the percentage of occurrence of the wind approaching from a certain direction together with the wind speed (b)..... 21
Figure 4.5: Equipment set-up of the upwind experiment (a) and a wind rose showing the percentage of occurrence of the wind approaching from a certain direction together with the wind speed (b) 22
Figure 4.6: Equipment set-up of the co-location experiment (a) and a wind rose showing the percentage of occurrence of the wind approaching from a certain direction together with the wind speed (b)..... 22
Figure 4.7: Top view (a) and side view (b) of equipment set-up of the first near engine exit plane measurement (not to scale, aircraft blueprint obtained from [167])..... 23
Figure 4.8: Top view of the equipment set-up of the second near engine exit plane measurement (not to scale, aircraft blueprint obtained from [167]). 23
Figure 4.9: Measurement site and aircraft orientation (map obtained from [168]) (a) and a wind rose showing the percentage of occurrence of the wind approaching from a certain direction together with the wind speed (b) 24
Figure 5.1: Overview of the applied method to process the acquired data..... 25
Figure 5.2: Example of the total signal, baseline signal and local signal 26
Figure 5.3: Position reports of a B78X during its take-off roll on the Polderbaan runway 27
Figure 5.4: Graphical representation of how a passive plume of a stationary source moves to a downwind sensor node..... 29
Figure 5.5: Example of the position reports (represented by black circles) of an arriving B739 for unlicensed OpenSky Network data (a) and licensed data (only displaying those while the aircraft is on the runway) (b) 30
Figure 5.6: Schematic of the exhaust plume of a departing aircraft in case of headwind and crosswind (a) and tailwind and crosswind (b) [1, 102] (modified by author) 31
Figure 5.7: Identification of the plume signal of a departing Boeing 787-9 whereby the horizontal axis represents a symmetric six-minutes window centred around the EPA time 32
Figure 5.8: Gaussian fitting and the superimposed Gaussian for a departing Boeing 787-9 whereby the horizontal axis represents part of the six-minute symmetric time window centred around the (refined) EPA time..... 35
Figure 5.9: Multi-modal Gaussian fit to the plume of a Boeing 737-800 (leading plume) and an Embraer 190 (trailing plume) that shortly (~50 sec) depart after each whereby the horizontal axis represents a symmetric six-minutes window centred around the (refined) EPA time..... 36
Figure 5.10: Visualisation of parameters used to characterise plume signals whereby the horizontal axis represents (part of) a symmetric six-minutes window centred around the EPA time..... 38
Figure 5.11: Rejected as no peak could be identified within 30 s of the (refined) EPA time (a), rejected as an overlapping peak could not be coupled to an aircraft operation (b), rejected based on goodness of fit metrics (c) and the figure legend (d)..... 39
Figure 5.12: Time-series showing the observed pollutant concentrations of NO and NO_2..... 40
Figure 7.1: Filtered signal of local time-series together with the (refined) estimated plume arrival time of landing aircraft for the measurement conducted at 22-01-2021 46
Figure 7.2: Number of times specific aircraft types were encountered versus the percentage of plumes passing quality control..... 48
Figure 7.3: Observed background-subtracted cumulative pollutant concentrations over time for different aircraft-engine combinations (upper graph) and the ICAO emission rate for the same aircraft-engine combinations (lower graph) for NO_x of departing aircraft (a) and CO of landing aircraft (b)..... 49
Figure 7.4: Plume width of the Gaussian representation of plumes in pollutant time-series (representing the duration of enhanced pollutant concentrations due to an aircraft) for different aircraft types for CO (a), NO (b) and NO_2 (c) 52

Figure 7.5: Observed background-subtracted cumulative pollutant concentrations over time for different engine models (upper graph) and the ICAO emission rate for the same engine models (lower graph) for NO_x for departures (a) and CO of landings (b) 53
Figure 7.6: Relationship between the peak height and area and width and area of Gaussian CO plumes 55
Figure 7.7: Correlation graph between the Gaussian plume peak concentration of NO and NO_2 with an increasingly light colour depicting increased plume travel time 55
Figure 7.8: Time-series of the local pollutant concentrations upwind and downwind of an active runway together with the prevailing wind and the (refined) estimated plume arrival time of landing aircraft for the measurement conducted on 06-05-2022 57
Figure 7.9: Comparison of pollutant concentrations obtained by two sensor nodes for the total pollutant concentrations (top row) and the local pollutant concentrations (bottom row) with the Pearson correlation coefficient (r), Root Mean Square Error (RMSE), Mean Absolute Error (MAE) and percentage difference between the time-series mean of each sensor node (%Δ mean) 59
Figure 7.10: Comparison of the Gaussian plume area, width and peak pollutant concentration of aircraft operations passing quality control with the Pearson correlation coefficient (r), Root Mean Square Error (RMSE), Mean Absolute Error (MAE) and the average percentage difference (Average %Δ)..... 60
Figure 7.11: Comparison between peak pollutant concentrations of the Gaussian representation of the plume observed during in-field downwind measurements and peak pollutant concentrations resulting from a (simple) dispersion model 63

Abbreviations and Acronyms

A/D	Analogue to Digital
ADS-B	Automatic Dependent Surveillance Broadcast
API	Application Programming Interface
AQM	Air Quality Monitoring
ATC	Air Traffic Control
ATS	Air Traffic Service
AUC	Area Under the Curve
AVIATOR	Assesing aViation emission Impact on local Air quality at airports: Towards regulation
BFFM2	Boeing Fuel Flow Method 2
EASA	European Aviation Safety Agency
ECS	Engine Control System
EI	Emission Index
ENEA	National Agency for New Technologies
EPA	Estimated Plume Arrival
FAA	Federal Aviation Administration
FTIS	Flight Test Instrumentation System
ICAO	International Civil Aviation Organization
KNMI	Royal Netherlands Meteorological Institute
LCS	Low-Cost Sensors
LIDAR	Light Detection and Ranging
MA	Moving Average
MAE	Mean Absolute Error

MTOW	Maximum Take Off Weight
NaN	Not-a-Number
OPR	Overall Pressure Ratio
Parts-per-billion	ppb
Part-per-million	ppm
PSL	Peak Separation Line
RMSE	Root Mean Square Error
S-G	Savitzky-Golay
SAGE	System for assessing Aviation's Global Emissions
SNAQ	Sensor Network for Air Quality
SNR	Signal to Noise Ratio
TDZ	Touch Down Zone
TN	True North
UTC	Coordinated Universal Time
VOC	Volatile Organic Compounds
VRB	Variable

This page has intentionally been left blank

Part I: Introduction and background

1 Introduction

This report starts off by introducing the reader to the research topic. Section 1.1 describes the research topic and its relevance. Hereafter, Section 1.2 looks into the work of existing research. Next, Section 1.3 presents the research objective, challenges, and research questions. The chapter concludes in Section 1.4 with an outline of the report.

1.1 Context and relevance

By emitting gases and particles aircraft degrade air quality which can negatively impact human health, ecosystems and cultural heritage [1–6]. When aircraft are operating near airports, these emissions are released into the atmosphere in close proximity of the surface which may pose a serious health threat [1, 2, 7–10]. For instance, Yim et al. [2] estimated that in Europe ~49% of the 3700 (2100 to 5500 with a 90% confidence interval) yearly pre-mature aviation attributable mortalities result from aircraft operations taking place at and near airports[1]. Despite ongoing technological and operational improvements it is expected that the aircraft attributable impact on air quality will continue to increase in the upcoming decades due to the rapid growth in air traffic [2, 11–13]. This has raised concerns about the current and future health of airport personnel and residents living in close proximity of airports [7, 14–17].

The air quality impact of aircraft and its associated health effects are however currently poorly quantified and not well understood. This is especially the case for individual aircraft operations (i.e., activities of specific aircraft-engine combinations) [18–29]. The impact of aircraft on air quality is commonly estimated using certified emissions data. However, this data is only published for four gases (carbon monoxide, unburnt hydrocarbons, oxides of nitrogen and smoke) and particles rather than for all pollutants emitted by aircraft [30]. Apart from this, certified data is based on a limited number of measurements of newly manufactured engines in an engine test-cell under predefined conditions for only four thrust settings. The emissions of in-service aircraft-engine combinations under actual ambient- and operating conditions may therefore be different [5, 6, 18, 31–38].

It is important that the impact specific aircraft types and engine models have on air quality gets quantified in order to reduce air pollution exposure and its related health impacts [19]. One way to perform this quantification, is by extracting pollutant concentrations resulting from individual aircraft operations from real-world air pollution data. Subsequently, the resulting data can be analysed to determine the pollution footprint of specific aircraft types and engine models. This can be used to update current emission inventories[2] and air quality models. Regulatory bodies and policymakers can then use this information when deciding about ways to mitigate the air quality impact of aircraft [19–21, 36, 41].

To acquire air pollution data, air quality research commonly uses Air Quality Monitoring (AQM) stations, which measure air pollution at high accuracy and reliability at fixed geographical locations. Such stations are generally sparse and their publicly available data typically consists of hourly mean values [18–25, 42–49]. To determine the air pollution impact of individual aircraft operations, higher temporal resolution data is required. Therefore, although AQM stations may be useful for air quality research of airports, its data is considered unsuitable for analysing the air pollution of individual aircraft operations.

Besides using AQM stations, a limited number of studies deployed lab grade instruments near airports to measure the air pollution confined in aircraft exhaust plumes [6, 37, 50–52]. This may be challenging due to the uncontrolled conditions under which measurements are taken.

[1] Aircraft operations at and near airports are defined as all aircraft activities taking place below 3000 feet above ground level.
[2] Emission inventories are databases containing information about the emission rate per emission source [39, 40].

Nevertheless, it enables the quantification of the pollution footprint of different in-service aircraft types and engine models in a short amount of time without the need to access an airport or engine test-cell. Lab grade instruments are however associated with a high cost of ~1000 to 10 000 USD per pollutant species [45, 46, 48, 53]. Furthermore, they may be impractical in terms of deployment as they are typically characterised by large dimensions and weight [45, 53].

Recent improvements in sensor technology makes the use of Low-Cost Sensors (LCS) (~10 to 100 USD per sensor) a promising alternative to obtain air pollution data of high temporal resolution [49]. Multiple LCS are generally fitted in an outer casing together with other components (such as a battery) to form a self-powered device, referred to as a sensor node. These nodes are typically characterised by low weight (~5 kilograms) and small dimensions (about the size of a shoe box) such that they can easily be deployed near airports [42, 45, 47, 54]. Besides, due to the price of LCS it is feasible[3] to simultaneously measure a multitude of pollutant species [45, 55–57]. Sensor nodes thus present an economical approach to analyse the air pollution resulting from individual aircraft operations.

On the downside, LCS have a relatively short life time (~2 – 3 years) and provide data of lower quality compared to AQM stations and lab grade instruments [58–61]. Research has however shown that their accuracy is sufficient to get a meaningful estimate of pollutant concentrations [56, 62]. Apart from this, both the lifetime and accuracy of LCS are expected to improve in the upcoming years due to the ongoing technological development [46, 47]. Despite their drawbacks it is therefore relevant to investigate the potential of using low-cost sensor nodes for analysing the pollution footprint of individual aircraft operations.

1.2 Previous work

It becomes clear from Table 1.1. that only a limited number of studies analysed gas-phase air pollutants for individual aircraft operations. The majority of these studies are 10 – 20 years old, hence the aircraft-engine combinations that were looked into may no longer be representative of the current global fleet. It can furthermore be observed that most research was limited to NO_x (consisting out of NO and NO_2) of departing aircraft. The actual contribution of in-service aircraft-engine combinations to pollutant concentrations for various activities (e.g., landings) is therefore currently not well understood [27].

To increase understanding in this area, the work carried out by Maes [63] is extended which focused on the development and demonstration of a low-cost sensor node. This follow-up research performs a series of field measurements with these nodes to assess the impact of departing- and landing aircraft on carbon monoxide (CO), nitric oxide (NO), nitrogen dioxide (NO_2) and sulphur dioxide (SO_2). Low-cost sensor nodes have only been used at or near airports by Popoola et al. [57], the AVIATOR campaign [64, 65] and Penza et al. [66]. However, these studies quantified the cumulative impact of airports on air quality rather than that of individual aircraft operations. To the author's knowledge, this research will therefore be the first that quantifies the real-world chemical composition of exhaust plumes for a wide variety of aircraft types and engine models representative of the current global fleet using low-cost sensor nodes.

[3] Although the term 'low-cost' is subjective, in this report the generally accepted definition is used that the cost is of a magnitude that it is considered feasible (in this case for the university) to deploy the equipment on a large scale (several dozens) [47].

Table 1.1: *Overview of existing research conducted in the past two decades that looked into gas-phase species of aircraft exhaust plumes based on measurements taken with lab grade instruments near airports*

Pollutant gases	Measurement site	Number of aircraft and activity	Year	Source
NO_x	~180 m downwind of a runway at London Heathrow airport	5618 departing transport aircraft	2005	Carslaw et al. [37, 67]
NO, NO_2, CO, HCHO	~100 – 600 m downwind of taxiways and runways at Hartsfield-Jackson International Airport	376 taxiing and departing transport aircraft	2004	Herndon et al. [6]
NO, NO_2,	~350 m of a taxiway and ~550 m of a runway at John F. Kennedy Airport	30 taxiing and departing transport aircraft	2001	Herndon et al. [68]
NO_x	~120 m of a taxiway and ~250 m of a runway at Roanoke Regional Airport	221 taxiing and departing commuter aircraft	2011	Klapmeyer et al. [69]
NO_x, CO, SO_2	~60 – 80 m of a taxiway at Brisbane Airport	60 departing transport aircraft	2007	Johnson et al. [70]
CO, NO, NO_2	~50 – 150 m downwind of gates and taxiways of Frankfurt Airport, London Heathrow Airport and Vienna Airport	138 stationary and taxiing transport aircraft	2003	Schäfer et al. [71]
NO_x, NO_2	~170 m from a runway of London Heathrow Airport	2877 departing transport aircraft	2017	Stacey et al. [52]
NO, NO_2	~210 m from a runway of Athens International Airport	30 departing transport aircraft	2007	Bossioli et al. [72]
NO, NO_x	~30 – 110 m from a runway at International Boryspol Airport	Unspecified number of taxiing, departing and landing transport aircraft	2017	Zaporozhets and Synylo [73]

1.3 Research framework

The objective of this research is as follows:

Research objective

To characterise exhaust plumes of individual departing- and arriving aircraft in terms of their chemical composition by performing field measurements with low-cost sensor nodes and comparing the resulting data to certified data using a (simple) dispersion model.

To reach this objective, aircraft attributable pollutant concentrations need to be extracted from the obtained air pollution data and coupled to specific aircraft operations. To assess the air pollution footprint of individual aircraft operations existing research (for example [37, 52, 69, 72, 73]) mainly focused on the maximum (i.e., peak) pollutant concentration. However, other parameters such as cumulative pollutant concentrations over time resulting from aircraft operations may provide important insights in the air quality impact of aircraft.

To extract these parameters, data can be analysed manually as was for instance done by Moore et al. [50] and Klapmeyer and Marr [69], but this is subjective and impractical due to the large amount of data acquired by sensor nodes. Therefore, preferably data would be processed automatically. This can however be complex as besides aircraft, (instrument) noise and other emission sources (e.g., road traffic) contribute to the obtained pollutant concentrations [19, 21, 37, 51, 67, 74–77]. Besides, aircraft may depart or arrive shortly after each other such that the exhaust plumes of multiple aircraft inter-mix [17, 37, 51, 52, 67, 74]. The first research question has therefore been formulated as shown below:

Research question 1

Is it possible to automatically characterise the pollution footprint of individual aircraft operations in terms of parameters such as the cumulative pollutant concentration?

After characterising the pollution footprint of individual aircraft operations, the results can be analysed to examine the variation in pollutant concentrations between different aircraft types, engine models and aircraft activity (i.e., taking off and landing). Therefore, the second research question is expressed as:

Research question 2

What is the pollution footprint of specific aircraft types and engine models and how does this footprint vary between take offs and landings?

For specific engine models the emission footprint is generally reported in terms of emission indices. The emission index is defined as the mass in grams of a pollutant *p* divided by the mass of fuel in kilograms. To estimate the emission index the emission ratio of pollutant *p* and CO_2 is multiplied with an assumed CO_2 emission index independent of the thrust setting as shown in Equation 1.1 [51, 78]. Hereby $A(p)$ and $A(CO_2)$ represent the cumulative aircraft attributable pollutant concentrations (or peak pollutant concentrations) of pollutant *p* and CO_2 respectively [51, 78].

$$EI_X = \frac{A(p)}{A(CO_2)} \times EI_{CO_2} \tag{1.1}$$

As the sensor nodes used in this research are not equipped with a CO_2 sensor, this approach cannot be used. However, similar to CO_2 the emission index of SO_2 is independent of the thrust setting [79–81]. It is therefore interesting to investigate whether SO_2 can be used instead to estimate emission indices. As far as the author is aware, no study exists in which this has been attempted. Therefore, the formulation of the third research question is:

Research question 3

Can an assumed emission index of SO_2 be used instead of CO_2 to estimate emission indices?

These research questions can be addressed using a single sensor node, but the simultaneous deployment of multiple sensor nodes offers the advantage of gathering additional information. By co-locating identical sensor nodes, the sensor-to-sensor variability can be quantified. This way, the level of agreement between low-cost gas sensors can be assessed. This is important, as a low level of agreement would suggest a high sensor-to-sensor variability, which gives lower confidence in the results [55, 57, 82]. Based on this, the fourth research question is given by:

Research question 4

What is the level of agreement between collocated sensor nodes?

Besides investigating the level of agreement, sensor nodes may be simultaneously deployed upwind- and downwind of the runway to investigate whether the difference in obtained signals can be used to determine aircraft attributable pollutant concentrations. The sensor nodes measure ambient pollutant concentrations, whereby to assess the emission footprint of individual aircraft operations the background concentration needs to be subtracted. As exhaust plumes of aircraft travel downwind under the influence of the prevailing wind, it is expected that aircraft emissions do not arrive at a sensor node placed upwind [1, 51, 83–89]. In this case, the aircraft attributable pollutant concentrations may be obtained by subtracting the concentrations obtained upwind from those that are retrieved downwind. Therefore, the fifth research question is formulated as:

Research question 5

Can pollutant concentrations measured upwind of a runway be subtracted from pollutant concentrations measured downwind of a runway to obtain the aircraft attributable pollutant concentrations?

The obtained results are compared to certified emission data using a (simple) dispersion model to assess the difference between actual pollutant concentrations and concentrations according to certified emission data. This leads to the sixth research question, which is described as:

Research question 6

What is the level of agreement between aircraft attributable peak pollutant concentrations resulting from field measurements and peak concentrations estimated using a (simple) plume dispersion model?

To answer the research questions and achieve the research objective the steps shown in Figure 1.1 will be performed. The main intended outcome is a novel tool capable of automatically processing the signals of low-cost nodes to assess the air quality impact of individual aircraft operations.

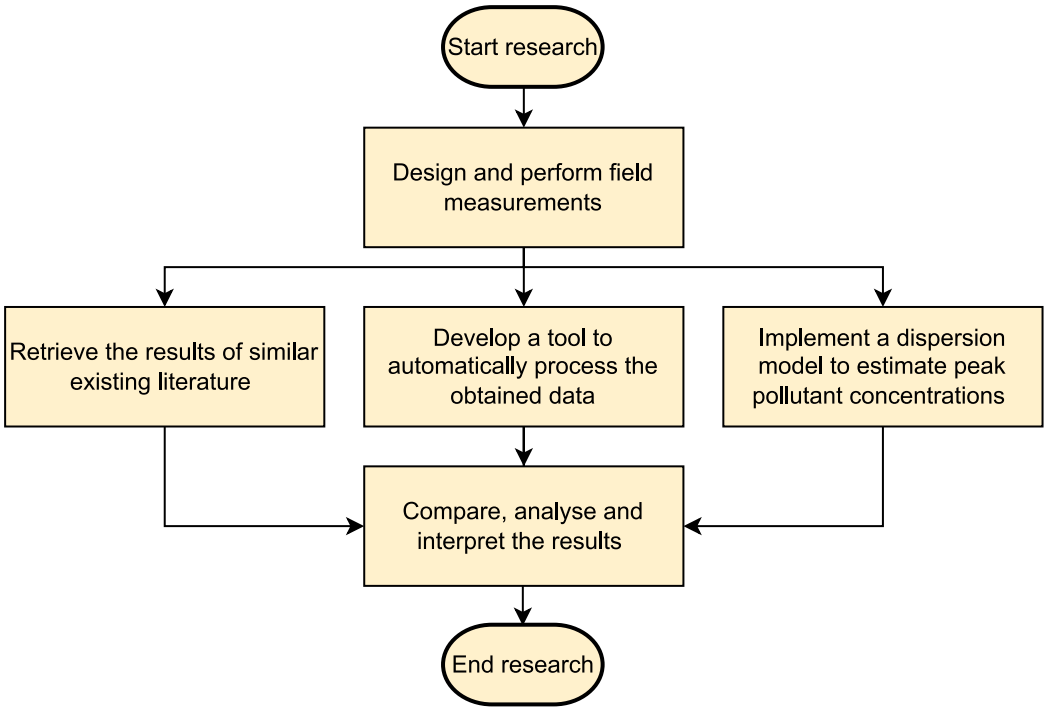

Figure 1.1: *Flow diagram summarising the steps performed during this research*

1.4 Outline of the report

This report is divided into three parts, which are divided into chapters. Part I includes the introduction and background. Chapter 1 first introduced the reader to the relevance of this research and the research framework. Next, Chapter 2 provides background information on aircraft emissions. Part II describes the materials and methods that were used and starts off with listing the external sources from which data was acquired in Chapter 3. Hereafter, Chapter 4 provides an overview of the designed experiments and equipment set-up. Chapter 5 explains how the acquired data is processed. Lastly, Chapter 6 describes the modelling approach to compare the obtained data to certified data. Part III includes the findings, conclusions and the recommendations. First, in Chapter 7 the results are presented and discussed after which Chapter 8 provides the conclusions as well as the recommendations for further research.

2 Background

This chapter provides background information relevant for the reader to better understand the methodology and the results of this research. First, Section 2.1 informs the reader of the species emitted by jet-engines and explains how a common aircraft exhaust plume is formed. Subsequently, different influences on measured aircraft emissions are discussed in Section 2.2. The chapter concludes with a summary in Section 2.3.

2.1 Aircraft exhaust plumes

The majority of the emitted gases and particles of commercial transport aircraft result from the combustion of hydrocarbon fuels by jet-engines [3, 13, 90]. Figure 2.1 provides an overview of the emitted species resulting from this combustion. The emissions considered in this study are carbon monoxide (CO), sulphur dioxide (SO_2), nitric oxide (NO) and nitrogen dioxide (NO_2) whereby the sum of NO and NO_2 is commonly referred to as nitrogen oxides (NO_x).

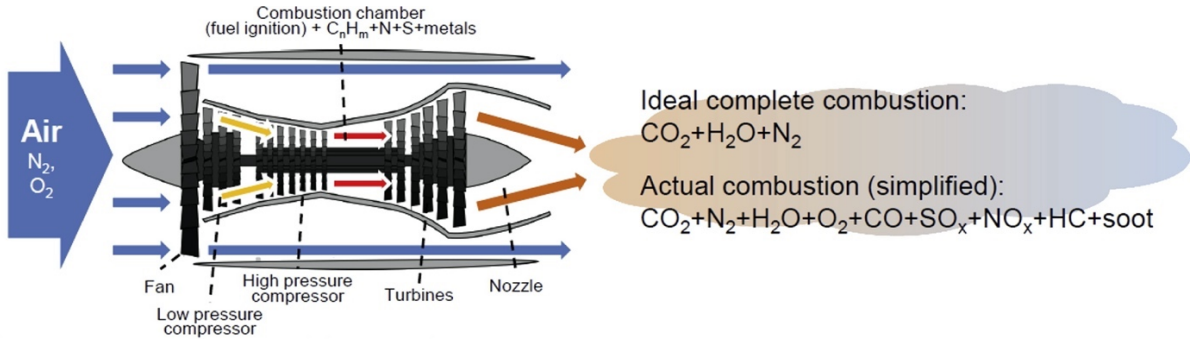

Figure 2.1: *Simplified representation of combustion emissions of a turbofan engine [3]*

These emissions leave the exhaust nozzle through a high momentum exhaust jet[4] [91, 92]. The exhaust jets of individual jet-engines are initially separated, but further downstream they may start to interact such that a region of integrated flow forms that exhibits the characteristics of a common (wider) exhaust jet [93–96]. Research of Bennett et al. [97], Christie et al. [94] and Graham et al. [85, 98, 99] observed that this common exhaust jet develops into a plume, hereafter referred to as the aircraft exhaust plume, in which the emission contribution of individual jet-engines can no longer be distinguished. Similar to other research (e.g., [1, 37, 67, 72, 100, 101]) it is therefore assumed for this research that aircraft generate a single exhaust plume encompassing the combined emissions of the main engines of the aircraft.

In case the ambient wind has a component acting perpendicular to the runway, this plume quickly turns in the direction of the wind due to the entrainment of ambient momentum[5] [1, 51, 83–89]. Aircraft exhaust plumes can therefore be captured by placing a sensor node downwind of an operational runway. The captured plume has undergone a physical and chemical evolution while travelling from the aircraft towards the downwind sensor node. While the plume ages it expands and dilutes as it mixes with ambient air. Meanwhile, buoyancy elongates the plume in vertical direction and may cause the plume to part contact with the ground [91, 103]. Furthermore, while the plume disperses into the atmosphere chemical reactions take place between the species contained in the plume as well as with ambient species that get entrained in the plume [20, 104]. The plume arriving at the downwind sensor node is therefore different from the exhaust jet leaving the jet-engine.

[4] In this report the term ‘exhaust jet’ is used to refer to the high-momentum exhaust flow in close proximity of the exhaust nozzle, while the term ‘exhaust plume’ is used to refer to the developed exhaust jet that exhibits lower momentum.

[5] Based on modelled results of an aircraft departing at 85% of the rated thrust in crosswinds of $V \gtrsim 2$ m/s the plume centreline approximately matches the wind direction after ~100 m with a plume velocity approximately equal to the wind speed [1, 102].

2.2 Influences on aircraft emissions

A variety of factors influence downwind aircraft attributable pollutant concentrations. Among the most important influences are the thrust setting, the engine state, ambient conditions, influences of the aircraft on the emission rate and plume dispersion and plume rise. These will now each be discussed in more detail.

2.2.1 Thrust setting

The thrust setting depends upon several operating- and meteorological conditions and can therefore differ up to ~40% between aircraft operations [13, 17, 105–108]. The rate at which pollutants are emitted depends upon the thrust setting. The emission rate can be expressed as the product of the fuel flow rate (the fuel mass burnt per second) and the emission index (the emitted mass of a pollutant per kilogram of fuel burnt). The emission index of CO is largest at low thrust due to the lower combustion temperature and pressure [4, 73, 80, 109, 110]. Conversely, the NO_x emission index is largest for high thrust settings when combustion temperatures are highest [4, 17, 71, 73, 110, 111]. Hereby the composition of NO_x depends upon the thrust setting with the large majority being emitted in terms of NO_2 during idle thrust while conversely at take-off thrust most NO_x comprises of NO [17, 71, 73, 110]. The emission index of SO_2 does not scale with thrust. SO_2 results from the oxidation of sulphur-containing compounds in the fuel and is therefore directly proportional to the amount of sulphur in the fuel [79, 80, 112, 113].

The thrust setting is not only of importance for departing aircraft, but may also affect the emissions of landing aircraft. During the landing roll thrust reversers may be deployed as an additional means to decelerate the aircraft [114, 115]. When more than idle reverse thrust is used, the rate at which pollutant species are emitted is altered [116]. Besides, reverse thrust has an impact on plume dispersion as it redirects (part of) the exhaust [89]. The reverse thrust setting is up to the pilot and depends on several factors such as airline policy [114, 115, 117, 118].

2.2.2 Ambient conditions

Ambient conditions affect the emissions of jet-engines and impact the evolution of aircraft exhaust plumes. Changes in ambient temperature, pressure and humidity alter the properties of the air entering the engine which can influence CO and NO_x emissions [119]. CO emissions generally decrease with increasing ambient temperature and pressure and tend to increase with increasing humidity. NO_x emissions generally increase with increasing ambient temperature and pressure and decrease with an increase in humidity [73, 120, 121].

Besides affecting the emissions of jet-engines, ambient conditions affect how a plume evolves whereby mainly the wind, turbulence and temperature play an important role [122]. Firstly, turbulence enhances plume dispersion as it causes gases to be transported more quickly in the atmosphere and furthermore increases the chemical reactivity between pollutant species [123, 124]. Secondly, ambient wind increases the entrainment rate[6] which decreases pollutant concentrations while on the other hand potentially decreasing plume rise and therefore increasing ground level pollutant concentrations [122, 124–126]. Furthermore, wind-shear may increase plume dispersion through a shear rate that distorts the plume [122, 125, 127, 128]. Lastly, ambient temperature influences plume dispersion, for example by enhancing the plume's vertical momentum when a temperature difference exists between the plume and the surrounding air [80, 97, 129].

[6] The entrainment rate is the rate at which the plume mixes with surrounding ambient air.

2.2.3 Aircraft influences

The aircraft (i.e., the airframe and its systems) can influence the dispersion of exhaust plumes and the rate at which species are emitted. Research of Aloysius and Wrobel [84, 130] revealed that an aircraft including its airframe has a higher horizontal and vertical dispersion compared to stand-alone jet-engines. The aircraft's airframe acts as a physical boundary for the plume and increases dilution through aircraft induced turbulence [84, 130]. Furthermore, airframe vortices, which are flows moving downstream with a circular motion, impact the dispersion of the plume [131]. Especially the vortices arising from each wingtip can play an important role as the exhaust jets can become entrained in the vortex of the corresponding wing and remain trapped in this vortex as shown in Figure 2.2 (a) until it breaks-up. The interaction between vortices and the plume depends upon the aircraft's speed, with the interaction being larger at higher speeds [1, 97, 99, 132].

The speed of the aircraft may also affect the rate at which pollutants are emitted. When an aircraft accelerates down the runway during the take-off roll, the velocity of the flow entering the engine inlet will increase [97, 133]. The associated change in momentum causes a reduction in thrust for a given mass flow rate. The Engine Control System (ECS) detects this and may command an increase in mass flow rate to maintain the thrust, which changes the emission rate [89, 134, 135].

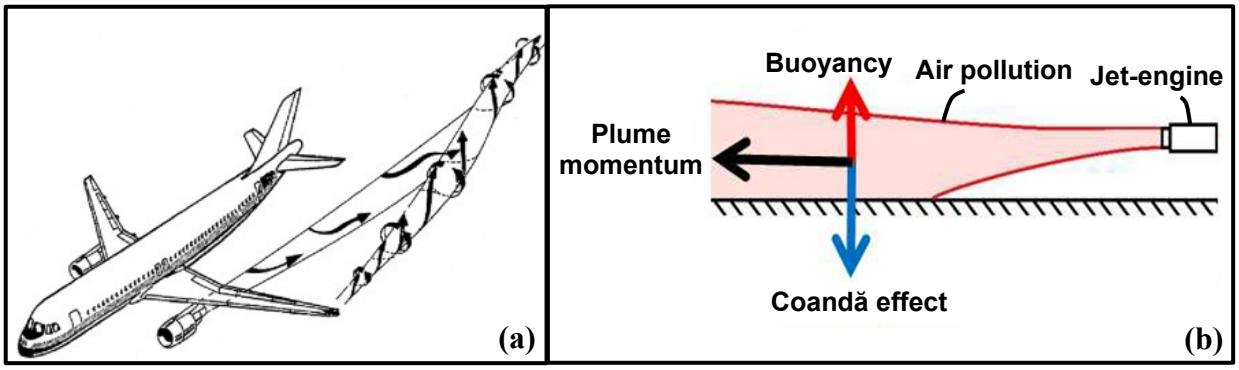

Figure 2.2: *Visualisation of the entrainment of an exhaust jet in a wingtip vortex [136] (a) and schematic representation of the main influences on plume formation and evolution [91] (modified by author) (b)*

2.2.4 Plume rise

Downwind aircraft attributable pollutant concentrations may be affected by plume rise. After the exhaust jet is released from the engine, the Coandă effect and buoyancy start to influence the formation and evolution of an aircraft exhaust plume as shown in Figure 2.2 (b) [91, 137]. For wing-mounted aircraft (which encompasses the majority of modern transport aircraft) the exhaust jet is released in close proximity to the ground [91]. This causes a low-pressure area to develop that tends to rapidly deflect the jet towards the runway, which is referred to as the Coandă effect [91–93, 97, 138, 139]. Plume buoyancy, which results from the temperature difference of the exhaust jet and the surrounding ambient air, forces the plume upwards. Initially the Coandă effect dominates over buoyancy such that the exhaust jet remains close to the ground [93, 97]. However, while the plume ages buoyancy may become dominating such that the plume may separate from the ground [36, 91, 92, 97, 129]. As a result the large majority of the plume rises upwards with only a small residual part being left close to the ground, resulting in low ground level pollutant concentrations [86].

The effect of plume rise on ground level pollutant concentrations is however currently not well understood (see e.g., [1, 140, 141]). Theoretically it is expected that whether the plume starts to rise above the ground depends upon the aircraft-engine combination, engine thrust, aircraft speed and meteorological conditions [36, 89, 92]. However, Wayson et al. [128, 142] found no

statistically significant dependence upon the aircraft type, ambient temperature, wind speed, wind direction or atmospheric stability. Similarly, Eberhard [36] did not observe statistically significant differences between the plume rise of different aircraft types. It is furthermore currently unclear if and at which point aircraft exhaust plumes part contact with the ground, although Graham et al. [92] and Bennett et al. [97] revealed that this may occur ~80 seconds after being emitted for modern transport aircraft with high bypass engines taking off in light winds.

2.2.5 Engine state

Another potential influence on downwind aircraft attributable pollutant concentrations is the engine state. Certified emission data is published by the International Civil Aviation Organization (ICAO) for newly manufactured engines. However, engines may deteriorate over time for a variety of reasons such as the build-up of dirt, which can alter the rate at which emissions are emitted [13, 143].

2.3 Summary

The majority of the emissions of commercial transport aircraft result from the combustion of hydrocarbon fuels. Research observed that the emissions released by the aircraft's jet-engines form a common plume, which quickly turns in the direction of the ambient wind such that it can be captured by a sensor node downwind of a runway. The captured plume has undergone a physical and chemical evolution while travelling towards a sensor node and its composition is therefore different than the emissions released by jet-engines. The aircraft attributable pollutant concentrations that are measured at a downwind location depend upon a variety of factors, among which are the thrust setting, ambient conditions, aircraft influences, plume rise and the engine state.

Part II: Materials and methods

3 External data sources

This chapter provides a description of the utilised data sources excluding the hardware and software, which will be described in the next chapter. An overview of these data sources is provided in Section 3.1. Section 3.2 discusses the purpose of the meteorological data sources, after which Section 3.3 provides the same information with respect to aircraft- and engine data. Lastly, Section 3.4 provides a summary of the chapter.

3.1 Overview of external data sources

The utilised external data sources can be subdivided into two categories: meteorological data and aircraft- and engine data, of which an overview is presented in Figure 3.1. The remainder of this chapter discusses each category and the associated sources.

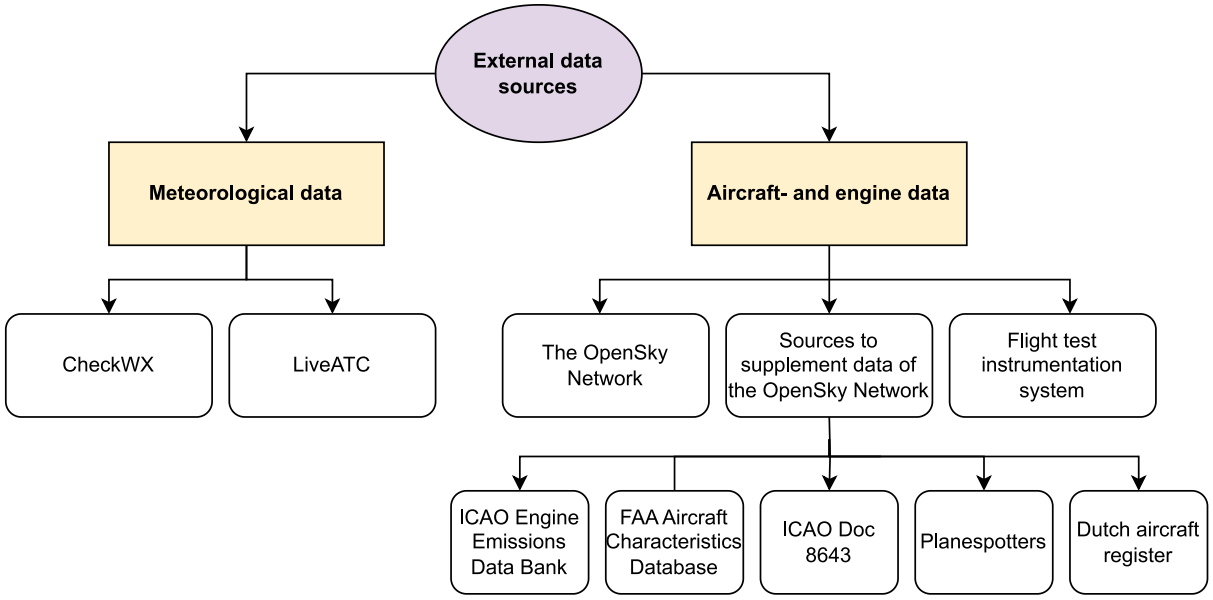

Figure 3.1: *Overview of external data sources used during this research*

3.2 Meteorological data

Meteorological data is retrieved from two sources: Meteorological Terminal Aviation Routine Weather Reports (METARs) and Air Traffic Control (ATC) voice recordings.

3.2.1 CheckWX

METARs are reports containing weather information associated with a specific airport. Each report consists of a range of meteorological parameters, of which the ones relevant for this research are listed in Table 3.1. METARS are issued by the Royal Netherlands Meteorological Institute (KNMI) and are automatically obtained from the website CheckWX [144] using an algorithm developed during previous research [144]. It was discovered that when KNMI reports the wind direction as variable[7] (VRB), CheckWX (incorrectly) reports this as 0°. However, this has no consequences on the results of this research.

[7] Wind is defined as variable in case the mean wind speed W_s < 3 KT and the wind direction W_d varies with >60° and <180° and when W_s >0 KT and the variation in W_d is ≥ 180° [145].

Table 3.1: *Overview of data acquired from CheckWX*

Parameter	Parameter description	Purpose in this research
Wind speed	Average surface wind speed in knots during the last 10 minutes before a METAR is issued	Used to couple measured pollutant concentrations to specific aircraft operations
Wind direction	Average surface wind direction in degrees from which wind is approaching with respect to true north (positive clockwise) during the last 10 minutes before a METAR is issued	Used to couple measured pollutant concentrations to specific aircraft operations
Temperature	Ambient air temperature in degrees Celsius	Used to correct emission indices for ambient conditions
Pressure	Ambient air pressure in hectopascals	Used to correct emission indices for ambient conditions
Relative humidity	Ambient relative humidity expressed as a percentage	Used to correct emission indices for ambient conditions

3.2.2 LiveATC

The use of METARs is suboptimal as the associated weather station is situated approximately six kilometres from the location where pollutant concentrations are measured[8]. Furthermore, METARs are normally only issued every 30 minutes and report the wind speed and wind direction for a height of 10 meters above the ground rather than at ground level [146]. As ambient conditions can continuously change in space and time the use of an alternative source is desired, especially in terms of wind as this is used to couple measured pollutant concentrations to specific aircraft operations.

To obtain higher resolution runway-specific wind data, ATC voice recordings are used. Air traffic controllers report the prevailing wind speed and wind direction to each departing- and arriving aircraft based on instruments situated near the Touch Down Zone (TDZ) of each runway. This information is typically provided to pilots on the order of a few minutes before touch-down and several seconds before aircraft initiate the take-off roll. Historical ATC voice recordings were kindly provided by LiveATC [147]. As this website only stores data up to a year, ATC-based wind data could only be used for measurements conducted after 22-03-2022, hence for measurements conducted before this date METARs are used.

3.3 Aircraft- and engine data

Besides meteorological data, aircraft- and engine data needs to be obtained to assess the pollution footprint of individual aircraft-engine combinations.

3.3.1 The OpenSky Network

To obtain aircraft-and engine data, primarily data of the OpenSky Network [148] is used, which is an open access flight tracking database based on a crowd-sourced network of receivers. The parameters relevant for this research that are obtained from this source are shown in Table 3.2 [149].

[8] The location of the Schiphol weather station is 52°19'08.8"N 4°47' 24.8"E.

Table 3.2: *Overview of data acquired from the OpenSky Network*

Parameter	Parameter description	Purpose in this research
ICAO address	Transponder identification code	Used as an identifier of aircraft operations
Registration	Alphanumerical character that is displayed on the exterior of aircraft	Used as the identifier of an aircraft operation
Callsign	Alphanumeric character used as an identifier of an aircraft operation for communications purposes	Used as the identifier of an aircraft operation
Aircraft type	Alphanumeric character used as a designator of the aircraft model	Used to compare the pollution footprint of different aircraft types
Position and time	Latitude and longitude of an aircraft operation at a specific moment in time	Used to couple measured pollutant concentrations to specific aircraft operations
Ground speed	Ground speed (in meters per second) of an aircraft operation	Used to determine the activity (e.g., landing) conducted by an aircraft operation
Barometric altitude	Altitude of an aircraft operation as measured by the aircraft's barometer	Used to determine the activity (e.g., landing) conducted by an aircraft operation
On ground Boolean	Boolean to indicate whether an aircraft is broadcasting surface positions or not	Used to determine the activity (e.g., landing) conducted by an aircraft operation
Engine model	Alphanumeric character as an identifier of the specific engine model an aircraft is equipped with	Used to compare the emission footprint of specific engine models

3.3.2 Supplemental data sources

Data of the OpenSky Network is supplemented by five sources including the International Civil Aviation Organization (ICAO) Emissions Databank [150], FAA Aircraft Characteristics Database [151], ICAO Doc 8643 [152], Planespotters.net [153] and the Dutch Aircraft registry [154]. Table 3.3 provides an overview of the parameters obtained from these sources.

With respect to aircraft registered out of the Netherlands, the OpenSky Network is used as the primary source to assign an engine model and aircraft type to an aircraft operation. For ~10% of the encountered aircraft operations no aircraft type was specified by this source. Similarly, for ~20% of the aircraft operations no engine model was specified by the OpenSky Network. To fill in the missing information, Planespotters.net [153] is used which contains crowd-sourced information of aircraft types and engine models. Regarding aircraft registered in the Netherlands the Dutch aircraft register is used to assign engine models to aircraft. This register is maintained by the Human Environment and Transport Inspectorate and is thus considered to be among the most up-to-date and reliable sources. Other aircraft registries were not implemented due to several complications such as the absence of a downloadable format of the register. Although both the OpenSky Network and Planespotters.net claim to utilise aircraft registers as their main source, it is acknowledged that the use of crowd-sourced information is less reliable [153, 155].

Table 3.3: *Overview of data acquired from sources to supplement OpenSky Network data*

Parameter	Parameter description	Purpose in this research	Source
Emission index	The mass in grams of an emitted pollutant per kilogram of fuel burnt	Used to compare obtained results with certified emission data	ICAO Emissions Databank [150] (version 28 C)
Fuel flow rate	The amount of fuel mass (in kilogram) consumed by an engine per second	Used to compare obtained results with certified emission data	
Rated thrust	The approved maximum static take-off thrust at standard atmospheric conditions at mean sea level	Required to obtain the emission index and fuel flow rate	
Maximum take-off weight	Maximum weight an aircraft type is certified for to take off with	Used to group aircraft types from light to heavier	FAA Aircraft Characteristics Database [151] (version corresponding to 07-02-2023)
Wake Turbulence Category	Single alphabetical character indicating the amount of wake turbulence generated by an aircraft	Used to group aircraft types from smaller to larger	ICAO Doc 8643 [152] (version corresponding to 24-02-2023)
Number of engines	Number of engines an aircraft is equipped with	Used to compare obtained results with certified emission data	
Aircraft type	Alphanumeric character used as a designator of the aircraft model	Used to compare the pollution footprint of different aircraft types	Planespotters.net [153] and the Dutch aircraft register [154]
Engine model	Alphanumeric character as an identifier of the specific engine model an aircraft is equipped with	Used to compare the pollution footprint of different engine models	

3.3.3 Flight test instrumentation system

An experiment was performed on a research aircraft that was equipped with a Flight Test Instrumentation System (FTIS) to record parameters of the aircraft and its engines. The parameters used for this research are shown in Table 3.4, which were retrieved from FTIS using an algorithm of F. Postema.

Table 3.4: *Overview of data acquired from the Flight Test Instrumentation System*

Parameter	Parameter description	Purpose in this research
Fuel flow rate	Amount of fuel mass (in kilograms) consumed by an engine per second	Used to compare obtained results with certified emission data
Turbine inlet temperature	Temperature inside the turbine stage of the engine	Used to verify that the combustor temperature is approximately constant
N1 power setting	Rotational speed of the low pressure system	Used to verify that engine thrust is approximately constant

3.4 Summary

From external data sources meteorological data and aircraft- and engine data are retrieved. Regarding meteorological data, wind, temperature, pressure, and relative humidity are obtained from METARs. Additionally, ATC voice recordings are used to get higher resolution and runway-specific wind data. Aircraft-and engine data are obtained from the OpenSky Network and supplemented by the ICAO Emissions Databank, FAA Aircraft Characteristics Database, ICAO Doc 8643, Planespotters.net and the Dutch Aircraft registry. With respect to aircraft registered out of the Netherlands, the OpenSky Network is used as the primary source to assign an engine model and aircraft type to aircraft operations. Planespotters.net is used in case this information was not specified by the OpenSky Network. For aircraft registered in the Netherlands, the Dutch aircraft register is used as the primary source to assign engine models to aircraft. Besides the OpenSky Network and supplemental sources, FTIS (a system that records aircraft- and engine parameters) was used for a research aircraft with which an experiment was performed.

4 Experimental set-up

Chapter 4 is devoted to a description of the experimental set-up. Section 4.1 focusses on the utilised hardware and software. Section 4.2 describes the measurement site where equipment was deployed. Subsequently, Section 4.3 discusses the designed experiments. The chapter concludes with a summary in Section 4.4.

4.1 Software and hardware

This chapter starts off by giving a description of the utilised software and hardware.

4.1.1 Software description

Coding was (predominantly) performed in Python (version 3.9) in Anaconda [156] (version 2.2.0) as the author was most familiar with this programming language and because the algorithms developed during previous research were developed in Python. Several additional packages were used which are listed in Appendix A.1. Besides this programming language, Arduino [157] (version 1.8.16) was used to manually set the time of the internal clocks of the sensor nodes for each measurement as these are prone to drift over time [63]. Furthermore, Microsoft Excel [158] (version 16.66.1) was used to store data in spreadsheets.

4.1.2 Hardware description

The utilised hardware consists of the components displayed in Figure 4.1.

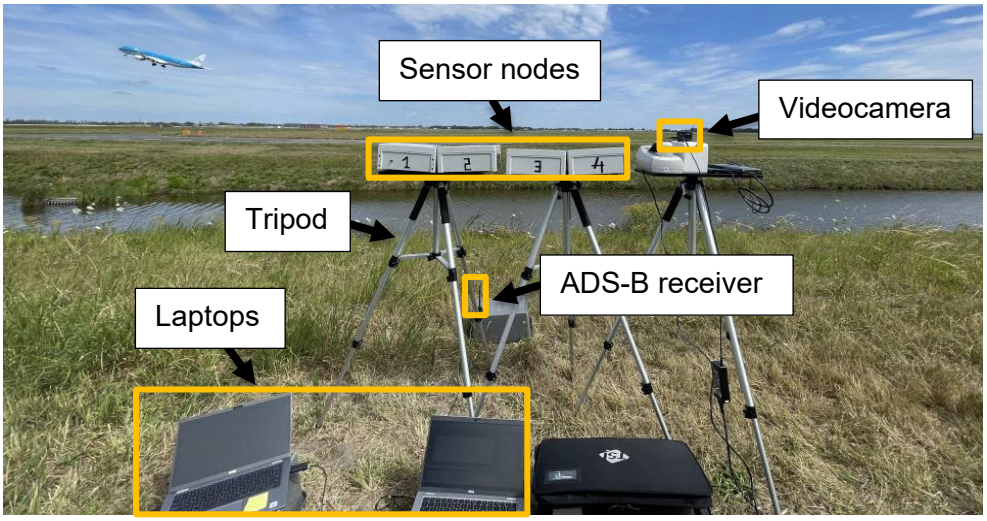

Figure 4.1: *Typical equipment set-up during a field measurement*

During previous research the low-cost sensor node depicted in Figure 4.2 was designed to measure air pollution and meteorological parameters. Throughout this follow-up research three additional nodes were built, which measure the pollutant species shown in Table 4.1.

Table 4.1: *Measured pollutant species and the name of the incorporated gas sensors*

Identifier	Measured gases	Gas sensors
Node 1	CO, NO, NO_2, SO_2,	Alphasense Ltd CO B4, NO B4, NO2 B43F, SO2 B4
Node 2	CO, NO, NO_2, VOC	Alphasense Ltd CO B4, NO B4, NO2 B43F, VOC B4
Node 3	NO, NO_2	Alphasense Ltd NO B4, NO2 B43F
Node 4	NO, NO_2	Alphasense Ltd NO B4, NO2 B43F

Except for the measured pollutant species, the four sensor nodes are identical. For a detailed description of the design of the sensor node, the reader is referred to the report of Maes [63]. Furthermore, an overview of the specifications of the employed gas sensors is provided in Appendix A.1. The gas sensors were powered one day prior to each measurement to ensure sufficient stabilisation time, as according to the sensor manufacturer [159] it generally takes several hours for the gas sensors to stabilise after powering a sensor node. The sensor nodes are placed on tripods to prevent vegetation from blocking the flow towards the sensors and to ensure that measurements are conducted near human breathing level, which is recommended for air quality research [49].

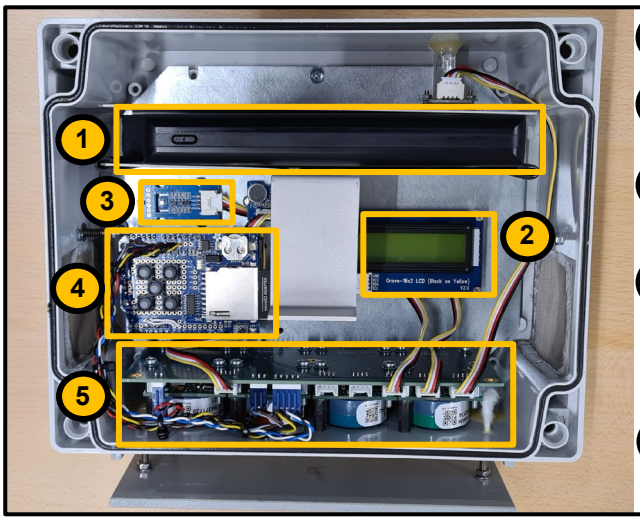

1. Battery (Ansmann 2A 5V) to power the node.
2. Liquid Crystal Display to show messages (e.g., errors) to the user.
3. Barometric sensor (Grove BME280) to measure internal pressure, relative humidity and temperature.
4. Microcontroller (Arduino UNO REV3) to power sensors and extract outputs, a clock (Adafruit PCF8523) to obtain timestamps, an external memory to store data and push buttons to start/stop recording.
5. Electro-chemical gas sensors and analogue to digital converters to obtain digital air pollution data.

Figure 4.2: *Overview of the components of a sensor node employed in this research*

Besides the sensor nodes, a video camera (GoPro Hero 3) was deployed which took a picture of the runway every 5 seconds. Pictures in which no vehicle (such as an aircraft) could be seen were removed by J. Maes and M. van Lent. The remaining pictures were used to verify whether aircraft were making use of the Polderbaan runway and to log the presence of potential sources of interference. Furthermore, an ADS-B receiver (the GNS 5890) was used in an attempt to gain higher resolution aircraft activity data compared to the OpenSky Network. All data was processed on a MacBook Pro (2,7 GHz Dual-Core Intel Core i5).

4.2 Measurement sites

The equipment described in the previous section was deployed at two measurement sites. These sites will now be discussed together with (potential) nearby sources of interference.

4.2.1 Selected measurement sites

Field measurements were (mainly) performed near the Polderbaan runway (18R/36L) of Amsterdam Airport Schiphol (hereafter referred to as Schiphol Airport for brevity), which is located ~10 kilometres south-west of the city Amsterdam in the Netherlands. This airport was selected as it enables to measure a large amount of aircraft operations in a short amount of time as Schiphol Airport is the 2nd largest airport of Europe in terms of air transport movements[9] [160]. Besides, Schiphol Airport serves aircraft types and engine models representative of the current global fleet, which ensures that the air quality impact of different in-use aircraft types and engine models can be determined [161]. Next to this, the Polderbaan runway of Schiphol Airport is detached from the main airport (see Figure 4.3 (a)), which minimises the interference

[9] Based upon the year 2021 during which ~267 000 take-offs and landings took place at the airport.

of other airport emission sources (e.g., airport road vehicles) on measured pollutant concentrations.

To determine where sensor nodes can be located for the selected airport-runway combination, four criteria were taken into account. Firstly, the site should be a safe non-intrusive location such that activities at and near the airport remain unimpaired. Secondly, it should allow the sensor nodes to be exposed to the prevailing ambient wind in the absence of obstructions such as walls that could disrupt the flow towards the gas sensors. Thirdly, the site should not be near pollutant sources other than aircraft. Lastly, the sensor nodes should be located at a distance close enough from aircraft such that exhaust plumes of individual aircraft operations can still be observed in the obtained data [51, 52, 162]. Based upon these criteria, the sensor nodes were placed to the west (52°20'53.08"N 4°42'48.2"E) and east (52°20'35"N 4°42'27"E) of the Polderbaan runway as depicted in Figure 4.3 (a). Both are publicly accessible locations at a distance of ~190 m from the runway. Note that all landings occurred on runway 18R while departures solely took place on runway 36L.

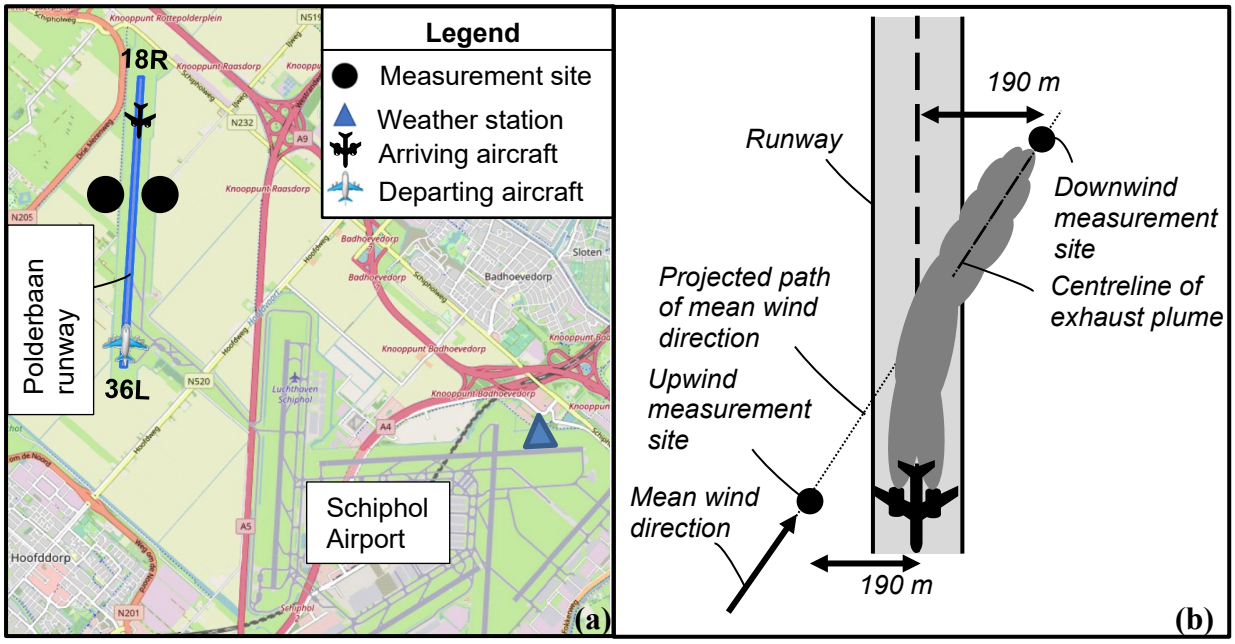

Figure 4.3: *Schematic overview of the measurement sites and weather station (a) and graphical explanation of upwind and downwind measurement sites (b)*

4.2.2 Sources of interference

Sources that may contribute to ambient pollutant concentrations at the selected measurement sites mainly consist of vehicles on highways, roads, paths, and fields. Nearby highways include the A9, A5 and A4 as shown in Figure 4.3 (a) and the closest local roads are the N205, N201, N519, N232 and N520. Besides, a path by the name '*Polderbaanpad*' alongside the Polderbaan runway is used by tractors, mopeds, and law-enforcement vehicles. Tractors may also be operating on nearby fields surrounding the runway. Furthermore, there are service roads parallel to the runway that are utilised by airport vehicles. The number of road vehicles on highways and local roads has not been kept track of, but activities on nearby paths and fields were logged in timestamped measurement notes.

4.3 Designed experiments

Four experiments were designed and executed during 10 measurements, which were performed in between 22-01-2021 and 28-07-2022 by J. Maes and the author of this report[10]. An overview of the measurement dates and ambient conditions can be found in Appendix A.2. Each of the designed experiments will now be discussed.

4.3.1 Downwind experiment

The downwind experiment has the aim to gather data required to assess the pollution footprint of aircraft types and engine models and thereby answer the first and the second research question. For this, a single sensor node (Node 1) was placed downwind of the runway with the gas sensors (approximately) pointing in the direction of the wind such that exhaust plumes could be captured as shown in Figure 4.3 (b) and Figure 4.4 (a)[11]. To make sure that plumes arrived at the sensor node, it was (similar to other studies such as [102, 126, 163]) chosen to solely measure when the forecasted crosswind was >2 m/s. Furthermore, measurements were not performed when crosswinds >10 m/s were forecasted as in this case the Polderbaan runway is not selected as the primary runway [164]. In total eight measurements were conducted in between 22-01-2021 and 28-07-2022 of which three could not be used as the crosswind was (continuously) <2 m/s. The wind of the remaining measurements is depicted in Figure 4.4 (b).

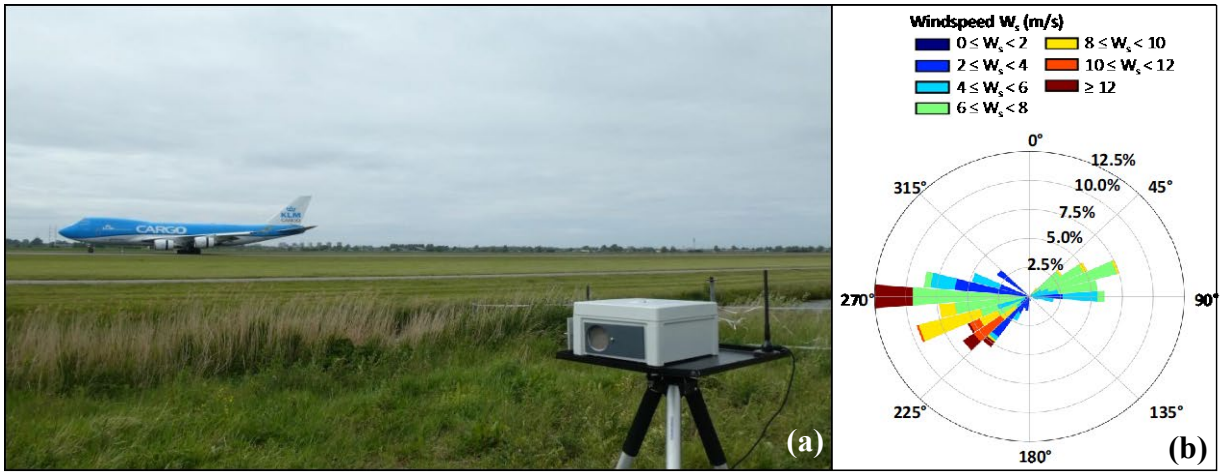

Figure 4.4: *Equipment set-up of the downwind experiment (a) and a wind rose showing the percentage of occurrence of the wind approaching from a certain direction together with the wind speed (b)*

4.3.2 Upwind experiment

The upwind experiment has the aim to assess whether pollutant concentrations measured upwind of a runway can be subtracted from downwind concentrations to retrieve the aircraft attributable concentrations and thereby answer the fifth research question. For this, a single sensor node (Node 2) was placed in opposite direction of the ambient wind (either east or west of the runway) as shown in Figure 4.3 (b) and Figure 4.5 (a). Three measurements were performed in between 22-03-2022 and 25-05-2022, of which the measurement conducted on 22-03-2022 was discarded as the prevailing crosswind was continuously <2 m/s. The wind of the remaining measurements is depicted in Figure 4.5 (b).

[10] An exception was the first measurement (conducted on 22-01-2021), which was only attended by J. Maes.

[11] For the experiment performed on 22-01-2021 the gas sensors were facing upwards, but it is assumed that this has a negligible effect on the obtained gas-concentrations.

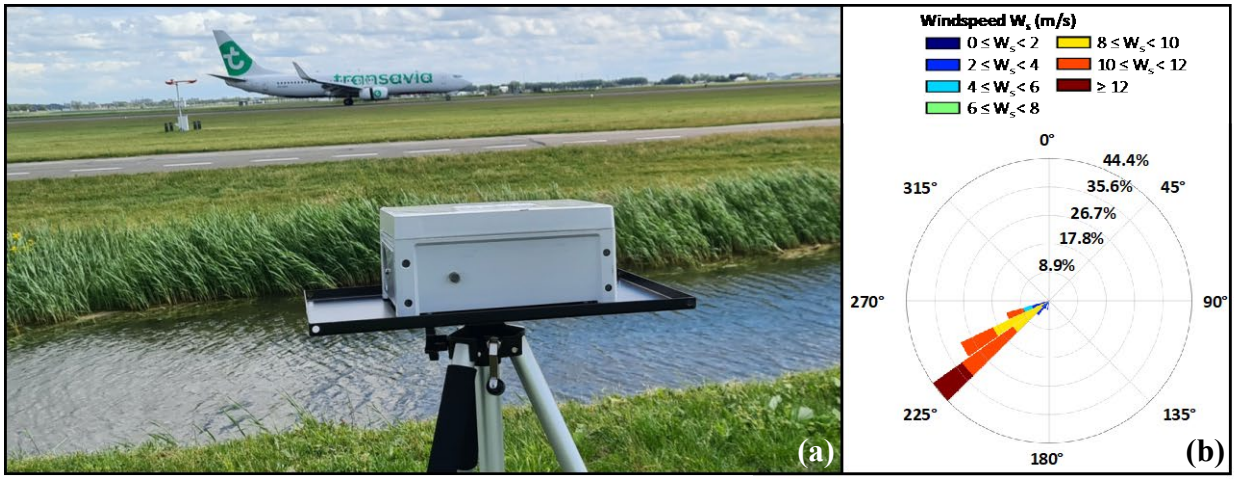

Figure 4.5: *Equipment set-up of the upwind experiment (a) and a wind rose showing the percentage of occurrence of the wind approaching from a certain direction together with the wind speed (b)*

4.3.3 Co-location experiment

The co-location experiment has the aim to determine the level of agreement between the output of identical sensor nodes such that the fourth research question can be answered. During this experiment multiple sensor nodes are collocated downwind of the runway to form a cluster as shown in Figure 4.6 (a). Excluding the measurement conducted on 22-03-2022 during which the crosswind was continuously below 2 m/s, four measurements were performed in between 06-05-2022 and 28-07-2022. The prevailing wind of these measurements is depicted in Figure 4.6 (b).

Figure 4.6: *Equipment set-up of the co-location experiment (a) and a wind rose showing the percentage of occurrence of the wind approaching from a certain direction together with the wind speed (b)*

4.3.4 Near engine exit plane experiment

The near engine exit plane experiment has the aim to assess whether SO_2 can be used to estimate emission indices and thereby address the third research question. This experiment involved two measurements near a stationary Cessna 550 Citation II equipped with two turbofan Pratt and Whitney JT15D-4 engines burning Jet-A1 fuel. Each measurement consisted of engine start-up, ~5 minutes of idle thrust (the maximum allowable thrust due to airport restrictions) and engine shut down.

Ideally sensor nodes would be located within a distance equal to half the engine's exhaust nozzle diameter as measurements of certified emissions are taken within this distance [79, 165, 166]. However, due to safety constraints and to protect the equipment sensor nodes were placed at a minimum distance of 10 m from the exhaust nozzle. During the first measurement a single node was therefore deployed 10 m behind the number 1 engine at a height of ~1.2 m with the gas sensors oriented parallel to the exhaust stream as depicted in Figure 4.7.

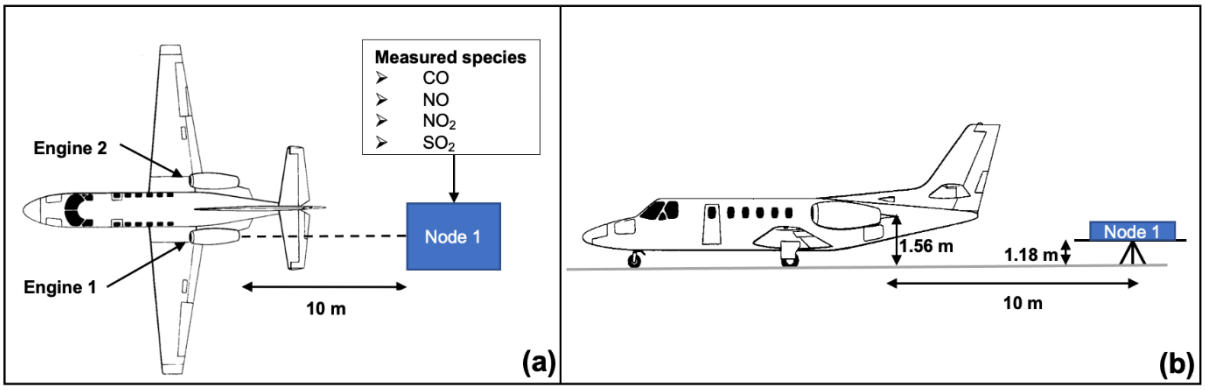

Figure 4.7: *Top view (a) and side view (b) of equipment set-up of the first near engine exit plane measurement (not to scale, aircraft blueprint obtained from [167])*

For the second measurement the first sensor node remained at the same location, but an additional sensor node was deployed 20 m behind the number 1 engine as shown in Figure 4.8[12]. This location was selected to investigate whether it can be observed that NO chemically converts to NO_2 with increased distance from the exhaust nozzle. Both sensor nodes were located at a height of ~0.5 m.

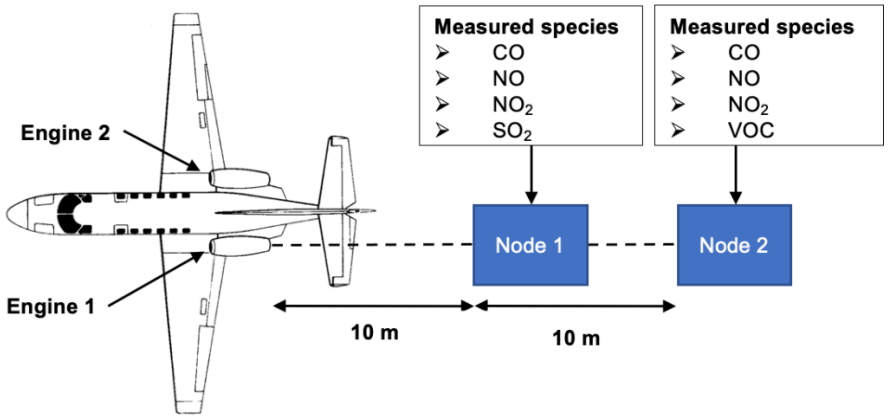

Figure 4.8: *Top view of the equipment set-up of the second near engine exit plane measurement (not to scale, aircraft blueprint obtained from [167]).*

These measurements took place at Rotterdam the Hague airport at 51°57'03"N 4°26'26"E (see Figure 4.9 (a)) on 04-04-2022. During the first measurement the ambient pressure (P) was 1008 hPa, the temperature (T) 6°C and the relative humidity (RH) ~87%. For the second measurement P, T and RH were 1007 hPa, 7°C and ~83% respectively. The prevailing wind is depicted in Figure 4.9 (b). For the first measurement the wind speed was 20 kts (~10 m/s) gusting 35 kts (~18 m/s) from a mean wind direction of 220°. For the second measurement, a wind speed of 20 kts (~10 m/s) from a (mean) wind direction of 230° was reported with the wind direction varying between 210° and 270°. It should therefore be noted that the

[12] As during the first measurement the sensor node fell on the ground it was chosen to lower the height.

measurements were conducted in non-ideal conditions with strong and variable winds, low temperature, and high relative humidity.

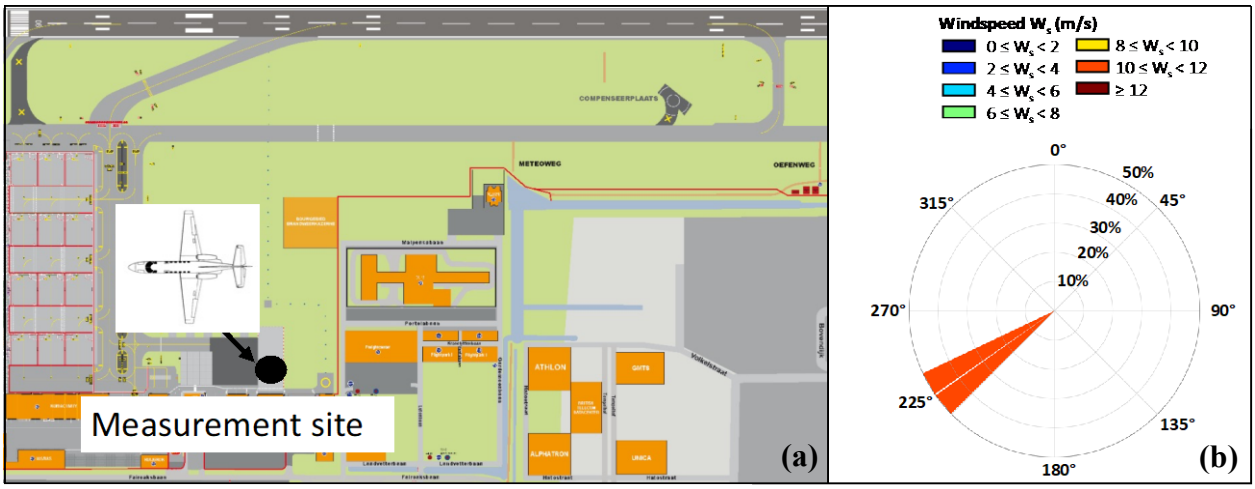

Figure 4.9: *Measurement site and aircraft orientation (map obtained from [168]) (a) and a wind rose showing the percentage of occurrence of the wind approaching from a certain direction together with the wind speed (b)*

4.4 Summary

The utilised hardware consists out of sensor nodes, tripods, a video camera, an ADS-B receiver and a laptop with coding (predominantly) performed in Python. This hardware was deployed ~190 m perpendicular to the Polderbaan runway of Schiphol Airport at which four experiments were performed. In the first experiment a sensor node is placed downwind to capture aircraft exhaust plumes. For the second experiment multiple nodes are collocated downwind of the runway to quantify their level of agreement. For the third experiment one sensor node is located upwind to observe whether its obtained pollutant concentrations can be subtracted from downwind concentrations to retrieve the aircraft attributable concentrations. Lastly, for the fourth experiment sensor nodes were located near an engine exhaust nozzle to compare measured- and certified emission indices. Nearby sources of interference at the selected location for these experiments mainly consist of vehicles on nearby highways, roads, paths, and fields.

5 Data processing

This chapter elaborates on the data processing method. First, an overview of the method is provided in Section 5.1. Thereafter, Section 5.2 describes how the data is prepared prior to further processing and analysis. Section 5.3 explains how the time at which an aircraft gives rise to a peak pollutant concentration at the measurement site is estimated. Next, Section 5.4 explains how this time is used to identify aircraft attributable signals in air pollution data. The subsequent section (Section 5.5) discusses how these signals are represented by a Gaussian curve. Section 5.6 explains the characterisation of Gaussian plumes in terms of parameters such as the plume area. The subsequent section, namely Section 5.7, elaborates on the quality control procedures. Thereafter, Section 5.8 explains how NO_2 plumes not passing quality control are characterised. Lastly, Section 5.9 provides a summary of the chapter.

5.1 Method overview

Prior to data analysis the acquired data is processed, for which the steps shown in Figure 5.1 are performed. These steps will be elaborated on in the upcoming sections.

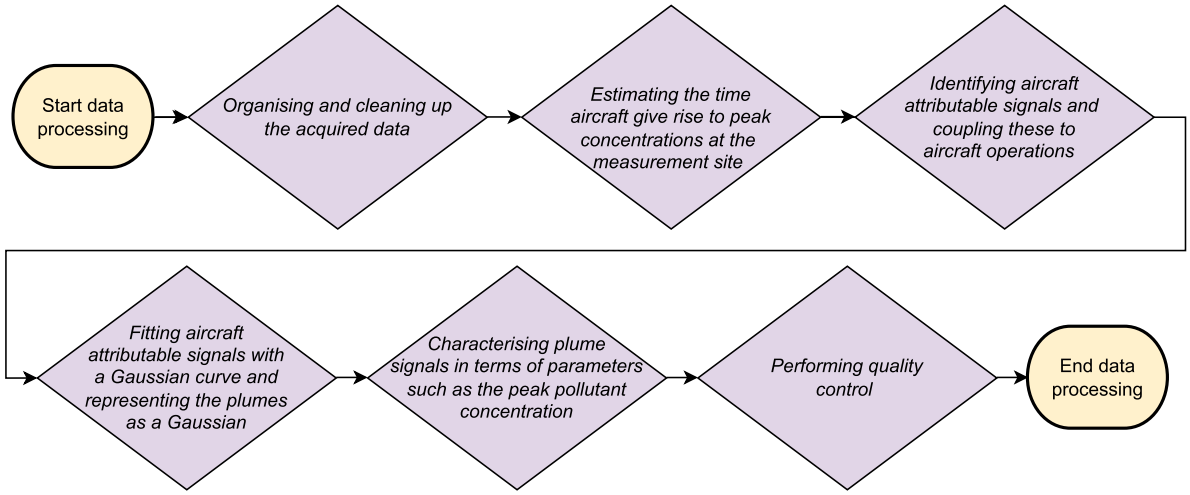

Figure 5.1: *Overview of the applied method to process the acquired data*

5.2 Data preparation

Data preparation is performed for air pollution data, meteorological data, and aircraft- and engine data.

5.2.1 Air pollution data

Raw data of sensor nodes consists of Analogue to Digital (A/D) converter counts. The converter counts are corrected for environmental conditions (e.g., ambient temperature) as these conditions can affect the output of gas sensors [46, 169–173]. The resulting values are converted to volume concentrations in part-per-billion (ppb). Hereafter, three-second mean values are computed as sensor nodes sample at a variable rate whereas a constant offset between data points is desired for subsequent processing. This is accomplished by an algorithm of J. Maes, which is elaborated on in Appendix B.1.

For these three-second mean values in ppb the baseline signal is estimated. Sensor nodes measure the ambient concentration of an air pollutant p at a time instance t. This is referred to as the total pollutant concentration or the total signal and is denoted as $C_T(p, t)$. Equation 5.1 and the time-series of Figure 5.2 show that $C_T(p, t)$ consist of a baseline component $C_B(p, t)$

and a local component $C_L(p, t)$, which are referred to as the baseline signal and local signal respectively[13]. The baseline signal represents the background concentrations and therefore shows more gradual changes. The local signal is caused by local pollution events such as aircraft exhaust plumes and is characterised by a larger variability in pollutant concentrations [174, 175]. To determine aircraft attributable concentrations above the background concentration, first $C_B(p, t)$ must be determined.

$$C_T(p,t) = C_B(p,t) + C_L(p,t) \tag{5.1}$$

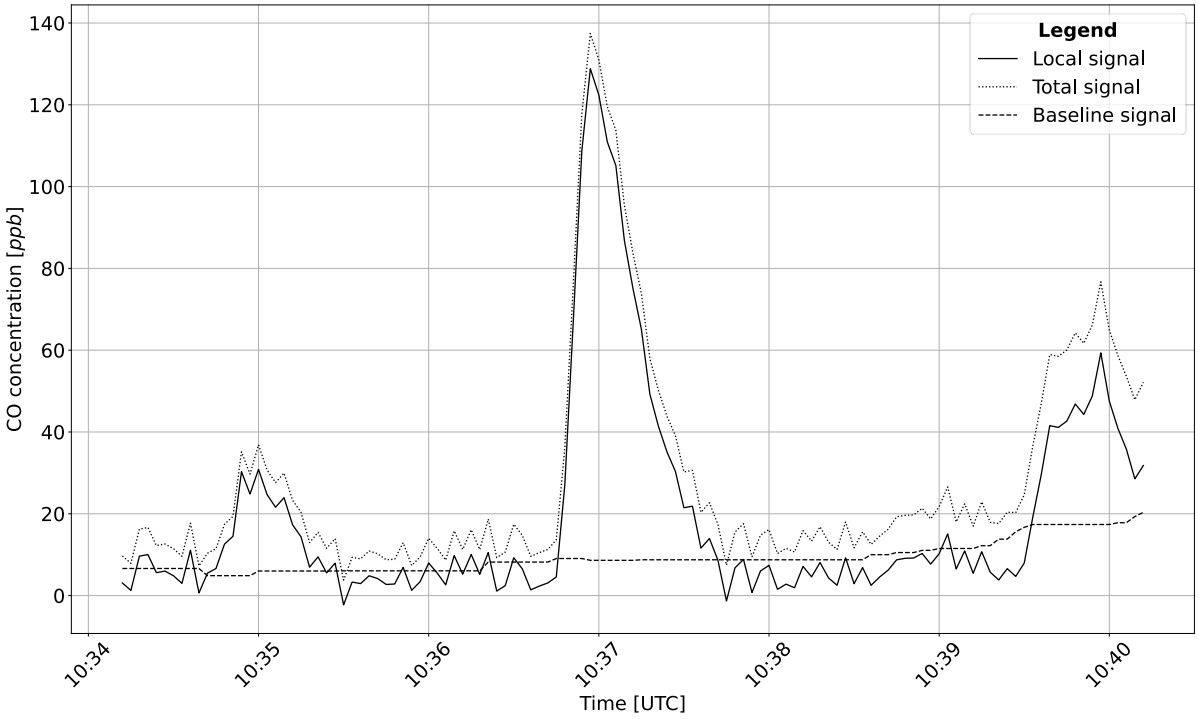

Figure 5.2: *Example of the total signal, baseline signal and local signal*

To estimate $C_B(p, t)$ an algorithm of previous research by Maes [63] is used in which the baseline is estimated as the 2% quantile of $C_T(p, t)$ on a rolling window basis with a time window of 100 seconds. The 2% quantile was used instead of the minimum value to account for measurement outliers. Furthermore, the time window of 100 seconds was set to be (generally) larger than the duration of aircraft plumes such that the 2% quantile value between aircraft plumes could be captured. It should be noted that the time window to extract the baseline is kept constant at 100 seconds for all measurements, even though in reality the required window length may vary with the ambient wind and the location of sensor nodes. However, changing the baseline estimation method is outside the scope of this research. $C_L(p,t)$ is hereafter obtained by subtracting $C_B(p, t)$ from $C_T(p, t)$.

$C_L(p,t)$ contains high frequency noise, which likely results from instrument noise and stochastic turbulent processes [176, 177]. This is undesired for further data processing. To attenuate this noise previous research [63] used a standard Moving Average (MA) filter. During this research a Savitzky-Golay (S-G) filter was used instead, which is one of the most frequently used filters in gas chromatography and mass spectrometry (see e.g., Katajamaa et al. [178]). The rationale behind this change is that, compared to the MA filter, the S-G filter is able to better retain the original shape (e.g., peak heights) of the local signal [179–181].
The working principle of the S-G filter is based on a least-squares polynomial approximation of data in a predefined window. A symmetric window of odd length n centred around point k is

[13] Pollutant time-series display how pollutant concentrations vary over time.

defined to which a polynomial of degree *p* is fitted in the least-squares sense. The value of the centre point *k* gets replaced by the value of the polynomial fit at this point to smoothen the data. After this the window is repeatedly shifted forward by one data point (i.e., 3 seconds) to generate a smoothed signal for the entire time-series [179, 181–185]. The window length *n* and polynomial degree *p* are user-specified whereby *p* should be less than *n* and *n* an odd number. No guidelines exist on how these values should be selected, except that *n* should not be too close to *p+1* as otherwise the fitted polynomial will interpolate the data rather than applying smoothing [182]. Based on trial-and-error $p = 2$ and $n = 9$ (equal to 27 seconds) were deemed most appropriate for this research. Using these values the filter was implemented in Python using the SciPy function *signal.savgol_filter() [186]*.

5.2.2 Meteorological data

Meteorological data consist of Meteorological Terminal Aviation Routine Weather Reports (METARs) and Air Traffic Control (ATC) voice recordings. METARS were processed through an algorithm developed during previous research which is documented in the report of Maes [63]. Preparation of ATC voice recordings consists of the extraction of the wind speed and the wind direction. Preferably this would be done automatically, but other research (see e.g., [187–190]) indicated that this can be challenging and prone to errors. To ensure data quality and due to time constraints, wind data was therefore manually extracted. However, especially during periods of low aircraft activity, the audio recordings contain (prolonged) periods of silence. Therefore, an algorithm was developed to trim out these periods of silence. This reduced the listening time from ~69 hours to ~7.5 hours. For a description of the algorithm the reader is referred to Appendix B.2.

5.2.3 Aircraft- and engine data

To prepare aircraft- and engine data, an algorithm was developed that verifies which vehicles are transmitting position reports within a two-dimensional polygon overlaying the Polderbaan runway (see Figure 5.3). As only aircraft operations going to and from the Polderbaan runway are of interest for this research, data of vehicles not transmitting position reports within this polygon are eliminated. A detailed description of the algorithm is provided in Appendix B.3.

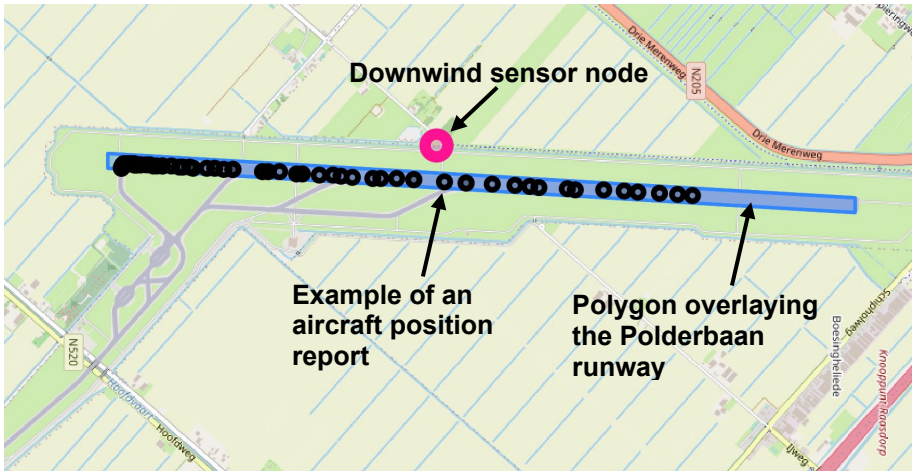

Figure 5.3: *Position reports of a B78X during its take-off roll on the Polderbaan runway*

The remaining transmitting vehicles are categorised as take offs, landings, overflights or road vehicles using an algorithm developed during previous research of Maes [63] which is described in Appendix B.3. This algorithm is based on conditional statements involving the geometric altitude H_{geo} and the ground speed V_{ground}[14]. During this follow-up research it was

[14] Conditional statements are 'AND', 'IF' and 'OR' statements whereby the algorithm checks whether for a given input the statement is true or false.

(similar to other research such as [191–196]) observed that H_{geo} and V_{ground} may contain erroneous values. Therefore, a Savitzky-Golay filter with polynomial order of 3 and a filter length of 15 was applied before applying the algorithm of Maes. This is one of the most frequently used filters for this purpose and was also used to filter the air pollution data [182, 197–202]. By categorising transmitting vehicles, overflights and ground vehicles can be filtered out such that only aircraft operations going to and from the Polderbaan runway remain.

For the remaining aircraft operations, the designator of the engine model specified by the OpenSky Network [148] is modified to match the ICAO engine designator using the conditional statements provided in Appendix B.3. This was required, as the OpenSky Network uses various designators for the same engine model, whereas a unique designator is required to investigate the pollution signature of engines.

5.3 Estimation of the plume arrival time

Following the completion of data preparation, the time in Coordinated Universal Time (UTC) needs to be estimated when an aircraft gives rise to a peak (i.e., a maximum) concentration in pollutant time-series. Subsequently, this time, referred to as the Estimated Plume Arrival (EPA) time, can be used to extract the contribution of specific aircraft operations to air pollution from pollutant time-series. During previous work of Maes [63] this was done by first determining the time t_{node} when an aircraft operation was closest to a sensor node based on aircraft activity data. Subsequently, the highest peak pollutant concentration occurring between t_{node} - 20 seconds to t_{node} + 180 seconds was coupled to the aircraft operation for which t_{node} was determined.

This method has however several shortcomings. First of all, the time at which an aircraft operation gives rise to a peak concentration in pollutant time-series depends on a variety of factors. Hereby ambient conditions, the combined thrust of the engines, the response time of the instrument, the resolution of the aircraft activity data and the offset between the clock time associated with aircraft activity data and the sensor nodes can play a role [1–5]. Therefore, the highest peak concentration occurring between t_{node} - 20 seconds to t_{node} + 180 seconds does not necessarily belong to the aircraft operation for which t_{node} was determined. Consequently, peak pollutant concentrations may be assigned to the wrong aircraft operation. Besides, this method assumes that all peak pollutant concentrations can be attributed to aircraft, while in reality (instrument) noise and other emissions sources (such as road traffic) contribute to the pollutant time-series [17, 19, 33, 62–67]. A different method was therefore implemented during this follow-up research.

5.3.1 Estimation approach

To estimate the EPA time the aircraft is regarded as a stationary (i.e., non-moving) single point source emitting a passive plume (implying that the initial plume velocity is zero) from the runway centreline. It is assumed that this plume is brought towards the downwind sensor node by the ambient wind without any interference, obstructions, or external forces acting on the plume. The wind is considered constant and equal to the wind obtained from the sources specified in Chapter 3. Additionally, it is assumed that the Polderbaan runway is aligned with both the Magnetic North (MN) and True North (TN). Note that this neglects the (small) angle (~2°) between the MN and TN and ignores that runway numbers are rounded to the nearest ten degrees.

Using these assumptions, the EPA time is estimated based on the ambient wind and the distance between the sensor node and the runway. First the runway section from which the plume going to the sensor node is emitted, referred to as the plume release point, is estimated. For this, the wind vector is decomposed into a component V perpendicular to the runway (defined positive to the east) and a component U parallel to the runway (defined positive to the

north). Denoting the wind speed as w_s and representing the clockwise direction relative to north from which the wind is approaching by α, U and V can be computed using Equation 5.2 and Equation 5.3 respectively[15].

$$U = -w_s \cdot \cos\left(\frac{\pi\alpha}{180}\right) \quad (5.2)$$

$$V = -w_s \cdot \sin\left(\frac{\pi\alpha}{180}\right) \quad (5.3)$$

After decomposing the wind vector into components, a streamwise distance S is defined between the downwind sensor node and the plume release point along which the plume's centreline travels as shown in Figure 5.4. The distance perpendicular to the runway centreline from the sensor node to the plume release point is denoted S_x (defined positive to the east). The distance parallel to the runway from the sensor node to the plume release point is denoted S_y (defined positive to the north). These can be expressed in terms of the ambient wind and the time τ it takes for the plume to travel the distance S as shown in Equation 5.4 and Equation 5.5 [1, 204]. As the components of the ambient wind and the perpendicular distance of the sensor node to the runway centreline are known, τ can be computed using Equation 5.4 after which S_y follows from Equation 5.5.

$$S_x = -V \times \tau \quad (5.4)$$

$$S_y = -U \times \tau \quad (5.5)$$

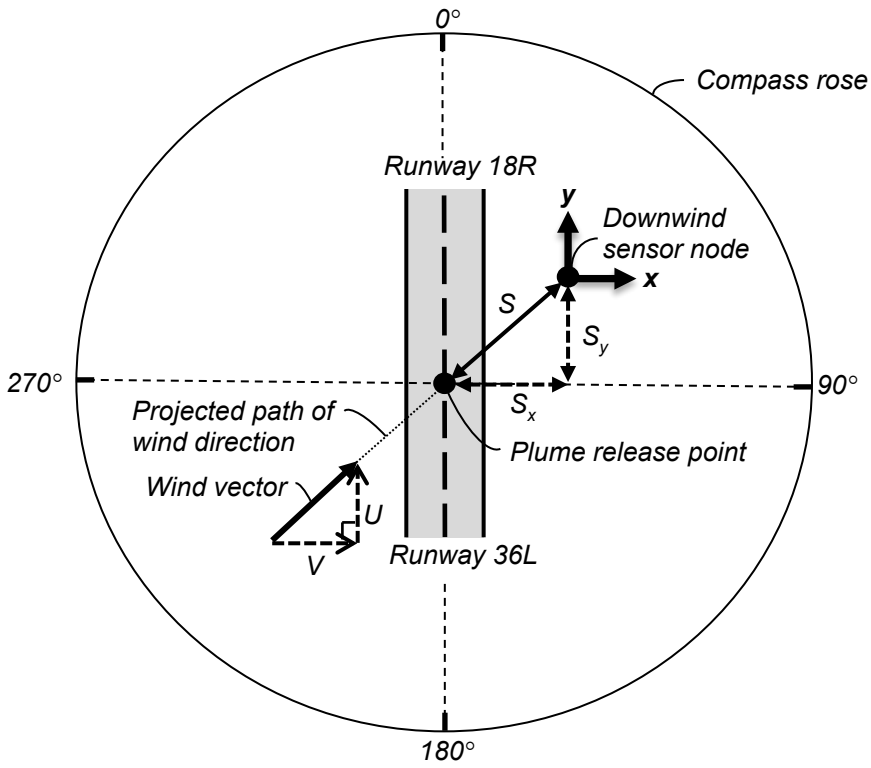

Figure 5.4: *Graphical representation of how a passive plume of a stationary source moves to a downwind sensor node*

The distances S_x and S_y between the sensor node and the plume release point are used to estimate the latitude (lat_{PRP}) and longitude ($long_{PRP}$) of the plume release point. Assuming the

[15] The wind direction provided by ATC is given with respect to MN while the wind-direction reported in METARs is referenced to TN [203], but for this research MN and TN are assumed to be aligned.

Earth to be a perfect sphere with a radius of R_{earth} = 6371 × 10^3 m, lat_{PRP} and $long_{PRP}$ can be approximated using Equation 5.6 and Equation 5.7 respectively [205–209][16].

$$lat_{PRP} = lat_{node} + \frac{S_y}{R_{earth}} \times \frac{180}{\pi} \tag{5.6}$$

$$long_{PRP} = long_{node} + \frac{S_x}{R_{earth}} \times \frac{180}{\pi} \times \frac{1}{\cos\left(lat_{node} \times \frac{\pi}{180}\right)} \tag{5.7}$$

After obtaining lat_{PRP} and $long_{PRP}$, it needs to be estimated when an aircraft is closest to this position. For this, the distance d between the plume release point and each position report (in terms of latitude and longitude) of the aircraft is computed in Python using the Geopy function *distance.distance()* [210, 211]. An aircraft is closest to the plume release point for the position report for which d is minimum, which is denoted as $d_{closest}$. The time in UTC $t_{closest}$ corresponding to $d_{closest}$ then corresponds to the time when the aircraft was closest to the plume release point.

Analysis revealed that using unlicensed OpenSky Network data $d_{closest}$ could be large. For instance, for the experiment conducted on 09-09-2021 the mean $d_{closest}$ was ~750 m with >35% of the aircraft operations having a $d_{closest}$ in excess of a kilometre. It could therefore be that $d_{closest}$ corresponds to a position report for which the aircraft was not on the runway as for example shown in Figure 5.5 (a). Consequently, $t_{closest}$ may be off by several tens of seconds with respect to the time that an aircraft actually arrives at the estimated plume release point. As aircraft may depart and arrive on the order of 60 seconds after each other, this could lead to air pollutant concentrations being assigned to the wrong aircraft operation.

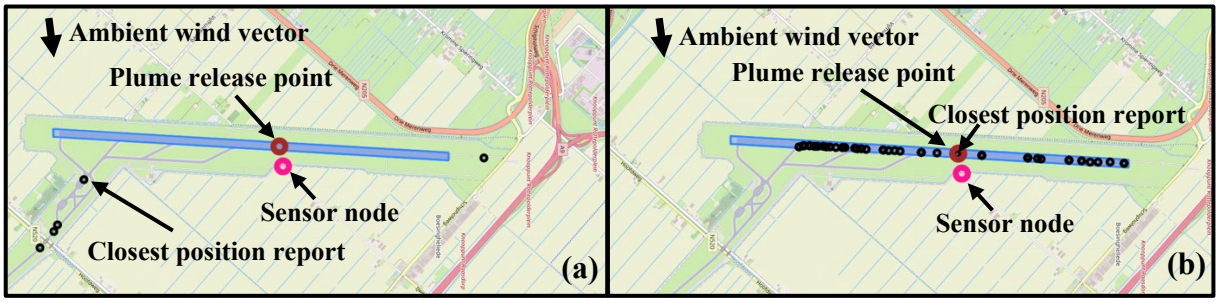

Figure 5.5: *Example of the position reports (represented by black circles) of an arriving B739 for unlicensed OpenSky Network data (a) and licensed data (only displaying those while the aircraft is on the runway) (b)*

To estimate $t_{closest}$ more accurately, higher resolution aircraft activity data is desired. Unexpectedly, data of the deployed ADS-B receiver did not yield substantial improvements in the number of aircraft position reports. The underlying cause of this was not investigated, as it was discovered that a significant improvement in the amount of aircraft position reports could be obtained by using licensed OpenSky Network data as shown in Figure 5.5 (b). For example, for the measurement conducted on 09-09-2021 the mean $d_{closest}$ was ~50 m for licensed OpenSky Network data compared to ~750 m for unlicensed OpenSky Network data. Therefore, this research uses licensed OpenSky Network data. After obtaining the value for $t_{closest}$, the EPA time is computed by the summation of $t_{closest}$ and the plume travel time τ. Note that this

[16] The Earth is not a perfect sphere hence no single value exists for its radius, but research has shown that the mean radius of the Earth can be approximated as 6371 km.

assumes that the internal clock of a sensor node and the clock on which the OpenSky Network data is based are perfectly synchronised[17].

5.3.2 Caveats of the chosen approach

The approach to estimate the EPA time assumes the aircraft to be a stationary source releasing a passive plume while in reality aircraft are moving sources releasing a plume with an initial velocity relative to the aircraft[18]. This impacts the location of the plume release point and the plume travelling time as illustrated in Figure 5.6 (a) when there is crosswind and headwind and in Figure 5.6 (b) during tailwind and crosswind.

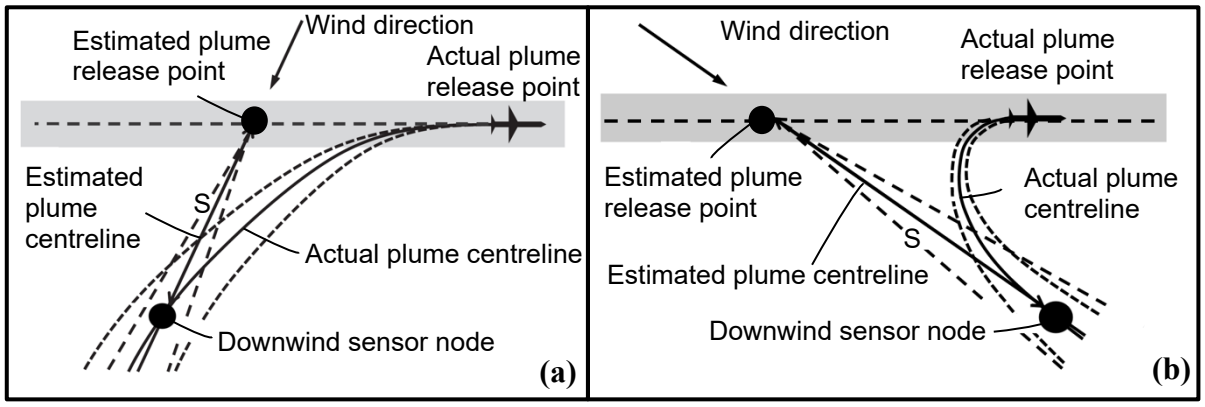

Figure 5.6: *Schematic of the exhaust plume of a departing aircraft in case of headwind and crosswind (a) and tailwind and crosswind (b) [1, 102] (modified by author)*

The most common scenario is the one displayed in Figure 5.6 (a) as aircraft generally take off and land against the wind. It is therefore likely that the actual plume release point is further down the runway compared to the one that was estimated. Furthermore, it can be seen in Figure 5.6 (a) that the plume travels along a longer curvilinear path than the linear distance *S* utilised during this research. Consequently, the EPA time is underestimated compared to the time at which the aircraft arrives at the actual plume release point. However, the chosen approach assumes the plume to be passive while in reality plumes are released with an initial velocity. The plume therefore travels faster towards the sensor node, which overestimates the EPA time.

Another inaccuracy with respect to the EPA time is introduced by neglecting the sensor node's response time. For the employed gas sensors, Appendix A.1 shows the time T_{90} it takes for the signal to, after being exposed to a step change in concentration, go from zero to 90% of the (stabilised) final value. However, it should be kept in mind that the values in Appendix A.1 are associated with concentrations one or two orders of magnitude higher than encountered during this research. As the response time is larger for higher pollutant concentrations, the actual response time may be less [212, 213]. Nevertheless, the EPA time may be underestimated by neglecting the sensor node's response time.

5.4 Plume identification and source appointment

Before the EPA time can be used to couple pollutant concentrations to aircraft operations, aircraft attributable pollutant concentrations need to be identified in pollutant time-series.

[17] The clock of a sensor node is manually set and may have an offset of ~1 – 2 seconds with respect to the OpenSky Network.

[18] Initial velocity is given to the plume by engine thrust and equals for instance ~295 m/s for a stationary CFM56-5C4 at its rated thrust during International Standard Atmosphere conditions at Mean Sea Level in the absence of wind [102].

5.4.1 Plume identification and source appointment

Aircraft exhaust plumes can be observed in time-series as short-term (~1 minute) intervals with a strong rise in local pollutant concentration up to a peak followed by a strong decay. The onset of this rise at time t_{start} and concentration C_{start} is defined as the start point whereas the cessation of signal decay at time t_{end} and concentration C_{end} is referred to as the end point. The pollutant concentrations in between the start- and end point are defined as the plume signal, as shown in Figure 5.7.

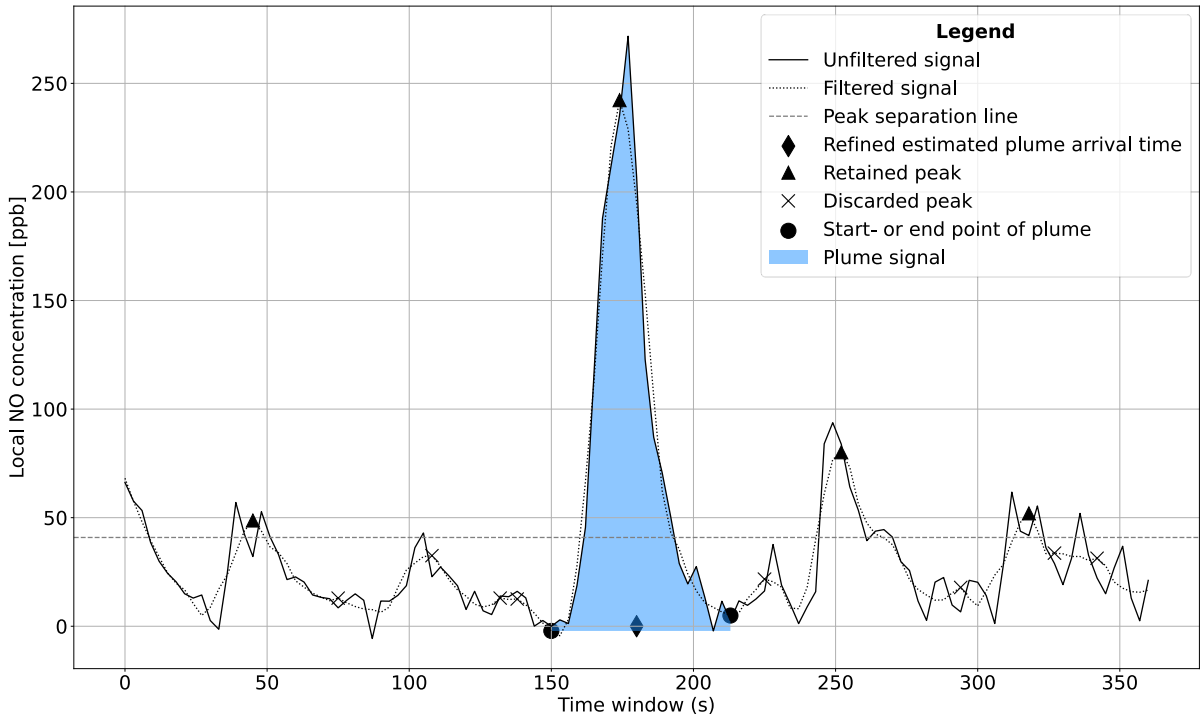

Figure 5.7: *Identification of the plume signal of a departing Boeing 787-9 whereby the horizontal axis represents a symmetric six-minutes window centred around the EPA time*

To identify these plume signals, first a symmetric six-minutes window centred around the EPA time is generated. In this window peak pollutant concentrations are identified through comparison of the local pollutant concentration of neighbouring points. This is accomplished in Python by using the Scipy function *find_peaks()* with as input the filtered local pollutant concentrations. However, as peaks may show up resulting from instrument noise, a changing baseline or other pollutant sources, an amplitude threshold is installed. This threshold, referred to as the Peak Separation Line (PSL), is set equal to the mean local pollutant concentration of the time-series of the measurement day. It was verified that the established PSL was higher than the manufacturer-specified Signal to Noise Ratio (SNR) of the gas sensors, which equals 4 ppb, 15 ppb, 15 ppb and 5 ppb for CO, NO, NO_2 and SO_2 respectively [214]. After identifying peak pollutant concentrations, the start- and end point are found based on changes in the first derivative of the filtered local concentration of a pollutant p over time t (e.g., d(NO)/dt) [215–218]. Subsequently each plume signal is represented by the set of pollutant concentrations between the start- and end point as shown in Figure 5.7.

To couple an identified plume signal to a specific aircraft operation, first the offset (denoted as t_{offset}) is computed between the EPA time and the time t_{peak} at which a peak is present. Subsequently, the peak closest to the EPA time gets coupled to the aircraft operation associated with this EPA time. Hereby peaks occurring before the aircraft has reached the plume release point are excluded, as the aircraft cannot cause a peak pollutant concentration before it has released its plume. For >85% of the departing and landing aircraft, the peak

coupled to an aircraft operation was to the left of the EPA time, which is likely to results from the inaccuracies in the EPA time that were discussed in Section 5.3.2. As the mean t_{offset} showed small variations per measurement date (see Appendix B.4), a constant was added to the EPA time to estimate the actual plume arrival time more accurately. This constant was set to 12 seconds for take offs and 17 seconds for arrivals based upon the average t_{offset} of all departing and arriving aircraft.

Subsequently, the symmetric six-minutes window in which peaks are identified is centred around this refined EPA time rather than the initial EPA time. Similarly, the peak closest to the refined EPA time gets coupled to the aircraft operation associated with this refined EPA time. Following this approach, the mean offset between the refined EPA time and the time at which the peak coupled to an aircraft operation occurs was <1 second for departures and ~1 – 8 seconds for landing aircraft, thereby closely approximating the actual plume arrival time.

5.4.2 Caveats of the chosen approach

The identification of plume signals relies upon appropriate settings of the Savitzky-Golay filter, as inappropriate filter settings may lead to under smoothing or over smoothing. Under smoothing leads to local slope changes in the signal, which can lead to the identification of the wrong start- or end point due to noise. On the contrary, over smoothing results in a start- and end point that are further away from the actual start- and end point. As a result, plumes belonging to multiple aircraft may be seen as a single plume. Besides, filtered plume characteristics such as the peak height may no longer be representative. The justification of the selected filter settings was provided in Section 5.2.

Besides the filter settings, the amplitude threshold influences the identified plume signals. Increasing the PSL value reduces the likelihood of non-aircraft attributable plumes being assigned to aircraft (hereafter referred to as ‘false’ plumes) thus making the algorithm more robust. However, on the downside it increases the likelihood of ‘real’ plumes to be (incorrectly) discarded. This may lead to valuable data loss and introduces bias towards higher pollutant concentrations in the results. Therefore, a sensitivity analysis is performed which will be presented in Section 7.1. Furthermore, to filter out false plumes several quality control procedures are in place as will be described in Section 5.7.

5.5 Gaussian representation of plumes

Plume signals that are coupled to aircraft operations are represented as Gaussian plumes, for which plume signals are first fitted with a curve fitting function.

5.5.1 Fitting procedure and goodness of fit assessment

Plumes are fitted with the Gaussian curve fitting function shown in Equation 5.8 with A the amplitude of the plume signal’s peak, μ the location of the plume signal’s peak and σ its standard deviation. This fitting function was selected based on visual inspection of pollutant time-series and insights from existing literature. For instance, similar research of Carslaw et al. [67, 126] stated that aircraft plumes appear in pollutant time-series approximately as Gaussian shapes independent of the aircraft type or the number of engines.

$$\hat{y}(t) = Ae^{-(t-\mu)^2/2\sigma^2} \tag{5.8}$$

The fitting is performed to the local unfiltered pollutant concentrations $C_L(t)$ in between the start- and end point of a plume signal using the *curve_fit()* function of SciPy. This function allows the user to provide an estimate of model parameters (A, μ and σ) to increase the likelihood of successfully performing the fitting and to decrease the running time [219]. For this, the A, μ and σ of the filtered plume signal are used. Subsequently, the *curve_fit()* function

searches for the parameters that result in the best fit between the local unfiltered pollutant concentrations $C_L(t)$ and the fitted values $\hat{y}(t)$. Specifically, it searches for the vector $\vec{p}_{optimum}$ containing the optimum model parameters such that the squared-residuals $\sum_{i=1}^{n}(C_L(t) - \hat{y}(t))^2$ are minimised [220].

After fitting a Gaussian curve to the observed plume signals, the quality of the fit is assessed. To get a first insight in this the observed curve and the model curve are plotted together with the distribution of the residuals as shown in Appendix B.5. Note that a residual is defined as the difference between the observed value y_i and the corresponding value of the fitted curve $\hat{y}_i$ such that for data-point *i* the residual equals $y_i - \hat{y}_i$ [221].

Additionally, five evaluation metrics were used including the coefficient of determination (R^2), the reduced Chi-squared (χ^{2*}), the Root Mean Square Error (RMSE), the Mean Absolute Error (MAE) and percentage differences in plume parameters between the observed plume signal and the fitted curve. The coefficient of determination (R^2) is computed using Equation 5.9 and can generally vary between $(-\infty, 1]$ with an R^2 closer to 1 indicating a better fit [222]. No universally accepted range of R^2 values exist for which a fitting is considered to be good [223]. Based on visual inspection, for this research the fitting curve is deemed a weak representation of the observed plume signal when $R^2 < 0.6$.

$$R^2(y, \hat{y}) = 1 - \frac{\sum_{i=1}^{n}(y_i - \hat{y}_i)^2}{\sum_{i=1}^{n}(y_i - \bar{y})^2} \tag{5.9}$$

The second metric is the reduced Chi-squared (χ^{2*}), for which first the Chi-squared value $\chi^2(\vec{p})$ is computed using Equation 5.10. This value is divided by the number of data points *n* minus the number of fitting parameters P (three for the Gaussian function) to obtain the reduced Chi-squared value as shown in Equation 5.11. The reduced Chi-squared value can vary between $(-\infty, \infty)$ with a value around 1 being indicative of a good fit [224, 225]. No universally accepted range of χ^{2*} values exist for which a fitting is considered to be good [226]. Based on visual inspection, the fitting is deemed an insufficient representation of observed plume signals when $|\chi^{2*}| > 90$.

$$\chi^2(\vec{p}) = \sum_{i=1}^{n} \frac{[y(i) - \hat{y}(i, \vec{p})]^2}{y(i)} \tag{5.10}$$

$$\chi^{2^*}(\vec{p}) = \frac{\chi^2(\vec{p})}{n - P} \tag{5.11}$$

The third and fourth metrics are the Root Mean Square Error (RMSE) and Mean Absolute Error (MAE), which are obtained using Equation 5.12 and Equation 5.13 respectively. Both metrics can vary between $[0, \infty)$, with smaller values being indicative of a better fit [222].

$$\text{RMSE} = \sqrt{\frac{1}{n}\sum_{i=1}^{n}(y_i - \hat{y}_i)^2} \tag{5.12}$$

$$\text{MAE} = \frac{1}{n}\sum_{i=1}^{n}|y_i - \hat{y}_i| \tag{5.13}$$

The fifth metric is the percentage difference between two values *A* and *B* as shown in Equation 5.14. The percentage difference is computed for the peak of the filtered plume signal and the peak of the fitted curve as well as for the area under the curve of the unfiltered plume signal and the fitted curve.

$$\text{Percentage difference} = 100 \times \frac{|A - B|}{(A + B)/2} \tag{5.14}$$

5.5.2 Gaussian representation of well resolved plumes

The Gaussian that is fitted to the observed plume signal does not always start and end at the baseline (i.e., the 0 ppb line) as shown in Figure 5.8. This is because noise surrounding the plume signals causes the points between which the Gaussian is fitted (i.e., the start- and end point of the plume signal) to be non-zero. It is however desired that the Gaussian fitting starts and ends near 0 ppb such that the characteristics of a plume signal (e.g., the area under the curve) can be approximated with respect to the baseline. The fitted Gaussian curves are therefore enforced to start and end at ~0 ppb. This is accomplished by superimposing a Gaussian with the model parameters of the fitted Gaussian on the fitted curve. Specifically, the model parameters of the fitted Gaussian that are stored in $\vec{p}_{optimum}$ are used as input to Equation 5.8 to generate a Gaussian that starts and ends at ~0 ppb. To prevent infinitely long tails, the superimposed Gaussian is truncated at three times its standard deviation.

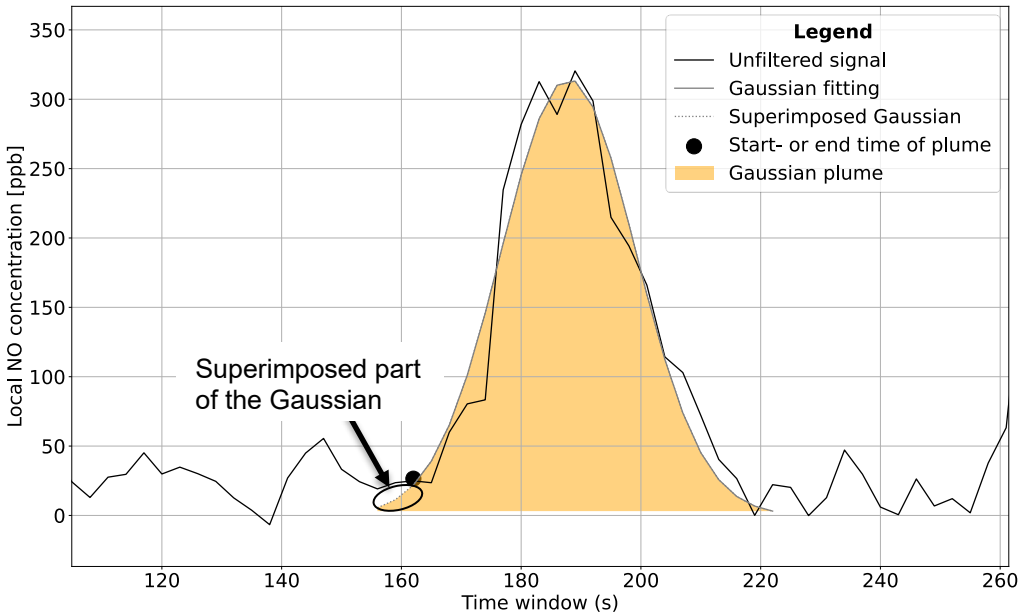

Figure 5.8: *Gaussian fitting and the superimposed Gaussian for a departing Boeing 787-9 whereby the horizontal axis represents part of the six-minute symmetric time window centred around the (refined) EPA time*

5.5.3 Gaussian representation of overlapping plumes

Superimposing a Gaussian on top of the fitted Gaussian may work for well resolved plume signals, but can result in plume characteristics such as the area under the curve that are no longer representative when plumes of multiple aircraft substantially overlap. Therefore, for overlapping plumes a multi-Gaussian fitting is performed from which the contribution of the individual aircraft operations is extracted as for example shown in Figure 5.9.

To accomplish this the algorithm starts by searching for the first point (t_{left}, C_{left}) to the left of the plume signal's peak for which the start point (t_{start}, C_{start}) is below a predefined threshold value. Recall that C_{start} is the (filtered) pollutant concentration value from which the plume signal starts to rise. The threshold value is set equal to the PSL defined in Section 5.4. Similarly, the algorithm searches for the first point to the right of the plume signal's peak (t_{right}, C_{right}) for which C_{end} (i.e., the filtered concentration value at the end of the plume signal's decay) is below the PSL. The searching process halts when (t_{left}, C_{left}) and (t_{right}, C_{right}) have been found. This way the time interval ranging from t_{left} to t_{right} is determined in between which a multi-modal Gaussian fitting is performed.

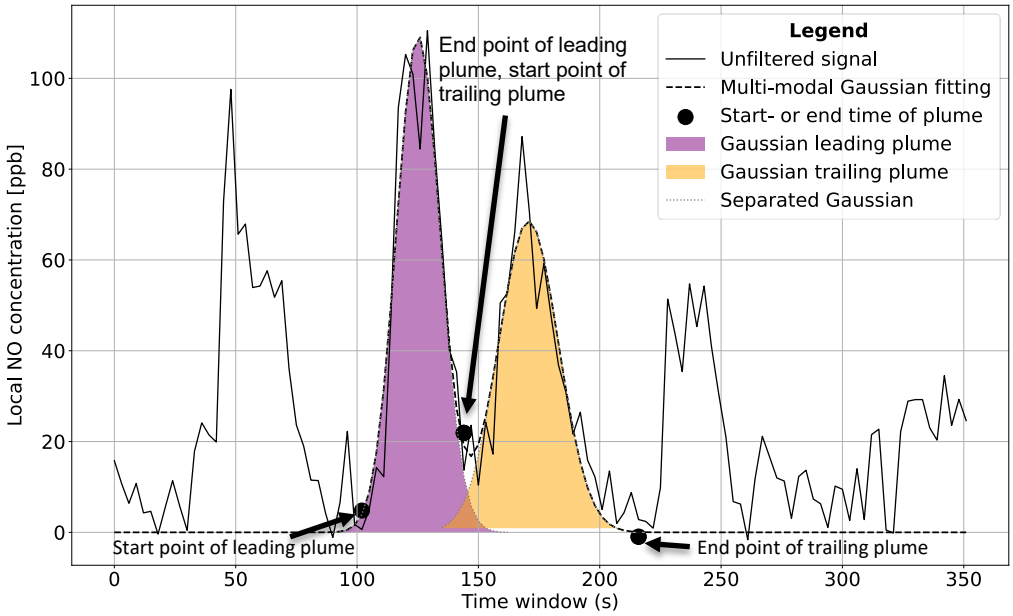

Figure 5.9: *Multi-modal Gaussian fit to the plume of a Boeing 737-800 (leading plume) and an Embraer 190 (trailing plume) that shortly (~50 sec) depart after each whereby the horizontal axis represents a symmetric six-minutes window centred around the (refined) EPA time*

The algorithm keeps track of the number of peaks N in the interval between t_{left} and t_{right} which is used as a counter for the Gaussian modal *N* (i.e., the number of Gaussians the multi-modal Gaussian consists of). Subsequently, a multi-modal Gaussian fit is performed to the observed (i.e., unfiltered) pollutant concentrations in between t_{left} and t_{right} with Equation 5.15 and modal N. The linear combination of these Gaussians forms the signal to which the multi-modal fitting was performed [227].

$$\hat{y}(t) = \sum_{k=1}^{N} A_k \, e^{-(t-\mu_k)^2/2{\sigma_k}^2} \tag{5.15}$$

Using the *curve_fit()* function of SciPy the squared residuals are minimised between the signal of the overlapping plumes and the signal of the linear combination of the *N* Gaussians. Subsequently, the optimal model parameters of each of the *N* Gaussians is extracted. It should be noted that this method assumes that the overlapping plume signal can be expressed as the linear combination of multiple Gaussians. For the example shown in Figure 5.9 this approach leads to N = 2 with $C_{start} = C_{left}$ and $C_{end} \neq C_{right}$.

It should be noted that ~15% of the NO plumes of departing aircraft and the CO plumes of landing aircraft show up in pollutant time-series with two closely spaced peaks. An example of this can be seen for the leading plume of Figure 5.9. These are believed to be associated with the engines installed on each side of the fuselage. However, this is contradictory to the statement in Chapter 2 that a common exhaust plume is formed in which the contribution of individual engines can no longer be distinguished.

To investigate this discrepancy, literature was consulted. This revealed that when lift is significant in relation to the (combined) thrust of the engines, wingtip vortices can trap the exhaust of the engines installed on its associated wing. This can lead to the formation of two plumes [1, 97, 99, 132]. Although it is currently not well understood when this occurs, literature

is in agreement that two plumes may form (shortly) before the aircraft becomes airborne [92, 97, 99]. Apart from wing tip vortices, two plumes may form when engines are spaced far apart as this decreases the interaction between exhaust jets [87, 228]. Therefore, for example for a Boeing 737 a common exhaust jet is rapidly formed while for a Boeing 747 two plumes may form which (at ground level) remain separated [87, 89, 229, 230]. Whether one or two plumes form furthermore depends upon the thrust setting and the amount of crosswind, as increased thrust and higher crosswinds enhance the formation of a single plume [87, 95].

It is therefore assumed for this research that closely spaced peaks belong to the same aircraft. Due to the proximity of the peaks and (typically) their minor differences in pollutant concentrations, the plume signal of the filtered pollutant concentrations consists of a single peak as for example shown in Figure 5.9. Consequently, plumes with closely spaced peaks are not seen as overlapping plumes by the algorithm.

5.5.4 Caveats of the chosen approach

It is assumed that aircraft plume signals are Gaussian-shaped while in reality this may not always be the case for a variety of reasons such as sudden changes in wind [86, 231, 232]. To prevent the representation of plume signals that do not exhibit a Gaussian shape by Gaussian curves, quality control is performed to exclude these from further analysis. Nevertheless, the resulting plume characteristics will be dependent upon the chosen fitting function. It should furthermore be noted that the noise surrounding plume signals may impact plume characteristics, which in the chosen approach is neglected. Additionally, the amplitude threshold below which plumes are not considered to be overlapping may influence the results, especially for peaks that are close to this threshold value. Therefore, a sensitivity analysis will be conducted.

5.6 Plume characterisation

After representing each plume by a Gaussian, plumes are characterised in terms of several parameters. Before computing these parameters, pollutant concentrations are converted from ppb to $\mu g/m^3$ (see Appendix B.1) as air quality research commonly reports concentrations in terms of mass.

5.6.1 Geometrical plume parameters

Plumes are characterised in terms of five geometrical parameters. The first parameter is the plume width, which is the difference between the plume's start- and end time and represents the duration of a plume at the measurement site. The second parameter is the plume area, which represents the cumulative pollutant concentrations over time caused by an aircraft operation at the measurement site. This parameter is estimated by computing the Area Under the Curve (AUC) with the trapezoidal rule using the function *metrics.auc*() of Sklearn [233]. For NO_x, the area is obtained by expressing NO in terms of NO_2 using the ratio of their molecular weights (30.0061 and 46.0055 for NO and NO_2 respectively) as shown in Equation 5.16. Hereby A_{NO} and A_{NO_2} represent the area of NO and NO_2 respectively.

$$A_{NO_x} = \frac{46.0055}{30.0061} \times A_{NO} + A_{NO_2} \tag{5.16}$$

The third parameter is the Gaussian peak height, which represents the maximum ground level pollutant concentration caused by an aircraft at the measurement site. The fourth parameter is the peak time, which is the time associated with the Gaussian plume's peak height. The peak concentration of NO and NO_2 are used as inputs in Equation 5.16 to get the NO_x peak height. The fifth parameter is the peak height of an equivalent top-hat representation (see Figure 5.10) of the Gaussian plume, which is obtained by dividing the area of the Gaussian plume by its

width. The top-hat peak represents the average ground level pollutant concentration caused by an aircraft operation at the measurement site.

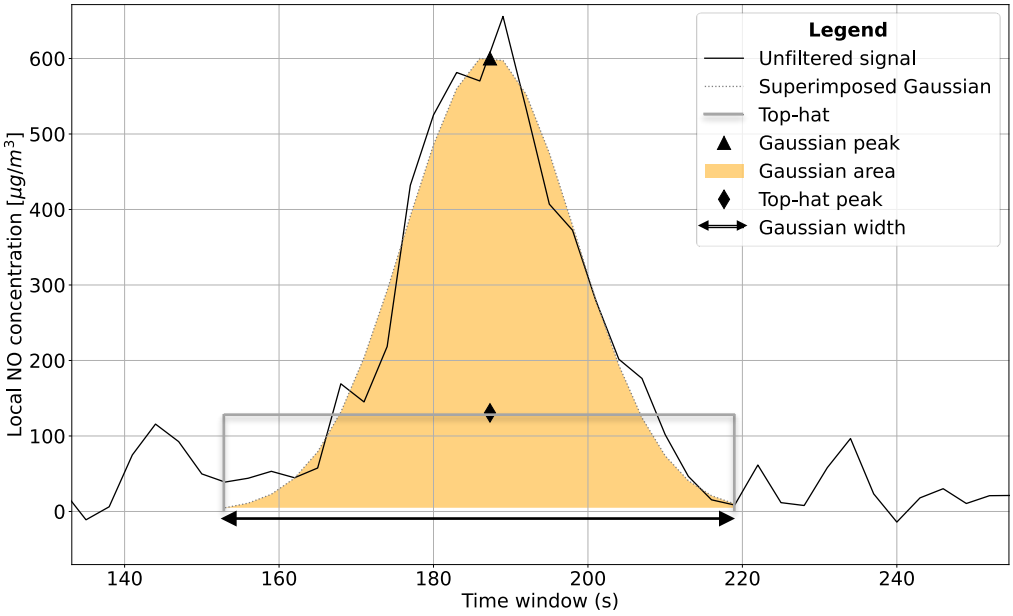

Figure 5.10: *Visualisation of parameters used to characterise plume signals whereby the horizontal axis represents (part of) a symmetric six-minutes window centred around the (refined) EPA time*

5.6.2 NO to NO_2 ratio

Currently uncertainties exist in the relative proportions of the compounds of NO_x (NO and NO_2) [38]. To increase understanding in this area, the ratio of NO to NO_2 is computed based upon the ratio of the Gaussian peak concentrations of these pollutant species.

5.6.3 SO_2-based emission indices

SO_2-based emission indices are computed using Equation 5.17 with $A(p)$ and $A(SO_2)$ the plume area of pollutant *p* and SO_2 respectively. Similar to other research (e.g. [234, 235]), it is hereby assumed that all sulphur is converted into SO_2. As the ICAO Emissions Databank [150] does not specify values for the SO_2 emission index, literature reviews of Lee et al. [90], Gierens et al. [236], Tait et al. [121] and Masiol and Harrison [3] were used instead. These studies were in agreement that the global mean SO_2 emission index is ~0.8 g/kg, hence similar to other research (e.g., [234, 237–239]) this value has been used for EI_{SO_2}.

$$EI_X = \frac{A(\mathrm{p})}{A(\mathrm{SO_2})} \times EI_{\mathrm{SO_2}} \tag{5.17}$$

5.7 Quality control

To ensure the quality of resulting plume characteristics data is automatically and manually screened.

5.7.1 Automated data screening

Plumes are automatically screened based on three criteria to filter out erroneous and questionable plumes. The first criterion is that aircraft must have passed the plume release point with a crosswind in the direction of the sensor nodes of >2 m/s. The second criterion is

that the actual peak of the filtered plume signal must be within ±30 s of the (refined) Estimated Plume Arrival (EPA) time. Analysis revealed that the shortest time in between two aircraft operations is ~50 – 60 s. Allowing for some margin in the inaccuracy of the refined EPA time, it is considered uncertain to which aircraft operation a plume belongs when the offset is >30 s. For overlapping plumes, each plume must be within ±30 s of its associated (refined) EPA time to prevent plumes from being separated while they may belong to the same aircraft operation. The third criterion is that the goodness of fit metrics discussed in Section 5.5.1 do not exceed predefined thresholds. These are set to R^2 > 0.6, $|\chi^{2^*}(\vec{p})|$ < 90, a percentage difference between the peak of the filtered plume signal and the peak of the fitted curve <20% and a percentage difference of the area under the curve of the unfiltered plume signal and the fitted curve of <20%. If any of these criteria are not met, the plume is classified as 'rejected' and excluded from further analysis. Examples of rejected plumes are shown in Figure 5.11.

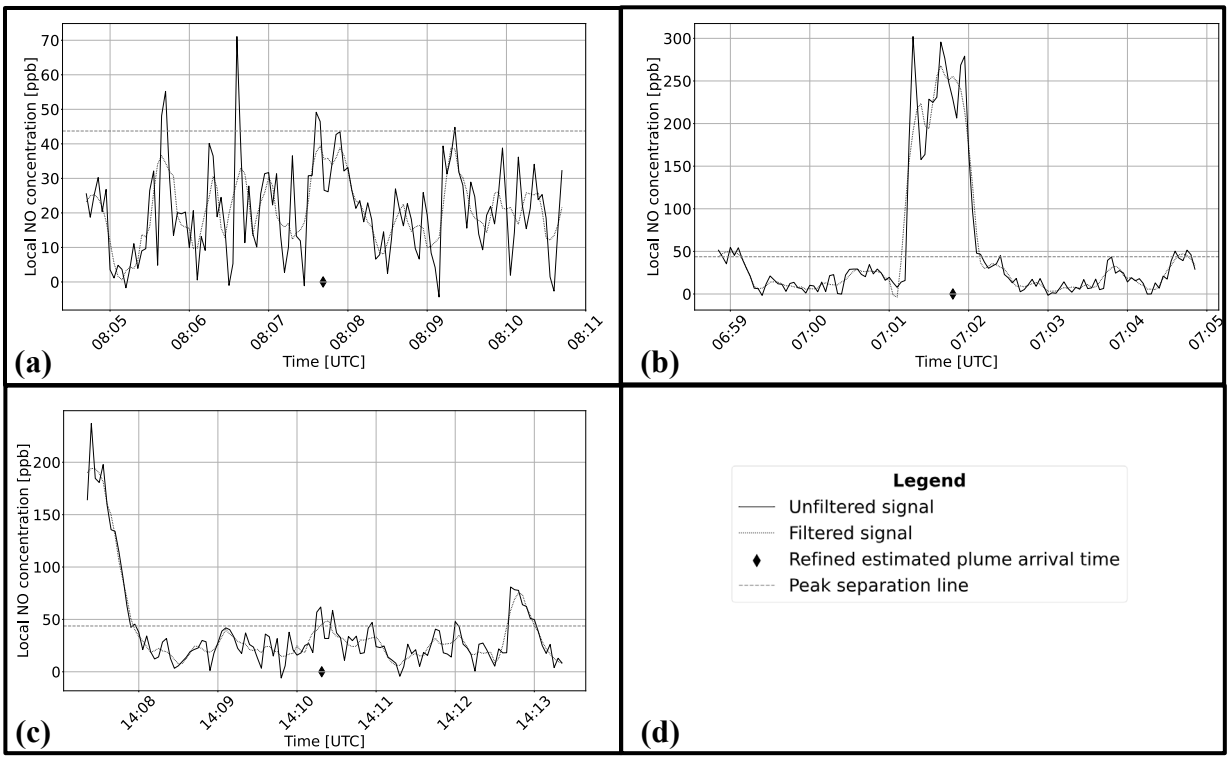

Figure 5.11: *Rejected as no peak could be identified within 30 s of the (refined) EPA time (a), rejected as an overlapping peak could not be coupled to an aircraft operation (b), rejected based on goodness of fit metrics (c) and the figure legend (d)*

5.7.2 Manual verification

The correct estimation of the (refined) EPA time is manually inspected using intervals of >20 minutes in time-series during which only a single aircraft made use of the Polderbaan runway. Due to the absence of other aircraft, it could be verified for these aircraft that the (refined) EPA time was correctly estimated. Besides verifying the correct (refined) EPA time estimation, outliers, which are values that are inconsistent with the remainder of the data set, were manually inspected [180]. Outliers were detected by generating box-plots and dealt with following the proposed method of Motulsky et al. [240]. Hereby it is first verified whether the outlier still yields a realistic value. Next, the input and performance of the algorithm are investigated after which the algorithm is adjusted in case of a mistake. Lastly, measurement notes are conducted to verify that no anomalies could have caused the outlier.

5.8 Estimation of NO_2 plume characteristics

For departing aircraft mostly NO plumes passed quality control while only a relatively small proportion of NO_2 plumes met the quality control criteria. One of the reasons for this, is that the observed NO_2 plumes were frequently not Gaussian shaped and therefore did not meet the predefined thresholds of the goodness of fit metrics. However, as shown in Figure 5.12 signals of NO and NO_2 track well with each other, with peaks being closely aligned and the plume width of NO_2 typically being smaller than the width of the NO plume. In case an NO plume passed quality control and the corresponding NO_2 plume did not, the NO_2 signal in between the start- and end point of the NO plume is therefore used to approximate the plume area- and peak of NO_2. It should be noted that this approximation may be less accurate.

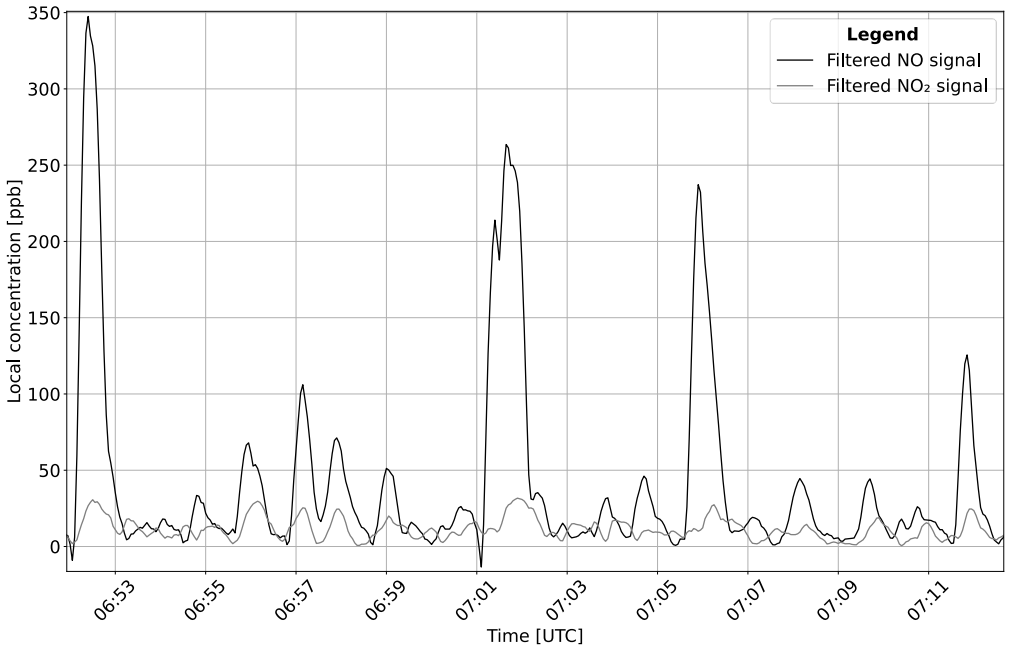

Figure 5.12: *Time-series showing the observed pollutant concentrations of NO and NO_2*

5.9 Summary

To identify aircraft exhaust plumes in the observed air pollution data, first the time is estimated when an aircraft gives rise to a peak concentration (referred to as the EPA time) based on the ambient wind and the perpendicular distance to the runway. To estimate this time more accurately, a constant time factor is added to the EPA time to get the refined EPA time. Peaks near this time above an amplitude threshold are identified after which the associated start- and end point are found based on changes in the first derivative. The peak closest to the refined EPA time is coupled to the aircraft operation. Hereafter the identified plume signals are fitted with a Gaussian curve. For well resolved plumes, the tails of the Gaussian fitting are forced to go to the baseline by superimposing a Gaussian curve on top of the fitted curve whereas for overlapping plumes a multi-Gaussian fitting is performed from which the individual Gaussians are extracted. Finally, plumes are characterised in terms of geometrical parameters, the ratio between NO and NO_2 and SO_2-based emission indices. For NO_2 this approach could typically not be followed, but as this pollutant species tracks well with NO the NO_2 signal in between the start- and end point of the NO plume was used to characterise NO_2 plumes.

6 Aircraft emissions estimation method

This chapter discusses the method utilised to compare the obtained peak pollutant concentrations of aircraft operations to certified pollutant concentrations. For this, a (simple) dispersion model is used. The model description and implementation method will be discussed in Section 6.1. The chapter concludes with a summary in Section 6.2.

6.1 Model description and implementation

Observed peak pollutant concentrations of aircraft exhaust plumes are compared to estimated concentrations using the model shown in Equation 6.1 [1, 102]. In this equation *E* represents the combined emission rate of all engines, *u* the ambient wind speed (assumed to be constant) and *R* the radius of the aircraft exhaust plume at the downwind location for which the pollutant concentration is estimated. This model was used due to its low level of complexity and as Barrett et al. [1, 102] stated that the model agrees within ~20 – 30% with concentrations measured at approximately the same distance from a runway as this research.

$$\chi = \begin{cases} \frac{E}{\pi u R^2} & \text{within the plume} \\ 0 & \text{outside the plume} \end{cases} \tag{6.1}$$

The chosen model is a simple two-dimensional model that assumes the plume dispersion to follow a top-hat distribution. The impact of the aircraft on plume dispersion are neglected. Furthermore, it is assumed that the plume is emitted and measured at ground level in the absence of plume rise. This plume is brought to the sensor nodes unobstructed by a constant speed that is equal to the wind speed. Lastly, it is assumed that the peak pollutant concentration is not influenced by other pollutant sources and that no chemical reactions are taking place. The chosen dispersion model therefore only serves to gain a crude approximation of peak concentrations.

It is worth mentioning that the same model was implemented during previous research of Maes [63]. A critical view on the implementation of Maes is provided in Appendix C.1. A different method was used during this follow-up research, which will be discussed in the remainder of this chapter.

6.1.1 Plume radius

It was reported by Barrett et al. [1, 102] that following mass conservation R^2 can be computed using Equation 6.2. In this equation the σ parameters represent the two-dimensional dispersion of the plume (i.e., the plume spread) with σ_y and σ_z the horizontal (σ_y) and vertical (σ_z) dispersion coefficients [124, 241, 242].

$$R^2 = 2\sigma_y\sigma_z \tag{6.2}$$

In order to estimate these dispersion coefficients various approaches exist, whereby for this research a look-up table (presented in Table C.4 in Appendix C.2) of Briggs [243] is used. This table lists empirical expressions for σ_y and σ_z. These empirical expressions are dependent upon the streamwise distance *S*, which is the distance along which the plume travels from the source to the downwind sensor node. The simplified assumption is made that aircraft are stationary sources releasing a passive plume (i.e., neglecting the initial velocity given to the plume by engine thrust). In this case *S* can be computed using Equation 6.3 with *d* the perpendicular distance to the runway, and *U* and *V* the headwind and crosswind components of the ambient wind.

$$S = d\sqrt{1 + (U/V)^2} \tag{6.3}$$

Besides the streamwise distance *S*, the empirical expressions to estimate σ_y and σ_z depend upon the atmospheric stability. In a stable atmosphere an air parcel, after being displaced upwards or downwards, tends to return to its original elevation after the displacement force ceases whereas in an unstable atmosphere the air parcel would continue to move in the direction of the displacement. In a neutral atmosphere the air parcel remains at the elevation to which it was displaced after the displacement force ceases [244, 245]. To estimate the atmospheric stability at a specific moment in space and time Pasquill stability classes are used. There are six classes, denoted by letters A to F. The classes relevant for this research are A, B, C and D which indicate extremely unstable, moderately unstable, slightly unstable and neutral atmospheric conditions respectively [242]. It should be noted that more advanced methods exist to determine the atmospheric stability, but Pasquill stability classes are able to provide a quick estimate of reasonable accuracy [242, 244, 246].

To determine the Pasquill stability class the ambient wind speed and an estimation of the insolation strength are used. To estimate the insolation strength, first the solar elevation angle (ψ) is estimated, which is the angle between the direction of the Sun and the local vertical [247]. This angle is computed using the *location.get_solarposition()* function of Pvlib [248] based on the position of the sensor node, the measurement date and the (refined) estimated plume arrival time. Next an insolation strength category is found using the procedure of Luna et al. [248, 249]. Hereby first an insolation code is obtained based on ψ using a look-up table (Table C.1 in Appendix C.2). Subsequently, this code is used to retrieve the insolation strength from a second look-up table (Table C.2 in Appendix C.2). Hereby it is assumed that clouds did not impact the insolation strength as METARs reported a low[19] cloud coverage. Based on this insolation strength the Pasquill stability class is determined using a third look-up table (Table C.3 in Appendix C.2).

Using the obtained Pasquill stability class, the dispersion parameters σ_y and σ_z are estimated using empirical expressions of Briggs [243] (see Table C.4 in Appendix C.2). As thermal convection and atmospheric turbulence are enhanced in urban areas compared to rural areas, these expressions are published for two types of terrain roughness: open-country (i.e., rural) conditions and urban conditions [241, 250]. In line with similar research of Barrett et al. [1, 102] urban conditions are assumed to be applicable, but a sensitivity analysis is performed to quantify the difference when open-country conditions are used instead.

6.1.2 Emission rate

The emission rate E is obtained by multiplying the fuel flow with the emission index and the number of engines that the aircraft is equipped with. The emission indices and fuel flow are obtained from the ICAO Emissions Databank [150], which are published for different thrust settings as a percentage of the rated thrust F_{00} (hereafter referred to as % F_{00}). ICAO assumes that aircraft take off at 100% F_{00}, but literature indicated that aircraft rarely use this thrust setting to extend the engine's life cycle and reduce maintenance cost [1, 251–254]. As the actual thrust setting is not known for this research, a representative thrust setting was determined based on literature.

A study of King et al. [255] revealed that for Boeing 777 aircraft the average [minimum, maximum] thrust is ~79.2% [74.6%, 99.5%] F_{00} at London Heathrow Airport and ~83.9% [67%, 99.4%] F_{00} at London Gatwick Airport. Another study, conducted by Koudis et al. [256], showed that the average [minimum, maximum] thrust A319 aircraft is ~78.9% [67%, 97%] F_{00} at London

[19] Cloud cover was reported as 'few' (i.e., a cover of 1/8th to 2/8th octas) for the majority of the obtained data.

Heathrow Airport. Morris [257] found that (depending on the aircraft-engine combination) the minimum thrust utilised at London Heathrow Airport is 60 – 75% F_{00}. Lastly, a study of Sherry [258] revealed that the average take-off thrust at Chicago O'Hare airport equals 86% F_{00} with a standard deviation of 11%.

Based on this it can be concluded that the thrust setting can range from as low as ~60% F_{00} to as high as ~100% F_{00} with (assuming an equal weight of each study) a mean value of the average thrust of ~82% F_{00}. The results for this research will therefore be presented for an assumed thrust setting of 82% F_{00} with error bars displaying the results for thrust settings ranging between 60% F_{00} and 100% F_{00}. It is acknowledged that the 60% F_{00} may not be fully representative for each aircraft operation as the minimum allowable thrust setting may be higher for certain aircraft-engine combinations and meteorological- and operating conditions [251, 257].

After looking into take-off thrust settings, a similar analysis is performed for landing aircraft. According to ICAO the landing roll corresponds to a thrust setting of 7% F_{00}, but aircraft may use reverse thrust in excess of idle thrust [150]. Only two studies in the last two decades could be found that looked into this. The first study, conducted by Morris [259], reported that ~3% of Boeing 777-200's, ~6% of Boeing 747-400's and ~13% of Boeing 767-300's used more than idle reverse thrust at London Heathrow Airport. This suggests that normally not more than idle reverse thrust is used, which has been confirmed by other reports (see e.g., [3, 108, 135]). The second study, conducted by Noel and Boeker [116], revealed that the average thrust during thrust reverser deployment is ~32% F_{00} for the A320, ~41% F_{00} for the B737-400, ~28% F_{00} for the B767-200ER and ~6% F_{00} for the B747-400. Based on this, the results will therefore be reported for an assumed thrust setting of 7% F_{00} with error bars indicating the results for thrust settings ranging between 7% F_{00} to 41% F_{00}.

After determining representative (reverse) thrust settings, the fuel flow and emission index need to be retrieved. However, these are only published in the ICAO Emissions Databank [150] for 7%, 30%, 85% and 100% of the rated thrust. Furthermore, the values are reported for standard atmospheric conditions and do not consider that bleed air is extracted from the engines (hereafter referred to as engine installation effects). To compute the emission indices and fuel flow for intermediate thrust settings and to correct for ambient conditions and engine installation effects, the Boeing Fuel Flow Method 2 (BFFM2) is used. This method is recommended by ICAO and has been extensively used in research (see e.g., [6, 260–262]).

The BFFM2 was implemented as described by Dubois [252] except for the humidity correction term for which the formula of Schaefer and Bartosch [263] was used [263]. Some engine models are known to raise issues when using the BMFF2, as the certified data is not in line with the expectations on which the BFFM2 methodology is based [264]. The SAGE Technical Manual [265] provides an overview of these issue cases and suggests ways to resolve them, which have been implemented accordingly in this research. A description of the implementation of the BFFM2 and the way issue cases are handled can be found in Appendix C.3. After obtaining the emission rate, the peak pollutant concentration of the plume can be computed using Equation 6.1.

6.2 Summary

Peak concentrations are estimated using a simple dispersion model and certified emission data. To compute the emission rate, certified emission indices and fuel flow rates are used for an assumed thrust setting of ~82% of the rated thrust (F_{00}) for take offs and 7% F_{00} for landings based on literature. However, the results will also be presented for thrust settings ranging between 60% F_{00} and 100% F_{00} for take offs and 7% F_{00} to 45% F_{00} for landings. To compute the emission indices and fuel flow rates for intermediate thrust settings and to correct for ambient conditions and engine installation effects, the Boeing Fuel Flow Method 2 is used.

Part III: Findings, conclusions and recommendations

7 Results and discussion

In this chapter the results are presented, discussed and compared to existing research. Section 7.1 till Section 7.4 present the results of the downwind-, upwind-, co-location- and near engine exit plane experiment respectively. Thereafter Section 7.5 compares the obtained results to certified emissions. Lastly, Section 7.6 provides a summary of the chapter.

7.1 Downwind experiment

This chapter starts off by discussing the results of the downwind experiment whereby one sensor node was placed downwind to measure the air pollution confined in aircraft exhaust plumes. With respect to these results, it should be kept in mind that around Schiphol airport yearly average ambient concentrations of NO_x, NO_2, SO_2 and CO are ~15 – 30 µg/m^3 [266].

7.1.1 Analysis based on flight activity

Local air pollutant concentrations (i.e., concentrations for which the background concentration has been removed) showed significant differences between departing- and landing aircraft and between pollutant species. Departing aircraft typically led to significant NO_x concentrations above the background with an average local peak (i.e., maximum) concentration of ~465 µg/m^3. In terms of the individual components of NO_x, significant local concentrations could be observed for NO with an average peak concentration of ~244 µg/m^3. These NO peaks were generally accompanied by discernible increases in NO_2 with an average local peak concentration of ~81 µg/m^3. Conversely, the remaining analysed pollutant species showed a continuously oscillating signal with an amplitude of ~40 µg/m^3 for CO and ~30 µg/m^3 for SO_2 irrespective of aircraft activity. It was expected that higher concentrations of NO_x (NO and NO_2) were measured compared to other species, as the rate at which CO and SO_2 are emitted at high thrust settings is significantly lower compared to NO_x (see Appendix D.1.1) [73, 109, 150].

Existing literature to compare these values to is scarce and is generally limited to NO_x. The comparison is therefore only performed for this pollutant species using Table 7.1, whereby it should be kept in mind that the applied measurement technique, data processing methods as well as meteorological- and operating conditions can impact peak concentrations. From this table it can be concluded that other research observed aircraft attributable NO_x peak pollutant concentrations of the same order of magnitude as this research. A potential explanation for the lower concentrations reported by Bossioli et al. [72, 267] is that plumes may have travelled over longer distances compared to this research due to the relatively small angle between departing aircraft and the wind direction.

***Table 7.1**: Observed aircraft attributable NO_x peak concentrations (i.e., the maximum background-subtracted concentrations resulting from departing aircraft) by this research and similar existing research*

Measurement location	Observed local NO_x peak concentrations [µg/m^3] of departing aircraft	Source
~180 m perpendicular to runway 27R of London Heathrow Airport	120 – 760	Carslaw et al. [37, 67]
~210 m perpendicular to runway 03L of Athens International Airport	25 – 460	Bossioli et al. [72, 267]
~190 m perpendicular to runway 36L of Schiphol Airport	168 – 1561	This research

Contrary to departing aircraft, substantial NO and NO_2 concentrations above the background were typically absent for landing aircraft. Instead, their time-series showed a continuously oscillating signal up to ~30 µg/m^3 regardless of the presence of aircraft. Besides, similar to departing aircraft the SO_2 time-series showed a continuously oscillating signal with an amplitude of ~20 µg/m^3 irrespective of aircraft activity. However, opposed to aircraft taking off, landing aircraft typically showed substantial CO concentrations above the background with a mean peak height of ~48 µg/m^3. Higher concentrations of CO were expected compared to the other pollutant species, as the rate at which CO is emitted during landings is substantially higher compared to NO_x and SO_2 (see Appendix D.1.1) [73, 109, 150].

Consequently, it was (for the large majority of aircraft) deemed impossible to unambiguously assign SO_2, NO and NO_2 peaks to landing aircraft and CO and SO_2 peaks to departing aircraft. Therefore, landings are only analysed in terms of CO while the analysis of take offs is limited to NO and NO_2. However, it is worth mentioning that for <15% of the aircraft operations substantial local NO concentrations accompanied by discernible increases in NO_2 could be observed near the (refined) Estimated Plume Arrival (EPA) time. An example of this is shown in Figure 7.1 around 11:48 UTC for a B77W and near 12:02 UTC for a B744.

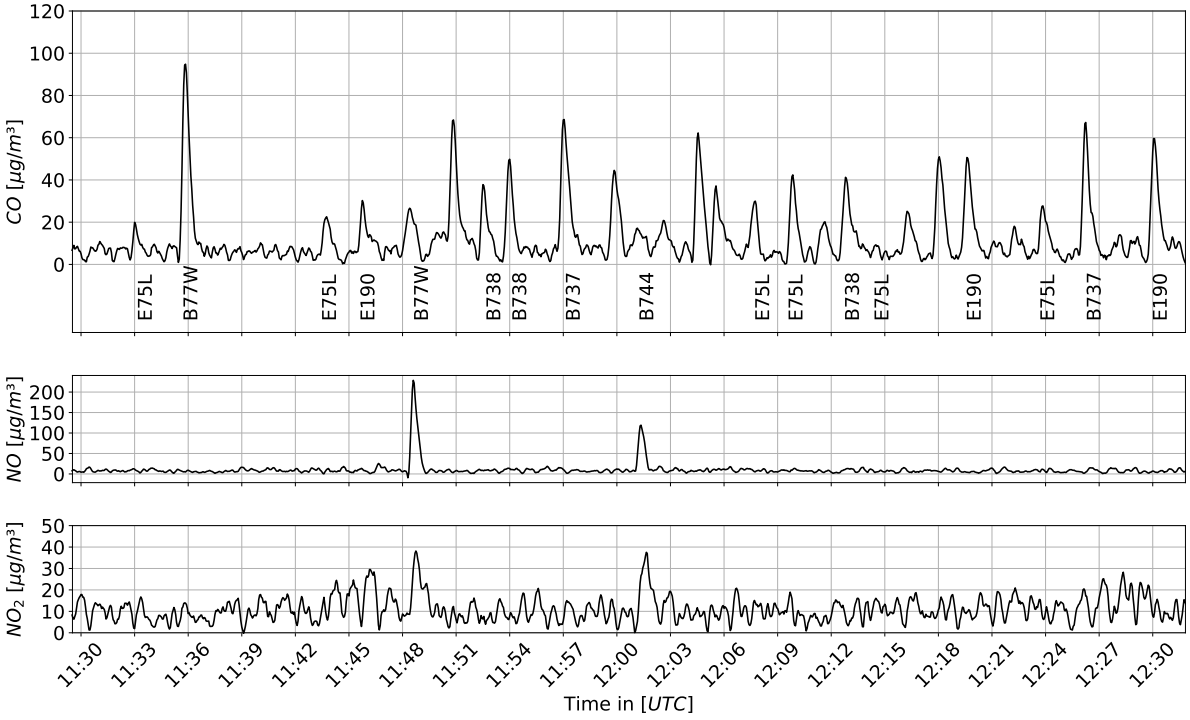

Figure 7.1: *Filtered signal of local time-series together with the (refined) estimated plume arrival time of landing aircraft for the measurement conducted at 22-01-2021*

These are believed to be associated with aircraft utilising more than idle reverse thrust for three reasons. Firstly, the plumes exhibit an NO/NO_2 ratio much larger than unity. Research of Wood et al. [17] stated based upon measurements of a CFM56-3B1 engine that in excess of 98% of NO_x consists of NO_2 at idle thrust while at 65 – 100% thrust over 90% of NO_x consists of NO. For the B77W and B744 of Figure 7.1 the NO/NO_2 ratios are ~6 and ~3 respectively, indicating that most NO_x consists of NO which suggests the use of a high thrust setting.

Secondly, the plumes exhibit a CO/NO_x ratio much lower than unity which, similar to a high NO/NO_2 ratio, corresponds to a high thrust setting. For example, a study of Yu et al. [268] stated that this ratio is significantly higher than unity for idle thrust. Another study conducted by Timko et al. [51] reported that that the NO_x/CO ratio ranges from ~4 – 6 for idle thrust and decreases monotonically to ~0.05 at maximum thrust. However, it is expected that this ratio was incorrectly reported and the values correspond to the inverse ratio (CO/NO_x) instead. The

CO/NO_x ratios of the B77W and B744 of Figure 7.1 are ~0.07 and ~0.08 respectively, which suggests that a high thrust setting was used.

Lastly, measurement notes frequently stated that around the time significant NO peaks were present in time-series a large increase in engine spool-up noise could be observed. However, as this is subjective more research is needed to confirm that these NO and NO_2 peaks are associated with more than idle reverse thrust operations.

7.1.2 Automated screening- and goodness of fit results

The results of the automated screening that took place as part of quality control are presented here together with an assessment of how well the Gaussian fitting matches the observed plume signals. During the downwind experiment 405 aircraft operations were measured including 165 take offs and 240 landings. In terms of departing aircraft, ~52% of the NO plumes (equivalent to 85 plumes) and ~25% of the NO_2 plumes (leading to 42 plumes) passed quality control. Regarding landing aircraft ~57% of the CO plumes (corresponding to 137 plumes) met the quality control criteria. The percentage of plumes passing quality control tends to be higher during higher crosswind speeds and differed up to ~30% among measurement dates (see Appendix D.1.2).

Regarding CO plumes of landing aircraft and NO plumes of departing aircraft, the main reason for plumes not to pass quality control is two-fold. Firstly, ~45% of the CO plumes and ~31% of the NO plumes showed overlap with another plume whereby the overlapping plume could not be coupled to another aircraft operation. Secondly, for ~35% of the CO plumes and ~44% of the NO plumes no peak could be identified within 30 seconds of the (refined) EPA time. This may be attributable to plume peaks being below the amplitude threshold or by the offset between the estimated- and actual plume arrival time being too large. With respect to NO_2 of departing aircraft, plumes mainly failed to pass quality control by not passing the goodness of fit criteria (~47%) or because overlapping plumes could not be coupled to aircraft operations (~45%)[20]. A detailed overview of the automated screening results is provided in Appendix D.1.2.

To investigate whether differences can be observed in the number of plumes passing quality control for different aircraft types, Figure 7.2 shows for various aircraft types the percentage of plumes passing quality control together with the number of times the aircraft type was encountered. With respect to departing aircraft, a slightly higher percentage (~58% versus ~49%) of NO plumes passes quality control for large aircraft compared to medium-sized ones. This difference is more pronounced for landing aircraft, with ~76% of the CO plumes of large aircraft meeting the quality control criteria compared to ~54% for medium-sized aircraft. The higher proportion of plumes of large aircraft passing quality control may be attributable to the amplitude threshold. Occasionally for some medium-sized aircraft the peak closest to the refined EPA time did not exceed the selected amplitude threshold such that no plume was identified.

[20] Note that plumes may not pass multiple quality control criteria, but the algorithm terminates for an aircraft operation after failing to pass a criterium such that the sequence in which the algorithm evaluates criteria influences the specified percentages.

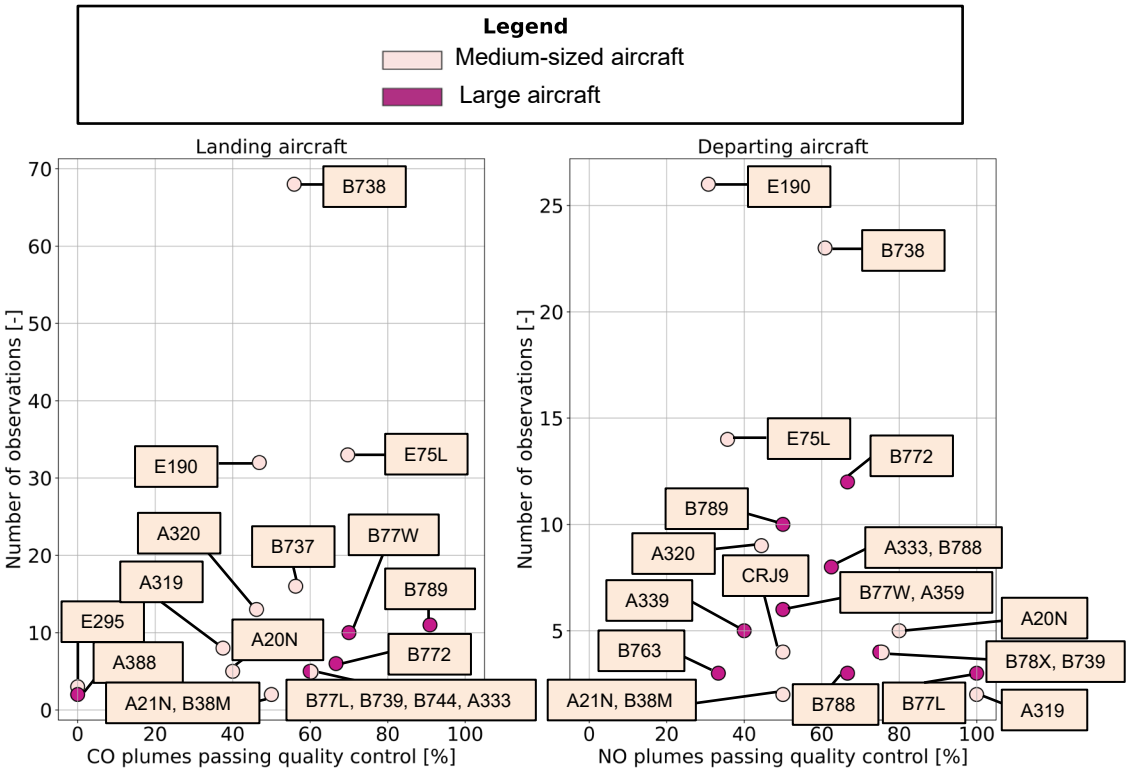

Figure 7.2: *Number of times specific aircraft types were encountered versus the percentage of plumes passing quality control*

For the plumes passing all automated screening criteria[21] the mean and standard deviation of the goodness of fit metrics described in Section 5.5 are presented in Table 7.2. Based upon these values it can be concluded that the Gaussian curve is a suitable representation for the actual plume signals. For all pollutant species the average percentage difference of the actual plume area and area of the Gaussian fitting is <10%. Similarly, the average percentage difference of the peak of the filtered plume signal and peak of the Gaussian fitting is <10% for all pollutant species. The reader is referred to Appendix D.1.3 for the results of the goodness of fit assessment per measurement date and per aircraft type.

Table 7.2: *Mean (and standard deviation) of the coefficient of determination (R^2), absolute value of the reduced Chi-squared ($|\chi^{2*}|$), Mean Absolute Error (MAE), Root Mean Square Error (RMSE), percentage difference between the area of the unfiltered plume signal and the Gaussian fitting ($A_{difference}$) and percentage difference between the peak pollutant concentration of the filtered plume signal and the Gaussian fitting for plumes passing quality control ($P_{difference}$)*

Species	R^2 [-]	$\lvert\chi^{2*}\rvert$ [-]	MAE $[\mu g/m^3]$	RMSE $[\mu g/m^3]$	$A_{difference}$ [%]	$P_{difference}$ [%]
CO	0.882 (0.073)	4.1 (8.0)	3.5 (1.9)	4.3 (2.2)	4.7 (6.7)	4.2 (3.8)
NO	0.825 (0.104)	19.5 (19.1)	18.5 (15.6)	23.1 (19.6)	5.4 (5.4)	5.0 (4.6)
NO_2	0.741 (0.088)	6.7 (6.2)	6.5 (1.9)	7.9 (2.2)	8.1 (6.5)	6.8 (2.2)

[21] In this table A_{diff} and $P_{diference}$ include well resolved plumes (see Section 5.5) while the remaining parameters include both well resolved plumes and overlapping plumes[21].

7.1.3 Aircraft-specific plume characteristics

For the plumes passing the automated screening criteria the results are analysed in terms of specific aircraft types. The upper graph of Figure 7.3 (a) shows the cumulative aircraft attributable NO_x concentrations over time (i.e., the area under the curve of plume signals in pollutant time-series) for different aircraft types. The aircraft types are sorted from low to high Maximum Take Off Weight (MTOW) and classified as 'medium-sized' or 'large' according to their ICAO Wake Turbulence Category (WTC) [269]. The lower graph of Figure 7.3 (a) shows the certified NO_x emission rate of the aircraft-engine combinations on which the top of Figure 7.3 (a) is based. The emission rate has been computed by multiplying the product of the fuel flow and emission index of the ICAO Emissions Databank [150] by the number of engines that the aircraft is equipped with under the assumption that aircraft take off using their maximum rated thrust. However, as the actual thrust setting is unknown error bars show the emission rate for thrust settings of 60 – 100% of the rated thrust. The reader is referred to Appendix D.1.3 for the cumulative aircraft attributable concentrations in terms of NO and NO_2.

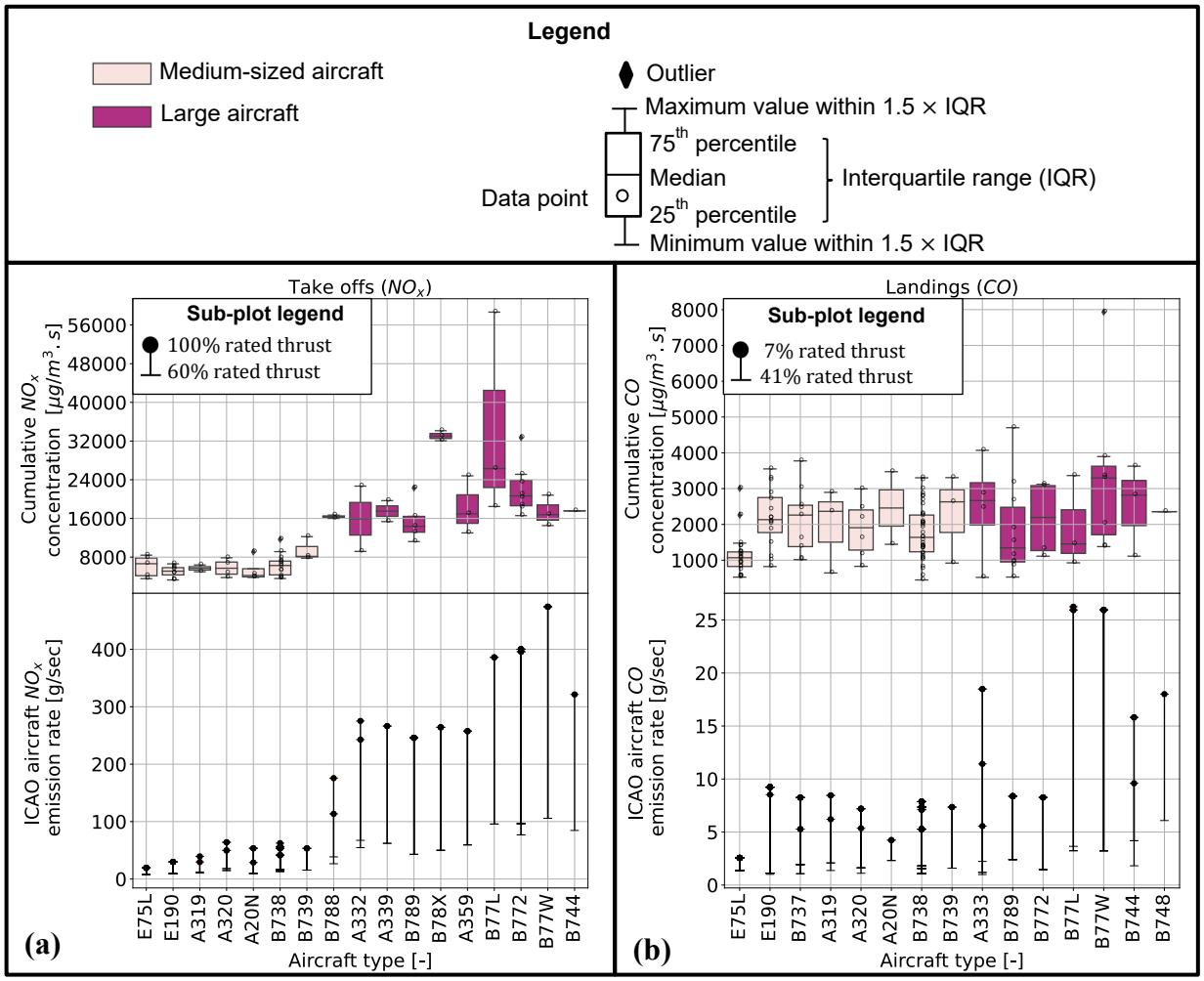

Figure 7.3: *Observed background-subtracted cumulative pollutant concentrations over time for different aircraft-engine combinations (upper graph) and the ICAO emission rate for the same aircraft-engine combinations (lower graph) for NO_x of departing aircraft (a) and CO of landing aircraft (b)*

Significant differences in cumulative NO_x concentrations exist among aircraft types. In the upper graph of Figure 7.3 (a) a systematic dependency on aircraft size is evident whereby large aircraft exhibit on average ~3.5 times higher cumulative NO_x concentrations (~21261 µg/m^3.s) compared to medium-sized ones (~6049 µg/m^3.s). The same conclusion can be drawn when looking at the maximum NO_x concentration (i.e., the peak height of plume signals

in local pollutant time-series) and the average plume concentration (i.e., the area over the width of plume signals in local pollutant time-series) as shown in Appendix D.1.3.

Similar to the observed cumulative NO_x concentrations, the certified NO_x emission rate is larger for large aircraft compared to medium-sized ones as shown in the lower graph of Figure 7.3 (a). Furthermore, the upper graph and lower graph of Figure 7.3 (a) show (roughly) a similar trend for the aircraft types between the B738 and the B789. However, the certified NO_x emission rate is lowest for the E75L while this aircraft type did not yield the lowest cumulative NO_x concentrations. Furthermore, the B78X yields the highest cumulative NO_x concentrations despite the B77L, B772, B77W and B744 having a higher certified emission rate (assuming all aircraft depart at 100% of the rated thrust). Besides, the B772 and B77W were not among the aircraft with the highest cumulative NO_x concentrations even though they exhibit the largest certified emission rate.

Similar to this research, Carslaw et al. [37, 67], Stacey et al. [52] and Synlo et al. [267] observed that larger aircraft result in higher downwind NO_x concentrations compared to medium sized ones. In line with the findings of this research, Carslaw et al. [37, 67] furthermore observed a trend of progressively higher peak concentrations for the A319, A320, B738 and A332 (see Table 7.3). Besides, the mean NO_x peak concentrations reported by Carslaw et al. [37, 67] were within 20 – 40 % of the ones observed during this research, except for the A332 for which the mean NO_x peak concentration was ~82% higher during this research. However, it should be kept in mind that the applied measurement technique, data processing methods as well as meteorological- and operating conditions may impact peak concentrations.

Table 7.3: *Difference in mean NO_x peak concentration observed during this research and similar research of Carslaw et al. for different aircraft types*

Aircraft type	Mean NO_x peak concentration observed during this research [$\mu g/m^3$]	Mean NO_x peak concentration observed by Carslaw et al. [37, 67] [$\mu g/m^3$]	Percentage difference [%]
A319	197	133	~39
A320	215	161	~29
B738	229	185	~21
A332	893	374	~82

After analysing the differences with respect to aircraft size, a similar analysis is performed to investigate potential discrepancies between older and more modern aircraft. The A320 exhibits on average ~8% higher cumulative NO_x concentrations compared to the A20N, which is the latest type of the same aircraft series [270]. Similarly, on average cumulative NO_x concentrations of the A319 are ~13% higher compared to the more modern E190 [270, 271]. Conversely, on average ~9% higher cumulative NO_x concentrations can be observed for the A339 compared to the older A332 [272].

Regarding these findings, it is important to note that these differences may be attributable to a difference in thrust setting, which (among other factors) depends on the aircraft's weight. The A319 has a higher Maximum Take Off Weight (MTOW) (~64 000 kg) compared to the E190 (~46 000 kg) [270, 271]. Similarly, the A332 has a higher MTOW than the A339 (~230 000 kg for the A332 compared to ~251 000 kg for the A339) [270, 271]. Aircraft with a higher MTOW may have taken off at a higher weight, which requires more thrust and increases NO_x emissions [67, 109, 150, 273]. More research is therefore required to assess whether a trend exists between the cumulative NO_x concentrations of modern aircraft compared to older aircraft.

After evaluating the difference between aircraft types, it is interesting to note that cumulative NO_x concentrations vary in excess of 50% for aircraft of the same type. A potential explanation for this is that aircraft of the same type may be equipped with different engine models. Additionally, an aircraft type may consist of various airframe models (e.g., four in case of the B739) that can potentially have a different impact on the dispersion of exhaust plumes. However, even for unique airframe-engine combinations (for example the Boeing 737-800 with CFM56-7B26E engines) differences in excess of 50% are present. The same was observed by research of Carslaw et al. [37, 67], in which peak concentrations varied up to 41% for aircraft utilising the same airframe- and engine model. It is expected that this variability is associated with differences in meteorological- and operating conditions, such as the thrust setting [37, 67]. Besides, other factors such as the engine-to-engine variability (due to manufacturing tolerances and engine state) are likely to contribute to this [37, 67, 71].

After analysing NO_x of departing aircraft, the same analysis is performed in terms of CO for landing aircraft using Figure 7.3 (b). In this figure the upper graph shows the cumulative aircraft attributable CO concentration over time for different aircraft types whereby aircraft are sorted from low to high MTOW. The lower graph of Figure 7.3 (b) shows (for the same aircraft-engine combinations on which the top of Figure 7.3 (b) is based) the certified CO emission rate at an assumed idle thrust setting equal to 7% of the rated thrust. However, as aircraft may use reverse thrust, error bars show the emission rate for thrust settings of 7 – 41% of the rated thrust.

Unlike the cumulative NO_x concentrations of departing aircraft, no dependency on aircraft size can be observed regarding cumulative CO concentrations of landing aircraft. However, similar to NO_x plumes of aircraft that are taking off, cumulative CO concentrations vary in excess of 50% between aircraft operations of the same type. This is expected to be attributable to differences in engine- and airframe models, engine-to-engine variability and difference in meteorological- and operating conditions (e.g., the use of reverse thrust) [37, 67, 71].

The bottom of Figure 7.3 (b) shows that, similar to the observed cumulative CO concentrations, no consistent trend is evident between the rate at which CO is emitted and aircraft size. The lowest certified CO emission rate is prominent for the E75L, which also yields the lowest observed cumulative CO concentrations. Conversely, the A20N exhibits a lower certified CO emission rate compared to the A320, A319, B737 and E190 but this is not reflected in the cumulative CO concentrations. Another interesting observation is that the B77L and B77W exhibit approximately the same certified CO emission rate, which is higher compared to the emission rate of the other aircraft types. However, the B77W is among the aircraft with the highest cumulative CO concentrations while the B77L is not. This may be indicative of the frequent use of (more than idle) reverse thrust for this aircraft type, as ~40% of the aircraft operations for which it was expected that more than idle reverse thrust was used were a B77L. Nevertheless, more research is needed into this matter.

After looking into cumulative pollutant concentrations, it is investigated how the duration of aircraft plumes varies among aircraft types. Note that this duration corresponds to the width of the Gaussian representation of a plume signal in pollutant time-series. On average plumes last for ~64 s, ~76 s and ~93 s for NO, NO_2 and CO respectively whereby Figure 7.4 reveals the width to be independent of aircraft size. This is in line with similar research of Carslaw et al. [102]. Furthermore, variations in excess of 40% can be observed in the width of plumes of the same aircraft type.

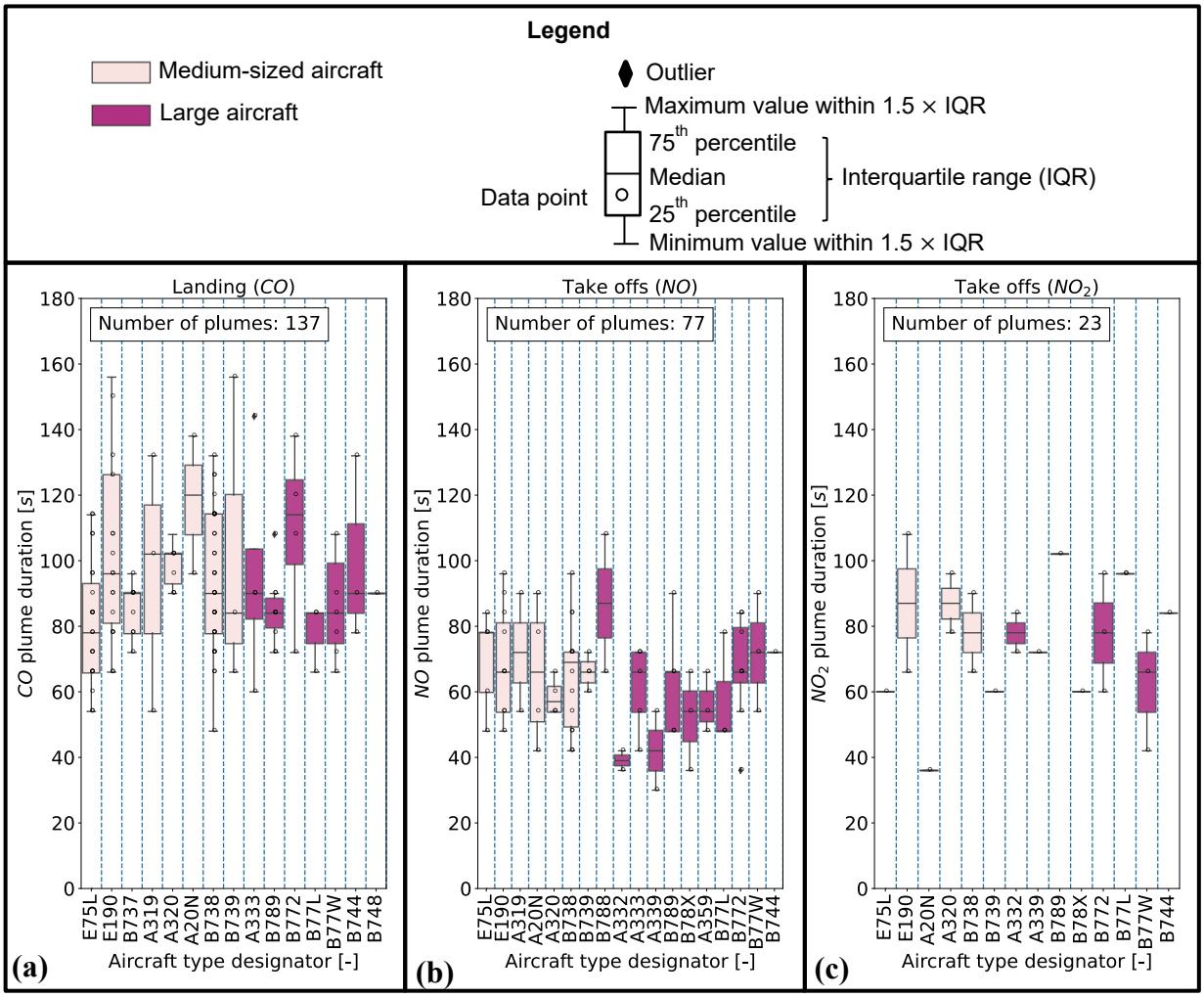

Figure 7.4: *Plume width of the Gaussian representation of plumes in pollutant time-series (representing the duration of enhanced pollutant concentrations due to an aircraft) for different aircraft types for CO (a), NO (b) and NO_2 (c)*

7.1.4 Engine-specific plume characteristics

The same analysis as conducted for specific aircraft types is performed for specific engine models. The upper graph of Figure 7.5 (a) shows the cumulative engine attributable NO_x concentrations over time for different engine models during take-off. Hereby it is assumed that each engine of the aircraft had an equal contribution, such that the cumulative NO_x concentrations are divided by the aircraft's number of engines to obtain the contribution per engine. The lower graph of Figure 7.5 (a) shows the corresponding certified NO_x emission rate, which has been computed by multiplying the fuel flow with the emission index that are listed in the ICAO Emissions Databank [150]. Hereby it is assumed that aircraft take off at their maximum rated thrust (100% of the rated thrust). However, as the actual thrust setting is unknown error bars display the emission rate for settings between 60 – 100% of the rated thrust. The engine models are listed based upon increasingly high emission rate. The analysis regarding NO and NO_2 is presented in Appendix D.1.4.

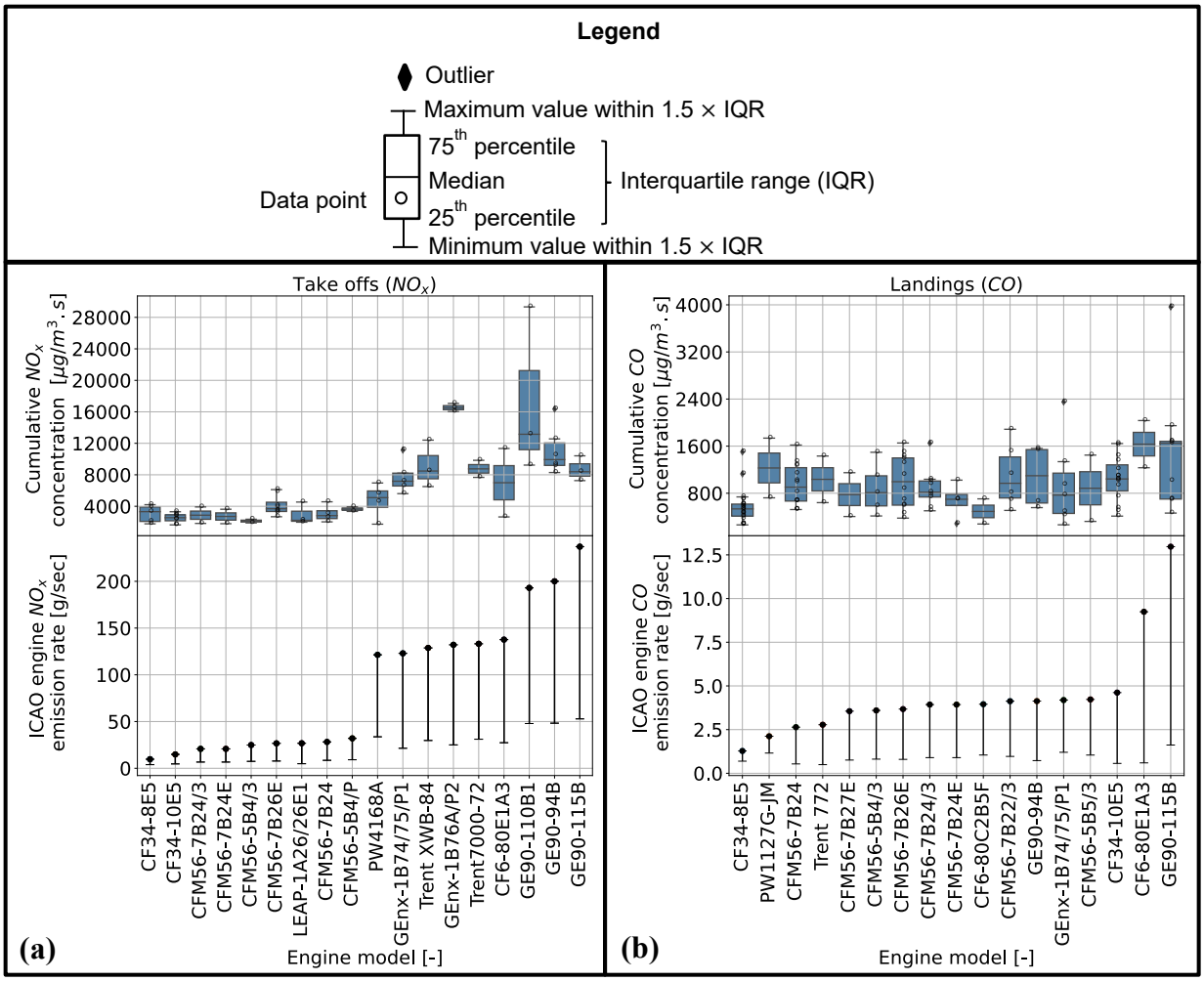

***Figure 7.5**: Observed background-subtracted cumulative pollutant concentrations over time for different engine models (upper graph) and the ICAO emission rate for the same engine models (lower graph) for NO_x for departures (assuming 100% of the rated thrust with error bars down to 60% of the rated thrust) (a) and CO of landings (assuming 7% of the rated thrust with error bars till 41% of the rated thrust) (b)*

Significant differences in cumulative NO_x concentrations exist among engine models. No consistent trend is evident that engine models with a higher certified NO_x emission rate yield higher cumulative NO_x concentrations. The lowest cumulative NO_x concentrations correspond to the CFM56-5B4/3, whereas the certified emission rate is lowest for the CF34-8E5. The certified emission rate is highest for the GE90-115B, while the highest cumulative NO_x concentrations can be observed for the GEnx-1B76A/P2 and the GE90-110B1. Furthermore, differences in the mean cumulative NO_x concentrations of up to ~50% exist among engine models of the same series. For example, the mean cumulative NO_x concentration of engine models belonging to the CFM56-7B series differ up to 48%.

After discussing the results in terms of NO_x for departures, the same analysis is performed regarding CO for landings using Figure 7.5 (b). In this figure the upper graph shows the cumulative CO concentrations over time for different engine models. The lower graph of Figure 7.5 (b) shows the certified CO emission rate for which an idle thrust setting (7% of the rated thrust) has been assumed. However, as aircraft may use reverse thrust error bars show the emission rate for settings between 7 – 41% of the rated thrust.

No trend is evident in Figure 7.5 (b) that engine models with a higher certified CO emission rate yield higher cumulative CO concentrations. The largest cumulative CO concentrations correspond to the CF6-80E1A3, which is also among the engines with the highest certified CO emission rate. The lowest certified CO emission rate is present for the CF34-8E5, which is also among the engine models for which the lowest cumulative CO concentrations can be observed. It is furthermore interesting to point out that variations up to ~50% can be observed between the mean cumulative CO concentration of engine models of the same series (for example for the CFM56-7B series).

7.1.5 Correlation between area, peak and width

After analysing engine-specific results, potential relationships between the area (i.e., the cumulative pollutant concentration), peak (i.e., the maximum pollutant concentration) and width (i.e., the plume duration) of plume signals are investigated. For this, the Pearson correlation coefficient *r* is used which can range from -1 to +1 and is indicative of the linear correlation between two variables *A* and *B*. A negative *r* indicates the tendency that when variable *A* increases variable *B* decreases and vice versa while a positive *r* indicates the tendency that when variable *A* increases variable *B* increases as well. When *r = 0* no linear relationship exists between the two variables [274]. The Pearson correlation coefficient between two datasets is computed with Equation 7.1, with *n* the number of observations, M_i the value at datapoint *i* of the first dataset (associated with variable A) and RM_i the value at datapoint *i* of the second dataset (associated with variable B). $\overline{M}$ is the mean of the values of the first dataset and $\overline{RM}$ is the mean of the values of the second dataset.

$$r = \frac{\frac{1}{n}\sum_{i=1}^{n}\left(M_i - \overline{M}\right)\left(M_i - \overline{RM}\right)}{\sqrt{\frac{1}{n}\sum_{i=1}^{n}(M_i - \overline{M})^2 \frac{1}{n}\sum_{i=1}^{n}\left(RM_i - \overline{RM}\right)^2}} \tag{7.1}$$

Figure 7.6 displays the area, peak and width for the Gaussian representation of CO plumes (see Appendix D.1.5 for similar graphs in terms of NO and NO_2). From this figure it is evident that an approximately linear relationship exists between the Gaussian area and peak height of plumes, which cannot be observed for the area and width. The Pearson correlation coefficient *r* of the area and peak equals 0.859, 0.905 and 0.725 for CO, NO and NO_2 respectively, thereby indicating an approximately linear correlation. For the area and width *r* equals 0.585, 0.058 and -0.175 for CO, NO and NO_2 respectively which indicates that (mainly for NO and NO_2) no linear correlation exists between the area and the width. Both Wei et al. [174] (who analysed road vehicle plumes) and research of Carslaw et al. [37, 67] (who analysed aircraft plumes) also concluded that no correlation exists between the plume area and the plume width. The peak height is therefore deemed an appropriate metric to quantify the contribution of aircraft operations to local air pollution, while the plume width is not.

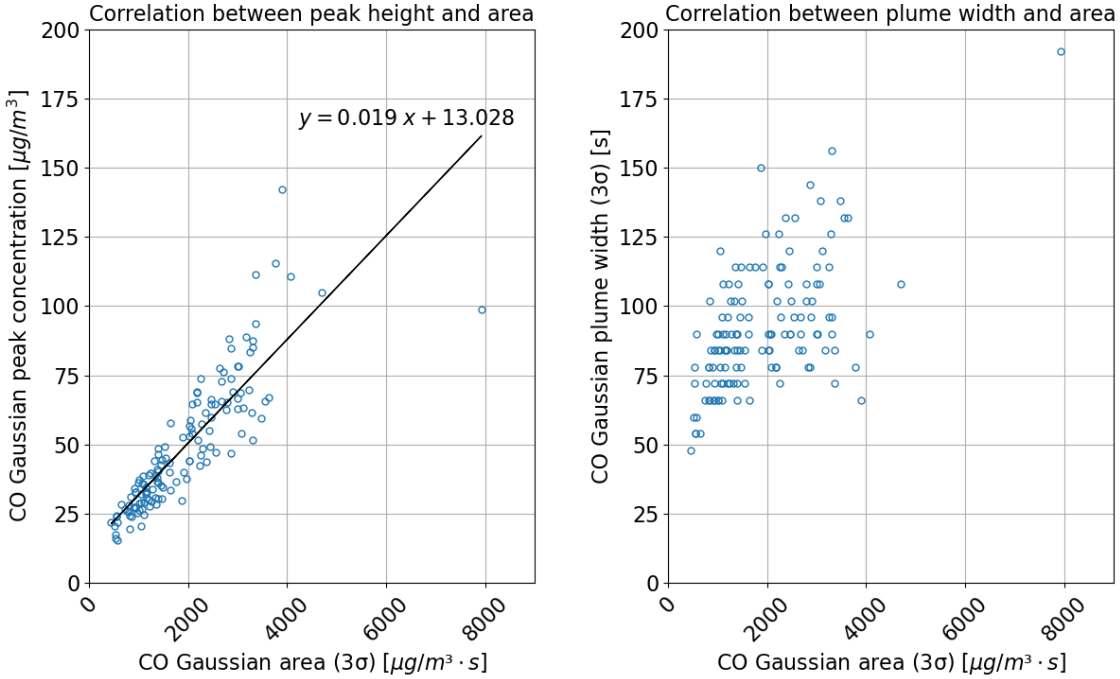

***Figure 7.6**: Relationship between the peak height and area and width and area of Gaussian CO plumes*

7.1.6 Ratio between NO_2 and NO

After examining relationships among plume characteristics, the relative proportion of the two pollutant species forming NO_x (NO and NO_2) are investigated. From Figure 7.7 it becomes clear that (for departing aircraft) NO_x mostly consists out of NO at the measurement site.

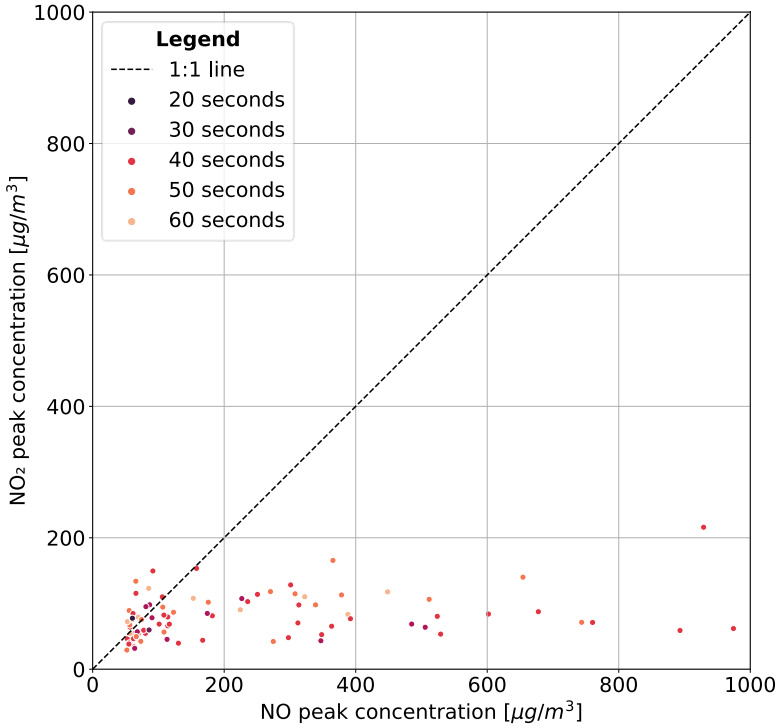

***Figure 7.7**: Correlation graph between the Gaussian plume peak concentration of NO and NO_2 with an increasingly light colour depicting increased plume travel time*

For modern high-bypass turbofan engines the large majority of NO_x is emitted in terms of NO at higher thrust settings, but NO is converted to NO_2 while the plume travels towards the sensor node [17, 71, 73, 110]. It is therefore expected that an increase in travelling time leads to a larger proportion of NO_2, but this is not reflected in the data. However, Figure 7.7 shows the peak concentrations for various aircraft-engine combinations during different operating- and meteorological conditions, which can impact the relative proportions of NO and NO_2 [17, 68, 165, 275, 276]. Therefore, more research is needed to investigate this.

During this research an average NO_2/NO ratio of ~0.6 was observed, which is compared to the ratios of other research using Table 7.4. With respect to the ratios reported by existing literature, it should be kept in mind that meteorological- and operating conditions, the equipment set-up, fuel composition, engine characteristics and the chemical reactions with other pollutant species have an impact on the ratio between NO and NO_2 [17, 68, 165, 275, 276]. It should furthermore be noted that the NO_2/NO ratio reported by Stacey et al. [52] was based on pollutant concentrations for which background concentrations were not subtracted, hence non-aircraft sources likely contributed to this ratio.

Table 7.4: *NO_2/NO ratios of departing aircraft observed during this research and similar existing research*

Mean NO_2/NO ratio	Measurement location	Number of plumes	Source
0.6	~170 m perpendicular to runway 27R of London Heathrow Airport	2877	Stacey et al. [52]
0.7	~200 m perpendicular to a runway of Athens International Airport	30	Bossioli et al. [72]
0.6	~190 m perpendicular to a runway at Amsterdam Schiphol Airport	85	This research

7.1.7 Limitations

It should be noted that the data analysed for this research includes a low (typically <10) number of observations per aircraft type and engine model. Furthermore, the amplitude threshold may introduce bias towards higher cumulative pollutant concentrations as plumes exhibiting lower peak concentrations may be discarded. Besides this, the method to extract the baseline may have impacted the results. To investigate the influence that changes to the baseline extraction window and amplitude threshold have on the results, a sensitivity analysis is conducted of which the results are presented in Appendix D.1.6.

Furthermore, the results may have been influenced by environmental conditions, as the baseline of the gas sensor's working electrode (which measures the ambient air pollution) varies with environmental conditions. To correct for this, the gas sensors are equipped with an auxiliary electrode which is isolated such that it remains unexposed to ambient pollutant concentrations. As (ideally) both electrodes respond similarly to changes in environmental conditions, the baseline variation of the working electrode can be removed by subtracting the signal of the auxiliary electrode. A detailed description of this is provided in Appendix B.1.

Other research however indicated that this may be insufficient as the working electrode and auxiliary electrode may respond differently to changes in environmental conditions [46, 170, 173, 277]. With respect to the sensors employed during this research, Mijling et al. [278] observed that the NO_2 sensor's output may no longer be representative at internal temperatures >30°C. Cross et al. [46] stated that environmental conditions have a large impact on the NO sensor's output at internal temperatures >25°C. On the contrary, the impact was small on the output of the CO sensor over the analysed temperature range (up to 28°C).

Besides temperature, the magnitude and rate of change of relative humidity can have an impact on the output of the gas sensors [279]. Ahumada et al. [60] stated that the performance of the SO_2 and NO_2 sensors employed during this research are affected when the humidity is $\lesssim$15% or $\gtrsim$90% or when the humidity rapidly changes. In terms of NO, Masson et al. [280] observed unpredictable sensor responses when the relative humidity was $\gtrsim$75%. Based on the temperature and relative humidity encountered during this research (see Appendix D.1.7) it is expected that the ambient temperature and humidity do not have a large impact on the results.

Besides temperature and relative humidity, co-pollutants can influence the sensor response through chemical interference. For example, ozone is known to interfere with NO_2 [43, 60]. The impact of this is sensor-specific and depends upon the ratio of co-pollutants to the measured pollutant [43]. Analysis of the influence of co-pollutants is outside the scope of this research, hence further research is needed to quantify this impact.

7.2 Upwind experiment

This section presents the results of the upwind experiment, whereby a sensor node was located upwind of an operational runway. Considerably higher concentrations are expected downwind of an active runway compared to upwind as aircraft exhaust plumes move downwind under the influence of wind [1, 51, 83–89]. This is however not reflected in the obtained data. For the measurement conducted on 06-05-2022 (during which the Polderbaan runway was in use for landings) CO concentrations upwind were typically higher than those obtained downwind as for example shown in Figure 7.8. The measurement performed on 25-05-2022 showed that, although higher CO concentrations were present downwind, the concentrations upwind are not negligible (see Appendix D.2).

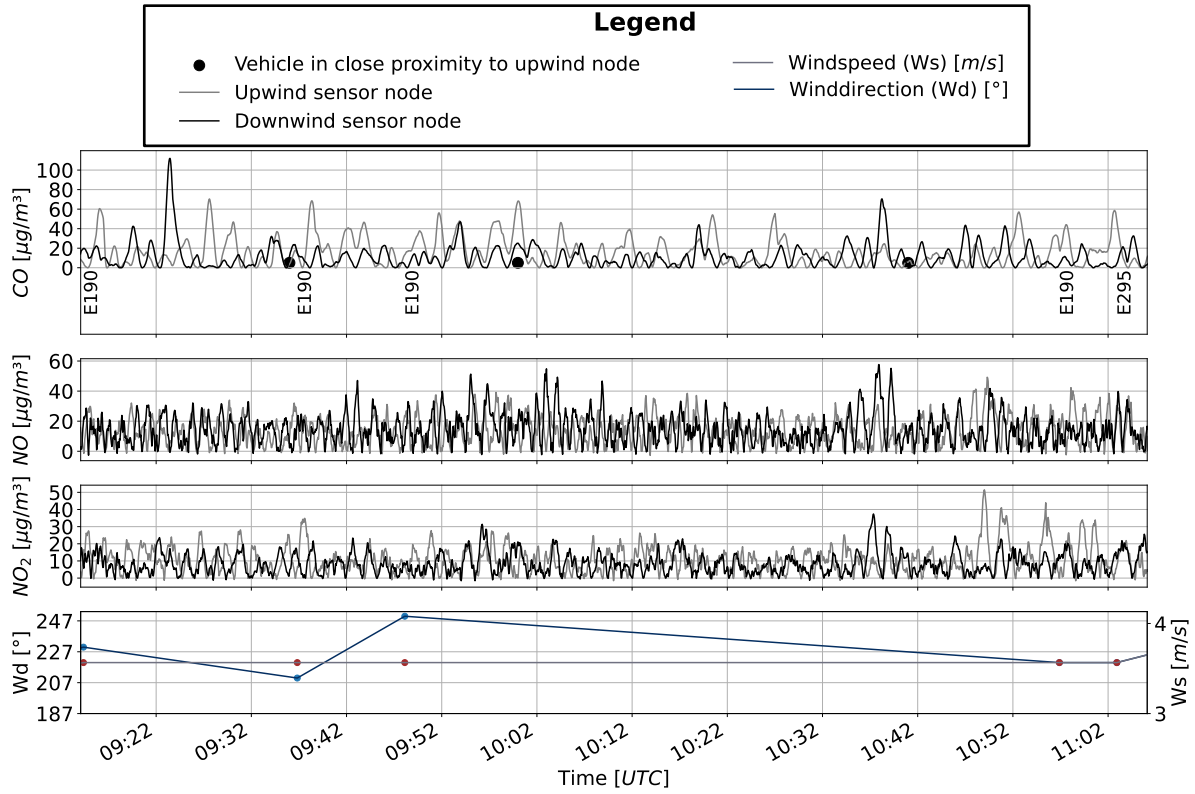

Figure 7.8: *Time-series of the local pollutant concentrations upwind and downwind of an active runway together with the prevailing wind and the (refined) estimated plume arrival time of landing aircraft for the measurement conducted on 06-05-2022*

As aircraft exhaust plumes expand, it is investigated whether plume dimensions could have been large enough to enhance upwind pollutant concentrations using three studies. The first study was performed by Koutsourakis et al. [87], who simulated the plume of a Boeing 737 with two CFM56-3C-1 engines and a Boeing 747 with four Pratt and Whitney 4056 engines at maximum take-off thrust. The second study was conducted by Underwood et al. [89] whereby plumes of two CFM56-X engines and two GE90-130B engines were simulated at the beginning of the take-off roll at 85% of the rated thrust. The third study, performed by Barrett et al. [1, 102], modelled the plume of an A320 with V2527-A5 engines at maximum take-off thrust. Based upon the concentration contours reported by these studies (see Appendix D.2), it is unlikely that aircraft exhaust plumes reached the upwind measurement site.

The expectation therefore arises that non-aircraft sources are responsible for enhanced upwind concentrations; especially as substantial CO peaks are present irrespective of aircraft activity (see Figure 7.8). Measurement notes revealed that during the upwind measurement an agricultural tractor was operating ~100 – 200 m from the upwind sensor node whereby the wind direction was such that its emissions were likely to be advected to the upwind sensor node. Arapatsakos et al. [281] performed stationary measurements of a tractor ploughing through a field with an engine similar to the one operating near the sensor node[22]. These measurements showed an average concentration of ~1189 part per million (ppm) and ~139 ppm for CO and NO_x respectively. Although the pollution signature of the tractor near the upwind sensor node may have been different due to a difference in utilised engine power, engine age, fuel and emission control technologies, this may explain why substantial CO peaks can be observed upwind compared to relatively small peaks in terms of NO and NO_2 [277, 278]. However, more research is needed to confirm that the enhanced upwind concentrations resulted from nearby tractors.

7.3 Co-location experiment

This section presents and discusses the results of the co-location experiment, whereby identical sensor nodes were collocated. To assess the level of agreement between sensor nodes, the Pearson correlation coefficient (*r*), Root Mean Square Error (RMSE), Mean Absolute Error (MAE) and the percentage difference between the time-series mean values (%Δ mean) are used. Mathematical expressions for these metrics were given in Section 5.5.1 and Section 7.1.5. It should be kept in mind that for newly manufactured gas sensors a difference of up to ~10% is expected between sensor nodes due to the manufacturer-specified sensor-to-sensor variability [282]. For gas sensors that have aged, this sensor-to-sensor variability may be higher [282, 283]. Furthermore, a small difference in clock time (~1 – 2 seconds) between sensor nodes may cause a small offset in timestamped pollutant concentrations and thereby contribute to the difference between sensor nodes.

7.3.1 Time-series comparison

Depending on the measurement date, sensor node combination and pollutant species significant differences exist between the total pollutant concentration readings (i.e., the ambient pollutant concentrations including the background) of collocated sensor nodes. For the sake of conciseness, the analysis presented here is limited to two collocated sensor nodes (Node 1 and Node 2). The reader is referred to Appendix D.3 for an analysis involving all sensor nodes.

An example of the variability between two collocated sensor nodes is given in Figure 7.9 for the measurement conducted on 25-05-2022. This figure shows the 3-second readings of the total pollutant concentrations (top row) and local pollutant concentrations (bottom row) of Node

[22] According to Voertuig-zoeker.nl the tractor that was active near the upwind sensor nodes was equipped with a 4-cylinder diesel engine similar to research of Arapatsakos et al. [281].

1 and Node 2. The reader is referred to Appendix D.3 for similar figures involving all measurement dates.

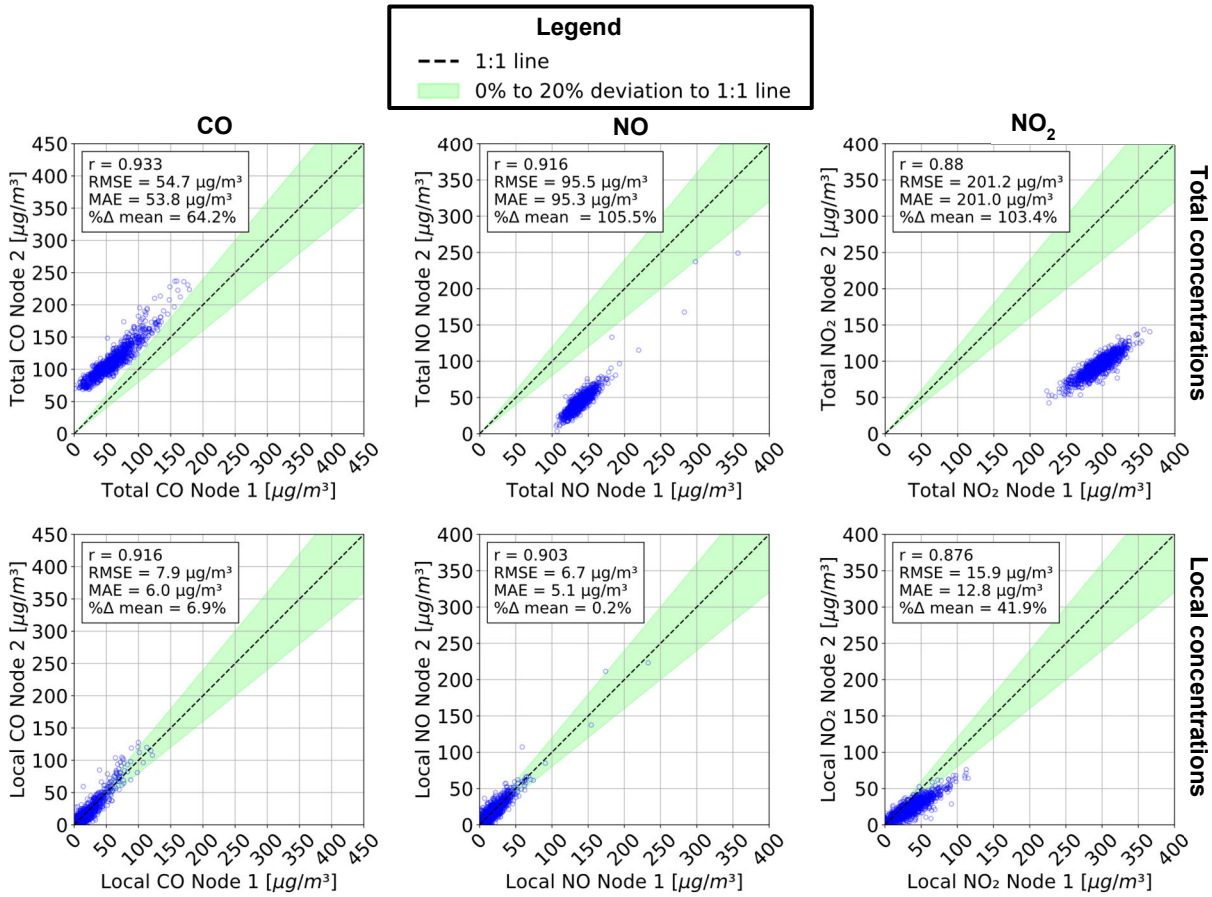

Figure 7.9: *Comparison of pollutant concentrations obtained by two sensor nodes for the total pollutant concentrations (top row) and the local pollutant concentrations (bottom row) with the Pearson correlation coefficient (r), Root Mean Square Error (RMSE), Mean Absolute Error (MAE) and percentage difference between the time-series mean of each sensor node (%Δ mean)*

Averaged over all measurement dates, the %Δ mean between Node 1 and Node 2 equals approximately 52%, 41% and 75% for CO, NO and NO_2 respectively. Similarly, existing studies (see e.g., [55, 284, 285]) observed that significant sensor-to-sensor variability may be present for uncalibrated (low-cost) gas sensors. To increase the accuracy of gas sensors and reduce the sensor-to-sensor variability, research therefore generally performs sensor calibration. Hereby gas sensors are calibrated against lab-grade instruments during in-field measurements or in a laboratory by exposing the gas sensor to a calibration gas [285]. Calibration can be challenging and time-consuming and may furthermore require access to lab-grade instruments [285, 286]. Therefore, during this research uncalibrated gas sensors were used.

However, for this research background-subtracted (i.e., local) pollutant concentrations are of interest rather than the ambient (i.e., total) pollutant concentrations. Interestingly, the agreement between collocated sensor nodes improves after removing the background concentration. An example of this is shown in Figure 7.9. Averaged over all measurement dates, the %Δ mean (i.e., the percentage difference between the time-series mean values of different pollutant species) is approximately 30 – 40% lower for local pollutant concentrations compared to the %Δ mean of total pollutant concentrations.

7.3.2 Plume-by-plume comparison

The local pollutant concentrations are used to characterise aircraft exhaust plumes in terms of their plume area (i.e., cumulative pollutant concentrations), width (i.e., plume duration) and peak (i.e., maximum pollutant concentration). Figure 7.10 shows the area, width and peak of aircraft operations for two collocated sensor nodes for the plumes passing quality control. Similar to before, the Pearson correlation coefficient (*r*), Root Mean Square Error (RMSE) and Mean Absolute Error (MAE) are used to quantify the difference between collocated sensor nodes. Furthermore, Figure 7.10 shows the percentage difference between Node 1 and Node 2 averaged over all data points (denoted as average %Δ).

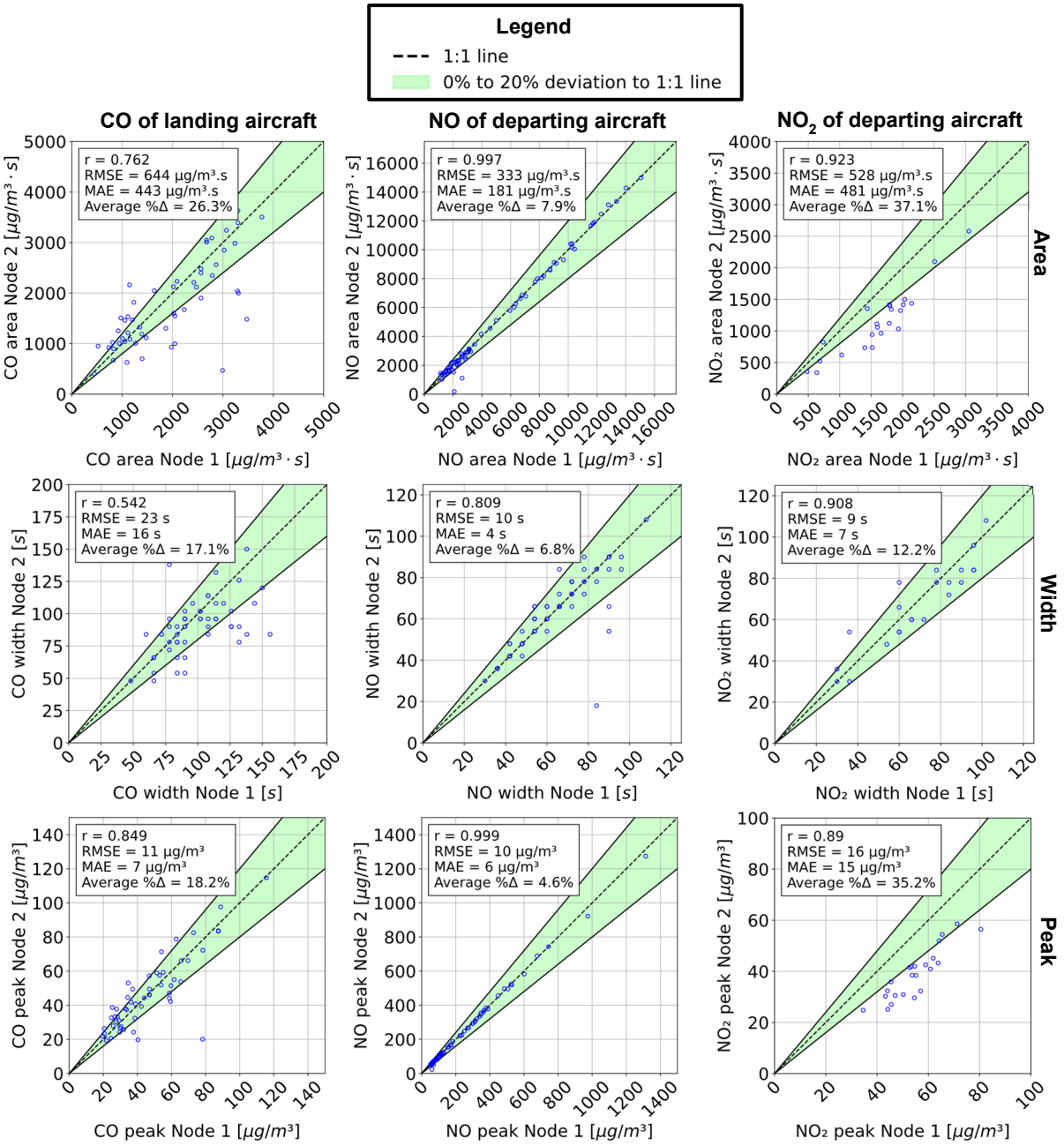

Figure 7.10: *Comparison of the Gaussian plume area, width and peak pollutant concentration of aircraft operations passing quality control with the Pearson correlation coefficient (r), Root Mean Square Error (RMSE), Mean Absolute Error (MAE) and the average percentage difference (Average %Δ)*

The highest level of agreement between sensor nodes can be observed for NO with differences of <10% for the plume area, width and peak. In terms of the area and peak the largest differences (<40%) are present for NO_2. For CO the plume area and peak differ by <30% with the width showing an offset of ~17% (compared to ~7% and ~12% for NO and NO_2 respectively).

7.4 Results and discussion of the near engine exit plane experiment

This section presents the results of the near engine exit plane experiment, whereby two sensor nodes were located in close proximity of a stationary aircraft. The results were analysed for when the fuel flow and N1 fan speed remained approximately constant as shown in Appendix D.4. It should be noted that the background concentration has not been subtracted from the measured pollutant concentrations as it is considered negligible for this experiment. The results of CO are excluded as for this species the maximum concentration for a stable response was exceeded for the sensor nodes during both measurements.

7.4.1 NO_2/NO_x ratios

The observed NO_2/NO_x ratios for this research and existing literature are presented in Table 7.5.

Table 7.5: *Ratio of NO_2 over NO_x at idle thrust for this research and existing literature*

Observed NO_2/NO_x ratio	Measurement set-up and location	Source
~0.6 ~0.5	~10 m behind a (stationary) engine mounted on an aircraft ~20 m behind a (stationary) engine mounted on an aircraft	This research
Average of 0.40 (CFM56-7B26) Average of 0.49 (CFM56-3B1) Average of 0.47 (CFM56-3B2)	Inside the exhaust nozzle in an engine test-cell	Turgut et al. [165, 275]
Up to 0.75 (RB211-535E4-B) Up to 0.98 (CFM56-3B1) 0.80 (CJ6108A)	1 – 15 m behind the exhaust nozzle of a (stationary) engine mounted on an aircraft	Timko et al. [287] and Wood et al. [17]
0.7 – 0.8 (CFM56-2B1)	1 m behind the exhaust nozzle of a (stationary) engine mounted on an aircraft	Presto et al. [288]
0.7 – 0.8 (CFM56-2C1)	1 m behind the exhaust nozzle of a (stationary) engine mounted on an aircraft	Wormhoudt et al. [78]
0.67 (CFM56-2C1)	1 m behind the exhaust nozzle of a (stationary) engine mounted on an aircraft	Wood et al. [17]
1.0 (CFM56-5C2)	50 m behind the exhaust nozzle of a (stationary) engine mounted on an aircraft	Schaefer et al. [71]

Compared to Turgut et al. [165, 275] a higher NO_2/NO_x ratio was observed during this research. The measurements of Turgut et al. were however performed inside the exhaust nozzle in an engine test cell before the bypass flow mixed with the exhaust jet, whereas during this research in-field measurements were conducted 10 – 20 m from the engine. Wood et al. [17] pointed out that the NO_2/NO_x ratio significantly increases within the first few meters from the exhaust nozzle. Besides, this ratio may increase due to dilution of bypass air of a jet-engine and the

ambient wind [17, 165, 275]. The difference in measurement set-up and location may therefore explain the higher observed NO_2/NO_x ratio during this research.

With respect to the remaining research published in Table 7.5, a lower NO_2/NO_x ratio was observed, even though a higher ratio may be expected for three reasons. Firstly, (except for the research of Schaefer et al. [71]) the measurements were conducted at a larger distance from the engine compared to existing research, which increases the NO_2/NO_x ratio. Secondly, the ambient temperature was ~6°C during the conducted measurements, which is likely to have been lower compared to other research and thus leads to a relative increase in the NO_2/NO_x ratio [165, 275]. Lastly, strong winds were present during the measurement, which increases the dilution and subsequently the NO_2/NO_x ratio.

However, it should be noted that direct comparison to other literature is difficult. The research listed in Table 7.5 investigated different engines which may have utilised different fuels. Both the engine model and the type of fuel are known to impact the NO_2/NO_x ratio [17, 165, 275]. For example, the engine used in this research exhibits a bypass flow which increases dilution and subsequently the NO_2/NO_x ratio, while the CJ6108A engine measured by Timko et al. [287] and Wood et al. [17] does not exhibit a bypass flow. Furthermore, the NO_2/NO_x ratio may be 10% to 20% lower for a warm engine (i.e., an engine that has been running for some time) compared to a cold engine (i.e., an engine shortly after start-up) [165, 275]. Additionally, the NO_2/NO_x ratio depends upon the part of the plume that is captured, which for this research is less certain due to the strong and fluctuating winds [276]. Lastly, the NO_2/NO_x ratio depends upon the chemical reactions that are taking place with other pollutant species [68].

After comparing the observed ratios to literature, the difference between sensor nodes is investigated. Due to the chemical evolution of NO to NO_2 while the plume ages, it is expected that the NO_2/NO_x ratio is higher for Node 2 (located at 20 m from the aircraft) compared to Node 1 (located 10 m from the aircraft) [17, 68]. This is however not reflected in the observed NO_2/NO_x ratios. The reason for this is unclear, but the short distance between Node 1 and Node 2, the sensor-to-sensor variability and meteorological conditions may have contributed to this discrepancy.

7.4.2 NO_x emission index

Using Equation 5.17 the NO_x (SO_2-based) emission index is estimated whereby (as the sulphur content of the fuel was unknown) the SO_2 emission index was assumed to be 0.8 gram SO_2 per kg of fuel burnt. This results in a NO_x emission index of ~0.2 g/kg for both measurements, which is ~172% lower than the certified NO_x emission index of 2.63 g/kg published in the ICAO Emissions Databank [150][23]. It is worth mentioning that the emission index was also estimated based on the measured fuel flow rate and an estimation of the plume volume (see Appendix D.4) which resulted in a NO_x emission index of ~0.02 g/kg. However, more research is needed to verify that the NO_x emission index can be estimated this way.

With respect to the observed SO_2-based NO_x emission index an uncertainty is introduced in the assumed SO_2 emission index. The maximum allowable SO_2 emission index (assuming all sulphur is emitted in terms of SO_2) per regulations is 3 g/kg, but research typically observed lower values as shown in Table 7.6 [12, 289]. However, even when using an SO_2 emission index of 3 g/kg instead of 0.8 g/kg to compute the NO_x emission index, the NO_x emission index is still ~3 times lower than the certified one.

[23] The certified NO_x emission index is ~4 g/kg after correcting for installation effects and ambient conditions

Table 7.6: *Global mean emission index and ranges between which the SO_2 emission index typically varies according to existing literature reviews whereby N.R. indicates no value was reported*

Mean [min, max] SO_2 emission index (g/kg)	Source
0.8 [0.6 – 1.0]	Lee et al. [90]
0.84 [N.R – N.R.]	Tait et al. [121]
N.R. [0.8 – 1.3]	Masiol and Harrison [3]
0.8 [0.6 – 1.0]	Gierens et al. [236]
N.R. [0.3 – 0.8]	Khou et al. [289]

During this research the reason behind this discrepancy was not further investigated. However, the difference in measurement set-up and non-ideal conditions (see Chapter 4.3) during which measurements were conducted may have been contributing factors. Furthermore, it could be that the employed sensors are not good enough to approximate the actual emission index. Another potential cause for the lower observed NO_x emission index is a difference in thrust setting. Certified emission indices are reported for 7% of the rated thrust, but ground idle typically corresponds to ~3 – 5 % of the rated thrust for most engines designed in the past 30 years [17, 38, 110, 259, 290–293]. Kim and Rachami [293] concluded that small differences in thrust can substantially impact NO_x emission indices, whereby for example for a CFM56-3-B1 engine the emission index at 5% of the rated thrust is ~29% lower compared to the emission index at 7% of the rated thrust. Future research may look into ways to obtain the percentage of the rated thrust based on the observed N1 fan speed and implement the method of Kim and Rachami [293] to obtain the certified emission index for the actual thrust setting.

7.5 Comparison to model results

In this section observed (i.e., measured) peak pollutant concentrations are compared to those that were estimated with the (simple) dispersion model described in Chapter 6 using Figure 7.11.

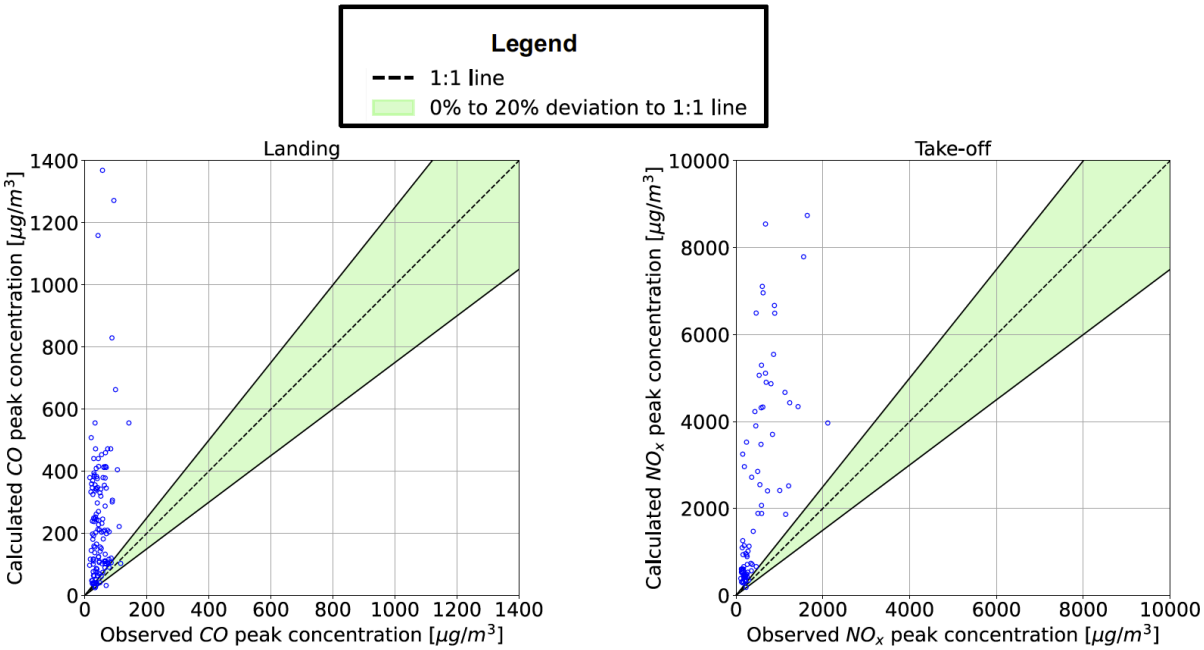

Figure 7.11: *Comparison between peak pollutant concentrations of the Gaussian representation of the plume observed during in-field downwind measurements and peak pollutant concentrations resulting from a (simple) dispersion model*

Both for CO and NO_x significant differences between modelled and observed peak concentrations are evident, with observed peak concentrations being lower than the modelled ones. On average, modelled peak concentrations are 106% and 119% higher compared to the observed concentrations for CO and NO_x respectively. It was shown in Table 7.3 that Carslaw et al. [37, 67] observed NO_x peak concentrations that were (roughly) similar to the ones observed during this research. The expectation is therefore that the discrepancy in Figure 7.11 can be attributed to modelled peak concentrations.

It should be noted that the chosen dispersion model was a simple two-dimensional model for which the impact of the moving aircraft and the initial characteristics of the exhaust jet are neglected. Besides, it is assumed that the plume is emitted and measured at ground level in the absence of plume rise without chemical reactions taking place. One of the uncertainties in the inputs to the model is the aircraft thrust setting, as aircraft may have utilised thrust settings other than 7% of the rated thrust for landings and 82% of the rated thrust for take offs that were used to generate the modelled results. The reader is referred to Appendix D.5 for a comparison between modelled and observed peak pollutant concentrations for different thrust settings.

Besides the thrust setting, uncertainties are introduced in the emission indices. The ICAO Emissions Databank [150] publishes these for newly manufactured engines, while in reality engines deteriorate over time, for example due to the build-up of dirt [13]. ICAO [13] states that the variability in engine state leads to a ~3% increase in fuel flow rate whereas according to research of QinetiQ [143] the fuel flow rate during the take-off roll increases by ~4.3% and the NO_x emission rate by ~4.5%. Another uncertainty regarding emission indices is introduced by the BFFM2 that was used to correct emission indices for engine installation effects and ambient conditions. Research has shown that the BFFM2 agrees with actual emission indices within $\pm$10% for most engine models at 7%, 30%, 85% and 100% of the rated thrust but higher uncertainties ($\pm 10 - 15\%$ for NO_x and larger uncertainties for CO) may be present for interpolated thrust settings [165, 294, 295].

Uncertainties are furthermore introduced by neglecting the effect of the forward speed on the emission rate. It was explained in Chapter 2 that the forward speed of the aircraft impacts the fuel flow and emission indices, which in turn changes the emission rate [143]. Underwood et al. [134, 143] stated that the increase in emission rate between the start and the end of the take-off roll is larger for engines with a higher Overall Pressure Ratio (OPR), with an increase of ~6% for an engine with an OPR of ~25 (e.g., CFM56-3C-1) and ~15% for an engine with an OPR of ~40 (e.g., the Trent 892). The impact of the aircraft's speed therefore depends, besides the speed of the aircraft, on the engine model that an aircraft is equipped with. Furthermore, depending upon the speed of the aircraft, airframe vortices affect the dispersion of the exhaust plume, for which more research is needed to quantify this impact.

Another uncertainty is introduced in modelled results by assuming the plume buoyancy to be zero. The effect of plume buoyancy on plume dispersion is however currently not well understood, such that it is difficult to quantify this impact [140]. However, neglecting buoyancy may result in an overestimation of modelled ground level pollutant concentrations.

The last uncertainty to be discussed are the dispersion coefficients (σ_y and σ_z). In reality aircraft are moving sources that release a plume with an initial velocity whereas the implemented model assumes a stationary source that emits a passive plume. Consequently, it is likely that in reality the streamwise distance between the sensor node and the aircraft was larger than the distance estimated for this research, which underestimates the values of the dispersion coefficients for this research and therefore overestimates peak pollutant concentrations. Another uncertainty with this regard is introduced in the formulas used to compute the dispersion coefficients. These were established ~50 years ago based on experiments during which particles were released from a stationary position and traced downwind over distances ranging from 100 m to 10 km [243, 296]. The dispersion of exhaust

plumes of moving aircraft over distances of several hundred meters is therefore likely to be different. It is furthermore currently unclear whether open country or urban conditions are most appropriate to estimate the dispersion coefficients. To assess how results differ when using open country conditions instead, a sensitivity analysis was conducted of which the results are presented in Appendix D.5.

7.6 Summary

Departing aircraft caused significant local NO_x concentrations (including significant NO concentrations and discernible NO_2 concentrations) while this could generally not be observed in terms of CO and SO_2. On the contrary, landing aircraft resulted in substantial local CO concentrations with generally no discernible SO_2, NO and NO_2 concentrations above the background. Regarding the results of specific aircraft types, the cumulative CO concentrations of landing aircraft show no dependency on aircraft size and are largest for the B77W. For departing aircraft, it was evident that cumulative NO_x concentrations are ~3.5 times larger for larger aircraft compared to medium-sized ones with the largest values being present for the B78X. With respect to the engine-specific results, significant differences in cumulative NO_x concentrations are evident between engine models with variations up to 50% between engine models belonging to the same series. In terms of departing aircraft, the largest cumulative NO_x concentrations were present for the GEnx-1B76A/P2 and the GE90-110B1 while for landings the largest cumulative CO concentrations are evident for the CF6-80E1A3.

After investigating aircraft exhaust plumes, analysis of the co-location experiment revealed that the pollutant concentration readings of sensor nodes can differ >100%, but that the differences are 30 – 40% lower after subtracting the background concentration. Furthermore, the cumulative concentrations of individual aircraft operations differ 26%, 8% and 37% between two collocated sensor nodes. Regarding the upwind experiment, it was observed that local pollutant concentrations upwind of a runway are not negligible compared to downwind concentrations. Lastly, the near engine exit plane experiment showed that the SO_2-based emission index is 172% lower compared to the certified one.

8 Conclusions and recommendations

The last chapter of this report presents the conclusions and recommendations. First, Section 8.1 provides concluding remarks after which Section 8.2 provides several recommendations for future research.

8.1 Conclusions

The research objective was to characterise the exhaust plumes of individual departing- and arriving aircraft in terms of their chemical composition by performing field measurements with low-cost sensor nodes and comparing the resulting data to certified data using a simple dispersion model. To reach this objective, a novel tool was developed to automatically characterise wind-advected exhaust plumes of individual aircraft operations. The results of this tool reflected that it is possible to automatically characterise NO and NO_2 plumes for the majority of departing aircraft and CO plumes for most arriving aircraft using low-cost sensor nodes. Departing aircraft generally caused significant local NO_x concentrations (comprising of significant NO concentrations and discernible NO_2 concentrations) while this could typically not be observed for CO and SO_2. The results therefore reveal that departing aircraft significantly contribute to NO_x concentrations downwind of a runway while not being the dominant source in terms of CO and SO_2 concentrations. However, it could also be an indication that the employed gas sensors are incapable of measuring the aircraft attributable concentrations.

With respect to landing aircraft, typically substantial local CO concentrations were present while this could typically not be observed for NO, NO_2 and SO_2. Therefore, a significant difference in pollutant concentrations is present between departing- and landing aircraft. Besides, based on this observation it can be concluded that landing aircraft have a substantial contribution to downwind CO concentrations while the same cannot be said in terms of NO, NO_2 and SO_2. However, it could also be an indication that the employed gas sensors are not capable of measuring concentrations of landing aircraft for these three pollutant species. It is however worth mentioning that occasionally landing aircraft showed significant local NO concentrations accompanied by a discernible increase in NO_2 concentrations. As this could only be observed for <15% of the encountered landings, this may be an indication that aircraft utilising the Polderbaan runway typically use low reverse thrust settings. This is in line with existing research, which generally agrees that typically not more than idle reverse thrust is used [3, 108, 135, 259]. However, more research is needed to investigate this.

Regarding specific aircraft types, the cumulative CO concentrations of landing aircraft turned out to be independent of aircraft size and largest for the B77W. In terms of departures, significant differences are evident in the NO_x footprint of different aircraft types. Cumulative NO_x concentrations of departing aircraft were ~3.5 times larger for large aircraft compared to those that are medium-sized. Subsequently, large aircraft have a relatively higher contribution to ambient NO_x concentrations downwind of a runway compared to medium-sized ones with the B78X being the largest contributor.

Based on this it can however not yet be concluded which aircraft have the largest impact on local air quality, as this impact also depends upon the time it takes to conduct the take-off. The impact of aircraft on local air quality is largest when pollutants are emitted below the Mixing Layer Height (MLH), which is defined to be 915 m by ICAO [13]. Although aircraft utilising a higher thrust setting may emit more NO_x during the take-off roll, they may also climb faster such that the MLH is reached in less time. Therefore, more research is required to investigate which aircraft types have the largest impact on local air quality.

Both for NO_x concentrations of departing aircraft and CO concentrations of landing aircraft the aircraft-specific results furthermore revealed that variations in excess of 50% are evident for aircraft of the same type. This may be indicative that meteorological- and operating conditions have a measurable impact on emissions leaving the jet-engines. However, these conditions are also known to influence the physical- and chemical evolution of the exhaust plume while it travels towards the sensor nodes, hence more research is needed to further investigate this.

With respect to the engine-specific results, significant differences in cumulative NO_x concentrations are evident between different engine models. Regarding engine models belonging to the same series variations up to 50% could be observed. It can therefore be concluded that the specific engine model may have a significant influence on the pollution footprint of an aircraft. In terms of NO_x of departing aircraft, the largest cumulative concentrations were present for the GEnx-1B76A/P2 and the GE90-110B1 while for landings the largest cumulative CO concentrations are evident for the CF6-80E1A3. Both in terms of NO_x of departing aircraft and CO of landing aircraft no consistent trend can be observed that engines with a higher certified emission rate yield higher observed cumulative pollutant concentrations, which is in line with existing research [37, 67]. This may be indicative that meteorological and operating conditions have a measurable impact on the emissions emitted by a jet-engine. Furthermore, it could be an indication that different aircraft types have a different influence on plume dispersion. However, more research is needed to confirm this.

Besides analysing emissions downwind of a runway, simultaneous measurements were taken upwind to investigate whether the difference between upwind- and downwind concentrations can be used to obtain aircraft attributable concentrations. However, the results reflect that upwind pollutant concentrations are not significantly lower (and may even be higher) compared to downwind concentrations, hence this approach cannot be used.

Next to analysing upwind concentrations, an experiment was performed with collocated sensor nodes to investigate their level of agreement. It was observed that the total pollutant concentration readings of sensor nodes can differ in excess of 100%, but the agreement between sensor nodes improves by ~30 – 40% after subtracting the background concentration. Cumulative concentrations resulting from individual aircraft operations differ 26%, 8% and 37% for CO, NO and NO_2 respectively between collocated sensor nodes which (mainly in terms of NO) gives confidence in the results of this research. Although, in line with existing research, this shows that calibration is required for gas sensors when analysing ambient air pollution, uncalibrated low-cost gas sensors can provide a meaningful estimate of the pollution footprint of individual aircraft operations. However, this is solely based on the variability between sensor nodes, hence more research is needed to quantify the precision of the low-cost gas sensors.

Finally, a near engine exit plane experiment was performed to determine whether SO_2 can be used to estimate emission indices rather than the commonly used CO_2. The observed NO_x emission index was 172% lower compared to the one specified in the ICAO Emissions Databank [150]. Based on this it cannot yet be concluded that SO_2 cannot be used to estimate emission indices, as the 'real-world' NO_x emission index and the fuel sulphur quantity were unknown. Furthermore, this experiment was conducted in non-ideal conditions, hence more research is needed to look into this. Nevertheless, by using SO_2 instead of CO_2 an uncertainty is introduced when the fuel sulphur quantity is unknown as the SO_2 emission index may vary from ~0 – 3 g/kg, although values of ~0.3 – 1.3 g/kg are more common.

Based upon the conducted experiments and the performed analysis, this research demonstrated the capability of low-cost sensor nodes for assessing the pollution footprint of individual aircraft operations. While this research focused on the Polderbaan runway of Schiphol Airport, the developed tool can be easily adapted for other airports. The findings of this report can be used by the scientific community, policymakers, and regulatory bodies to further study the air quality impact of individual aircraft and to develop mitigation strategies.

8.2 Recommendations

The conducted research may serve as a stepping stone for future research, for which several recommendations are provided.

8.2.1 Sensor node recommendations

A Global Positioning System (GPS) may be incorporated in the sensor nodes[24]. The position of sensor nodes is used for estimating the arrival time of aircraft exhaust plumes. This position is currently manually written down but this is impractical, especially when in the future more sensor nodes are deployed. Therefore, GPS can be incorporated to automatically log the latitude and longitude of each sensor node. Besides GPS, an anemometer may be added to continuously log the prevailing ambient wind speed and wind direction in real-time[25]. The ambient wind is used to couple air pollutant concentrations to aircraft operations. Currently the wind direction and wind speed are obtained by manually transcribing ATC voice recordings. As this is impractical, an anemometer can be used instead. Next to this, components may be added to sensor nodes to prevent or reduce the internal temperature rise as this can affect the output of gas sensors.

Furthermore, the sensor nodes could be equipped with additional gas sensors. First of all, a CO_2 sensor may be added such that CO_2-based emission indices can be computed. Additionally, sensor nodes could be equipped with a multitude of identical gas sensors. This research revealed that differences up to approximately 40% exist between the resulting plume parameters of collocated sensor nodes. When each node is equipped with several identical gas sensors, the value averaged over all gas sensors of the same pollutant species can be used rather than the value of a single gas sensor to make the results more robust.

8.2.2 Recommendations for future experiments and analysis

Future research may improve the developed algorithm by altering the way aircraft exhaust plumes are coupled to aircraft operations. Occasionally the OpenSky Network failed to acknowledge the presence of an aircraft operation or did not provide the required information to categorise aircraft as a take-off or landing. For these aircraft timestamped GoPro pictures could be used to automatically identify when aircraft are present on the Polderbaan runway. Additionally, the estimated plume arrival time may be improved by modelling the aircraft as a moving source releasing a plume with a non-zero initial velocity rather than a stationary source releasing a passive plume as for this research. For this, it is recommended to utilise the methods described in the user guide of ADMS-Airport [133] and by Barrett et al. [1, 102]. Besides this, to estimate the plume arrival time future work may look into ways to automatically extract wind information from ATC voice recordings (see e.g., [297]) rather than manually writing this down[26]. The developed algorithm may furthermore be improved by assessing whether other fitting functions (e.g., the Lorentzian, Voigt or Weibull) provide a better fit compared to the Gaussian fitting employed for this research.

Besides these improvements to the algorithm, it is recommended that future research analyses Volatile Organic Compounds (VOC) as this species was not looked into during this research. This pollutant may provide important insights in the chemistry of aircraft exhaust plumes as well as the amount of applied engine thrust through the VOC/NO_x ratio. Furthermore, during this research particles were measured which have not been analysed during this research. As simultaneous observations of gases and particles can provide important insights in the air quality impact of aircraft, it is recommended that future work looks into this. Besides, future work may assess the impact changes in environmental conditions and orientation of the sensor

[24] Near the end of this research all sensor nodes were equipped with a GPS based on this recommendation.
[25] Towards the end of this research an anemometer was acquired based on this recommendation.
[26] Alternatively, an anemometer may be used rather than ATC voice recordings.

nodes have on the output of gas sensors. It is furthermore recommended to perform Computational Fluid Dynamics (CFD) analysis to get better insight in how aircraft exhaust plumes move towards the sensor nodes and what parameters such as the width of plume signals in pollutant time-series physically represent.

Additionally, it is recommended that future work performs several experiments. A downwind experiment similar to this research may be performed as currently the number of plumes on which the results are based is limited. Hereby it is recommended to also analyse aircraft activities (e.g., taxiing) other than take offs and landings. Besides, an experiment can be performed to analyse the dispersion of aircraft exhaust plumes by placing sensor nodes at strategic locations. For example, sensor nodes can be placed downwind at increased distance from the runway to investigate the horizontal dispersion of plumes or at different heights above the ground to study their vertical dispersion. Furthermore, the near engine exit plane experiment may be repeated as this experiment was conducted during non-ideal conditions. Hereby it is recommended to perform the measurements at various distances from the exhaust nozzle and for different thrust settings to investigate changes in the NO_2/NO_x ratio. Lastly, it is recommended to validate the obtained air pollution data by collocating the low-cost sensor nodes with lab grade instruments to investigate their level of agreement.

8.2.3 Recommended future work on dispersion modelling

It is recommended that future work investigates the use of more advanced dispersion models. A good starting point would be to investigate the employed methods of some well-established and frequently used dispersion models that are listed in ICAO Doc 9889 [13]. An example of this is the Advanced Dispersion Modelling of Emissions (ADMS) Airport, which provides a detailed description on the modelling of individual aircraft exhaust plumes in their user guide [133]. Besides the dispersion models listed by ICAO, it is worth to look into other models such as the ones described by Synlo et al. [100, 267, 298–301], Kraabøl et al. [302, 303], Tian et al. [304] Cretu et al. [305], Smith et al. [306], Wan et al. [307] and Brzozowski and Kotlarz [308].

Besides implementing a new dispersion model, the currently implemented dispersion model can be extended. First of all, future work may incorporate the chemical reactions that are taking place while the aircraft exhaust plume travels towards the downwind sensor node. For this, it is recommended to look into the work of Kraabøl et al. [302, 303], Underwood et al. [89] and Kenney [309]. Besides, future research may estimate the actual engine (reverse) thrust setting based upon aircraft activity data, weather data and aircraft performance data (see e.g., [256, 258, 310] or noise measurements (see e.g., [311]). Additionally, future research may include the measurement height and the emission source height (i.e., the engine installation height). The source height can be obtained by adding the engine fan radius (which can be obtained from aircraft-database.com [312]) to the distance between the ground and the bottom of an engine. The latter can be found in airport planning documents of aircraft (see e.g., [229, 313, 314])

Furthermore, future research may incorporate plume buoyancy in the dispersion model following the procedures described by Underwood et al. [133], Graham et al. [92], Synlo et al. [100, 267, 298–301], Barrett et al. [1, 102] and the ADMS-Airport user guide [133]. Additionally, the aircraft may be modelled as a moving source according to the method described by Synlo et al. [100, 267, 298–301] or the ADMS-Airport user guide [133]. Besides this, the impact of the aircraft's speed on the emission rate may be incorporated by obtaining the fuel flow from an aircraft performance database such as Base of Aircraft Data (BADA) of Eurocontrol [315]. Lastly, it is worth mentioning that the comparison to certified pollutant concentrations was only conducted for engine models specified in the ICAO Emissions Databank [150], which is limited to gas turbine engines. However, turboprops may be included in future work by incorporating the database of the Swedish Defence Research Agency [316].

Bibliography

1. Barrett SRH, Britter RE, Waitz IA (2013) Impact of aircraft plume dynamics on airport local air quality. Atmospheric Environment 74:247–258. https://doi.org/10.1016/j.atmosenv.2013.03.061

2. Yim SHL, Lee GL, Lee IH, et al (2015) Global, regional and local health impacts of civil aviation emissions. Environ Res Lett 10:034001. https://doi.org/10.1088/1748-9326/10/3/034001

3. Masiol M, Harrison RM (2014) Aircraft engine exhaust emissions and other airport-related contributions to ambient air pollution: A review. Atmospheric Environment 95:409–455. https://doi.org/10.1016/j.atmosenv.2014.05.070

4. Yılmaz İ (2017) Emissions from passenger aircraft at Kayseri Airport, Turkey. Journal of Air Transport Management 58:176–182. https://doi.org/10.1016/j.jairtraman.2016.11.001

5. Schürmann G, Schäfer K, Jahn C, et al (2007) The impact of NOx, CO and VOC emissions on the air quality of Zurich airport. Atmospheric Environment 41:103–118. https://doi.org/10.1016/j.atmosenv.2006.07.030

6. Herndon SC, Jayne JT, Lobo P, et al (2008) Commercial Aircraft Engine Emissions Characterization of in-Use Aircraft at Hartsfield-Jackson Atlanta International Airport. Environ Sci Technol 42:1877–1883. https://doi.org/10.1021/es072029+

7. Yim SH, Stettler ME, Barrett SR (2013) Air quality and public health impacts of UK airports. Part II: Impacts and policy assessment. Atmospheric environment 67:184–192. https://doi.org/10.1016/j.atmosenv.2012.10.017

8. Ratliff G, Sequeira C, Waitz I, et al (2009) Aircraft impacts on local and regional air quality in the United States. Massachusetts Institute of Technology, PARTNER report (Report No PARTNER-COE-2009-002)

9. Levy JI, Woody M, Baek BH, et al (2012) Current and future particulate-matter-related mortality risks in the United States from aviation emissions during landing and takeoff. Risk Analysis: An International Journal 32:237–249. https://doi.org/10.1111/j.1539-6924.2011.01660.x

10. Lin S, Munsie J, Herdt-Losavio M, et al (2008) Residential proximity to large airports and potential health impacts in New York State. International archives of occupational and environmental health 81:797–804. https://doi.org/10.1007/s00420-007-0265-1

11. Hasan MA, Mamun AA, Rahman SM, et al (2021) Climate Change Mitigation Pathways for the Aviation Sector. Sustainability 13:3656. https://doi.org/10.3390/su13073656

12. Barrett SR, Yim SH, Gilmore CK, et al (2012) Public health, climate, and economic impacts of desulfurizing jet fuel. Environmental science & technology 46:4275–4282. https://doi.org/10.1021/es203325a

13. International Civil Aviation Organization (2020) Doc 9889: Airport Air Quality Manual. Montreal, QC, Canada

14. Liu Y, Sun X, Sethi V, et al (2017) Review of modern low emissions combustion technologies for aero gas turbine engines. Progress in Aerospace Sciences 94:12–45. https://doi.org/10.1016/j.paerosci.2017.08.001

15. Merzenich H, Riccetti N, Hoffmann B, et al (2021) Air pollution and airport apron workers: A neglected occupational setting in epidemiological research. International journal of hygiene and environmental health 231:113649. https://doi.org/10.1016/j.ijheh.2020.113649

16. Archilla V, Hormigo D, Sánchez-García M, Raper D (2019) AVIATOR - Assessing aViation emission Impact on local Air quality at airports: TOwards Regulation. MATEC Web Conf 304:02023. https://doi.org/10.1051/matecconf/201930402023

17. Wood EC, Herndon SC, Timko MT, et al (2008) Speciation and Chemical Evolution of Nitrogen Oxides in Aircraft Exhaust near Airports. Environmental Science & Technology 42:1884–1891. https://doi.org/10.1021/es072050a

18. Synylo K, Kazhan K (2014) Monitoring of air pollution produced by aircraft in the vicinity of airport. Proceedings of National Aviation University 61:153–161. https://doi.org/10.18372/2306-1472.61.7607

19. Dodson RE, Houseman EA, Morin B, Levy JI (2009) An analysis of continuous black carbon concentrations in proximity to an airport and major roadways. Atmospheric Environment 43:3764–3773. https://doi.org/10.1016/j.atmosenv.2009.04.014

20. Ghedhaïfi W, Montreuil E, Chouak M, Garnier F (2022) 3D High-Resolution Modeling of Aircraft-Induced NO x Emission Dispersion in CAEPport Configuration Using Landing and Take-Off Trajectory Tracking. Water, Air, & Soil Pollution 233:418. https://doi.org/10.1007/s11270-022-05889-y

21. Hsu H-H, Adamkiewicz G, Houseman EA, et al (2012) The relationship between aviation activities and ultrafine particulate matter concentrations near a mid-sized airport. Atmospheric Environment 50:328–337. https://doi.org/10.1016/j.atmosenv.2011.12.002

22. Ghedhaifi W, Desprez L, Montreuil E, et al (2019) 3D Simulation of aircraft emissions dispersion in the CAEPport area by tracking aircraft as mobile sources

23. Penn SL, Arunachalam S, Tripodis Y, et al (2015) A comparison between monitoring and dispersion modeling approaches to assess the impact of aviation on concentrations of black carbon and nitrogen oxides at Los Angeles International Airport. Science of The Total Environment 527–528:47–55. https://doi.org/10.1016/j.scitotenv.2015.03.147

24. Garmory A, Mastorakos E, Bilger R (2010) Simulations of the chemical transformations in a jet engine exhaust plume. 48th AIAA Aerospace Sciences Meeting Including the New Horizons Forum and Aerospace Exposition, p 429

25. Carslaw DC, Taylor PJ (2009) Analysis of air pollution data at a mixed source location using boosted regression trees. Atmospheric Environment 43:3563–3570. https://doi.org/10.1016/j.atmosenv.2009.04.001

26. Barrett SRH, Britter RE, Waitz IA (2010) Global Mortality Attributable to Aircraft Cruise Emissions. Environ Sci Technol 44:7736–7742. https://doi.org/10.1021/es101325r

27. Stacey B (2019) Measurement of ultrafine particles at airports: A review. Atmospheric Environment 198:463–477. https://doi.org/10.1016/j.atmosenv.2018.10.041

28. Zhu Y, Fanning E, Yu RC, et al (2011) Aircraft emissions and local air quality impacts from takeoff activities at a large International Airport. Atmospheric Environment 45:6526–6533

29. Berkson EE, Messinger DW (2016) Multispectral imaging of aircraft exhaust. SPIE, pp 34–47

30. Filippone A, Bojdo N (2018) Statistical model for gas turbine engines exhaust emissions. Transportation Research Part D: Transport and Environment 59:451–463. https://doi.org/10.1016/j.trd.2018.01.019

31. Synylo K, Gurevych M (2015) The evaluation of local atmospheric air pollution via the assessment of jet engines emission. Science-based technologies 25:74–79. https://doi.org/10.18372/2310-5461.25.8238

32. Morris KM (2005) Results from a number of surveys of power settings used during taxi operations. British Airways EJT/KMM/1126/148

33. Morris K (2005) Reverse Thrust Examples from British Airways Operations. British Airways Environmental Affairs, British Airways Technical Documents Relating to the Aircraft Operations Supporting the Project for the Sustainable Development of Heathrow, Document 3:

34. Khadilkar H, Balakrishnan H (2012) Estimation of aircraft taxi fuel burn using flight data recorder archives. Transportation Research Part D: Transport and Environment 17:532–537. https://doi.org/10.2514/6.2011-6383

35. Stettler M, Eastham S, Barrett S (2011) Air quality and public health impacts of UK airports. Part I: Emissions. Atmospheric environment 45:5415–5424. https://doi.org/10.1016/j.atmosenv.2011.07.012

36. Eberhard WL, Brewer WA, Wayson RL (2005) LIDAR observations of jet engine exhaust for air quality. 85th AMS Annual Meeting, American Meteorological Society 5119–5125

37. Carslaw DC, Ropkins K, Laxen D, et al (2008) Near-field commercial aircraft contribution to nitrogen oxides by engine, aircraft type, and airline by individual plume sampling. Environmental science & technology 42:1871–1876. https://doi.org/10.1021/es071926a

38. Xu H, Fu Q, Yu Y, et al (2020) Quantifying aircraft emissions of Shanghai Pudong International Airport with aircraft ground operational data. Environmental Pollution 261:114115. https://doi.org/10.1016/j.envpol.2020.114115

39. United Sates Environmental Protection Agency (2022) Managing Air Quality - Emissions Inventories. https://www.epa.gov/air-quality-management-process. Accessed 3 Apr 2022

40. Taylor E, McMillan A (2013) Air quality management: Canadian perspectives on a global issue. Springer Science & Business Media

41. Lobo P, Hagen DE, Whitefield PD, Raper D (2015) PM emissions measurements of in-service commercial aircraft engines during the Delta-Atlanta Hartsfield Study. Atmospheric Environment 104:237–245. https://doi.org/10.1016/j.atmosenv.2015.01.020

42. Buček P, Maršolek P, Bílek J (2021) Low-cost sensors for air quality monitoring-the current state of the technology and a use overview. Chemistry-Didactics-Ecology-Metrology 26:41–54. https://doi.org/10.2478/cdem-2021-0003

43. Lewis AC, Lee JD, Edwards PM, et al (2016) Evaluating the performance of low cost chemical sensors for air pollution research. Faraday Discuss 189:85–103. https://doi.org/10.1039/C5FD00201J

44. Tiwary A, Williams I (2018) Air pollution: measurement, modelling and mitigation, 4th ed. Crc Press, Boca Raton

45. Castell N, Dauge FR, Schneider P, et al (2017) Can commercial low-cost sensor platforms contribute to air quality monitoring and exposure estimates? Environment international 99:293–302. https://doi.org/10.1016/j.envint.2016.12.007

46. Cross ES, Williams LR, Lewis DK, et al (2017) Use of electrochemical sensors for measurement of air pollution: correcting interference response and validating measurements. Atmos Meas Tech 10:3575–3588. https://doi.org/10.5194/amt-10-3575-2017

47. Ródenas García M, Spinazzé A, Branco PT, et al (2022) Review of low-cost sensors for indoor air quality: Features and applications. Applied Spectroscopy Reviews 57:747–779. https://doi.org/10.1080/05704928.2022.2085734

48. Mead MI, Popoola OAM, Stewart GB, et al (2013) The use of electrochemical sensors for monitoring urban air quality in low-cost, high-density networks. Atmospheric Environment 70:186–203. https://doi.org/10.1016/j.atmosenv.2012.11.060

49. Mihăiţă AS, Dupont L, Chery O, et al (2019) Evaluating air quality by combining stationary, smart mobile pollution monitoring and data-driven modelling. Journal of Cleaner Production 221:398–418. https://doi.org/10.1016/j.jclepro.2019.02.179

50. Moore RH, Shook MA, Ziemba LD, et al (2017) Take-off engine particle emission indices for in-service aircraft at Los Angeles International Airport. Scientific Data 4:1–15. https://doi.org/10.1038/sdata.2017.198.

51. Timko MT, Fortner E, Franklin J, et al (2013) Atmospheric Measurements of the Physical Evolution of Aircraft Exhaust Plumes. Environmental Science & Technology 47:3513–3520. https://doi.org/10.1021/es304349c

52. Stacey B, Harrison RM, Pope FD (2021) Evaluation of aircraft emissions at London Heathrow Airport. Atmospheric Environment 254:118226. https://doi.org/10.1016/j.atmosenv.2021.118226

53. Drajic DD, Gligoric NR (2020) Reliable Low-Cost Air Quality Monitoring Using Off-The-Shelf Sensors and Statistical Calibration. Elektronika ir Elektrotechnika 26:32–41. https://doi.org/10.5755/j01.eie.26.2.25734

54. Rai A, Kumar P (2017) Summary of air quality sensors and recommendations for application. Summary of air quality sensors and recommendations for application iSCAPE 1–10. https://doi.org/10.1007/978-981-15-6887-9_16

55. Smith KR, Edwards PM, Evans MJ, et al (2017) Clustering approaches to improve the performance of low cost air pollution sensors. Faraday Discuss 200:621–637. https://doi.org/10.1039/C7FD00020K

56. Schalm O, Carro G, Lazarov B, et al (2022) Reliability of Lower-Cost Sensors in the Analysis of Indoor Air Quality on Board Ships. Atmosphere 13:1579. https://doi.org/10.3390/atmos13101579

57. Popoola O, Mead I, Bright V, et al (2013) A Portable Low-Cost High Density Sensor Network for Air Quality at London Heathrow Airport. EGU General Assembly 7–12

58. Sun L, Wong KC, Wei P, et al (2016) Development and application of a next generation air sensor network for the Hong Kong marathon 2015 air quality monitoring. Sensors 16:211. https://doi.org/10.3390/s16020211

59. Samad A, Obando Nuñez DR, Solis Castillo GC, et al (2020) Effect of relative humidity and air temperature on the results obtained from low-cost gas sensors for ambient air quality measurements. Sensors 20:5175. https://doi.org/10.3390/s20185175

60. Ahumada S, Tagle M, Vasquez Y, et al (2022) Calibration of SO2 and NO2 Electrochemical Sensors via a Training and Testing Method in an Industrial Coastal Environment. Sensors 22:7281. https://doi.org/10.3390/s22197281

61. Essl C, Seifert L, Rabe M, Fuchs A (2021) Early detection of failing automotive batteries using gas sensors. Batteries 7:25. https://doi.org/10.3390/batteries7020025

62. Topalović DB, Davidović MD, Jovanović M, et al (2019) In search of an optimal in-field calibration method of low-cost gas sensors for ambient air pollutants: Comparison of linear, multilinear and artificial neural network approaches. Atmospheric Environment 213:640–658. https://doi.org/10.1016/j.atmosenv.2019.06.028

63. Maes J (2021) Quantification of Aviation's Impact on Air Quality near Schiphol Airport using Low-Cost Gas Sensors. In: Delft University of Technology. http://repository.tudelft.nl/

64. Archilla V, Hormigo D, Sánchez-García M, Raper D (2019) Aviator-assessing aviation emissions impact on local air quality at airports towards regulation. https://doi org/101051/matecconf/201930402023

65. Kilic D, Williams PI, Prat VA, et al The monitoring of airborne pollutants by developing a low-cost sensor network as part of AVIATOR. 1

66. Penza M, Suriano D, Pfister V, et al (2017) Urban Air Quality Monitoring with Networked Low-Cost Sensor-Systems. Proceedings 1:573. https://doi.org/10.3390/proceedings1040573

67. D. Laxen, B. Marner, D. Carslaw, K. Ropkins (2007) Analysis of Fast-Response NOx Measurements at Heathrow Airport. Air Quality Consultants

68. Herndon SC, Shorter JH, Zahniser MS, et al (2004) NO and NO2 emission ratios measured from in-use commercial aircraft during taxi and takeoff. Environmental science & technology 38:6078–6084. https://doi.org/10.1021/es049701c

69. Klapmeyer ME, Marr LC (2012) CO2, NO x, and Particle Emissions from Aircraft and Support Activities at a Regional Airport. Environmental science & technology 46:10974–10981. https://doi.org/10.1021/es302346x

70. Johnson GR, Mazaheri M, Ristovski ZD, Morawska L (2008) A Plume Capture Technique for the Remote Characterization of Aircraft Engine Emissions. Environ Sci Technol 42:4850–4856. https://doi.org/10.1021/es702581m

71. Schäfer K, Jahn C, Sturm P, et al (2003) Aircraft emission measurements by remote sensing methodologies at airports. Atmospheric Environment 37:5261–5271. https://doi.org/10.1016/j.atmosenv.2003.09.002

72. Bossioli E, Tombrou M, Helmis C, et al (2013) Issues related to aircraft take-off plumes in a mesoscale photochemical model. Science of the total environment 456:69–81. https://doi.org/10.1016/j.scitotenv.2013.02.091.

73. Zaporozhets O, Synylo K (2017) Improvements on aircraft engine emission and emission inventory asesessment inside the airport area. Energy 140:1350–1357. https://doi.org/10.1016/j.energy.2017.07.178

74. Lobo P, Whitefield PD, Hagen DE, et al (2008) Final report: Delta–Atlanta Hartsfield (UNA-UNA) Study. Massachusetts Institute of Technology, Cambridge

75. Yu K, Cheung Y, Cheung T, Henry RC (2004) Identifying the impact of large urban airports on local air quality by nonparametric regression. Atmospheric Environment 38:4501–4507. https://doi.org/10.1016/j.atmosenv.2004.05.034

76. Iavicoli I, Chiarotti M, Bergamaschi A, et al (2007) Determination of airborne polycyclic aromatic hydrocarbons at an airport by gas chromatography–mass spectrometry and evaluation of occupational exposure. Journal of Chromatography A 1150:226–235. https://doi.org/10.1016/j.chroma.2006.08.010

77. Frins E, Shaiganfar R, Platt U, Wagner T (2016) Determination of NO x emissions from Frankfurt Airport by optical spectroscopy (DOAS)–A feasibility study. Atmospheric Measurement Techniques Discussions 1–18. https://doi.org/10.5194/amt-2016-255

78. Wormhoudt J, Herndon SC, Yelvington PE, et al (2007) Nitrogen oxide (NO/NO2/HONO) emissions measurements in aircraft exhausts. Journal of Propulsion and Power 23:906–911. https://doi.org/10.2514/1.23461

79. Penner J, et al., (1999) Aviation and the global atmosphere: a special report of the Intergovernmental Panel on Climate Change. Cambridge University Press

80. Daley B (2010) Air transport and the environment. Ashgate Pub. Co, Farnham, Surrey, England ; Burlington, VT

81. (2000) Chemical ionization mass spectrometric measurements of SO2 emissions from jet engines in flight and test chamber operation. 105:26841–26855

82. Narayana MV, Jalihal D, Nagendra SMS (2022) Establishing A Sustainable Low-Cost Air Quality Monitoring Setup: A Survey of the State-of-the-Art. Sensors 22:394. https://doi.org/10.3390/s22010394

83. Aloysius S, Pearce D, Wrobel L, Fuller I (2007) ALAQS Comparison of CFD and Lagrangian Dispersion Methods – Simple Scenario during Take-off. School of Engineering and Design. https://doi.org/10.1163/1570-6664_iyb_SIM_org_39214

84. Aloysius SS, Wrobel LC (2009) Large eddy simulation of plume dispersion behind an aircraft in the take-off phase. Environmental Fluid Mechanics 9:457–470. https://doi.org/10.1007/s10652-009-9137-4

85. Graham A, Raper D, Manchester Metropolitan University, et al (2006) Air quality at Heathrow airport: impact of emissions from aircraft in ground run and flight: Second Tech Report. https://doi.org/10.13140/RG.2.2.25575.34726

86. Velikov S (2014) Wind Tunnel Modelling of Aerodynamic Baffle Arrays for Aircraft Exhaust Plume Control. Cranfield University

87. Koutsourakis N, Bartzis JG, Venetsanos A, Rafailidis S (2006) Computation of pollutant dispersion during an airplane take-off. Environmental Modelling & Software 21:486–493. https://doi.org/10.1016/j.envsoft.2004.07.011

88. Mihaiella C, Victoria T, Marius D (2016) Highlighting the contribution of aircraft take off activity to air pollution from airport areas by nitrogen oxides monitoring. In: Acoustics, Vibrations,Phisical and Chemical Testing Laboratory. NCAS, Bucharest, Romania

89. Underwood, BY, Walker CT, Peirce MJ (2010) Air Quality Modelling for Heathrow Airport 2008/9: Methodology, Appendix I. AEA Technology plc, Birchwood, United Kingdom

90. Lee DS, Pitari G, Grewe V, et al (2010) Transport impacts on atmosphere and climate: Aviation. Atmospheric Environment 44:4678–4734. https://doi.org/10.1016/j.atmosenv.2009.06.005

91. Spanelis A, Garry K, Savill M (2013) Large Eddy Simulations of Turbofan Engine Exhaust Plume Dispersion on Take-Off Runway. American Society of Mechanical Engineers, Texas

92. Graham A, Bennett M, Christie S Representing the dispersion of emissions from aircraft on runways. Hrvatski meteorološki časopis 4343/2 563–568

93. Velikov S (2014) Wind Tunnel Modelling of Aerodynamic Baffle Arrays for Aircraft Exhaust Plume Control. Cranfield University

94. Christie S, Bennett M, Graham A, Raper D (2006) Lidar monitoring of aircraft emissions for environmental air quality. Journal of Atmospheric and Oceanic Technology 27:1638–1651. https://doi.org/10.1175/2010JTECHA1412.1

95. Lee J, Birch SF, Scovill BA (1996) Airport jet plume zone mapping. Journal of Aircraft 33:737–742. https://doi.org/10.2514/3.47009

96. Korotaeva TA, Turchinovich AO (2016) Simulation of the spatial pollutant jets exiting from the aircraft engine nozzles. IEEE, pp 373–378

97. Bennett M, Christie S, Graham A, Raper D (2010) Lidar Observations of Aircraft Exhaust Plumes. Journal of Atmospheric and Oceanic Technology 27:1638–1651. https://doi.org/10.1175/2010JTECHA1412.1

98. Graham A, Raper D, Christie S, Bennett M (2005) Air quality at Heathrow airport: impact of emissions from aircraft in ground run and flight: First Tech Report. UK Department for Transport

99. Graham A, Jones R, Tsanev V, et al (2010) Final Report Aviation Emissions and their Impact on Air Quality. Omega Consortium, Manchester Metropolitan University: M1 5GD

100. Synylo K, Kurtenbach R, Wiesen P, Zaporozhets O (2016) Modelling of aircraft emissions in the airport area. Making Aviation Environmentally Sustainable: 2nd ECATS Conference, Proceedings

101. Schäfer K, Emeis S, Jahn C, et al (2009) Airport air quality data bank for modelling studies. In: Proceedings of the 3rd conference Environment and Transport and of the 17th conference Transport and Air Pollution (ETTAP2009). National de Recherche Sur les Transports et leur Securite, Bron cedex, France

102. Barrett SRH, Britter RE, Waitz IA (2013) The impact of aircraft plume dynamics on airport local air quality: Supplementary Material. Atmospheric Environment 74 74:247–258. https://doi.org/10.1016/j.atmosenv.2013.03.061

103. Wayson RL, Fleming GG, Iovinelli R (2009) Methodology to estimate particulate matter emissions from certified commercial aircraft engines. Journal of the Air & Waste Management Association 59:91–100. https://doi.org/10.3155/1047-3289.59.1.91

104. Lee GGL (2012) Development of techniques for rapidly assessing the local air quality impacts of airports. Massachusetts Institute of Technology, Berkeley, California

105. Fleuti E, Hofmann P, Talerico C (2004) Airport Local Air Quality Studies, ALAQS Case Study: Zurich Airport 2004, a comparison of modelled and measured air quality.

106. Herndon SC, Onasch TB, Frank BP, et al (2005) Particulate Emissions from in-use Commercial Aircraft. Aerosol Science and Technology 39:799–809. https://doi.org/10.1080/02786820500247363

107. Mokalled T, Adjizian Gérard J, Abboud M, et al (2019) VOC tracers from aircraft activities at Beirut Rafic Hariri International Airport. Atmospheric Pollution Research 10:537–551. https://doi.org/10.1016/j.apr.2018.09.009

108. Fleuti E (2006) ALAQS project - Airport Local Air Quality, Sensitivity Analysis Zurich Airport. EUROCONTROL

109. Yang X, Cheng S, Lang J, et al (2018) Characterization of aircraft emissions and air quality impacts of an international airport. Journal of Environmental Sciences 72:198–207. https://doi.org/10.1016/j.jes.2018.01.007

110. Herndon SC, Wood EC, Northway MJ, et al (2009) Aircraft Hydrocarbon Emissions at Oakland International Airport. Environ Sci Technol 43:1730–1736. https://doi.org/10.1021/es801307m

111. Lefebvre AH, Ballal DR (2010) Gas turbine combustion: alternative fuels and emissions, 3rd ed. CRC Press, Boca Raton

112. Rogers HL, Lee DS, Raper DW, et al (2002) The impacts of aviation on the atmosphere. The Aeronautical Journal 106:521–546. https://doi.org/10.1017/S0001924000018157

113. Mazaheri M, Johnson G, Morawska L (2009) Particle and gaseous emissions from commercial aircraft at each stage of the landing and takeoff cycle. Environmental science & technology 43:441–446. https://doi.org/10.1021/es8013985

114. Yetter A (1995) Why Do Airlines Want and Use Thrust Reversers? National Aeronautics and Space Administration, Hampton, Virginia

115. Rice CC (2002) Restricting The Use Of Reverse Thrust As An Emissions Reduction Strategy. In: Designing, Constructing, Maintaining, and Financing Today's Airport Projects. American Society of Civil Engineers, Orlando, Florida, United States, pp 1–12

116. Noel GJ, Boeker E (2007) Thrust Reverser Analysis for Implementation in the Aviation Environmental Design Tool. Federal Aviation Administration

117. Rice C (2002) Restricting Use of Reverse Thrust as an Emissions Reduction Strategy. Transportation Research Record 1788:124–131. https://doi.org/10.3141/1788-16

118. Mahmood T, Jackson A, Sethi V, Pilidis P (2011) Thrust Reverser for a Separate Exhaust High Bypass Ratio Turbofan Engine and its Effect on Aircraft and Engine Performance. In: Volume 1: Aircraft Engine; Ceramics; Coal, Biomass and Alternative Fuels; Wind Turbine Technology. ASMEDC, Vancouver, British Columbia, Canada, pp 301–313

119. Turgut ET, Usanmaz O (2017) An assessment of cruise NOx emissions of short-haul commercial flights. Atmospheric Environment 171:191–204. https://doi.org/10.1016/j.atmosenv.2017.10.013

120. Turgut ET (2016) Effects of ambient air temperature on gaseous emissions of turbofan engines. Journal of Propulsion and Power 32:713–725. https://doi.org/10.2514/1.B35916

121. Tait KN, Khan MAH, Bullock S, et al (2022) Aircraft Emissions, Their Plume-Scale Effects, and the Spatio-Temporal Sensitivity of the Atmospheric Response: A Review. Aerospace 9:355. https://doi.org/10.3390/aerospace9070355

122. Naiman AD, Lele SK, Wilkerson JT, Jacobson MZ (2010) Parameterization of subgrid plume dilution for use in large-scale atmospheric simulations. Atmos Chem Phys 10:2551–2560. https://doi.org/10.5194/acp-10-2551-2010

123. Dosio A (2005) Turbulent dispersion in the atmospheric convective boundary layer. Wageningen University and Research

124. Steinfeld JI (1998) Atmospheric chemistry and physics: from air pollution to climate change. Environment: Science and Policy for Sustainable Development 40:26–26

125. Dürbeck T, Gerz T (1996) Dispersion of aircraft exhausts in the free atmosphere. J Geophys Res 101:26007–26015. https://doi.org/10.1029/96JD02217

126. Carslaw D, Beevers S, Ropkins K, Bell M (2006) Detecting and quantifying aircraft and other on-airport contributions to ambient nitrogen oxides in the vicinity of a large international airport. Atmospheric Environment 40:5424–5434. https://doi.org/10.1016/j.atmosenv.2006.04.062

127. Schumann U, Konopka P, Baumann R, et al (1995) Estimate of diffusion parameters of aircraft exhaust plumes near the tropopause from nitric oxide and turbulence measurements. J Geophys Res 100:14147. https://doi.org/10.1029/95JD01277

128. Wayson RL, Fleming GG, Noel GJ, et al (2008) Lidar Measurement of Exhaust Plume Characteristics from Commercial Jet Turbine Aircraft at the Denver International Airport. United States. Federal Aviation Administration, Denver, Colorado

129. Bennett M, Christie SM, Graham A, et al (2013) Abatement of an Aircraft Exhaust Plume Using Aerodynamic Baffles. Environ Sci Technol 47:2346–2352. https://doi.org/10.1021/es303586x

130. Aloysius SS, Pearce D, Wrobel L, Fuller I (2007) ALAQS-Comparison of CFD and Lagrangian Dispersion Methods–Simple Scenario during Take-off. School of Engineering & Design, Middlesex, United Kingdom

131. Anderson JD (2012) Introduction to flight, 7th ed. McGraw Hill, New York

132. Unterstrasser S, Paoli R, Sölch I, et al (2014) Dimension of aircraft exhaust plumes at cruise conditions: effect of wake vortices. Atmos Chem Phys 14:2713–2733. https://doi.org/10.5194/acp-14-2713-2014

133. Church S, Lad C (2014) ADMS-Airport Airport Air Quality Management System User Guide. Cambridge Environmental Research Consultants Ltd, Cambridge, United Kingdom

134. (2021) Preliminary Environmental Information Report Appendix 13.4.1: Air Quality Assessment Methodology. London Airport Gatwick, London Gatwick, United Kingdom

135. Underwood BY (2010) Heathrow Airport Emission Inventory 2008/9. AEA Technology plc, Birchwood, United Kingdom

136. Guignery F, Montreuil E, Thual O, Vancassel X (2012) Contrail microphysics in the near wake of a realistic wing through RANS simulations. Aerospace Science and Technology 23:399–408. https://doi.org/10.1016/j.ast.2011.09.011

137. Synylo K, Ulianova K, Zaporozhets O (2021) Air Quality Studies at Ukrainian Airports. International Journal of Aviation Science and Technology 2:4–14. https://doi.org/10.23890/IJAST.vm02is01.0101

138. Graham A, Raper D (2003) Air quality in airport approaches: impact of emissions entrained by vortices in aircraft wakes. Manchester Metropolitan, Manchester, United Kingdom

139. Testa E, Giammusso C, Bruno M, Maggiore P (2013) Fluid dynamic analysis of pollutants' dispersion behind an aircraft engine during idling. Air Quality, Atmosphere & Health 6:367–383. https://doi.org/10.1007/s11869-012-0188-1

140. Gordijn E (2020) Nieuw normen- en handdhaving stelsel Schiphol. Advanced Decision Systems Airinfra BV, To70 BV. https://open.overheid.nl/documenten/ronl-efa5937c-8f7f-44dc-845a-5e023d365720/pdf

141. (2006) Project for the Sustainable Development of Heathrow - Report of the Air Quality Technical Panels. Department for Transport, London, United Kingdom

142. Wayson RL, Fleming GG, Kim B, et al (2004) The use of LIDAR to characterize aircraft initial plume characteristics. U.S. Department of Transportation, Washington, D.C,

143. Underwood BY (2010) Appendix H: Heathrow Airport Emission Inventory 2008/9. AEA Technology plc, Birchwood, United Kingdom

144. CheckWX Aviation Weather: METAR, TAF, AIRMET, SIGMET and OUTLOOK Weather Reports. https://www.checkwx.com/. Accessed 9 Jun 2022

145. Inspectie leefomgeving en transport (2013) FM 15-XIV AUTO METAR. https://www.ilent.nl/binaries/ilt/documenten/publicaties/2019/2/7/leidraad-handboek-rpas--metar/METAR.pdf

146. Air Traffic Control the Netherlands (2022) GEN 3.5 Meteorological Services. https://www.lvnl.nl/eaip/2022-01-13-AIRAC/html/eAIP/EH-GEN-3.5-en-GB.html. Accessed 5 Mar 2023

147. LiveATC.net Live Air Traffic - From their headsets to you. https://www.liveatc.net/. Accessed 19 Mar 2022

148. Schäfer M, Strohmeier M, Lenders V, et al (2014) Bringing up OpenSky: A large-scale ADS-B sensor network for research. IEEE, pp 83–94

149. The OpenSky Network (2022) Opensky Data Sample. https://opensky-network.org/datasets/states/README.txt. Accessed 15 Mar 2023

150. ICAO (2021) ICAO Aircraft Engine Emissions Databank. European Aviation Safety Agency, Montreal, QC, Canada

151. Federal Aviation Administration (2023) Aircraft Characteristics Database. https://www.faa.gov/airports/engineering/aircraft_char_database. Accessed 4 Mar 2023

152. International Civil Aviation Organization ICAO Doc 8643: Aircraft Type Designators. https://www.icao.int/publications/doc8643/Pages/default.aspx

153. T. Noack About planespotters.net. https://www.planespotters.net/about

154. Human Environment and Transport, Inspectorate (2022) Luchtvaartuigregister / Aircraft register. https://www.ilent.nl/onderwerpen/luchtvaartuigregister#/. Accessed 6 Mar 2023

155. The OpenSky Network (2022) Opensky aircraft database sources. https://opensky-network.org/sources

156. Anaconda Start Coding Immediately. https://www.anaconda.com/. Accessed 12 Mar 2023

157. Arduino IDE 2.0.4. https://www.arduino.cc/en/software. Accessed 20 Feb 2022

158. Microsoft Microsoft Excel: Turn data into insights with free and premium spreadsheets. https://www.microsoft.com/en-us/microsoft-365/excel. Accessed 12 Mar 2023

159. Alphasense Ltd (2023) The stabilisation time for Toxic sensors when first plugged in. https://www.alphasense.com/faqs/

160. Royal Schiphol Group (2021) Traffic review 2021. https://www.schiphol.nl/en/schiphol-group/page/traffic-review/#:~:text=In%202021%2C%20Schiphol%20welcomed%2025.5,of%2017%25%20compared%20with%202020. Accessed 21 Mar 2023

161. Schiphol Group How high and fast does it fly? https://www.schiphol.nl/en/you-and-schiphol/page/five-questions-about-aircraft/

162. Mazaheri M (2009) Investigation into submicrometer particle and gaseous emissions from airport ground running procedures. Queensland University of Technology

163. Klapmeyer ME, Marr LC (2012) CO2, NO x, and Particle Emissions from Aircraft and Support Activities at a Regional Airport. Environmental Science & Technology 46:10974–10981. https://doi.org/10.1021/es302346x

164. (2023) Weather conditions. https://en.lvnl.nl/safety/achieving-safety/weather-conditions. Accessed 3 Apr 2023

165. Turgut ET, Cavcar M, Yay OD, et al (2015) Analysis of Test-Cell Emission Measurements of Newly Overhauled Turbofan Engines. Journal of Propulsion and Power 31:559–572. https://doi.org/10.2514/1.B35328

166. International Civil Aviation Organization (2008) International Standards and Recommended Practices: Annex 16 to the Convention on International Civil Aviation

167. Aviastar Cessna Model 550 Citation II. http://www.aviastar.org/pictures/usa/cessna_citation2.gif. Accessed 25 Feb 2023

168. Rotterdam The Hague Airport Overzichtskaart Rotterdam the Hague Airport. https://rotterdamtransport.com/nl/overzichtskaart-rotterdam-hague-airport/#gallery-1. Accessed 3 May 2022

169. Masic A, Bibic D, Pikula B, Razic F (2018) New Approach of Measuring Toxic Gases Concentrations: Principle of Operation. In: Katalinic B (ed) DAAAM Proceedings, 1st ed. DAAAM International Vienna, pp 0882–0887

170. Zimmerman N, Presto AA, Kumar SPN, et al (2018) A machine learning calibration model using random forests to improve sensor performance for lower-cost air quality monitoring. Atmos Meas Tech 11:291–313. https://doi.org/10.5194/amt-11-291-2018

171. Alphasense Ltd (2022) APPLICATION NOTE AAN 104: How Electrochemical Gas Sensors Work. https://www.alphasense.com/wp-content/uploads/2022/10/AAN_104_App-Note_V0.pdf. Accessed 9 Mar 2023

172. Jiang Q, Kresin F, Bregt AK, et al (2016) Citizen Sensing for Improved Urban Environmental Monitoring. Journal of Sensors 2016:1–9. https://doi.org/10.1155/2016/5656245

173. Hagan DH, Isaacman-VanWertz G, Franklin JP, et al (2018) Calibration and assessment of electrochemical air quality sensors by co-location with regulatory-grade instruments. Atmos Meas Tech 11:315–328. https://doi.org/10.5194/amt-11-315-2018

174. Wei P, Brimblecombe P, Yang F, et al (2021) Determination of local traffic emission and non-local background source contribution to on-road air pollution using fixed-route mobile air sensor network. Environmental Pollution 290:118055. https://doi.org/10.1016/j.envpol.2021.118055

175. Popoola OAM, Carruthers D, Lad C, et al (2018) Use of networks of low cost air quality sensors to quantify air quality in urban settings. Atmospheric Environment 194:58–70. https://doi.org/10.1016/j.atmosenv.2018.09.030

176. Tchepel O, Costa AM, Martins H, et al (2010) Determination of background concentrations for air quality models using spectral analysis and filtering of monitoring data. Atmospheric Environment 44:106–114. https://doi.org/10.1016/j.atmosenv.2009.08.038

177. Wells G, Prest H, Russ CW Signal, noise, and detection limits in mass spectrometry. Technical Note for Agilent Technologies Inc

178. Katajamaa M, Orešič M (2005) Processing methods for differential analysis of LC/MS profile data. BMC Bioinformatics 6:179. https://doi.org/10.1186/1471-2105-6-179

179. Xu C, Yu R, Ni X, et al (2021) An Envelope Algorithm for Single Nanoparticle Collision Electrochemistry †. Chin J Chem 39:1936–1940. https://doi.org/10.1002/cjoc.202100079

180. Tranter RL (2000) Design and Analysis in Chemical Research. Wiley-Blackwell, Hoboken, New Jersey

181. Schmid M, Rath D, Diebold U (2022) Why and How Savitzky–Golay Filters Should Be Replaced. ACS Meas Au 2:185–196. https://doi.org/10.1021/acsmeasuresciau.1c00054

182. Rudnyk J, Ellerbroek J, Hoekstra J (2018) Derivation of Trajectory Predictor Input Distributions from Observed Data. In: 2018 Aviation Technology, Integration, and Operations Conference. American Institute of Aeronautics and Astronautics, Atlanta, Georgia

183. Savitzky Abraham, Golay MJE (1964) Smoothing and Differentiation of Data by Simplified Least Squares Procedures. Anal Chem 36:1627–1639. https://doi.org/10.1021/ac60214a047

184. Gallagher NB (2022) Savitzky-Golay Smoothing and Differentiation Filter. Eigenvector Research Incorporated. https://doi.org/10.1021/acsmeasuresciau.1c00054

185. Luo J, Ying K, Bai J (2005) Savitzky–Golay smoothing and differentiation filter for even number data. Signal Processing 85:1429–1434. https://doi.org/10.1016/j.sigpro.2005.02.002

186. SciPy SciPy: Fundamental algorithms for scientific computing in Python. https://scipy.org/. Accessed 12 Mar 2023

187. Badrinath S, Balakrishnan H (2022) Automatic Speech Recognition for Air Traffic Control Communications. Transportation Research Record 2676:798–810. https://doi.org/10.1177/036119812110363

188. Blatt A, Kocour M, Vesely K, et al (2022) Call-Sign Recognition and Understanding for Noisy Air-Traffic Transcripts Using Surveillance Information. In: International Conference on Acoustics, Speech and Signal Processing (ICASSP). IEEE, Singapore, Singapore, pp 8357–8361

189. Prasad A, Zuluaga-Gomez J, Motlicek P, et al (2022) Grammar Based Speaker Role Identification for Air Traffic Control Speech Recognition

190. Zuluaga-Gomez J, Nigmatulina I, Prasad A, et al (2021) Contextual Semi-Supervised Learning: An Approach To Leverage Air-Surveillance and Untranscribed ATC Data in ASR Systems

191. Filippone A, Parkes B, Bojdo N, Kelly T (2021) Prediction of aircraft engine emissions using ADS-B flight data. Aeronaut j 125:988–1012. https://doi.org/10.1017/aer.2021.2

192. Filippone A, Bojdo N, Mehta S, Parkes B (2022) Using the OpenSky ADS-B Data to Estimate Aircraft Emissions. In: The 9th OpenSky Symposium. MDPI, p 11

193. Sun J, Ellerbroek J, Hoekstra J (2016) Modeling and Inferring Aircraft Takeoff Mass from Runway ADS-B Data. 7th International Conference on Research in Air Transportation

194. Lemetti A, Polishchuk T, Polishchuk V, et al (2020) Identification of Significant Impact Factors on Arrival Flight Efficiency within TMA. ICRAT 2020: papers & presentations

195. Schafer M, Strohmeicr M, Smith M, et al (2018) OpenSky Report 2018: Assessing the Integrity of Crowdsourced Mode S and ADS-B Data. In: 2018 IEEE/AIAA 37th Digital Avionics Systems Conference (DASC). IEEE, London, pp 1–9

196. Proud SR (2020) Go-Around Detection Using Crowd-Sourced ADS-B Position Data. Aerospace 7:16. https://doi.org/10.3390/aerospace7020016

197. Filippone A, Bojdo N, Mehta S, Parkes B (2022) Using the OpenSky ADS-B Data to Estimate Aircraft Emissions. In: The 9th OpenSky Symposium. MDPI, p 11

198. Figuet B, Monstein R, Waltert M, Barry S (2020) Predicting Airplane Go-Arounds Using Machine Learning and Open-Source Data. In: 8th OpenSky Symposium 2020. MDPI, p 6

199. Sun J, Ellerbroek J, Hoekstra J (2017) Flight Extraction and Phase Identification for Large Automatic Dependent Surveillance–Broadcast Datasets. Journal of Aerospace Information Systems 14:566–572. https://doi.org/10.2514/1.I010520

200. Weifan Z, Qiang T, Yuli,c, et al (2022) A trajectory prediction model for commercial flight based on representative trajectory. SPIE 12451:112--121. https://doi.org/10.1117/12.2656766

201. Lu J, Pan L, Deng J, et al (2023) Deep learning for Flight Maneuver Recognition: A survey. era 31:75–102. https://doi.org/10.3934/era.2023005

202. Sheets D, Amiruzzaman M, Stringer DB, et al (2022) AVES: A data-driven approach for airman certification. In: AIAA AVIATION 2022 Forum. American Institute of Aeronautics and Astronautics, Chicago, IL & Virtual

203. Flight Safety Foundation (2009) FSF ALAR briefing note 8.6: Wind Information. https://ulc.gov.pl/_download/bezpieczenstow_lotow/ALAR/BN_8.6_-_Wind_Information.pdf

204. Takegawa N, Murashima Y, Fushimi A, et al (2021) Characteristics of sub-10 nm particle emissions from in-use commercial aircraft observed at Narita International Airport. Atmos Chem Phys 21:1085–1104. https://doi.org/10.5194/acp-21-1085-2021

205. Strahler A (2011) Introducing Physical Geography. John Wiley & Sons, Inc.

206. Perger T, Auer H (2020) Energy efficient route planning for electric vehicles with special consideration of the topography and battery lifetime. Energy Efficiency 13:1705–1726. https://doi.org/10.1007/s12053-020-09900-5

207. O'Daniel T (2017) Essential Functions for Localization in Wireless Sensor Networks Using Geographic Coordinates. Journal of Applied Technology and Innovation 10–27

208. Mutiawani V, Rahmany S, Abidin TF (2018) Anti-theft Vehicle Monitoring and Tracking Android Application Using Firebase as Web Service. In: 2018 International Conference on Electrical Engineering and Informatics (ICELTICs)(44501). IEEE, Banda Aceh, pp 72–77

209. Zhang W, Jiang F, Yang C-F, et al (2021) Research on Unmanned Surface Vehicles Environment Perception Based on the Fusion of Vision and Lidar. IEEE Access 9:63107–63121. https://doi.org/10.1109/ACCESS.2021.3057863

210. GeoPy Welcome to GeoPy's documentation. https://geopy.readthedocs.io/en/stable/. Accessed 12 Mar 2023

211. Karney CFF (2013) Algorithms for geodesics. J Geod 87:43–55. https://doi.org/10.1007/s00190-012-0578-z

212. Buck A, Roberts MI, Overfelt R (2013) Transient Response Characteristics of Electrochemical Carbon Monoxide Sensors. In: 43rd International Conference on Environmental Systems. American Institute of Aeronautics and Astronautics, Vail, CO

213. Buck AL (2014) Steady State and Transient Response Characteristics of Commercial Carbon Monoxide Sensors. Auburn University

214. Alphasense Ltd (2022) Datasheets. https://www.alphasense.com/downloads/

215. Ropkins K, Carlsaw DC, Goodman PS, Tate JE (2009) Application of non-linear time-alignment and integration methods to environmental time series. TrAC Trends in Analytical Chemistry 28:373–391. https://doi.org/10.1016/j.trac.2008.11.013

216. Schmuker M, Bahr V, Huerta R (2016) Exploiting plume structure to decode gas source distance using metal-oxide gas sensors. Sensors and Actuators B: Chemical 235:636–646. https://doi.org/10.1016/j.snb.2016.05.098

217. Wang JM, Jeong C-H, Zimmerman N, et al (2015) Plume-based analysis of vehicle fleet air pollutant emissions and the contribution from high emitters. Atmos Meas Tech 8:3263–3275. https://doi.org/10.5194/amt-8-3263-2015

218. Ježek I, Drinovec L, Ferrero L, et al (2015) Determination of car on-road black carbon and particle number emission factors and comparison between mobile and stationary measurements. Atmos Meas Tech 8:43–55. https://doi.org/10.5194/amt-8-43-2015

219. Gobbett D, Hunt J (2017) Detecting trends in cereal crop sowing dates using Landsat. Research@ Locate17" Sydney, NSW www ceur-ws org 1913:

220. Gardegaront M, Farlay D, Peyruchaud O, Follet H (2018) Automation of the Peak Fitting Method in Bone FTIR Microspectroscopy Spectrum Analysis: Human and Mice Bone Study. Journal of Spectroscopy 2018:1–11. https://doi.org/10.1155/2018/4131029

221. Harvey M, Christopoulos A (2004) Fitting models to biological data using linear and nonlinear regression: a practical guide to curve fitting. Oxford University Press

222. Chicco D, Warrens MJ, Jurman G (2021) The coefficient of determination R-squared is more informative than SMAPE, MAE, MAPE, MSE and RMSE in regression analysis evaluation. PeerJ Computer Science 7:e623. https://doi.org/10.7717/peerj-cs.623

223. Saunders LJ, Russell RA, Crabb DP (2012) The coefficient of determination: what determines a useful R2 statistic? Investigative ophthalmology & visual science 53:6830–6832. https://doi.org/10.1167/iovs.12-10598

224. Sadat A, Joye IJ (2020) Peak Fitting Applied to Fourier Transform Infrared and Raman Spectroscopic Analysis of Proteins. Applied Sciences 10:5918. https://doi.org/10.3390/app10175918

225. Singh B, Hesse R, Linford MR (2015) Good Practices for XPS (and other Types of) Peak Fitting. Vacuum Technology & Coating 25–31

226. Kitis G, Peng J, Li B, Pagonis V (2022) Testing new analytical expression for dose response curves originating from the OTOR model. Journal of Luminescence 244:118747. https://doi.org/10.1016/j.jlumin.2022.118747

227. Komstra L, Van der Heyden Y, Sherma J (2018) Chemometrics in chromatography, 1st ed. CRC Press, Bothell, WA

228. Carruthers D, McHugh C, Jackson M, Johnson K (2011) Developments in ADMS-Airport to take account of near field dispersion and applications to Heathrow Airport. International Journal of Environment and Pollution 44:332

229. Boeing (2002) 747-400 Airplane Characteristics for Airport Planning. https://www.boeing.com/commercial/airports/plan_manuals.page. Accessed 18 Mar 2023

230. Boeing (2005) 737 Airplane Characteristics for Airport Planning. https://www.boeing.com/commercial/airports/plan_manuals.page. Accessed 18 Mar 2023

231. Dinger F, Kleinbek T, Dörner S, et al (2021) SO2 and BrO emissions of Masaya volcano from 2014 to 2020. Atmos Chem Phys 21:9367–9404. https://doi.org/10.5194/acp-21-9367-2021

232. Wayson RL, Fleming GG, Kim B, et al (2004) The use of LIDAR to characterize aircraft initial plume characteristics. U.S. Department of Transportation, Washington, D.C,

233. Scikit-learn Scikit-learn: machine learning in Python. https://scikit-learn.org/stable/. Accessed 12 Mar 2023

234. Pinheiro JG de O, Fernandes E, da Silva M Galeão International Airport's Lto Cycle Pollutant Emissions Assessment. Available at SSRN: https://ssrn.com/abstract=4377163. https://doi.org/10.2139/ssrn.4377163

235. Kinsey JS, Timko MT, Herndon SC, et al (2012) Determination of the emissions from an aircraft auxiliary power unit (APU) during the Alternative Aviation Fuel Experiment (AAFEX). Journal of the Air & Waste Management Association 62:420–430

236. Gierens K, Braun-Unkhoff M, Le Clercq P, et al (2016) Condensation trails from biofuels/kerosene blends scoping study

237. Otero E, Tengzelius U, Moberg B (2022) Flight Procedure Analysis for a Combined Environmental Impact Reduction: An Optimal Trade-Off Strategy. Aerospace 9:683. https://doi.org/10.3390/aerospace9110683

238. Fan W, Sun Y, Zhu T, Wen Y (2012) Emissions of HC, CO, NOx, CO2, and SO2 from civil aviation in China in 2010. Atmospheric Environment 56:52–57. https://doi.org/10.1016/j.atmosenv.2012.03.052

239. Righi M, Hendricks J, Sausen R (2013) The global impact of the transport sectors on atmospheric aerosol: simulations for year 2000 emissions. Atmospheric Chemistry and Physics 13:9939–9970. https://doi.org/10.5194/acp-13-9939-2013

240. Motulsky H, Christopoulos A (2004) Fitting models to biological data using linear and nonlinear regression: a practical guide to curve fitting. Oxford University Press

241. Gifford F (1972) Atmospheric transport and dispersion over cities. Nuclear safety 13:391–402

242. Kahl JDW, Chapman HL (2018) Atmospheric stability characterization using the Pasquill method: A critical evaluation. Atmospheric Environment 187:196–209. https://doi.org/10.1016/j.atmosenv.2018.05.058

243. Hanna SR, Briggs GA, Hosker RP (1982) Handbook on atmospheric diffusion: prepared for the Office of Health and Environmental Research, Office of Energy Research, U.S. Department of Energy. Technical Information Center, U.S. Dept. of Energy, Oak Ridge, TN

244. Rohli RV, Li C (2021) Meteorology for Coastal Scientists. Springer Cham

245. Almethen OM, Aldaithan ZS (2017) The State of Atmosphere Stability and Instability Effects on Air Quality. The International Journal of Engineering and Science 06:74–79. https://doi.org/10.9790/1813-0604017479

246. Leelőssy Á, Molnár F, Izsák F, et al (2014) Dispersion modeling of air pollutants in the atmosphere: a review. Open Geosciences 6:. https://doi.org/10.2478/s13533-012-0188-6

247. Wald L (2019) Basics in solar radiation at earth surface-revised version. https://hal-mines-paristech.archives-ouvertes.fr/hal-02164311

248. Holmgren WF, Hansen CW, Mikofski MA (2018) pvlib python: A python package for modeling solar energy systems. Journal of Open Source Software 3:884. https://doi.org/10.21105/joss.00884

249. Luna RE, Church HW (1972) A comparison of turbulence intensity and stability ratio measurements to pasquill stability classes. Journal of Applied Meteorology and Climatology 663–669

250. Carrascal MD, Puigcerver M, Puig P (1993) Sensitivity of Gaussian plume model to dispersion specifications. Theor Appl Climatol 48:147–157. https://doi.org/10.1007/BF00864921

251. Koudis GS, Hu SJ, Majumdar A, et al (2017) Airport emissions reductions from reduced thrust takeoff operations. Transportation Research Part D: Transport and Environment 52:15–28. https://doi.org/10.1016/j.trd.2017.02.004

252. DuBois D, Paynter GC (2006) “Fuel Flow Method2” for Estimating Aircraft Emissions. 2006-01–1987. https://doi.org/10.4271/2006-01-1987

253. Penner JE, Lister DH, Griggs DG, et al Aviation and the Global Atmosphere. Intergovernmental panel on climate change

254. Pederson DM (1988) AC 25-13: Reduced and derated takeoff thrust (power) procedures. https://www.faa.gov/regulations_policies/advisory_circulars/index.cfm/go/document.information/documentid/22468

255. King D, Waitz IA (2005) Assessment of the effects of operational procedures and derated thrust on American Airlines B777 emissions from London's Heathrow and Gatwick airports. The Partnership for AiR Transportation Noise and Emission Reduction

256. Koudis GS, Hu SJ, North RJ, et al (2017) The impact of aircraft takeoff thrust setting on NO X emissions. Journal of Air Transport Management 65:191–197. https://doi.org/10.1016/j.jairtraman.2017.06.009

257. Morris, MM (2002) Take-off at less than full Power. British Airways Environmental Affairs, British Airways Technical Documents Relating to the Aircraft Operations Supporting the Project for the Sustainable Development of Heathrow, Document

258. Sherry L (2015) Improving the accuracy of airport emissions inventories using disparate datasets. IIE Transactions 47:577–585. https://doi.org/10.1080/0740817X.2014.938845

259. Morris KM (2005) Reverse Thrust Examples from British Airways Operations. British Airways Environmental Affairs, British Airways Technical Documents Relating to the Aircraft Operations Supporting the Project for the Sustainable Development of Heathrow, Document 3:

260. Wilkerson J, Jacobson MZ, Malwitz A, et al (2010) Analysis of emission data from global commercial aviation: 2004 and 2006. Atmospheric Chemistry and Physics 10:6391–6408

261. Jacobsen M, Ringertz UT (2010) Airspace constraints in aircraft emission trajectory optimization. Journal of Aircraft 47:1256–1265. https://doi.org/10.2514/1.47109

262. Wasiuk D, Lowenberg M, Shallcross D (2015) An aircraft performance model implementation for the estimation of global and regional commercial aviation fuel burn and emissions. Transportation Research Part D: Transport and Environment 35:142–159. https://doi.org/10.1016/j.trd.2014.11.022

263. Schaefer M, Bartosch S (2013) Overview on fuel flow correlation methods for the calculation of NOx, CO and HC emissions and their implementation into aircraft performance software. Institut für Antriebstechnik

264. Koopmann J, Ahearn M (2012) Aviation environmental design tool (aedt) 2a: Technical manual. U.S. Department of Transportation, Washington, D.C,

265. Kim B, Fleming G, Balasubramanian S, et al (2005) System for assessing Aviation's Global Emissions Technical Manual Version 1.5

266. Rijksinstituut voor Volksgezondheid en Milieu (2022) Grootschalige Concentratie- en Depositiekaarten Nederland (GCN en GDN). https://data.rivm.nl/apps/gcn/. Accessed 1 Jul 2023

267. Synylo K, Kurtenbach R, Wiesen P, Zaporozhets O (2017) Comparison between modelled and measured NOX concentrations in aircraft plumes at Athens International Airport. International Journal of Sustainable Aviation 3:279. https://doi.org/10.1504/IJSA.2017.090296

268. Yu Z, Herndon SC, Ziemba LD, et al (2012) Identification of lubrication oil in the particulate matter emissions from engine exhaust of in-service commercial aircraft. Environmental science & technology 46:9630–9637. https://doi.org/10.1021/es301692t

269. EUROCONTROL (2018) European Wake turbulence categorisation and separation minima on approach and departure. EUROCONTROL

270. European Aviation Safety Agency (2022) Type certificate data sheet No. EASA.A.064 for AIRBUS A318 – A319 – A320 – A321. https://www.easa.europa.eu/en/document-library/type-certificates/noise/easaa064-airbus-a318-a319-a320-a321-single-aisle

271. European Aviation Safety Agency (2022) Type certificate data sheet No.EASA.IM.A.071 for EMBRAER ERJ-190. https://www.easa.europa.eu/en/document-library/type-certificates/noise/easaima071-erj-190

272. European Aviation Safety Agency (2020) Type certificate data sheet No. EASA.A.004 for AIRBUS A330. https://www.easa.europa.eu/en/document-library/type-certificates/noise/easaa004-airbus-a330

273. European Civil Aviation Conference (2011) RECOMMENDATION ECAC/27-4: NOx emission classification scheme

274. Schober P, Boer C, Schwarte LA (2018) Correlation coefficients: appropriate use and interpretation. Anesthesia & analgesia 126:1763–1768. https://doi.org/10.1213/ANE.0000000000002864

275. Turgut ET, Cavcar M, Yay OD, et al (2015) A gaseous emissions analysis of commercial aircraft engines during test-cell run. Atmospheric Environment 116:102–111. https://doi.org/10.1016/j.atmosenv.2015.06.031

276. Lobo P, Whitefield PD, Hagen DE, et al (2008) Delta – Atlanta Hartsfield (UNA-UNA) Study. The Partnership for AiR Transportation Noise and Emissions Reduction

277. Popoola OAM, Stewart GB, Mead MI, Jones RL (2016) Development of a baseline-temperature correction methodology for electrochemical sensors and its implications for long-term stability. Atmospheric Environment 147:330–343. https://doi.org/10.1016/j.atmosenv.2016.10.024

278. Mijling B, Jiang Q, de Jonge D, Bocconi S (2018) Field calibration of electrochemical NO2 sensors in a citizen science context. Atmos Meas Tech 11:1297–1312. https://doi.org/10.5194/amt-11-1297-2018

279. Mueller M, Meyer J, Hueglin C (2017) Design of an ozone and nitrogen dioxide sensor unit and its long-term operation within a sensor network in the city of Zurich. Atmos Meas Tech 10:3783–3799. https://doi.org/10.5194/amt-10-3783-2017

280. Masson N, Piedrahita R, Hannigan M (2015) Quantification Method for Electrolytic Sensors in Long-Term Monitoring of Ambient Air Quality. Sensors 15:27283–27302. https://doi.org/10.3390/s151027283

281. Arapatsakos C, Gemtos TA (2008) Tractor engine and gas emissions. WSEAS Transactions on Environment and Development 1000:4

282. Alphasense Ltd Air Quality Sensors. https://www.alphasense.com/product_type/air/. Accessed 2 Jun 2022

283. Moltchanov S, Levy I, Etzion Y, et al (2015) On the feasibility of measuring urban air pollution by wireless distributed sensor networks. Science of The Total Environment 502:537–547. https://doi.org/10.1016/j.scitotenv.2014.09.059

284. Han P, Mei H, Liu D, et al (2021) Calibrations of low-cost air pollution monitoring sensors for CO, NO2, O3, and SO2. Sensors 21:256. https://doi.org/10.3390/s21010256

285. Ariyaratne R, Elangasinghe M, Zamora ML, et al (2023) Understanding the effect of temperature and relative humidity on sensor sensitivities in field environments and improving the calibration models of multiple electrochemical carbon monoxide (CO) sensors in a tropical environment. Sensors and Actuators B: Chemical 390:133935

286. Spinelle L, Gerboles M, Villani MG, et al (2015) Field calibration of a cluster of low-cost available sensors for air quality monitoring. Part A: Ozone and nitrogen dioxide. Sensors and Actuators B: Chemical 215:249–257. https://doi.org/10.1016/j.snb.2015.03.031

287. Timko MT, Herndon SC, Wood EC, et al (2010) Gas turbine engine emissions—part I: volatile organic compounds and nitrogen oxides. Journal of Engineering for Gas Turbines and Power 132:. https://doi.org/10.1115/1.4000131

288. Presto AA, Nguyen NT, Ranjan M, et al (2011) Fine particle and organic vapor emissions from staged tests of an in-use aircraft engine. Atmospheric environment 45:3603–3612. https://doi.org/10.1016/j.atmosenv.2011.03.061

289. Khou J, Ghedhaïfi W, Vancassel X, et al (2017) CFD simulation of contrail formation in the near field of a commercial aircraft: Effect of fuel sulfur content. Meteorologische Zeitschrift 585–596. https://doi.org/10.1127/metz/2016/0761

290. Cross E, Hunter J, Carrasquillo A, et al (2013) Online measurements of the emissions of intermediate-volatility and semi-volatile organic compounds from aircraft. Atmospheric Chemistry and Physics 13:7845–7858. https://doi.org/10.5194/acp-13-7845-2013

291. Santoni GW, Lee BH, Wood EC, et al (2011) Aircraft emissions of methane and nitrous oxide during the alternative aviation fuel experiment. Environmental science & technology 45:7075–7082. https://doi.org/10.1021/es200897h

292. Kim H-J, Baik H (2020) Empirical method for estimating aircraft fuel consumption in ground operations. Transportation Research Record 2674:385–394. https://doi.org/10.1177/03611981209610

293. Kim B, Rachami J (2008) Aircraft Emissions Modeling Under Low Power Conditions. Proceedings of the A & WMA's 101st Annual Conference and Exhibition

294. Lee JJ, Waitz IA, Kim BY, et al (2007) System for assessing aviation's global emissions (SAGE), part 2: uncertainty assessment. Transportation Research Part D: Transport and Environment 12:381–395

295. Allaire D, Noel G, Willcox K, Cointin R (2014) Uncertainty quantification of an Aviation Environmental Toolsuite. Reliability Engineering & System Safety 126:14–24. https://doi.org/10.1016/j.ress.2014.01.002

296. McElroy JL, Pooler F (1968) St. Louis dispersion study. US Department of Health, Education, and Welfare; Public Health Service

297. Zuluaga-Gomez J, Veselý K, Blatt A, et al (2020) Automatic call sign detection: Matching air surveillance data with air traffic spoken communications. MDPI, p 14

298. Zaporozhets O, Synylo K (2016) New and improved LAQ models for assessment of aircraft engine emissions and air pollution in and around airports. ON BOARD A SUSTAINABLE FUTURE, ICAO ENVIRONMENTAL REPORT 82–84

299. Zaporozhets O, Synylo K (2016) Estimation of buoyancy effect and penetration length of jet from aircraft engine by large eddy simulation method. IJSA 2:34. https://doi.org/10.1504/IJSA.2016.076070

300. Zaporozhets O, Synylo K (2015) Modelling and measurement of aircraft engine emissions inside the airport area. Proceedings of the NAU 63:65–72. https://doi.org/10.18372/2306-1472.63.8862

301. Synylo K, Zaporozhets O (2017) PolEmiCa model for local air quality assessment in airports. 16th Annual CMAS Conference. https://doi.org/10.5772/intechopen.84172

302. Kraabøl AG, Konopka P, Stordal F, Schlager H (2000) Modelling chemistry in aircraft plumes 1: comparison with observations and evaluation of a layered approach. Atmospheric Environment 34:3939–3950. https://doi.org/10.1016/S1352-2310(00)00156-4

303. Kraabøl AG, Stordal F (2000) Modelling chemistry in aircraft plumes 2: The chemical conversion of NOx to reservoir species under different conditions. Atmospheric Environment 34:3951–3962. https://doi.org/10.1016/S1352-2310(00)00155-2

304. Tian Y, Huang W, Ye B, Yang M (2019) A New Air Quality Prediction Framework for Airports Developed with a Hybrid Supervised Learning Method. Discrete Dynamics in Nature and Society 2019:1–13. https://doi.org/10.1155/2019/1562537

305. Cretu M, Teleaba V, Ionescu S, Ionescu A (2010) Pollution scenarios through atmospheric dispersion modelling based on real measurements - impact on human health. 6:. https://doi.org/10.4236/acs.2012.23033

306. Smith DG, Taylor EA, Doucette SM, Egan BA (1979) Validation Studies of Air Quality Models at Dulles Airport. Journal of the Air Pollution Control Association 29:110–113. https://doi.org/10.1080/00022470.1979.10470762

307. Wan L, Peng Q, Tian Y, et al (2020) Airport capacity evaluation based on air traffic activities big data. J Wireless Com Network 2020:227. https://doi.org/10.1186/s13638-020-01851-w

308. Brzozowski K, Kotlarz W (2005) Modelling of air pollution on a military airfield. Atmospheric Environment 39:6130–6139. https://doi.org/10.1016/j.atmosenv.2005.06.040

309. Kenney M (2017) Development of a NOx Chemistry Module for EDMS/AEDT to Predict NO2 Concentrations. https://doi.org/10.17226/24706

310. Sherry L, Neyshabouri S (2014) Estimating takeoff thrust from surveillance track data. Transportation Research Board Annual Meeting

311. Pott-Pollenske M, Dobrzynski W, Buchholz H, Almoneit D (2007) Characteristics of noise from aircraft ground operations. 13th AIAA/CEAS Aeroacoustics Conference (28th AIAA Aeroacoustics Conference), p 3560

312. Broutier J Aircraft database. https://aircraft-database.com/. Accessed 3 Jun 2023

313. Bombardier Aerospace (2015) Airport Planning Manual. https://customer.aero.bombardier.com/webd/BAG/CustSite/BRAD/RACSDocument.nsf/51aae8b2b3bfdf6685256c300045ff31/ec63f8639ff3ab9d85257c1500635bd8/$FILE/ATT1ES4H.pdf/CRJ200APMR8.pdf. Accessed 12 Apr 2022

314. Airbus (2020) A320 Aircraft characteristics: airport and maintenance planning. https://www.airbus.com/sites/g/files/jlcbta136/files/2021-11/Airbus-Commercial-Aircraft-AC-A320.pdf. Accessed 23 Apr 2023

315. EUROCONTROL (2023) Base of aircraft data. https://www.eurocontrol.int/model/bada. Accessed 3 Apr 2022

316. Swedish Defence Research Agency (2021) Confidential database for Turboprop Engine Emissions. https://www.foi.se/en/foi/research/aeronautics-and-space-issues/environmental-impact-of-aircraft.html

317. Numpy Numpy: The fundamental package for scientific computing with Python. https://numpy.org/. Accessed 12 Mar 2023

318. Pandas Pandas webpage. https://pandas.pydata.org/. Accessed 12 Mar 2023

319. Shapely The Shapely User Manual. https://shapely.readthedocs.io/en/stable/manual.html. Accessed 12 Mar 2023

320. Sqlite3 sqlite3: DB-API 2.0 interface for SQLite databases. https://docs.python.org/3/library/sqlite3.html. Accessed 12 Mar 2023

321. McFee B, Raffel C, Liang D, et al (2015) librosa: Audio and Music Signal Analysis in Python. Austin, Texas, pp 18–24

322. Robert J Pydub 0.25.1: Manipulate audio with an simple and easy high level interface. https://pypi.org/project/pydub/. Accessed 22 Mar 2022

323. Bishop S Pytz 2023.3: World timezone definitions, modern and historical. https://pypi.org/project/pytz/. Accessed 9 Feb 2022

324. Matplotlib Matplotlib 3.7.1 documentation. https://matplotlib.org/stable/index.html. Accessed 12 Mar 2023

325. Folium Folium: Python data, leaflet.js maps. https://python-visualization.github.io/folium/. Accessed 12 Mar 2023

326. Seaborn Seaborn: statistical data visualization. https://seaborn.pydata.org/. Accessed 12 Mar 2023

327. Windrose Windrose 1.8.1. https://pypi.org/project/windrose/. Accessed 12 Mar 2023

328. Microchip (2009) 18-Bit, Multi-Channel ΔΣ Analog-to-Digital Converter with I2C™ Interface and On-Board Reference

329. U.S. Environmental Protection Agency Indoor Air Unit Conversion. https://www3.epa.gov/ceampubl/learn2model/part-two/onsite/doc/Indoor%20Air%20Unit%20Conversions.pdf

330. National Library of Medicine Periodic Table of Elements. https://pubchem.ncbi.nlm.nih.gov/ptable/. Accessed 23 Apr 2023

331. Maes J (2021) Quantification of Aviation's Impact on Air Quality near Schiphol Airport using Low-Cost Gas Sensors. Delft University of Technology

332. Dedoussi IC (2021) AE4462-17 Aircraft Emissions and Climate Effects Lecture 11. Delft University of Technology

333. Meier M (2021) Jet Engine Specification Database. https://www.jet-engine.net/. Accessed 20 Jun 2023

334. Rosell D, Grönstedt T (2022) Design Considerations of Low Bypass Ratio Mixed Flow Turbofan Engines with Large Power Extraction. Fluids 7:21. https://doi.org/10.3390/fluids7010021

335. Vallero DA (2008) Fundamentals of air pollution, 4th ed. Elsevier, Amsterdam ; Boston

336. Delaney BT, Zetlen BA, Tai RC, et al (1986) Aircraft engine exhaust plume dynamics. Engineering & Services laboratory, Florida

337. Zaporozhets O, Synylo K (2019) Modeling of Air Pollution at Airports. https://www.intechopen.com/books/7403

Appendix A: Supplemental data of the experimental set-up

A.1 Specifications of hardware and software

An overview of the Python packages and corresponding version utilised during this research is provided in Table A.1.

Table A.1: *Python packages and corresponding version used in this research*

Package	Version	Purpose in this research
Numpy [317]	1.24.1	Used to read, process and analyse data
Pandas [318]	1.4.3	
Math	Inbuilt version	
Scikit-learn [233]	1.1.1	
Shapely [319]	1.8.4	
Sqlite3 [320]	3.39.2	
Geopy [210]	2.2.0	
Librosa [321]	0.9.2	
Pydub [322]	0.25.1	
Pvlib [248]	0.9.5	
Pytz [323]	2022.1	
Matplotlib [324]	3.5.1	Used to visualise the data
Folium [325]	0.14.0	
Seaborn [326]	0.11.2	
Windrose [327]	1.7.0	

Table A.2 provides the specifications of the gas sensors according to data sheets of the sensor manufacturer (Alphasense Ltd). This includes the noise level, operating range, response time and operating lifetime. The noise level is a pollutant concentration threshold below which signal variations are likely (±2 standard deviations) to be the result of instrument noise rather than an actual change in signal. The operating range is the range of pollutant concentrations for which sensor performance is warranted. The lower limit of this operating range is zero, but it should be noted that reliable concentration readings are only provided above the noise level. The response time is the time it takes for the sensor to generate an output from 0 to 90% of a predefined value. The operating lifetime is defined as number of months until the signal output has decreased to 50% of the original signal due to sensor aging. For a complete list of sensor specifications, the reader is referred to documentation of the sensor manufacturer [214].

Table A.2: *Technical specifications of gas sensors according to datasheets [214] of Alphasense Ltd*

Sensor name	Noise level (ppb equivalent)	Operating range (ppm)	Response time to reach 90% of a predefined value	Operating lifetime (months)
CO B4	4	0 – 1000	30 s to reach 10 ppm	36
NO B4	15	0 – 20	45 s to reach 2 ppm	24
NO2 B43F	15	0 – 20	80 s to reach 2 ppm	24
SO2 B4	5	0 – 100	60 s to reach 2 ppm	36

A.2 Meteorological conditions during measurements

Measurement 1
Date: 22-01-2021
Location: Polderbaan runway of Schiphol airport
Time: 08:47 - 15:01 UTC

Table A.3: *Ambient conditions specified by METAR of measurement 1*

Time (UTC)	Temperature (°C)	Relative humidity (%)	Wind direction (°)	Wind speed (kts)
08:25	5	75.33	250	11
08:55	5	75.33	250	13
09:25	6	75.50	250	13
09:55	6	75.50	250	15
10:25	7	70.48	260	13
10:55	6	75.50	250	18
11:25	7	70.48	260	16
11:55	7	70.48	250	18
12:25	7	70.48	250	18
12:50	7	70.48	250	18
13:25	7	70.48	250	17
13:55	7	70.48	250	15
14:25	7	70.48	240	12
14:55	6	75.50	240	14

Measurement 2
Date: 09-09-2021
Location: Polderbaan runway of Schiphol airport
Time: 10:40 - 15:16 UTC

Table A.4: *Ambient conditions specified by METAR of measurement 2*

Time (UTC)	Temperature (°C)	Relative humidity (%)	Wind direction (°)	Wind speed (kts)
10:25	3	86.69	300	4
10:55	5	80.93	300	5
11:25	5	86.89	360	3
11:55	6	81.07	310	4
12:25	6	81.07	300	4
12:50	6	75.50	290	6
13:25	6	75.50	290	7
13:55	5	80.93	290	7
14:25	5	80.93	30	5
14:55	4	86.79	300	6

Measurement 3
Date: 11-11-2021
Location: Polderbaan runway of Schiphol airport
Time: 10:34 - 14:54 UTC

Table A.5: *Ambient conditions specified by METAR of measurement 3*

Time (UTC)	Temperature (°C)	Relative humidity (%)	Wind direction (°)	Wind speed (kts)
10:25	11	93.55	180	4
10:55	11	93.55	190	5
11:25	11	93.55	170	5
11:55	12	93.60	170	5
12:25	12	93.60	200	7
12:50	12	93.60	200	5
13:25	12	93.60	200	6
13:55	12	93.60	210	5
14:25	12	87.56	180	6

Measurement 4
Date: 24-11-2021
Location: Polderbaan runway of Schiphol airport
Time: 10:44 - 15:26 UTC

Table A.6: *Ambient conditions specified by METAR of measurement 4*

Time (UTC)	Temperature (°C)	Relative humidity (%)	Wind direction (°)	Wind speed (kts)
10:25	8	87.19	180	8
10:55	8	87.19	180	8
11:25	8	87.19	170	9
11:55	9	81.47	160	8
12:25	8	81.34	160	11
12:50	9	76.01	170	10
13:25	8	81.34	180	9
13:55	8	81.34	190	9
14:25	8	75.84	190	10
14:55	8	75.84	180	9
15:25	7	81.20	190	8

Measurement 5
Date: 22-03-2022
Location: Polderbaan runway of Schiphol airport
Time: 08:16 - 15:43UTC

Table A.7: *Ambient conditions specified by METAR of measurement 5*

Time (UTC)	Temperature (°C)	Relative humidity (%)	Wind direction (°)	Wind speed (kts)
07:55	10	76.18	110	3
08:25	11	71.26	140	4
08:55	12	66.70	140	3
09:25	12	66.70	150	6
09:55	14	58.52	140	6
10:25	15	58.77	150	4
10:55	16	55.12	160	3
11:25	17	48.28	160	3
11:55	18	45.32	160	3
12:25	18	42.28	160	4
12:50	19	42.57	160	5
13:25	19	39.72	150	5
13:55	19	37.03	110	6
14:25	19	34.51	170	5
14:55	20	34.80	110	3
15:00	19	39.72	140	5
15:25	19	37.03	140	4

Measurement 6
Date: 04-04-2022
Location: Platform J of Rotterdam The Hague Airport
Time: 09:05 – 09:20 UTC (measurement 1) and 11:22 – 11:38 UTC (measurement 2)

Table A.8: *Ambient conditions specified by METAR of measurement 6*

Measurement	Time (UTC)	Temperature (°C)	Relative humidity (%)	Wind direction (°)	Wind speed (kts)
1	08:55	4	64.93	120	10
2	11:25	8	57.00	100	8

Measurement 7
Date: 06-05-2022
Location: Polderbaan runway of Schiphol airport
Time: 08:11 – 14:25 UTC

Table A.9: *Ambient conditions specified by METAR of measurement 7*

Time (UTC)	Temperature (°C)	Relative humidity (%)	Wind direction (°)	Wind speed (kts)
07:55	12	81.87	200	5
08:25	13	76.66	170	5
08:55	15	72.01	180	5
09:25	16	67.54	220	6
09:55	17	63.38	210	5
10:25	18	59.50	M	5
10:55	18	59.50	240	7
11:25	19	55.88	270	8
11:55	19	52.25	250	6
12:25	20	49.10	260	8
12:50	20	49.10	280	10
13:25	20	49.10	270	10
13:55	20	49.10	270	11
14:25	20	49.10	260	10

Measurement 8
Date: 25-05-2022
Location: Polderbaan runway of Schiphol airport
Time: 08:36 – 14:48 UTC

Table A.10: *Ambient conditions specified by METAR of measurement 8*

Time (UTC)	Temperature (°C)	Relative humidity (%)	Wind direction (°)	Wind speed (kts)
08:25	16	72.20	210	15
08:55	16	72.20	220	16
09:25	16	59.01	230	19
09:55	16	55.12	250	21
10:25	16	55.12	240	20
10:55	17	48.28	230	22
11:25	17	55.37	240	22
11:55	17	55.37	240	18
12:25	17	51.72	230	24
12:50	16	59.01	240	24
13:25	16	59.01	240	20
13:55	17	51.72	240	23
14:25	17	55.37	230	25

Measurement 9
Date: 15-07-2022
Location: Polderbaan runway of Schiphol airport
Time: 08:53 – 14:05 UTC

Table A.11: *Ambient conditions specified by METAR of measurement 9*

Time (UTC)	Temperature (°C)	Relative humidity (%)	Wind direction (°)	Wind speed (kts)
08:25	18	55.63	Variable	4
08:55	18	55.63	280	7
09:25	19	52.25	290	7
09:55	19	52.25	280	7
10:25	20	52.51	290	8
10:55	19	55.88	280	7
11:25	19	55.88	280	11
11:55	20	52.51	280	12
12:25	21	49.37	260	12
12:50	21	52.77	270	13
13:25	20	56.13	270	13
13:55	20	56.13	270	13

Measurement 10
Date: 28-07-2022
Location: Polderbaan runway of Schiphol airport
Time: 06:52- 14:25 UTC

Table A.12: *Ambient conditions specified by METAR of measurement 10*

Time (UTC)	Temperature (°C)	Relative humidity (%)	Wind direction (°)	Wind speed (kts)
06:25	15	72.01	80	10
06:55	16	67.54	80	7
07:25	16	63.15	90	9
07:55	17	55.37	80	11
08:25	18	55.63	80	12
08:55	17	55.37	90	11
09:25	18	55.63	80	10
09:55	18	55.63	80	11
10:25	19	52.25	80	10
10:55	18	55.63	70	10
11:25	19	48.83	70	10
11:55	19	52.25	50	11
12:25	20	52.51	60	11
12:50	20	49.10	50	13
13:25	20	52.51	40	12
13:55	21	49.37	50	12

Appendix B: Supplemental data of data processing

B.1 Conversion of raw sensor node data

The data obtained with the nodes needs to be processed in order to provide useful air pollution data, for which four steps are performed. In the first step, the Analogue to Digital (A/D) converter counts are converted to voltages. In the second step, these voltages are corrected for zero offset and environmental conditions. In the third step, the corrected voltages are converted to part-per-billion (ppb) concentration values. In the fourth step, the ppb values are resampled to 3 s. These steps will now be discussed in more detail.

The raw data of a node consists out of A/D converter counts for the working electrode and auxiliary (AUX) electrode of each gas sensor. These integer values (*I*) are converted to voltages using the reference voltage (2.048 V) and resolution (17 bits) of the A/D converter as shown in Equation B.1 and Equation B.2 [172, 278, 328].

$$\mathrm{S_{AUX}}[V] = \frac{I \times 2.048}{2^{17}} \tag{B.1}$$

$$\mathrm{S_{WE}}[V] = \frac{I \times 2.048}{2^{17}} \tag{B.2}$$

In the second step, $\mathrm{S_{AUX}}$ and $\mathrm{S_{WE}}$ are corrected for zero offset using correction factors defined as $S_{WE,0}$ and $S_{AUX,0}$ for the working electrode and AUX electrode respectively, provided by the sensor manufacturer. The corrected auxiliary electrode signal and corrected working electrode signal then follow from Equation B.3 and Equation B.4.

$$S_{AUX_{cor}} = D_{AUX} - D_{AUX,0} \tag{B.3}$$

$$S_{WE_{cor}} = D_{WE} - D_{WE,0} \tag{B.4}$$

The corrected auxiliary electrode signal is subtracted from the corrected working electrode signal in step 3 to account for environmental conditions. The baseline of the working electrode, which measures the target pollutant (i.e., the measured species), can vary due to changes in environmental conditions. To correct for this, an AUX electrode is installed which is isolated from the target gas but (similar to the working electrode) responds to changes in environmental conditions. Therefore, a correction can be applied to account for environmental conditions by subtracting $S_{AUX,cor}$ from $S_{WE,cor}$ [46, 169–173].

In the fourth step, the remaining voltages are converted to part-per-billion concentration values using a sensitivity correction factor *s* supplied by the sensor manufacturer as shown in Equation B.5.

$$C_t[ppb] = \frac{S_{WE_{cor}} - S_{AUX_{cor}}}{s} \tag{B.5}$$

Lastly, in the fifth step the obtained ppb values are averaged into 3-minute readings. This step is performed as it is desired for post-processing and analysis to work with data with a fixed time step while the nodes sample at a non-constant sampling rate (providing a data-point every ~2 seconds).
To convert these volume concentrations in parts per billion (ppb) to mass concentrations in $\mu g m^{-3}$ first the measured mass of a contaminant is converted to a volume using the ideal gas

law shown in Equation B.6. In this equation P is the pressure of the ambient air, V is the volume of the contaminant, n is the number of moles of a contaminant, R is the universal gas constant (set to 8.3144 L kPa (mol K)$^{-1}$) and T is the temperature of the ambient air [329].

$$P\,V = n\,R\,T \tag{B.6}$$

The number of moles of a contaminant equals the mass of a contaminant *m* divided by its molecular mass *M* [329]. The molecular mass is obtained from a periodic table of elements published by the National Library of Medicine (see Table B.1) [330].

Table B.1: *Molecular mass of the pollutant species relevant for this research*

Pollutant species	Molecular mass [g/mole]
NO	30
NO_2	46
CO	28.01
SO_2	64.0638

To obtain the volume of the contaminant, Equation L.1 is rewritten to Equation B.7 [329].

$$V[L] = \frac{m\,[g]}{M\,\left[\frac{g}{mole}\right]} R \left[\frac{L\,kPa}{mol\,K}\right] T[K] \frac{1}{P[kPa]} \tag{B.7}$$

After obtaining the volume of the contaminant, the concentration *C* in ppb is multiplied by the molecular mass *M* in gram per mole and divided by this volume *V* to obtain the concentration *C* in $\mu g m^{-3}$ as shown in Equation B.8 [329].

$$\mathrm{C}\left[\mu g\, m^{-3}\right] = \mathrm{C}\,[ppb] \cdot \frac{\mathrm{M}\left[\frac{g}{mole}\right]}{\mathrm{V}[L]} \tag{B.8}$$

All steps discussed in this section are performed using an algorithm of J. Maes.

B.2 Processing of ATC data

As LiveATC stores audio recordings every half an hour, in the first step these recordings are loaded in using *pydub.AudioSegment.from_mp3()* and merged into a single audio file using the *.extend()* function [322]. In the second step the mp3 extension of the merged audio file is converted to wav using the *export()* function as this is required for further processing. In the third step the wav file is imported as a floating point time-series using *librosa.load()* and split into parts containing a signal >40 decibels (dB) and parts whereby the signal is <40 dB using *librosa.effects.split()*. In the fourth step parts where the signal is <40 dB are eliminated and parts where the signal is >40 dB are merged together using *extend()*.

B.3 Processing of aircraft- and engine data

Preparation of the aircraft- and engine data involves three steps: filtering out irrelevant data, categorising aircraft operations into flight phase (i.e., take-off or landing) and modifying the engine model designator to match the ICAO designator. Data of aircraft transmitting within 30 squared kilometres around the ATC tower of Schiphol airport is obtained from the OpenSky Network using an algorithm developed during previous research [331]. This data is organised into 'tracks' containing information (e.g., the velocity) of a specific aircraft operation. As only tracks of aircraft using the Polderbaan runway are of interest, previous research discarded

data for which the (minimum) distance between aircraft and the sensor node is >1500 m. However, this may include taxiing aircraft, which are not analysed during this research. A different method was therefore implemented.

This method consists of an algorithm that automatically verifies whether aircraft transmit position reports within a two-dimensional polygon overlaying the Polderbaan runway (see Figure 5.3 in main report). The polygon is defined using *geometry.Polygon()* of the Shapely package. The aircraft position reports (i.e. latitude and longitude) of departing and arriving aircraft are converted to Shapely geometry objects using the Shapely function *geometry.Point().* An example of these geometry objects, hereafter referred to as track points, together with the defined Polygon can be observed in Figure 5.4 in Chapter 5. The function *.contains()* of Shapely is thereafter used to search for the track points that an aircraft is present within the defined polygon. Aircraft operations with zero track points on the runway are discarded. Subsequently, aircraft not transmitting within this polygon are discarded.

After removing irrelevant data, aircraft operations are classified into flight phases (take-off, landing or over-flight) in the second data preparation step using an algorithm developed during previous research [331]. This algorithm is based on conditional statements[27] involving the geometric altitude H_{geo}, ground speed V_{ground} and the 'on-ground' Boolean. Similar to other research (e.g., [191–196]) it was observed that H_{geo} and V_{ground} contain erroneous values and high frequency noise, which can lead to the wrong flight phase categorisation[28]. To filter out erroneous values NaN (Not-a-Number) instances are discarded, and data of unrealistic magnitude are filtered out using the conditional statements shown in Figure B.1.

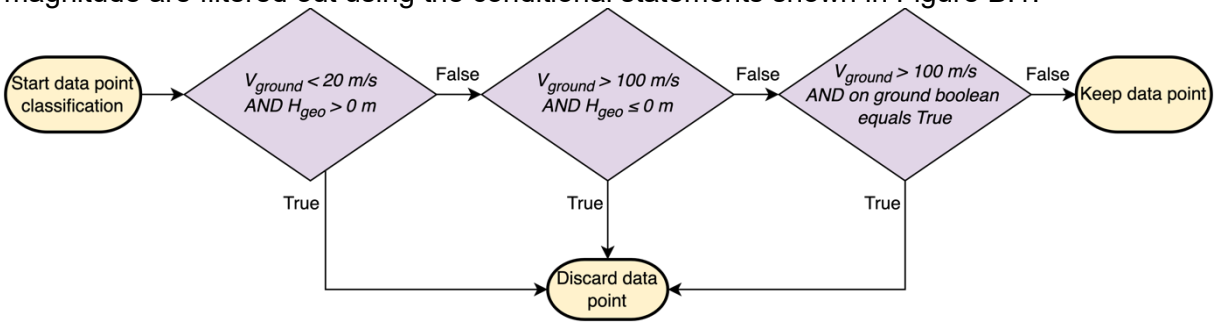

Figure B.1: *Procedure to search for and discard potentially erroneous data*

Hereafter, implausible fluctuations in geometric altitude and ground speed are removed using the Savitzky-Golay filter, which is one of the most frequently used filters for this purpose (see e.g., [182, 197–202]). Note that the same filter was used for air pollution data and has been described in Section 5.2.1 (see main report). Similar to other research (e.g., [182, 202]), the filter was implemented using a polynomial order of 3 with a filter length of 15. Subsequently, the filtered values are used to categorise aircraft operations into flight phases whereby aircraft operations other than take offs and landing are discarded. This is accomplished by an algorithm developed during precursory research of which the steps are shown in Figure B.2.

[27] Conditional statements are 'AND', 'IF" and 'OR' statements whereby the algorithm checks whether for a given input the statement is true or false.

[28] As during this research ~10 times higher resolution data was used compared to previous research, more extensive data removal procedures and filtering were necessary than applied during previous research.

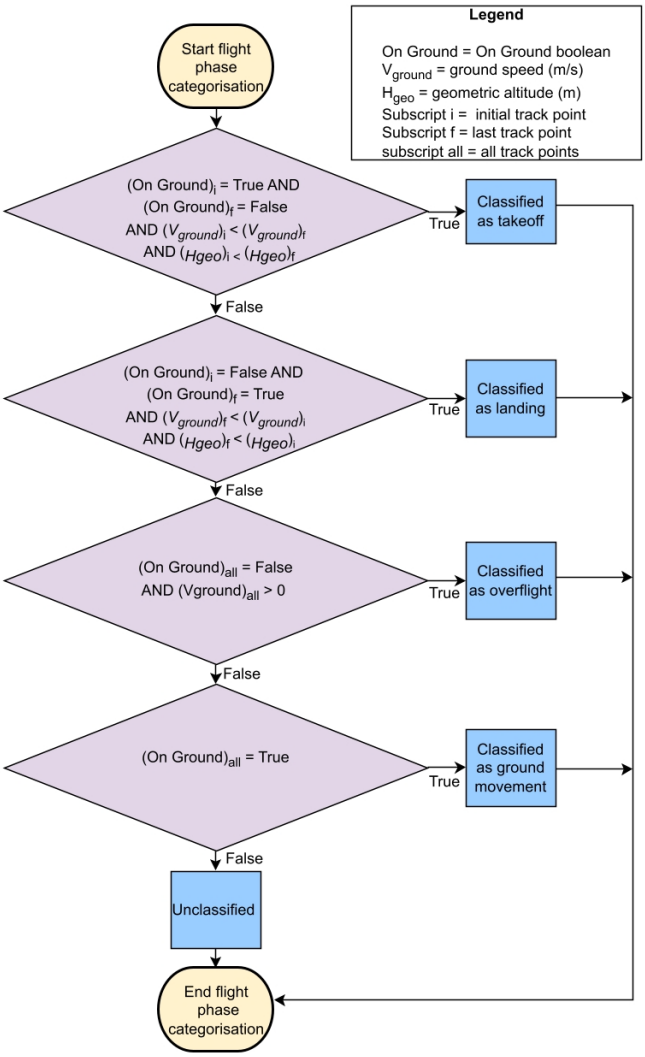

Figure B.2: *Logic of flight phase categorisation developed during previous research*

Besides filtering out aircraft that are not utilising the Polderbaan runway, another step of aircraft data processing involves the modification of the engine designator provided by the OpenSky Network. This engine designator is automatically rewritten to the ICAO designator based upon Boolean logic (i.e., if a condition is met, then action is taken) using the steps of Figure B.3 and Figure B.4. Note that the algorithm is presented in two parts for displaying purposes.

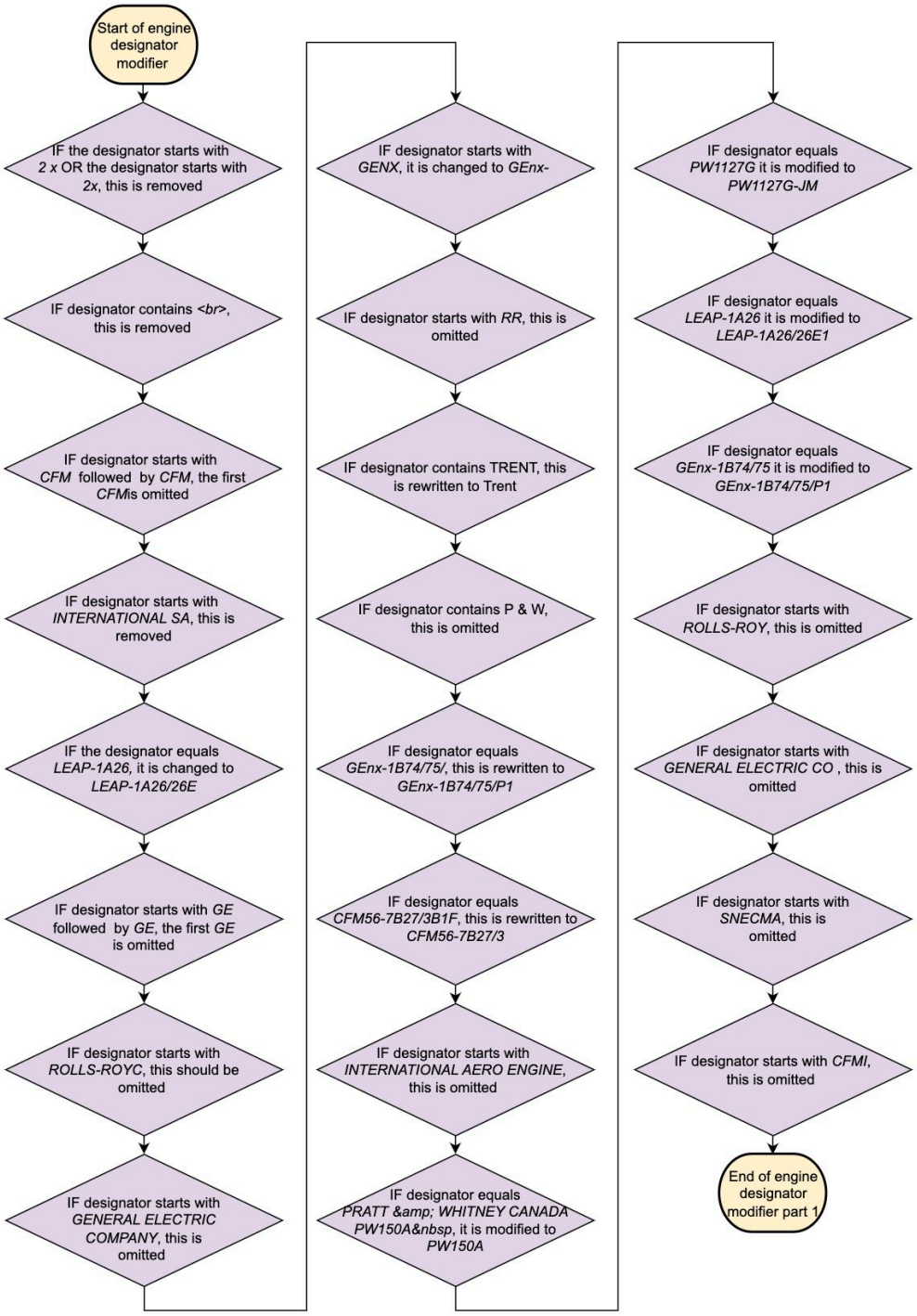

Figure B.3: *First part of engine model designator modification algorithm*

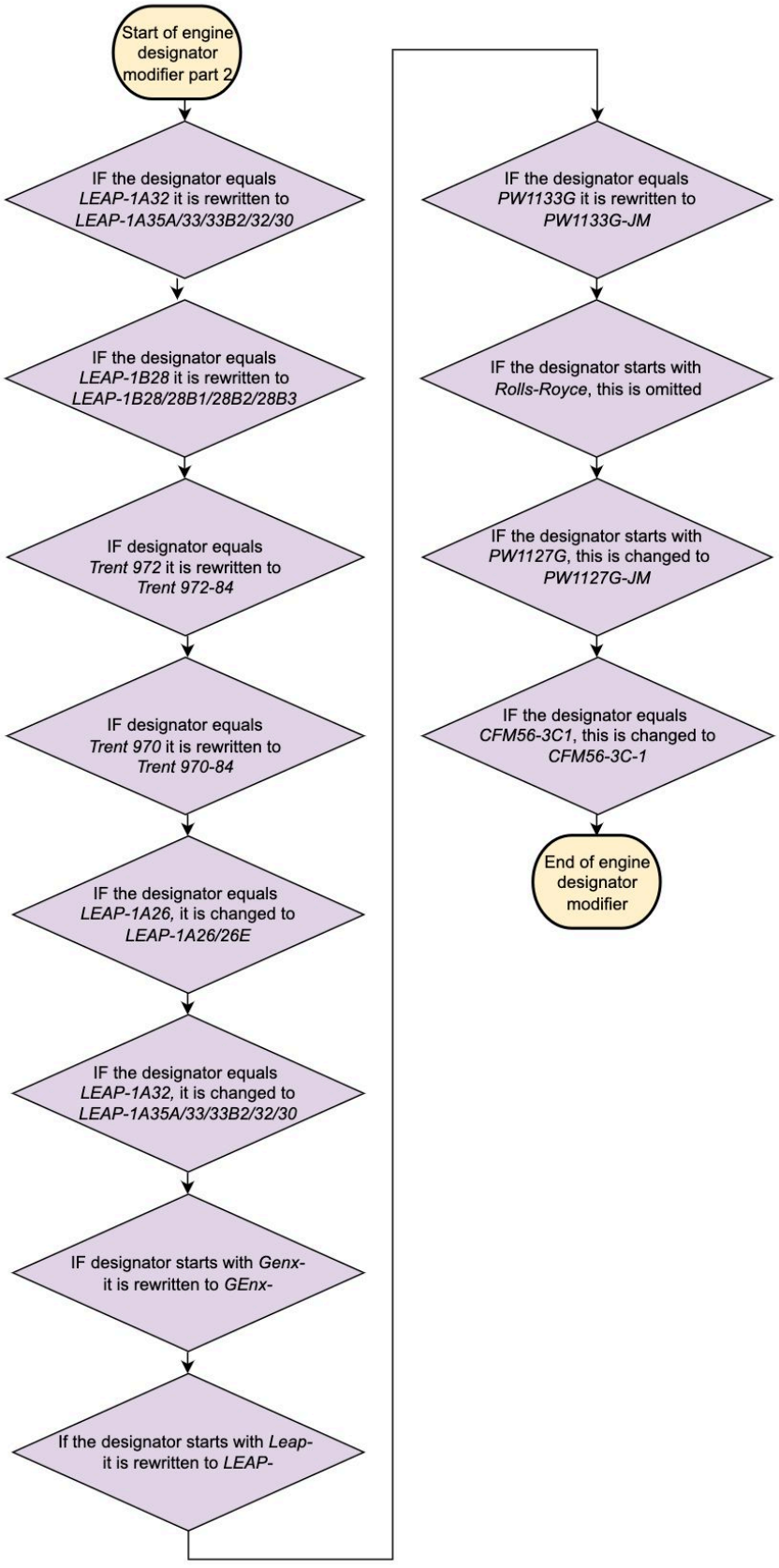

Figure B.4: *Second part of engine model designator modification algorithm*

B.4 Offset in initial estimated plume arrival time

Table B.2: *Offset between the estimated and actual time at which an aircraft operation gives rise to a peak pollutant concentration in time-series*

Date of measurement	Aircraft activity	Mean offset (s)	Standard deviation (s)
06-05-2022	Landing	21.8	7.6
25-05-2022	Landing	19.8	9.2
15-07-2022	Landing	10.9	18.4
28-07-2022	Take-off	6.3	12.2

B.5 Graphical goodness of fit assessment

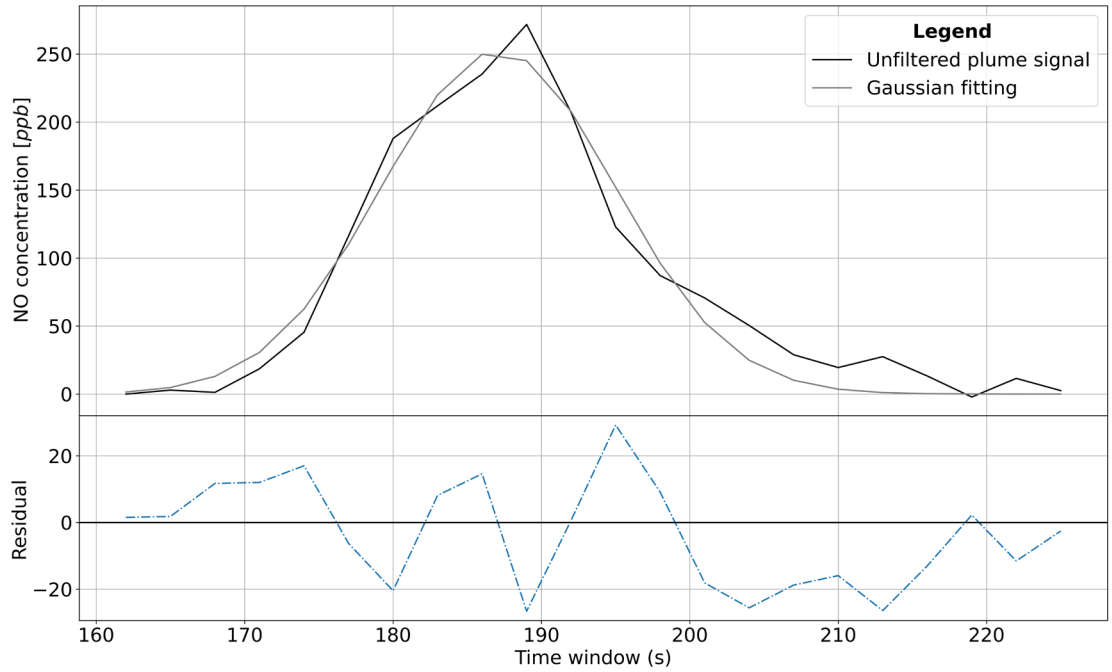

Figure B.5: *Graphical assessment of goodness of fit whereby residuals are defined as the difference between the fitted- and observed value*

Appendix C: Supplemental data of the dispersion model

C.1 Implementation of dispersion model during previous research

The selected dispersion model was already implemented during precursory research of Maes [63], of which the method of implementation will be described here. The dispersion model is shown in Equation C.1. where *E* represents the emission rate, *u* the plume velocity and *R* the plume radius at the location of interest.

$$\chi = \begin{cases} \frac{E}{\pi u R^2} & \text{within the plume} \\ 0 & \text{outside the plume} \end{cases} \tag{C.1}$$

The plume velocity *u* can be expressed in terms of the streamwise distance *S* between the aircraft and the sensor node, the initial plume velocity u_0, the initial plume radius R_0 and the universal entrainment coefficient α using Equation C.2. Similarly, the radius *R* can be expressed in terms of the streamwise distance *S* and the initial plume radius R_0 [332].

$$u = R_0 u_0 (2\alpha S + R_0)^{-1} \tag{C.2}$$

$$R = 2\alpha S + R_0 \tag{C.3}$$

Substituting these expressions into Equation C.1 leads to Equation C.4.

$$\chi = \begin{cases} \frac{E}{\pi R_0 u_0 (2\alpha S + R_0)} & \text{within the plume} \\ 0 & \text{outside the plume} \end{cases} \tag{C.4}$$

The universal entrainment coefficient α was set equal to 0.057 assuming the fluid to be a pure momentum jet. For fluid to be a pure momentum jet, the initial momentum of the fluid must be much larger than the initial buoyancy of the fluid [124]. An exhaust jet leaving the engine exhaust has a high release momentum and (initially) dominates over buoyancy. Jet exhaust can thus be assumed to be a pure momentum jet, for which it was experimentally determined that α = 0.057 [92].

The emission rate *E* was obtained in previous research by multiplying the fuel flow rate of an aircraft's engine model with the emission index. However, this provides the emission index of a single jet-engine, while all aircraft that were measured during previous research and this follow-up research were equipped with two or four engines. As stated in Chapter 2 of the main report, it is assumed that ambient wind brings the combined plume of all jet-engines towards the node(s). Therefore, the emission rate per jet engine needs to be multiplied by the number of engines *N* that an aircraft is equipped with.

To estimate the streamwise distance *S* previous research used the minimum distance between the aircraft and the downwind sensor node. However, it was explained in Chapter 5 of the main report that this distance is a function of the thrust setting and the wind speed and wind direction. Making the simplified assumption that aircraft are stationary sources releasing a passive plume (i.e., neglecting the initial velocity given to the plume by engine thrust) *S* can be estimated with Equation C.5. In this equation *d* represents the perpendicular distance to the runway, and *U* and *V* the headwind and crosswind components of the ambient wind.

$$S = d\sqrt{1 + (U/V)^2} \tag{C.5}$$

The initial plume radius R_0 was assumed to be equal to the engine fan diameter D during previous research, which was obtained from a publicly accessible online database [333]. Preferably, this parameter would be set equal to the actual engine exhaust nozzle radius but this information is generally not publicly available. In the ADMS-Airport user guide [133] it was stated that (based upon `private communication with an expert') a relationship exists between the jet-engine's fan diameter and exhaust diameter. For mixed flow turbofan engines (MTF), which are engines with a common exhaust for the mixed flow of the inner core flow and outer bypass flow, the exhaust nozzle is typically approximately equal to 0.75 times the exhaust diameter. For unmixed turbofan engines (TF), which are engines with a separate exhaust for the core flow and bypass flow, the combined exhaust diameter is typically approximately equal to the fan diameter [13, 133, 334].

Figure C.1 shows the relationship between the fan diameter and exhaust diameter for different engine models. In this figure it can be observed that for both MTF and TF engines the exhaust diameter is approximately equal to 0.75 times the fan diameter. Whereas previous research assumed $R_0 = D$, a better approximation would therefore be $R_0 = 0.75D$ to estimate the plume radius. This gives however the radius of a single engine, whereas the main report explained that a common aircraft exhaust plume is formed.

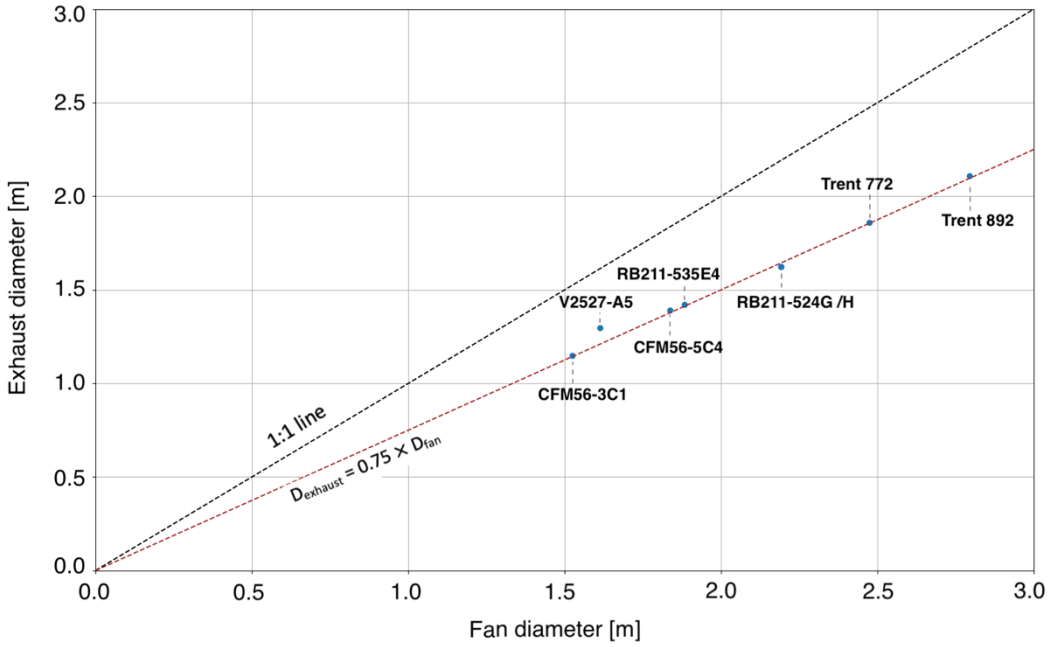

Figure C.1: *Relationship between the engine exhaust diameter and fan diameter*

The initial plume velocity u_0 was assumed to be equal to the jet engine exhaust velocity of a Boeing 787-8 during previous research as reported by Boeing, irrespective of the actual aircraft type or engine model[29]. Hereby the jet engine exhaust velocity refers to the mixed flow (i.e., the combined flow of the core, fan and surrounding air). However, engine performance data of eight engines published by Barrett et al. [102] revealed that the exhaust velocity at 100% thrust can differ >70% between engine models. Therefore, using the engine exhaust velocity of a Boeing 787-8 may largely differ with the actual engine exhaust velocity. Engine exhaust velocity data is generally not made publicly available, but the exhaust velocity of different engine models may be approximated using the method described by Barrett et al. [102].

[29] 15.56 m/s for idle engine power and 44.72 m/s for take-off power during standard atmospheric conditions at mean sea-level

Rather than modifying the model implementation of previous research, it was chosen to follow the method of Barrett et al. [102] as this improved the agreement between measured and modelled pollutant concentrations. Furthermore, it is unclear whether Equation C.4 can be used for aircraft exhaust plumes as the expressions are formulated for a single jet rather than the combined jet formed by all engines of an aircraft.

C.2 Tables used for the aircraft emissions estimation method

Table C.1: *Clear sky insolation codes corresponding to solar elevation angles*

Clear sky insolation code	Solar elevation angle [degrees]
3	ψ>60
2	<35 ψ ≤60
1	<15 ψ ≤35
0	<0 ψ ≤15
-2	ψ = 0

Table C.2: *Insolation strengths associated with insolation codes*

Insolation strength	Insolation code
Strong	3
Moderate	2
Slight	1
None	0
Night	-2

Table C.3: *Pasquill stability classes for daytime insolation*

W_s (m/s)	Daytime insolation strength		
	Strong	Moderate	Slight
$W_s < 2$	A	A – B	B
$2 \leq W_s < 3$	A – B	B	C
$3 \leq W_s < 5$	B	B – C	C
$5 \leq W_s < 6$	C	C – D	D
$W_s > 6$	C	D	D

Table C.4: *Empirical expressions by Briggs [243] to estimate dispersion parameters for distances between 100 and 10 000 m assuming urban conditions*

Pasquill stability class	y [m]	z [m]
A - B	$0.32S(1+0.0004S)^{-0.5}$	$0.24S(1+0.001S)^{0.5}$
C	$0.22S(1+0.0004S)^{-0.5}$	$0.20\,S$
D	$0.16S(1+0.0004S)^{-0.5}$	$0.14S(1+0.0003S)^{-0.5}$
E - F	$0.11S(1+0.0004S)^{-0.5}$	$0.08S(1+0.0015S)^{-0.5}$

It is worth noting that in above table combinations of Pasquill stability classes may be obtained (e.g. B - C) that are not shown in the previous table. For these cases, as suggested by Vallero [335], the dispersion parameters are computed for both Pasquill stability classes and subsequently the average of these values will be used.

C.3 Boeing Fuel Flow Method 2

This appendix provides a step-by-step overview of how the Boeing Fuel Flow Method 2 (BFFM2) was implemented. In the first step the fuel flow of the aircraft is estimated. For this, the fuel flow values for 7%, 30%, 85% and 100% of the rated thrust are obtained from the ICAO Emissions Databank and corrected for engine installation effects using the correction factor *r* shown in Table C.5.

Table C.5: *Engine installation effects correction factor r per flight activity*

	Take off	Climb	Approach	Idle
Thrust setting as percentage of the rated thrust	100%	85%	30%	7%
Correction factor *r*	1.010	1.013	1.020	1.100

As fuel flow scales approximately linear with thrust, linear interpolation is used in between the fuel flow values that were obtained after correcting for installation effects. From this, the fuel flow value W_f corresponding to the thrust setting of the aircraft is obtained. This value is corrected for ambient conditions using Equation C.1. In this equation the Mach number M = 0, and θ_{amb} and δ_{amb} follow from Equation C.2 and Equation C.3 respectively in which T_{amb} is the ambient temperature in Kelvin and p_{amb} the ambient pressure according to the prevailing METAR report.

$$PW_{ff} = \frac{W_f}{\delta_{amb}} \cdot \theta_{amb}^{3.8} \cdot e^{0.2 \cdot M^2} \tag{C.1}$$

$$\theta_{amb} = \frac{T_{amb}}{288.15K} \tag{C.2}$$

$$\delta_{amb} = \frac{p_{amb}}{101325Pa} \tag{C.3}$$

In the second step log-log graphs are generated with the horizontal axis showing the fuel flows (corrected for engine installation effects and ambient conditions) and the vertical axis displaying the corresponding of CO or NO_x. For this, first the ICAO fuel flows are corrected for engine installation effects and ambient conditions similar as for the aircraft fuel flow and converted to $\log_{10}$. Next, the four emission indices reported in the ICAO Emissions Databank (hereafter referred to as reference emission indices) are obtained and, similar to the fuel flow converted to $\log_{10}$. Hereafter a graph is created showing the $\log_{10}$ fuel flows and corresponding $\log_{10}$ emission indices (hereafter referred to as data-points). To be able to retrieve the emission index for fuel flow values other than those corresponding to the four reference emission indices, for NO_x a point-to-point fit is used between the four data-points. For CO a bilinear fit is used which is typically created by extending the linear fit through the data points corresponding to 7% and 30% of the rated thrust until it intersects with the horizontal line at a value equal to the midpoint between the data points corresponding to 85% and 100% of the rated thrust [263, 293].

In the third step the aircraft fuel flow W_{ff} obtained in step 1 is converted to $\log_{10}$ and used to find the corresponding emission index $EI_{ref,log}$ using the graphs generated in step 2. Hereafter 10 to the power of $EI_{ref,log}$ is raised to retrieve the non-logarithmic value EI_{ref}. This value is corrected for ambient conditions using Equations C.4 and C.5 for CO and NO_x respectively.

$$EICO = EI_{ref,CO} \cdot \frac{\theta_{amb}^{3.3}}{\delta_{amb}^{1.02}} \tag{C.4}$$

$$EINO_X = EI_{ref,NO_x} \cdot \sqrt{\frac{\delta_{amb}^{1.02}}{\theta_{amb}^{3.3}}} \cdot e^{H} \tag{C.5}$$

In Equation C.5 H represents a humidity correction factor which can be obtained using Equation C.6:

$$H = -19.0 \cdot (\omega - 0.00634) \tag{C.6}$$

Hereby ω is the specific humidity, Φ the relative humidity factor (obtained as percentage from the METAR and divided by 100 to get the relative humidity factor), P_{amb} the ambient pressure (obtained from the METAR hPa and converted to psia) and P_V the saturation vapour pressure in psia which can be computed using Equation C.7, Equation C.8 and Equation C.9 respectively with T_{amb} in Kelvin.

$$\omega = \frac{0.62197058 \cdot \Phi \cdot P_V}{P_{amb} - \Phi \cdot P_V} \tag{C.7}$$

$$P_V = 0.014504 \cdot 10^{\beta} \tag{C.8}$$

$$\beta = 7.90298 \cdot (1 - \tau) + 3.00571 + 5.02808 \cdot \log(\tau) + 1.3816 \cdot 10^{-7}\left[1 - 10^{11.344 \cdot (1 - 1/\tau)}\right] + (8.1328 \cdot 10^{-3})\left[10^{3.49149 \cdot (1-\tau)} - 1\right] \tag{C.9}$$

$$\tau = \frac{373.16}{T_{amb}} \tag{C.10}$$

Some engine models are known to raise issues when using the BMFF2 as displayed in Table C.6, for which the suggested solutions have been implemented accordingly.

Table C.6: *Issue cases of the BFFM2 and implemented methods to resolve these issues (table extracted from Schaefer and Bartosch [263])*

	Description	Suggested Solution
1	For some engines, the slanting line of the bilinear fit for CO and HC intersects the horizontal line beyond the 85% power point.	Extend the slanting line from the 30% point until the fuel flow value of the 85% point is reached. Then move vertically downwards until the horizontal line is intersected. This results in a vertical intermediate line between the two "normal" lines.
2	For some engines, the horizontal line of the bilinear fit for CO and HC intersects the slanting line above the 30% point.	Create a horizontal line at the 30% point and use that line to form the bilinear fit.
3	For some engines the slanting line of the bilinear fit for CO and HC has an increasing slope.	Use the horizontal line formed by the higher power points to conduct all of the modeling. This was done for simplicity due to the fact that the two lines do not even intersect within the normal LTO power range (i.e. 7% to 100%).
4	In a few cases, the EI and/or fuel flow values may not be available for some engines in the ICAO databank.	The missing data points were assigned zero values and plots developed accordingly. In case of missing EIs also consider issue number 6.
5	Due to the asymptotic nature of the bilinear fit for CO and HC, low fuel flows can result in unreasonably high EI values.	A lower limit on fuel flow can be placed corresponding to the fuel flow from the ICAO databank for the 7% (idle) power condition.
6	In the ICAO databank, some EI values are zeros which cannot be modeled on log plots.	The zero values were replaced by reasonably low values of 10^{-6}.
7	For some engines, the EI values of HC and CO are all zeros. As a result, HC and CO plots cannot be developed.	Emissions are modeled as zeros.

Appendix D: Supplemental data of results

D.1 Downwind experiment

D.1.1 Certified emission rate

Figure D.1 shows the rate at which pollutants are emitted during standard atmospheric conditions with a thrust setting corresponding to 7% and 85% of the rated thrust for landing- and departing aircraft respectively. The results are shown for some of the most frequently encountered aircraft-engine combinations, which includes the E190 (CF34-10E5 engines), A320 (LEAP-1A26/26E1 engines), B738 (CFM56-7B24 engines) and B787 (GEnx-1B74/75/P1 engines). Certified emissions data of the ICAO emissions databank was used for the fuel flow, NO_x emission index and CO emission index. An emission index of 0.8 (ranging from 0.01 to 3 g/kg) was assumed for SO_2.

In this figure it can be seen that for departures the emission rate of CO and SO_2 is much lower than the emission rate of NO_x, which is likely to explain why only for NO_x strong enhancements above the background concentration can be observed the measured data. Similarly, for landing aircraft the emission rate of CO is much higher than the emission rate of NO_x and SO_2 which is likely to explain why for landing aircraft only CO shows strong enhancements above the background concentration in observed time-series.

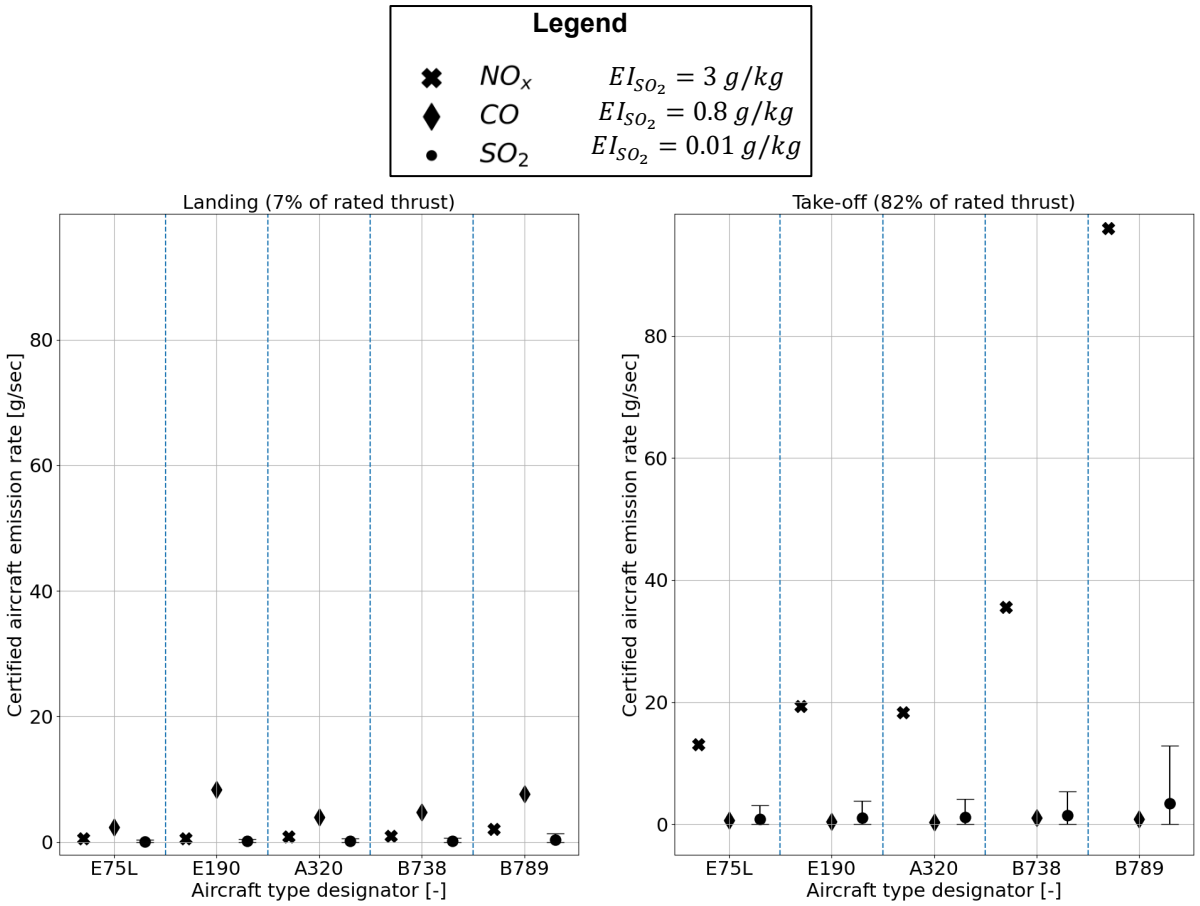

Figure D.1: *Emission rate of the combined jet-engines of an aircraft according to certified fuel flow rates and emission indices (except for SO_2)*

D.1.2 Automated screening results

Table D.1: *Overview of plumes not satisfying individual quality control criteria with respect to the total number of plumes not passing quality control for CO (landing aircraft) and NO and NO_2 (departing aircraft)*

Criterium	Species	Number of plumes failing to pass criterium	Plumes failing to pass criterium with respect to total number of plumes not passing quality control [%]
Overlapping plumes cannot be coupled to aircraft operations	CO	47	~45
	NO	25	~31
	NO_2	56	~45
Goodness of fit criteria not satisfied	CO	20	~19
	NO	20	~25
	NO_2	58	~47
No peak identified within 30 seconds from (refined) EPA time	CO	37	~35
	NO	35	~44
	NO_2	10	~8
Crosswind below threshold value	CO	1	~1
	NO	0	0
	NO_2	0	0

22-01-2021
Total number of aircraft operations: 51 (51 landings, 0 take-offs)
Accepted / accepted after separation / flagged: 37 / 0 / 14

Table D.2: *Quality control analysis of the measurement conducted at 22-01-2021*

Reason for plume not passing quality control	Number of plumes not passing quality control	Percentage of plumes not passing quality control
Either start-point or end-point below concentration threshold	0	0%
Statistics	3	~21%
No plume identified	1	~7%
Identified peak too far from EPA	2	~14%
Overlapping plume could not be coupled to flight	8	~57%

09-09-2021
Total number of aircraft operations: 39 (39 landings, 0 take-offs)
Accepted / accepted after separation / flagged: 24/0/15

Table D.3: *Quality control analysis of the measurement conducted at 09-09-2021*

Reason for plume not passing quality control	Number of plumes not passing quality control	Percentage of plumes not passing quality control
Statistics	7	~47%
No plume identified	0	0%
Identified peak too far from EPA	1	~6%
Overlapping not coupled to flight	7	~47%
Either start-point or end-point below concentration threshold	0	0%

06-05-2022
Total number of aircraft operations: 27 (16 landings, 11 take-offs)

Landing (CO)
Accepted / accepted after separation / flagged: 9/1/7

Table D.4: *CO quality control analysis of the measurement conducted at 06-05-2022*

Reason for plume not passing quality control	Number of plumes not passing quality control	Percentage of plumes not passing quality control
Either start-point or end-point below concentration threshold	1	~14%
Statistics	0	0%
No plume identified	0	0%
Identified peak too far from EPA	3	~43%
Overlapping plume could not be coupled to flight	3	~43%

Take-off (NO)
Accepted / accepted after separation / flagged: 2/0/9

Table D.5: *NO quality control analysis of the measurement conducted at 06-05-2022*

Reason for plume not passing quality control	Number of plumes not passing quality control	Percentage of plumes not passing quality control
Either start-point or end-point below concentration threshold	0	0%
Overlapping	4	~44%
Statistics	3	~33%
No plume identified	0	0%
Identified peak too far from EPA	2	~22%
Crosswind below threshold	0	0%

Take-off (NO_2)
Accepted / accepted after separation / flagged: 1/0/10

Table D.6: *NO_2 quality control analysis of the measurement conducted at 25-05-2022*

Reason for plume not passing quality control	Number of plumes not passing quality control	Percentage of plumes not passing quality control
Either start-point or end-point below concentration threshold	2	20%
Overlapping	5	50%
Statistics	2	20%
No plume identified	0	0%
Identified peak too far from EPA	1	10%
Crosswind below threshold	0	0%

25-05-2022
Total number of aircraft operations: 19
Accepted / accepted after separation / flagged: 14/0/5

Table D.7: *CO quality control analysis of the measurement conducted at 25-05-2022*

Reason for plume not passing quality control	Number of plumes not passing quality control	Percentage of plumes not passing quality control
Either start-point or end-point below concentration threshold	0	0%
Statistics	0	0%
No plume identified	2	40%
Identified peak too far from EPA	1	20%
Crosswind below threshold	0	0%
Overlapping plume could not be coupled to flight	2	40%

15-07-2022
Total number of aircraft operations: 115
Accepted / accepted after separation / flagged: 51/1/64

Table D.8: *CO quality control analysis of the measurement conducted at 15-07-2022*

Reason for plume not passing quality control	Number of plumes not passing quality control	Percentage of plumes not passing quality control
Either start-point or end-point below concentration threshold	2	~3%
Statistics	10	~16%
No plume identified	4	~6%
Identified peak too far from EPA	23	~36%
Crosswind below threshold	1	~2%
Overlapping	24	~38%

28-07-2022
Total number of aircraft operations: 154

NO
Accepted / accepted after separation / flagged: 83/0/71

***Table D.9**: CO quality control analysis of the measurement conducted at 28-07-2022*

Reason for plume not passing quality control	Number of plumes not passing quality control	Percentage of plumes not passing quality control
Either start-point or end-point below concentration threshold	1	~1%
Statistics	17	~24%
No plume identified	10	~14%
Identified peak too far from EPA	23	~32%
Crosswind below threshold	0	0%
Overlapping	20	~28%

NO_2
Accepted / accepted after separation / flagged: 40/1/114

***Table D.10:** NO_2 quality control analysis of the measurement conducted at 28-07-2022*

Reason for plume not passing quality control	Number of plumes not passing quality control	Percentage of plumes not passing quality control
Either start-point or end-point below concentration threshold	8	~7%
Statistics	56	~49%
No plume identified	0	0%
Identified peak too far from EPA	9	~8%
Crosswind below threshold	0	0%
Overlapping	41	~36%

D.1.3 Goodness of fit results

Goodness of fit results for CO are presented in Table D.11.

Table D.11: *Mean (and standard deviation) of the coefficient of determination (R^2), absolute value of the reduced chi squared ($|\chi^{2*}|$), Mean Absolute Error (MAE), Root Mean Square Error (RMSE), percentage difference between the area of the unfiltered plume signal and Gaussian fitting ($A_{difference}$) and percentage difference between the peak CO concentration of the filtered plume signal and Gaussian fitting for plumes passing quality control ($P_{difference}$)*

Date		R^2 [-]	χ^{2*} [-]	MAE $[\mu g/m^3]$	RMSE $[\mu g/m^3]$	$A_{difference}$ [%]	$P_{difference}$ [%]
22-01-2021	Node 1	0.856 (0.08)	6.7 (13.224)	4.6 (2.2)	5.4 (2.6)	3.6 (2.7)	4.3 (3.3)
	Node 2	N.A.	N.A.	N.A.	N.A.	N.A.	N.A.
09-09-2021	Node 1	0.843 (0.08)	2.6 (2.047)	3.9 (1.7)	4.8 (2.0)	5.6 (6.3)	4.4 (5.4)
	Node 2	N.A.	N.A.	N.A.	N.A.	N.A.	N.A.
06-05-2022	Node 1	N.A.	N.A.	N.A.	N.A.	N.A.	N.A.
	Node 2	N.A.	N.A.	N.A.	N.A.	N.A.	N.A.
25-05-2022	Node 1	0.924 (0.044)	3.9 (6.216)	3.3 (1.9)	3.9 (2.2)	2.8 (2.8)	2.9 (2.6)
	Node 2	0.905 (0.065)	5.4 (9.296)	4.0 (2.2)	4.8 (2.5)	4.4 (4.6)	3.5 (3.0)
15-07-2022	Node 1	0.902 (0.059)	3.5 (5.415)	2.8 (1.4)	3.5 (1.7)	5.0 (5.1)	4.0 (3.1)
	Node 2	0.894 (0.067)	3.9 (7.555)	2.6 (1.1)	3.1 (1.3)	7.0 (7.2)	3.9 (3.1)

Goodness of fit results for NO are presented in Table D.12.

Table D.12: *Mean (and standard deviation) of the coefficient of determination (R^2), absolute value of the reduced chi squared ($|\chi^{2*}|$), Mean Absolute Error (MAE), Root Mean Square Error (RMSE), percentage difference between the area of the unfiltered plume signal and Gaussian fitting ($A_{difference}$) and percentage difference between the peak NO concentration of the filtered plume signal and Gaussian fitting for plumes passing quality control ($P_{difference}$)*

Date		R^2 [-]	χ^{2*} [-]	MAE $[\mu g/m^3]$	RMSE $[\mu g/m^3]$	$A_{difference}$ [%]	$P_{difference}$ [%]
06-05-2022	Node 1	0.61 (N.A.)	13.6 (N.A.)	7.5 (N.A.)	10.3 (N.A.)	11.3 (N.A.)	10.9 (N.A.)
	Node 2	0.703 (0.048)	25.5 (31.434)	5.4 (0.9)	6.9 (1.3)	7.5 (0.8)	9.2 (2.0)
28-07-2022	Node 1	0.75 (0.088)	6.1 (6.015)	6.3 (1.8)	7.7 (2.2)	7.8 (5.0)	6.9 (6.3)
	Node 2	0.758 (0.094)	7.1 (10.317)	3.8 (0.9)	4.7 (1.1)	7.2 (5.1)	6.1 (5.4)

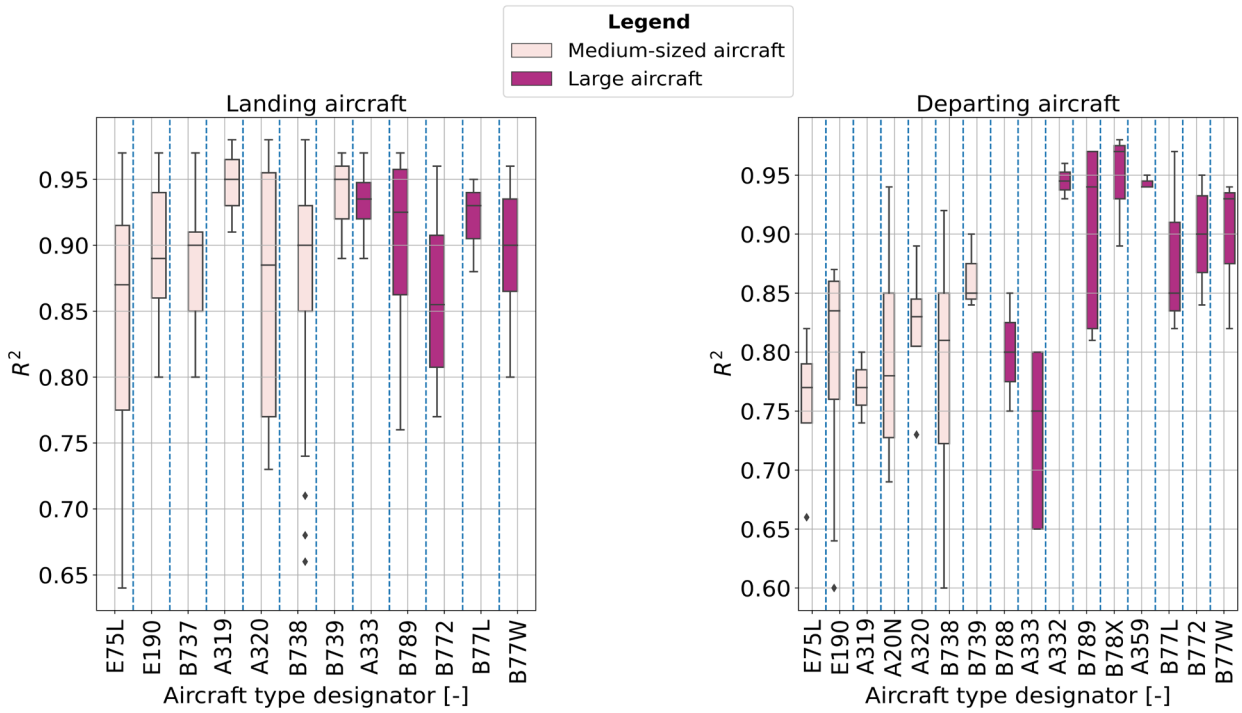

Figure D.2: *Coefficient of determination for various aircraft types*

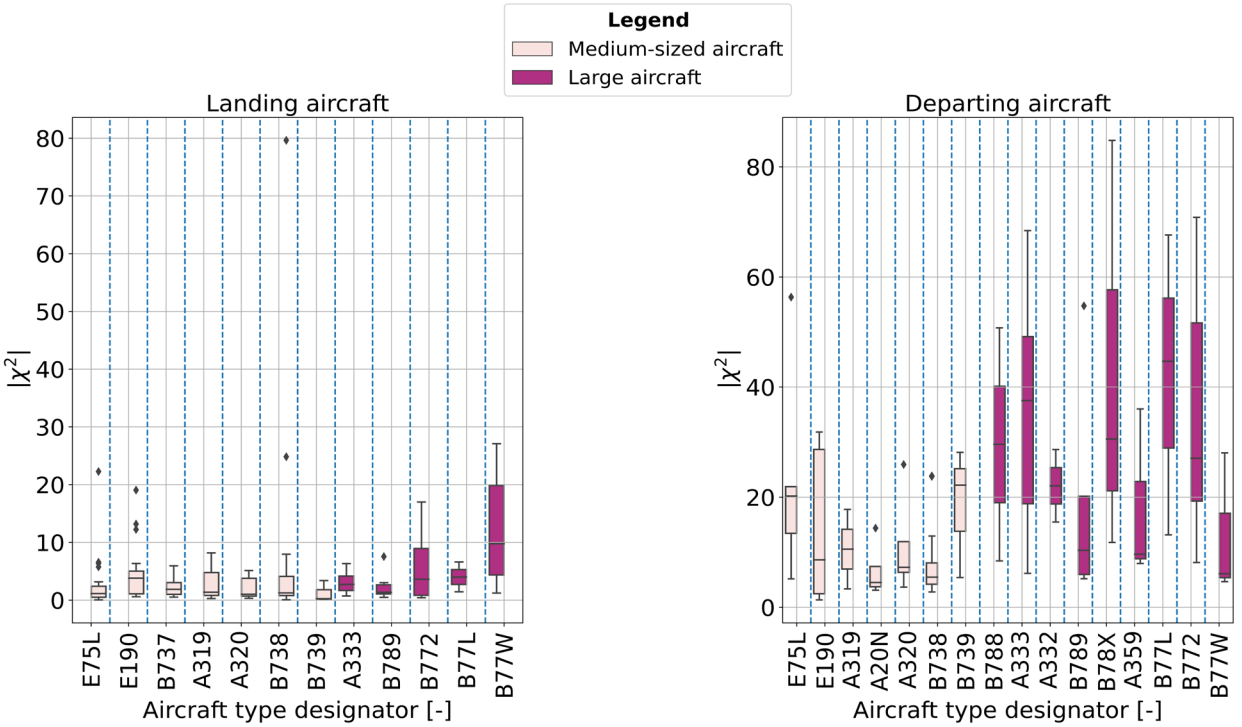

Figure D.3: *Absolute value of the reduced Chi-squared for various aircraft types*

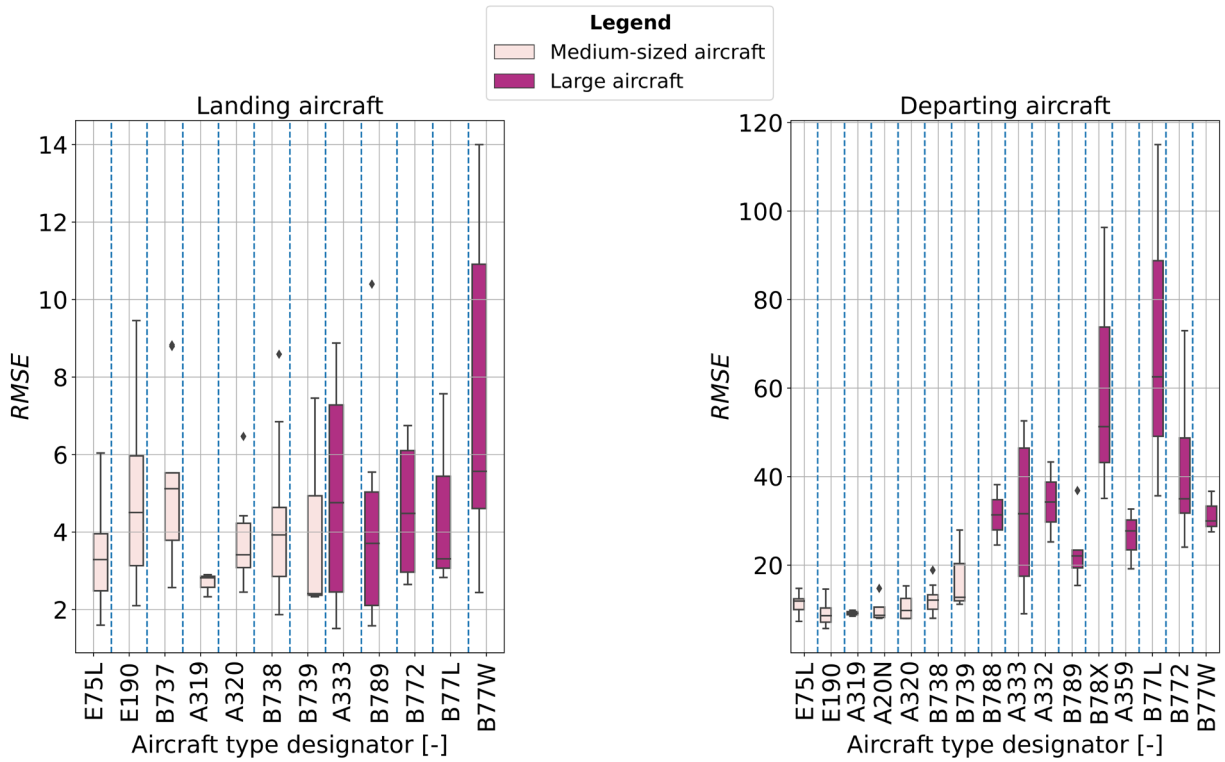

Figure D.4: *RMSE for various aircraft types*

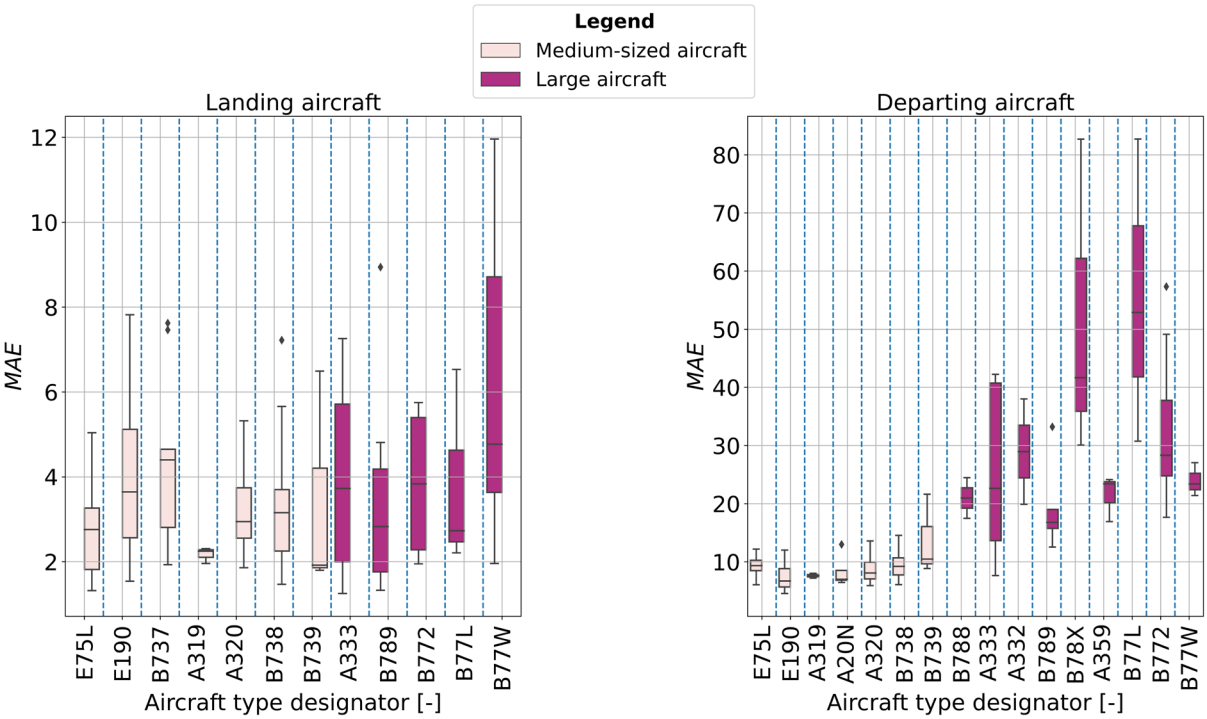

Figure D.5: *Absolute value of the MAE for various aircraft types*

D.1.3 Aircraft-specific results

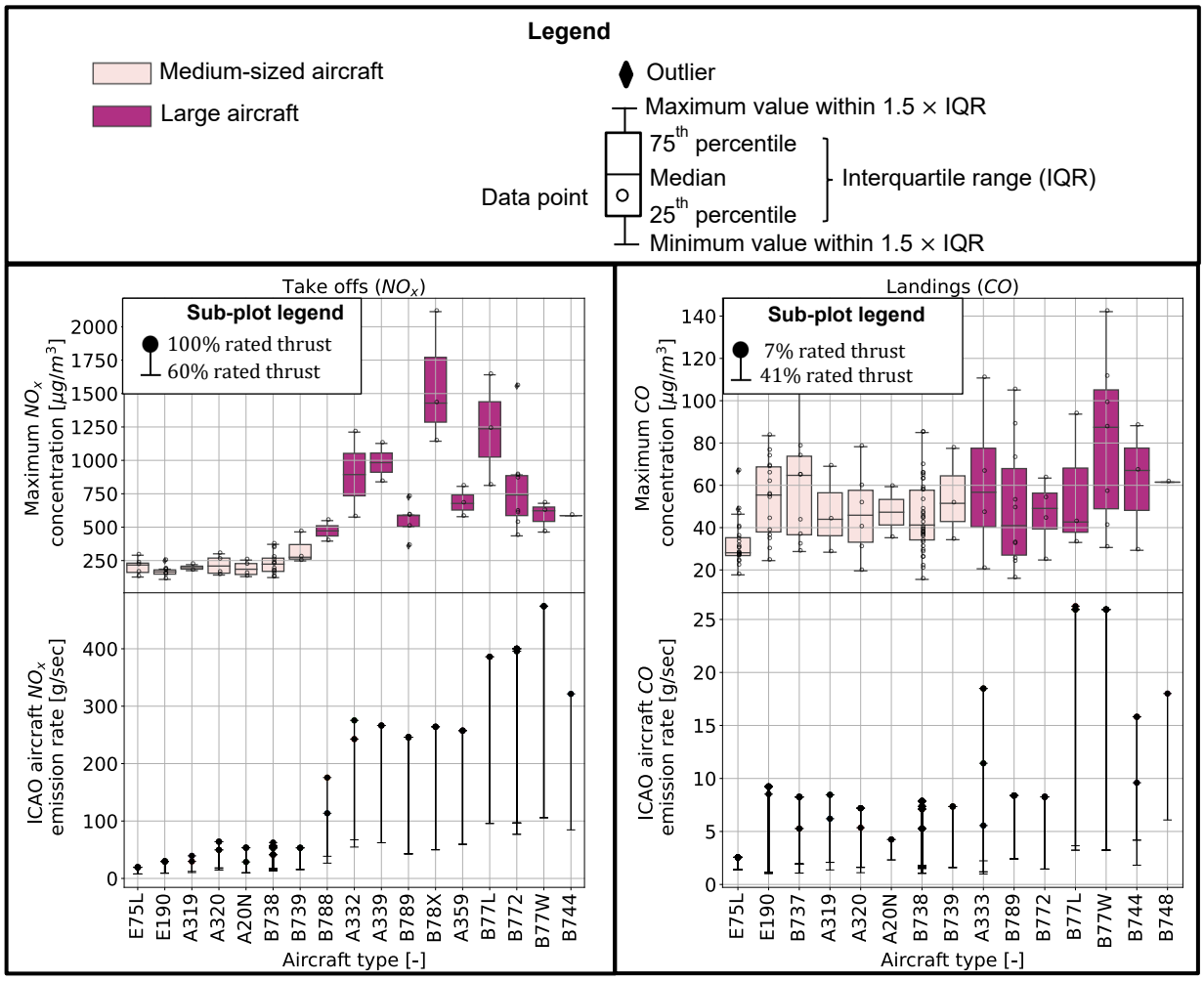

Figure D.6: *Observed background-subtracted peak pollutant concentrations for different aircraft-engine combinations (upper graph) and the ICAO emission rate for the same aircraft-engine combinations (lower graph) for NO_x of departing aircraft (a) and CO of landing aircraft (b)*

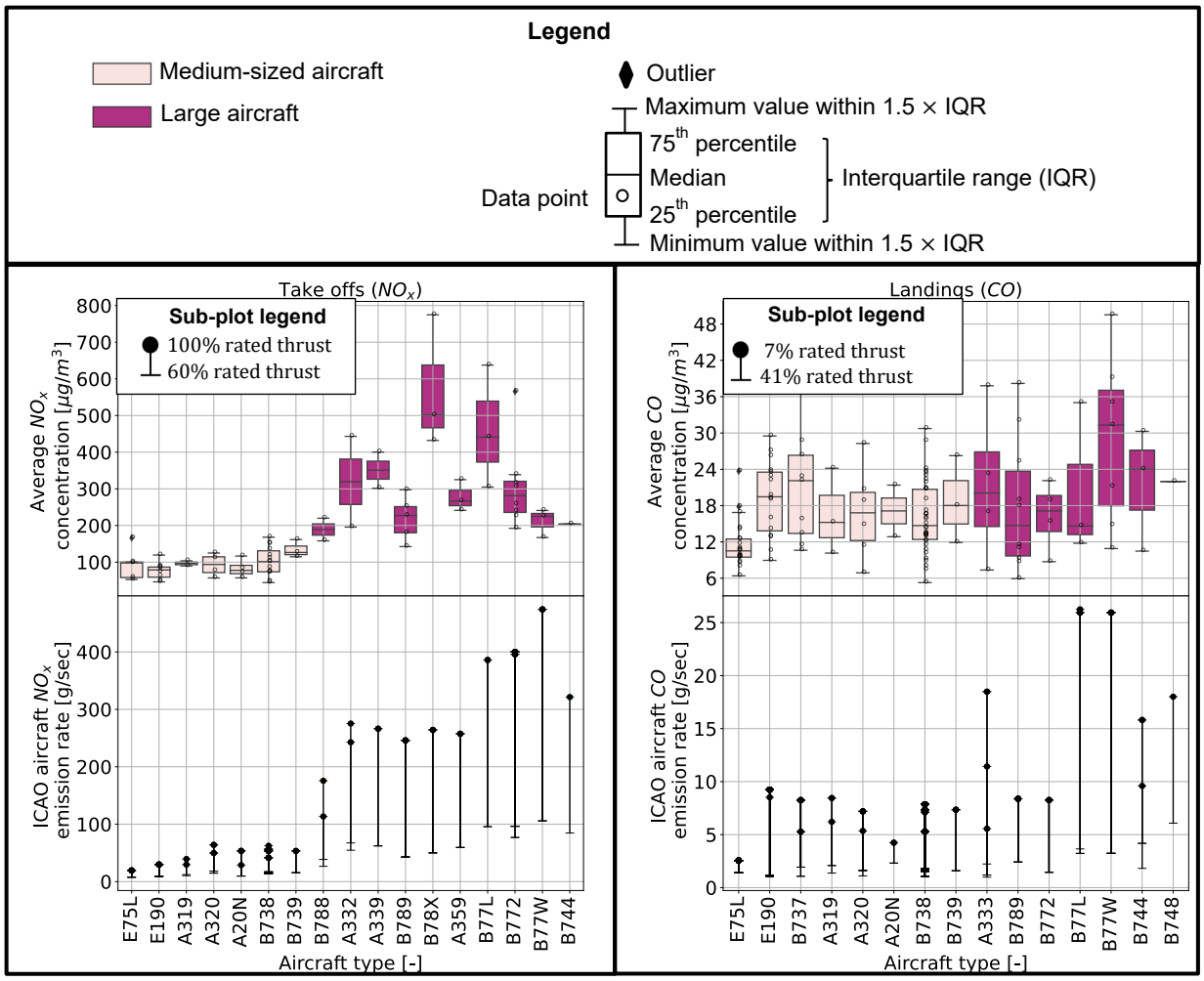

Figure D.7: *Observed background-subtracted average plume concentrations for different aircraft-engine combinations (upper graph) and the ICAO emission rate for the same aircraft-engine combinations (lower graph) for NO_x of departing aircraft (a) and CO of landing aircraft (b)*

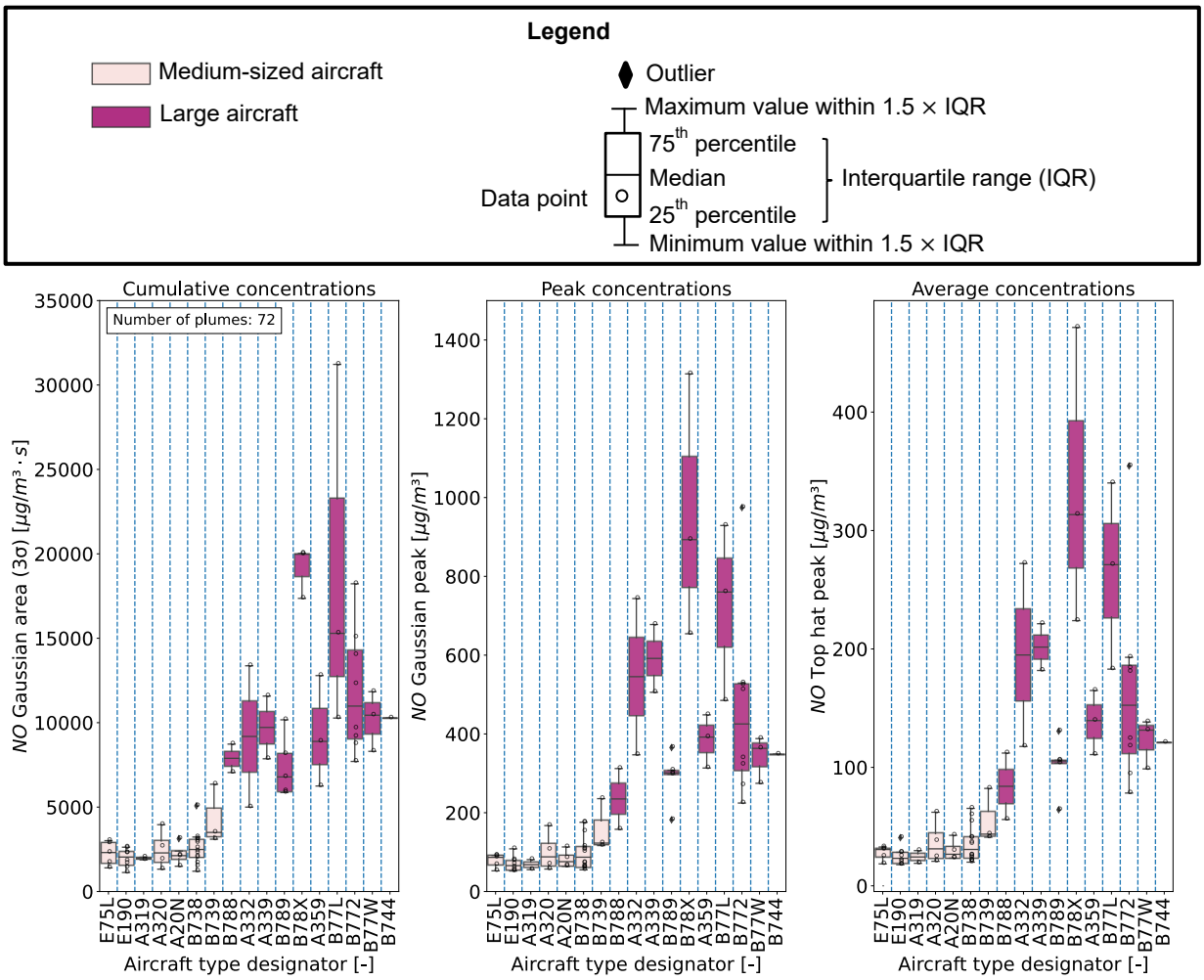

Figure D.8: *NO plume characteristics of departing aircraft whereby aircraft are sorted based on increasing MTOW and grouped as large and medium-sized according to their ICAO wake turbulence category*

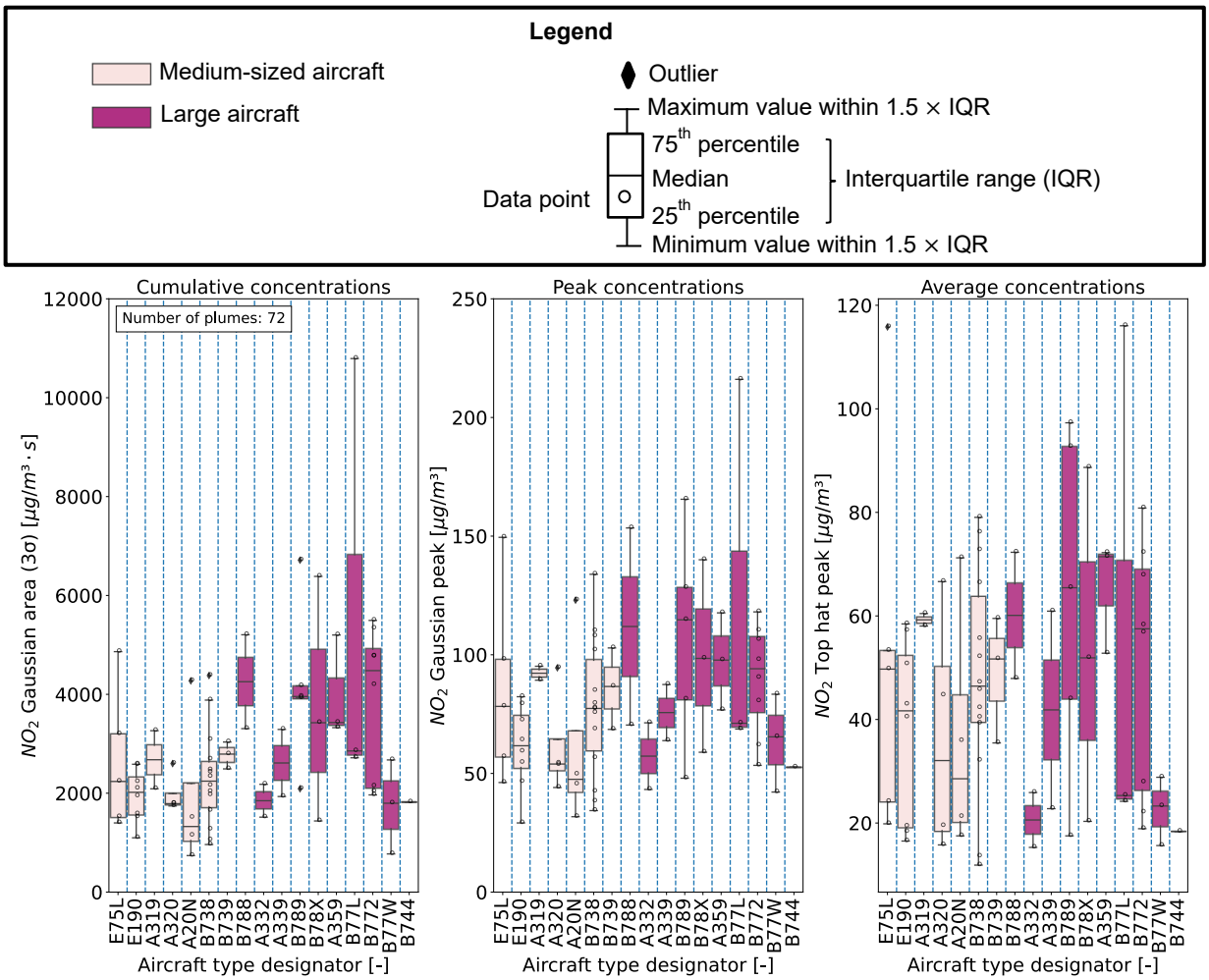

Figure D.9: *NO_2 plume characteristics of departing aircraft whereby aircraft are sorted based on increasing MTOW and grouped as large and medium-sized according to their ICAO wake turbulence category*

D.1.4 Engine-specific results

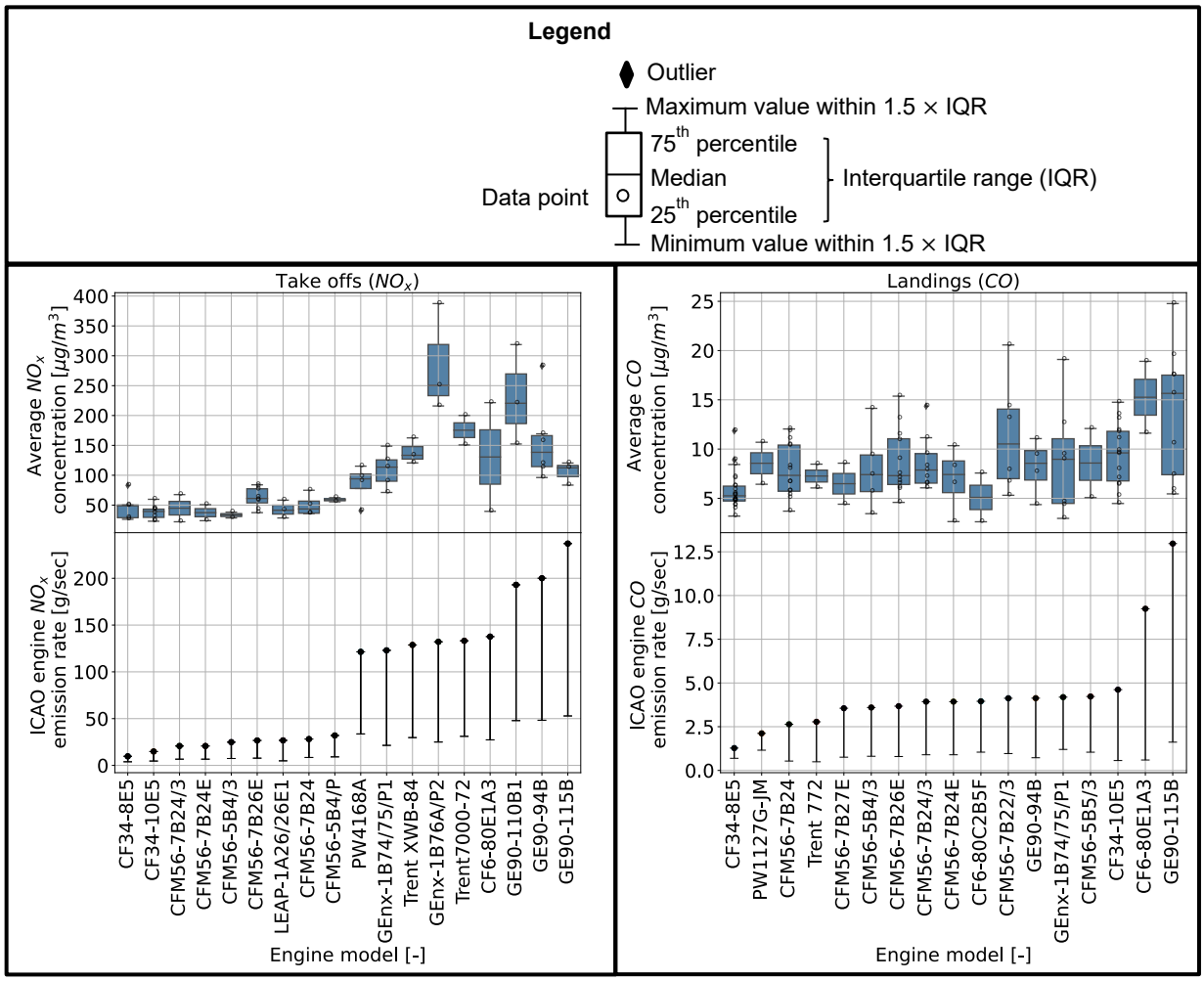

Figure D.10: *Observed background-subtracted average plume concentrations for different engine models (upper graph) and the ICAO emission rate for the same engine models (lower graph) for NO_x for departures (a) and CO of landings (b)*

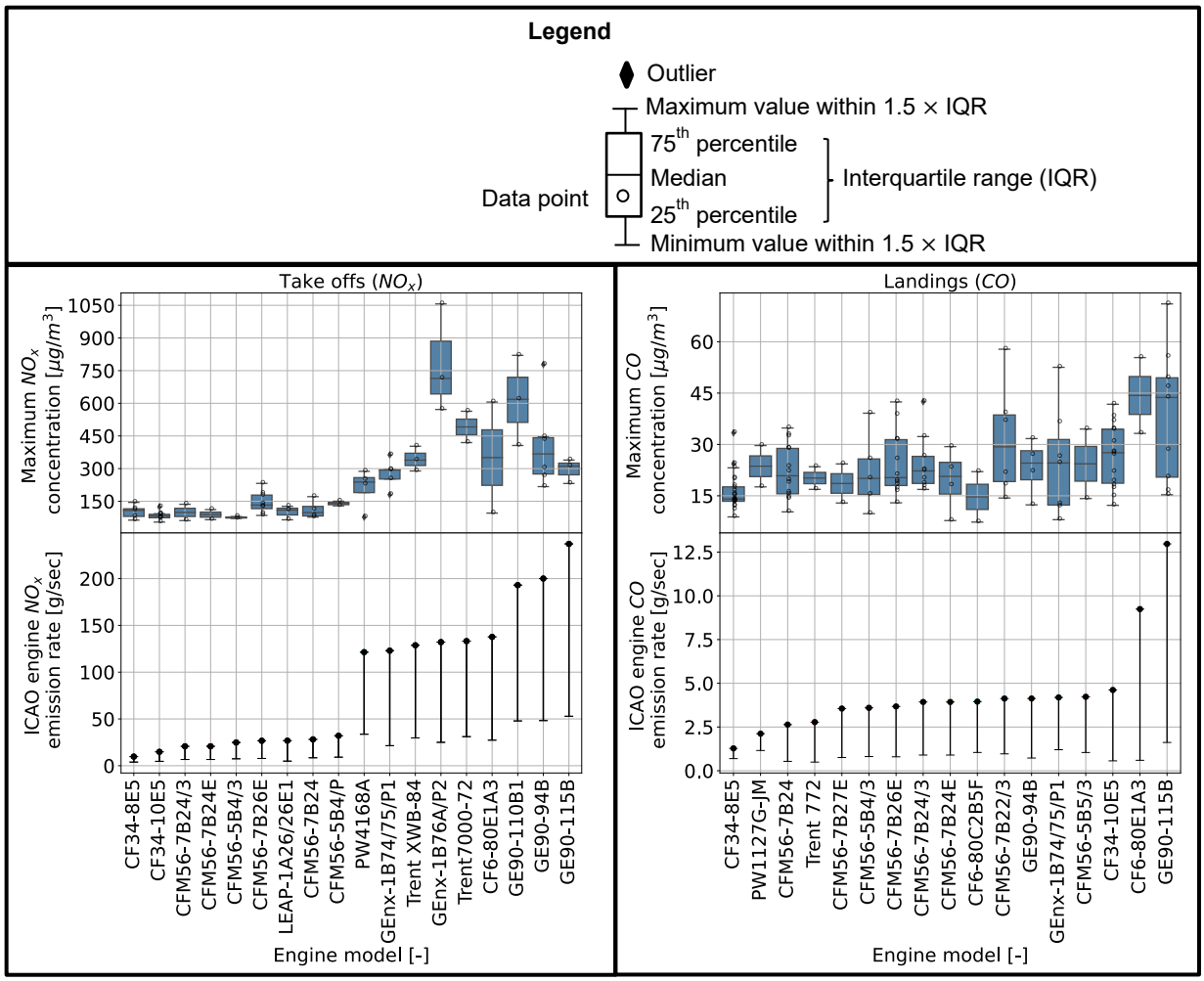

Figure D.11: *Observed background-subtracted peak pollutant concentrations for different engine models (upper graph) and the ICAO emission rate for the same engine models (lower graph) for NO_x for departures (a) and CO of landings (b)*

D.1.5 Relationship between plume characteristics

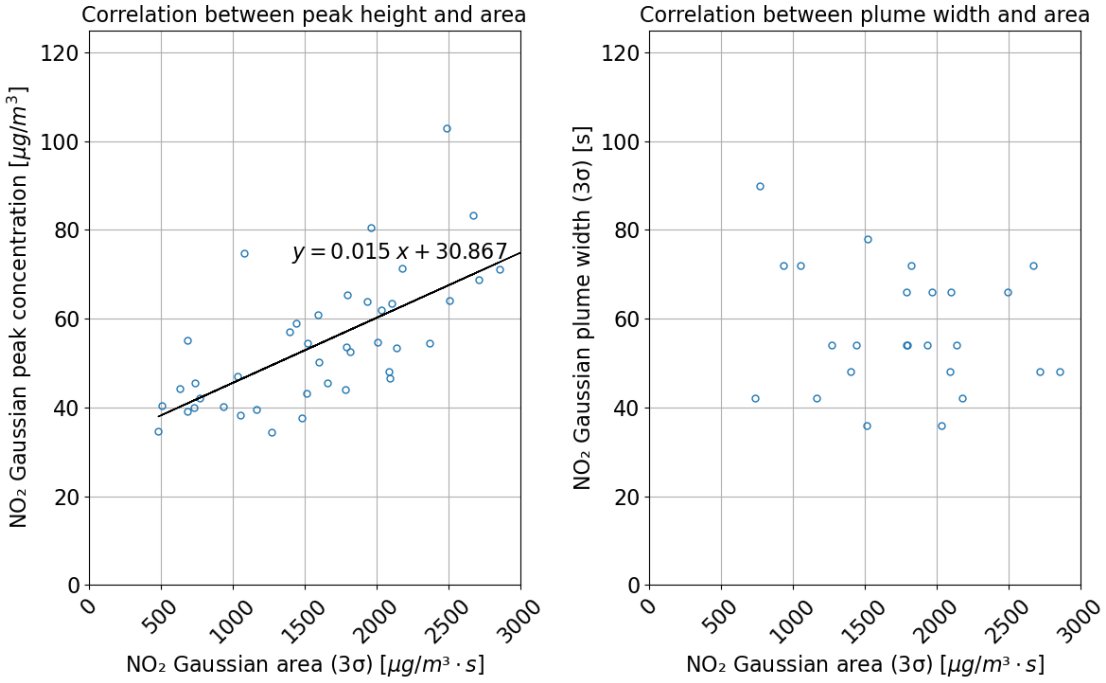

***Figure D.12**: Relationship between the peak height and area and width and area of Gaussian NO_2 plumes*

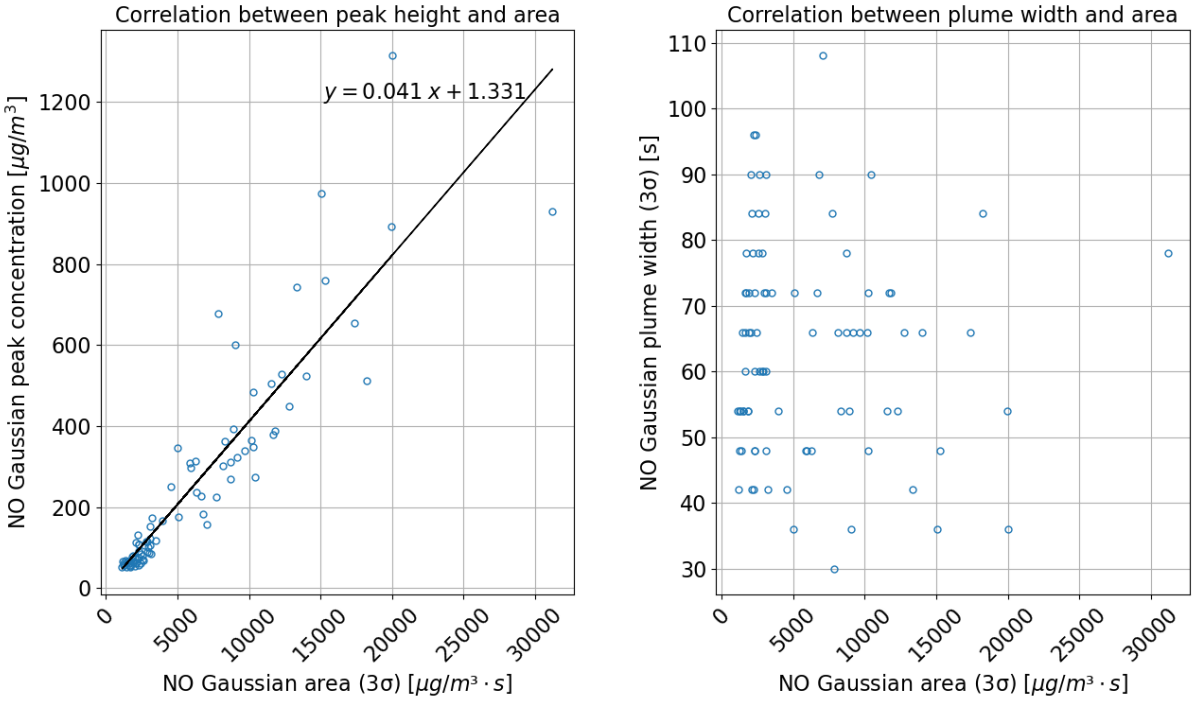

***Figure D.13**: Relationship between the peak height and area and width and area of Gaussian NO plumes*

D.1.6 Sensitivity analysis

The results are potentially influenced by the amplitude threshold (see Section 5.4) and window to estimate the background concentration (see Section 5.2). To study the effect of these inputs on the results, a sensitivity analysis is performed. To conduct this analysis the input parameter

is changed, after which the results are generated to evaluate how resulting plume characteristics are altered. The results of the sensitivity are presented in Appendix T, and reveal that the mean peak, area and top-hat peak can vary up to up to ~30%, ~69% and ~32% respectively depending upon the baseline window, whereby values typically increase for a larger window. Furthermore, increasing the amplitude threshold increases the mean peak, area and top-hat peak of the analysed aircraft and decreases the number of aircraft that could be included in this analysis.

Table D.13: *Variation in mean CO plume characteristics with changes in baseline time window*

Baseline extraction window (seconds)	Gaussian peak [µg/m^3]	Gaussian area [µg/m^3.s]	Top-hat peak [µg/m^3]
60	44.0	1431.0	14.6
100	48.4	1913.8	17.2
200	59.7	2886.2	19.1
300	59.0	2812.5	19.3
400	58.4	2944.5	20.2

Table D.14: *Variation in mean NO_x plume characteristics with changes in baseline time window*

Baseline extraction window (seconds)	Gaussian peak [µg/m^3]	Gaussian area [µg/m^3.s]	Top-hat peak [µg/m^3]
60	626.6	15348.3	156.1
100	489.0	12809.7	192.1
200	803.1	21729.3	203.9
300	831.9	22711.2	214.7
400	815.6	22298.3	212.8

Table D.15: *Variation in mean CO plume characteristics with changes amplitude threshold*

Peak separation line	Gaussian peak [µg/m^3]	Gaussian area [µg/m^3.s]	Top-hat peak [µg/m^3]
$\mu - 0.5\sigma$	47.9	1877.2	16.0
μ	48.4	1913.8	17.2
$\mu + \sigma$	62.3	2523.0	21.2
$\mu + 2\sigma$	71.4	2825.8	25.2
$\mu + 3\sigma$	82.2	3084.5	29.3

Table D.16: *Variation in mean NO_x plume characteristics with changes amplitude threshold*

Peak separation line	Gaussian peak [µg/m^3]	Gaussian area [µg/m^3.s]	Top-hat peak [µg/m^3]
$\mu - 0.5\sigma$	676.1	17847.2	178.6
μ	489.0	12809.7	192.1
$\mu + \sigma$	987.8	24686.3	236.9
$\mu + 2\sigma$	1145.6	28914.8	283.7
$\mu + 3\sigma$	1249.4	31596.3	312.2

D.1.7 Internal temperature and relative humidity

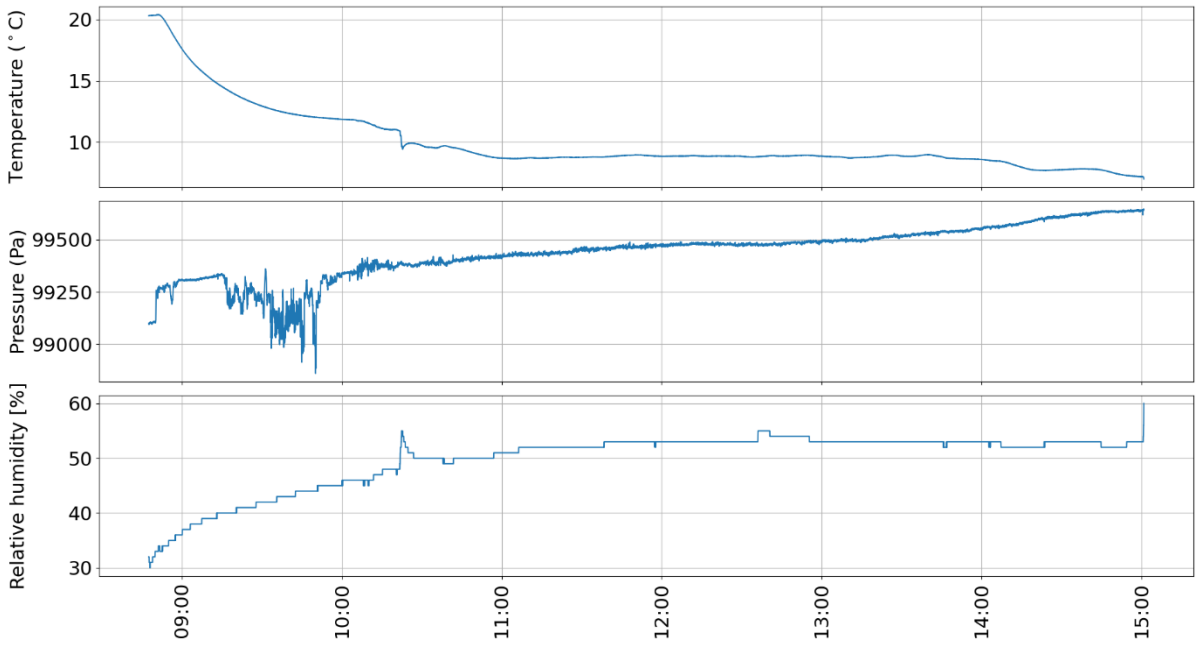

Figure D.14: *Internal node conditions for the measurement conducted on 22-01-2021*

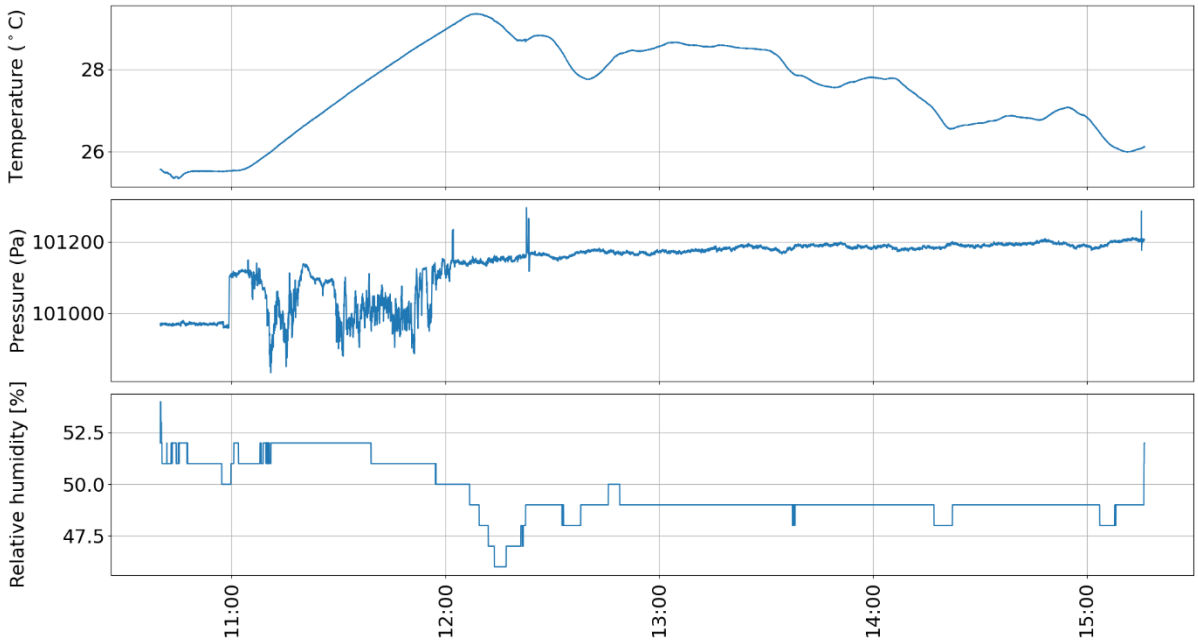

Figure D.15: *Internal node conditions for the measurement conducted on 09-09-2021*

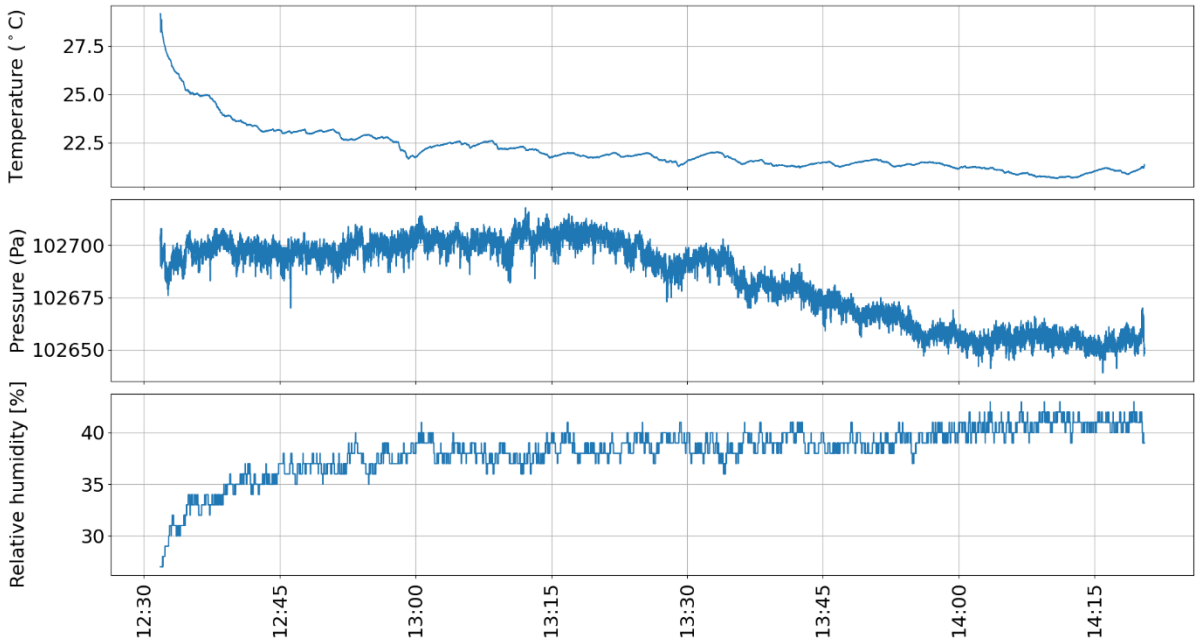

Figure D.16: *Internal node conditions for the measurement conducted on 06-05-2022*

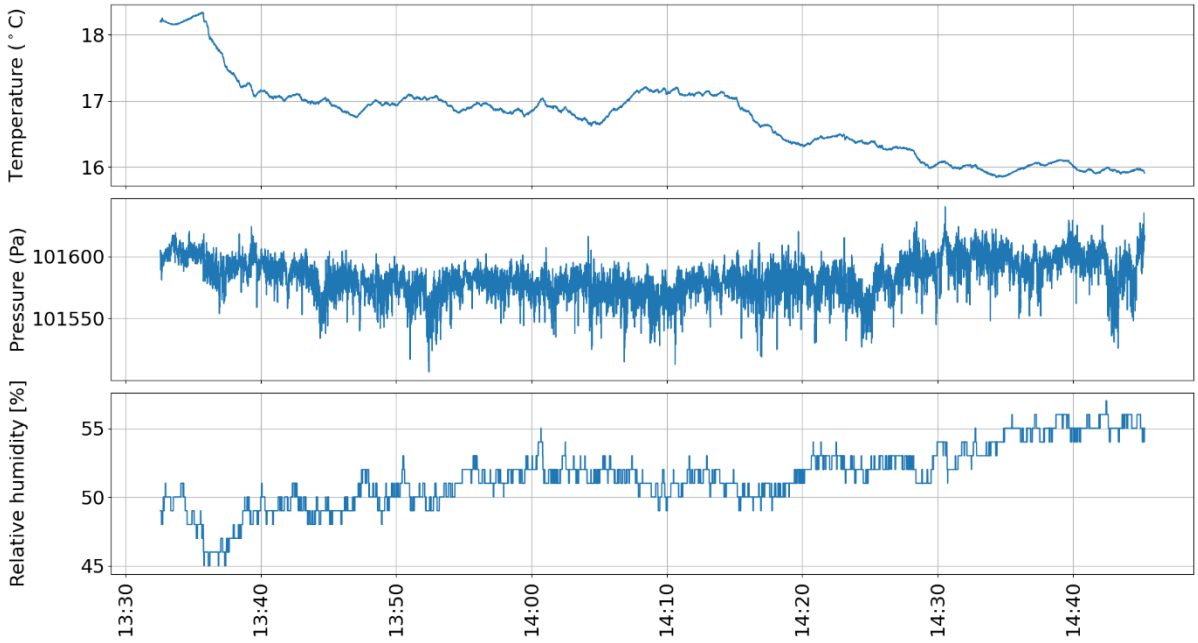

Figure D.17: *Internal node conditions for the measurement conducted on 25-05-2022*

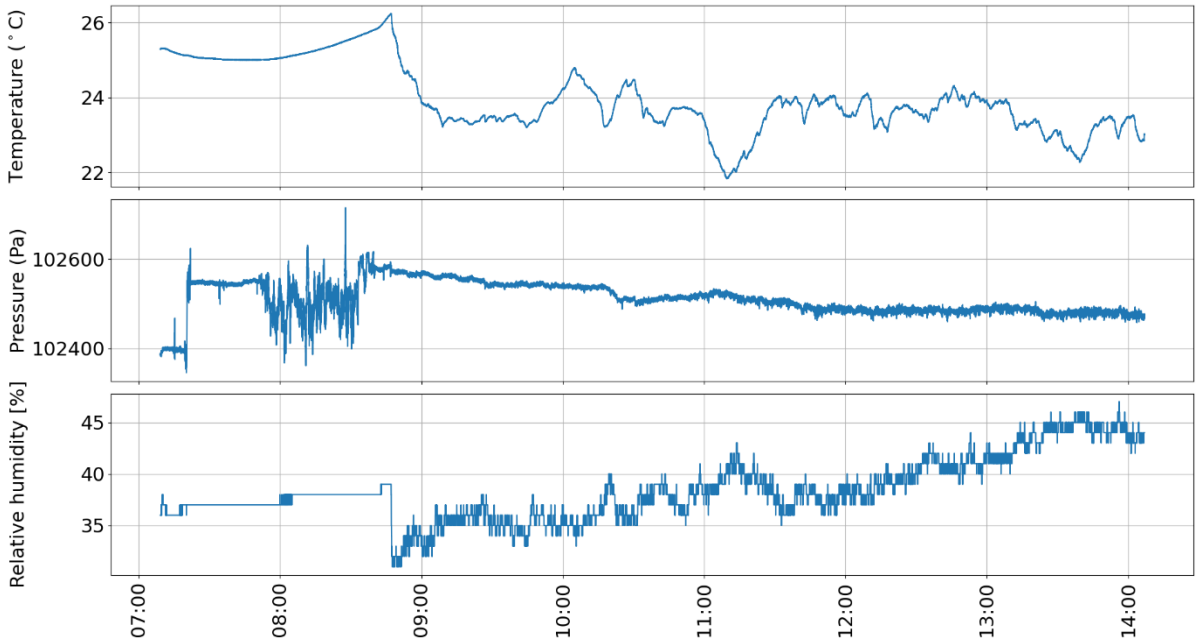

Figure D.18: *Internal node conditions for the measurement conducted on 15-07-2022*

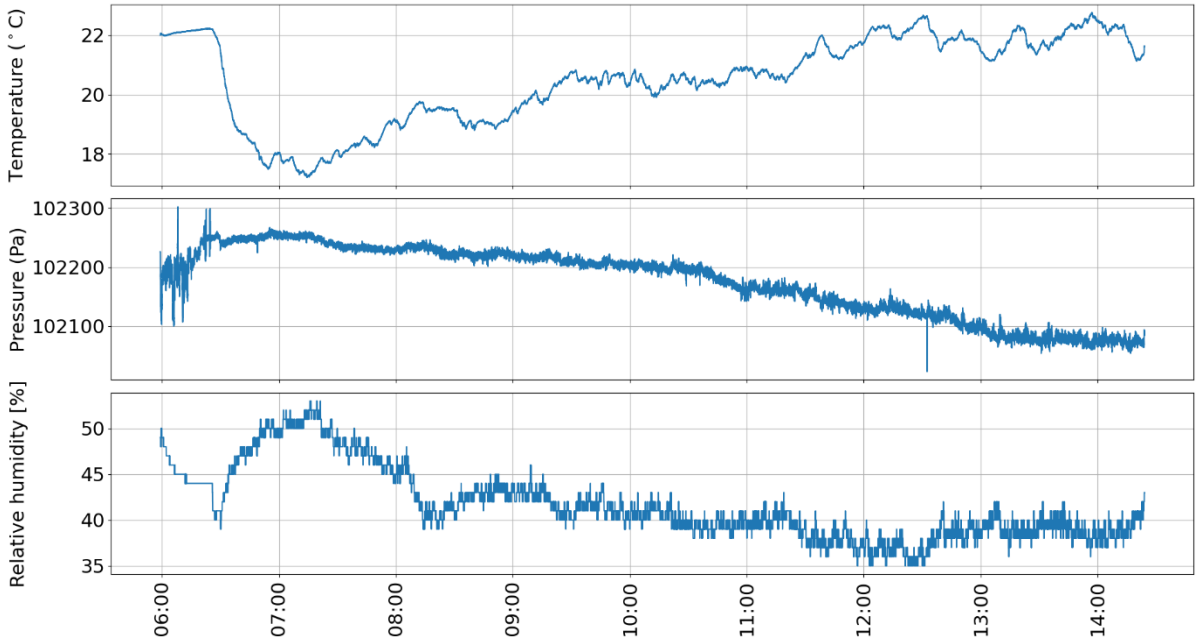

Figure D.19: *Internal node conditions for the measurement conducted on 28-07-2022*

D.2 Upwind pollutant concentrations

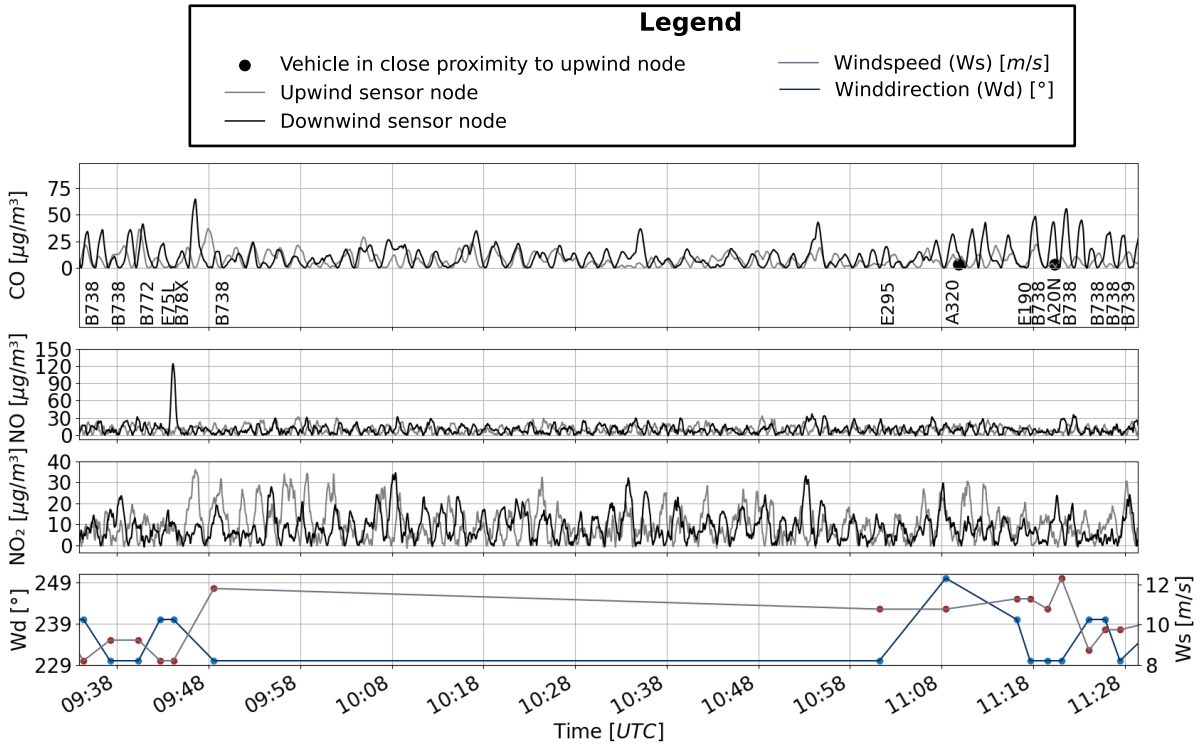

***Figure D.20**: Time-series of the local pollutant concentrations upwind and downwind of the runway together with the prevailing wind and the (refined) estimated plume arrival time at downwind the downwind sensor node for the measurement conducted on 25-05-2022*

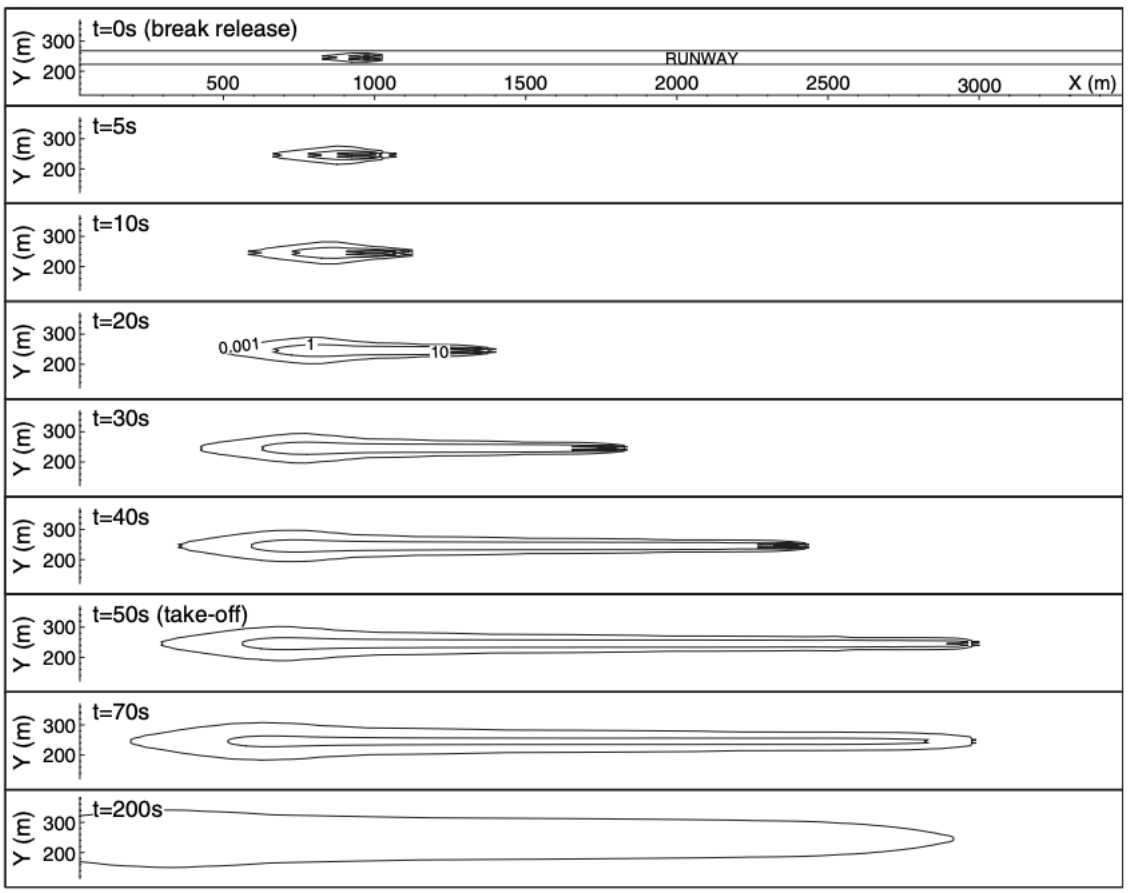

Figure D.21: *NO_x concentration contours (0.001 ppm, 1 ppm and 10 ppm) for Boeing 737 at ground level during take-off [87]*

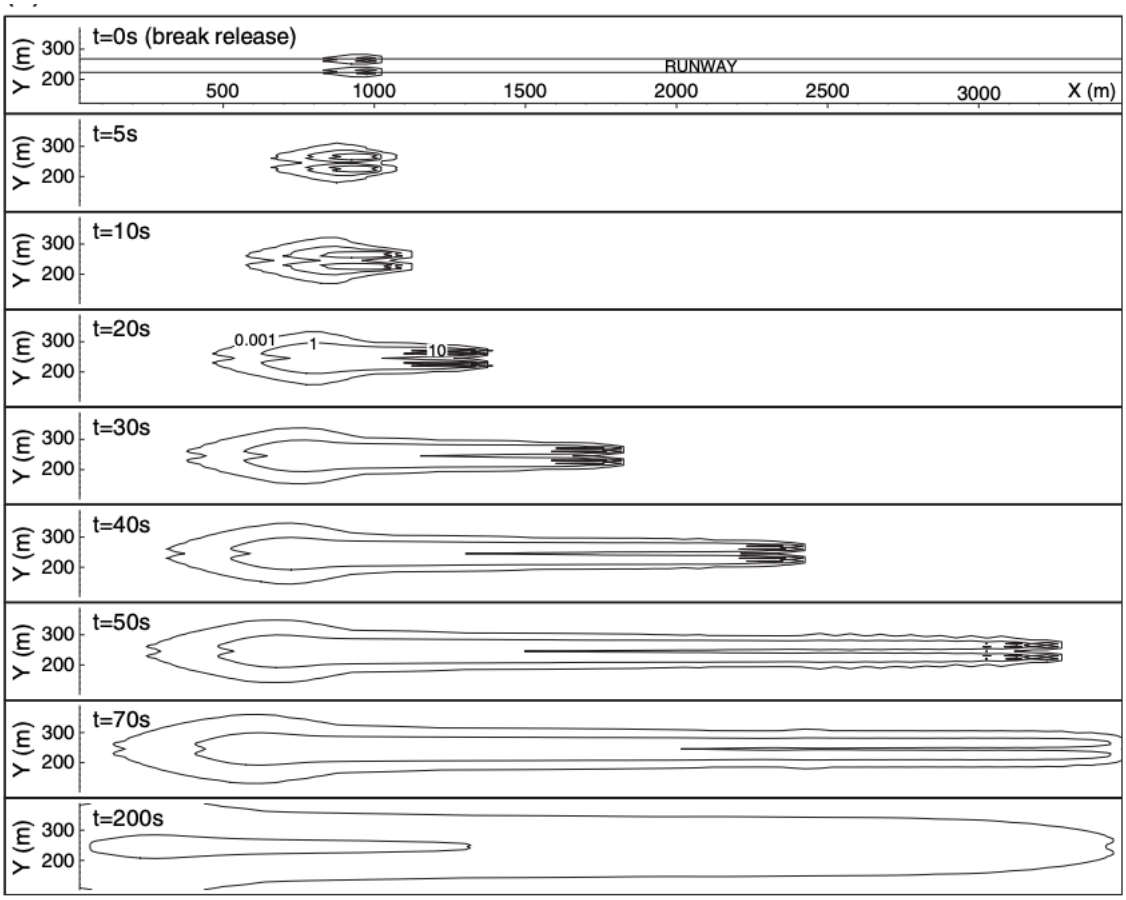

Figure D.22: *NO_x concentration contours (0.001 ppm, 1 ppm and 10 ppm) for Boeing 747 at ground level during take-off at 100% of the rated thrust [87]*

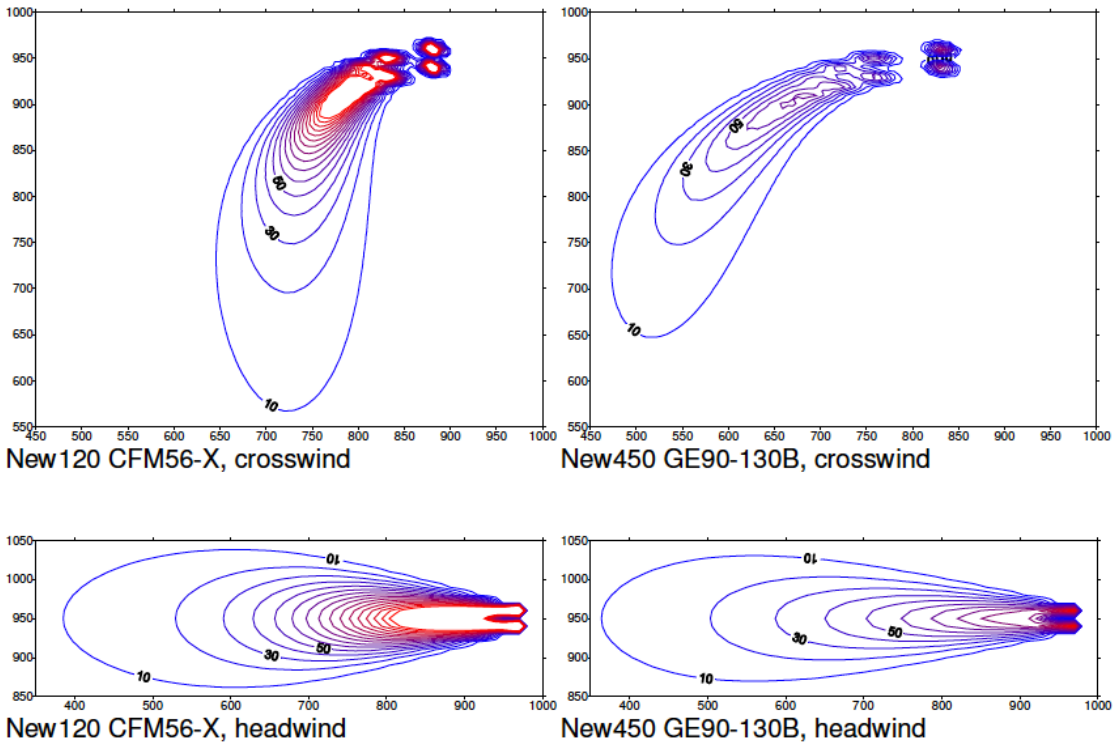

Figure D.23: *NO_x concentration contours of separate of different aircraft-engine combinations at ground level during take-off at 85% of the rated thrust [89]*

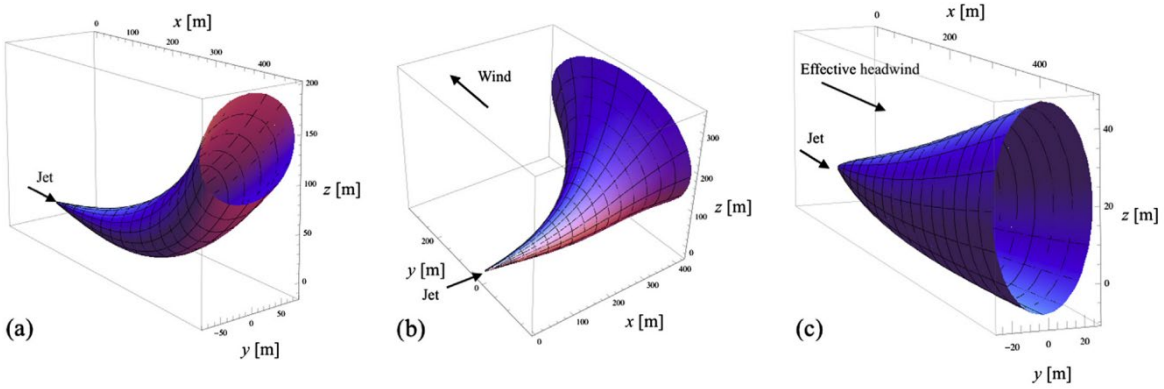

Figure D.24: *NO_x concentration contours of an A320 at 100% of the rated thrust in wind still conditions (a), at 0.5 m/s crosswind (b) and for a roll speed of 10 m/s (c) [1]*

D.3 Collocation results

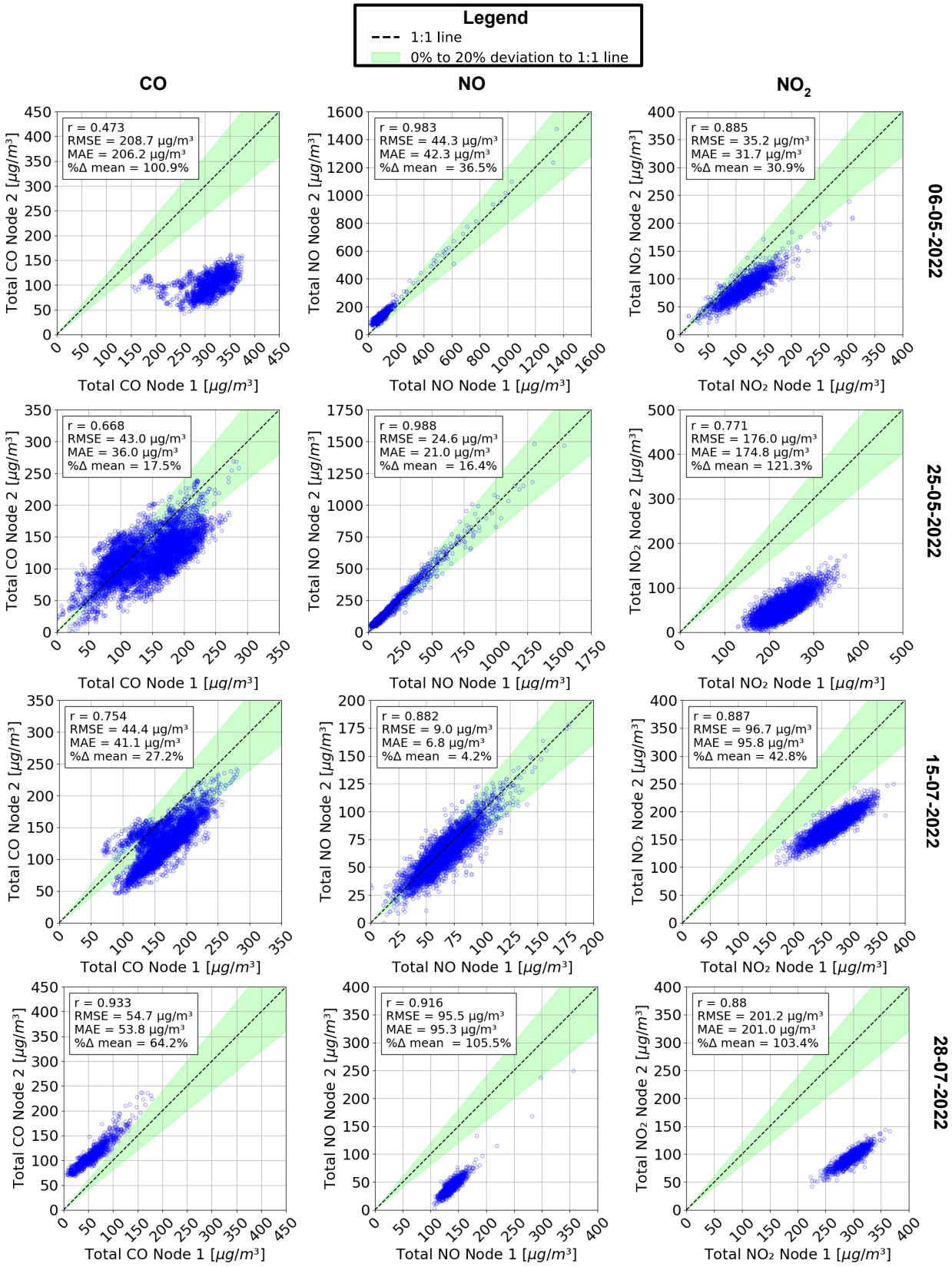

Figure D.25: *Comparison of total pollutant concentrations obtained by two sensor nodes with the Pearson correlation coefficient (r), Root Mean Square Error (RMSE), Mean Absolute Error (MAE) and percentage difference between the time-series mean of each sensor node (%Δ mean)*

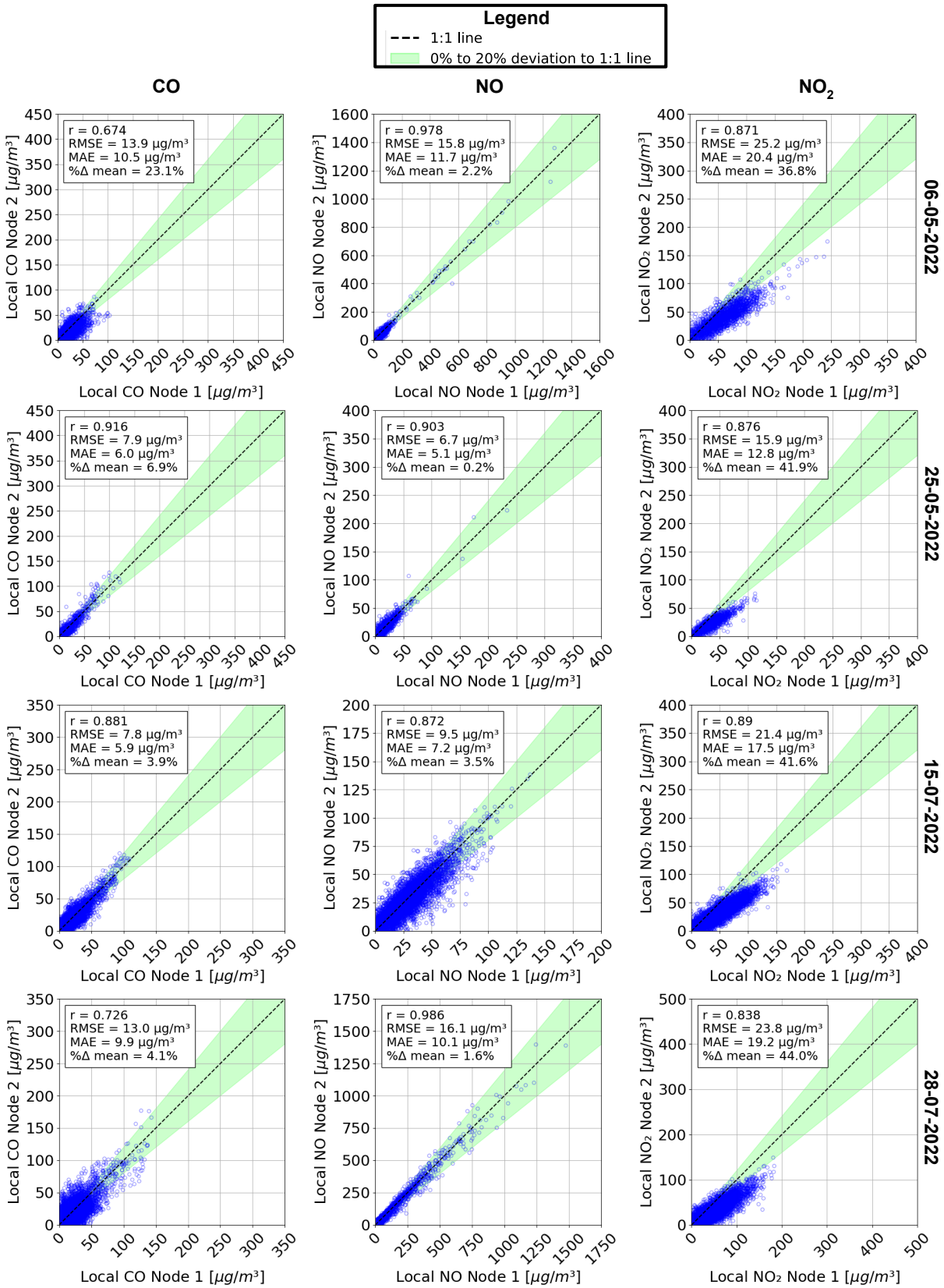

Figure D.26: *Comparison of local pollutant concentrations obtained by two sensor with the Pearson correlation coefficient (r), Root Mean Square Error (RMSE), Mean Absolute Error (MAE) and percentage difference between the time-series mean of each sensor node (%Δ mean)*

Table D.17: *Total pollutant time-series mean in ppb of sensor nodes for different measurement dates*

Date		Node 1	Node 2	Node 3	Node 4
06-05-2022	CO	243.9	111.2	N.A.	N.A.
	NO	75.0	94.6	N.A.	N.A.
	NO_2	58.7	52.7	N.A.	N.A.
25-05-2022	CO	52.9	99.4	N.A.	N.A.
	NO	109.6	33.4	N.A.	N.A.
	NO_2	151.5	49.1	N.A.	N.A.
15-07-2022	CO	152.2	130.4	N.A.	N.A.
	NO	56.4	54.5	123.3	52.3
	NO_2	138.1	88.4	24.4	25.7
28-07-2022	CO	166.8	118.7	N.A.	N.A.
	NO	80.2	94.4	61.7	57.2
	NO_2	117.0	31.1	38.4	45.7

Table D.18: *Local pollutant time-series mean in ppb of sensor nodes for different measurement dates*

Date		Node 1	Node 2	Node 3	Node 4
06-05-2022	CO	21.5	14.2	N.A.	N.A.
	NO	39.3	37.0	N.A.	N.A.
	NO_2	29.1	21.0	N.A.	N.A.
25-05-2022	CO	15.8	12.8	N.A.	N.A.
	NO	18.0	18.1	N.A.	N.A.
	NO_2	21.3	14.5	N.A.	N.A.
15-07-2022	CO	14.2	13.5	N.A.	N.A.
	NO	18.1	17.4	12.9	15.0
	NO_2	19.1	12.3	5.7	7.9
28-07-2022	CO	20.7	16.9	N.A.	N.A.
	NO	39.0	36.6	33.1	29.0
	NO_2	23.6	14.1	9.0	10.3

D.4 Near engine exit plane experiment results

Figure D.27 shows the obtained data for the two conducted near engine exhaust nozzle measurements.

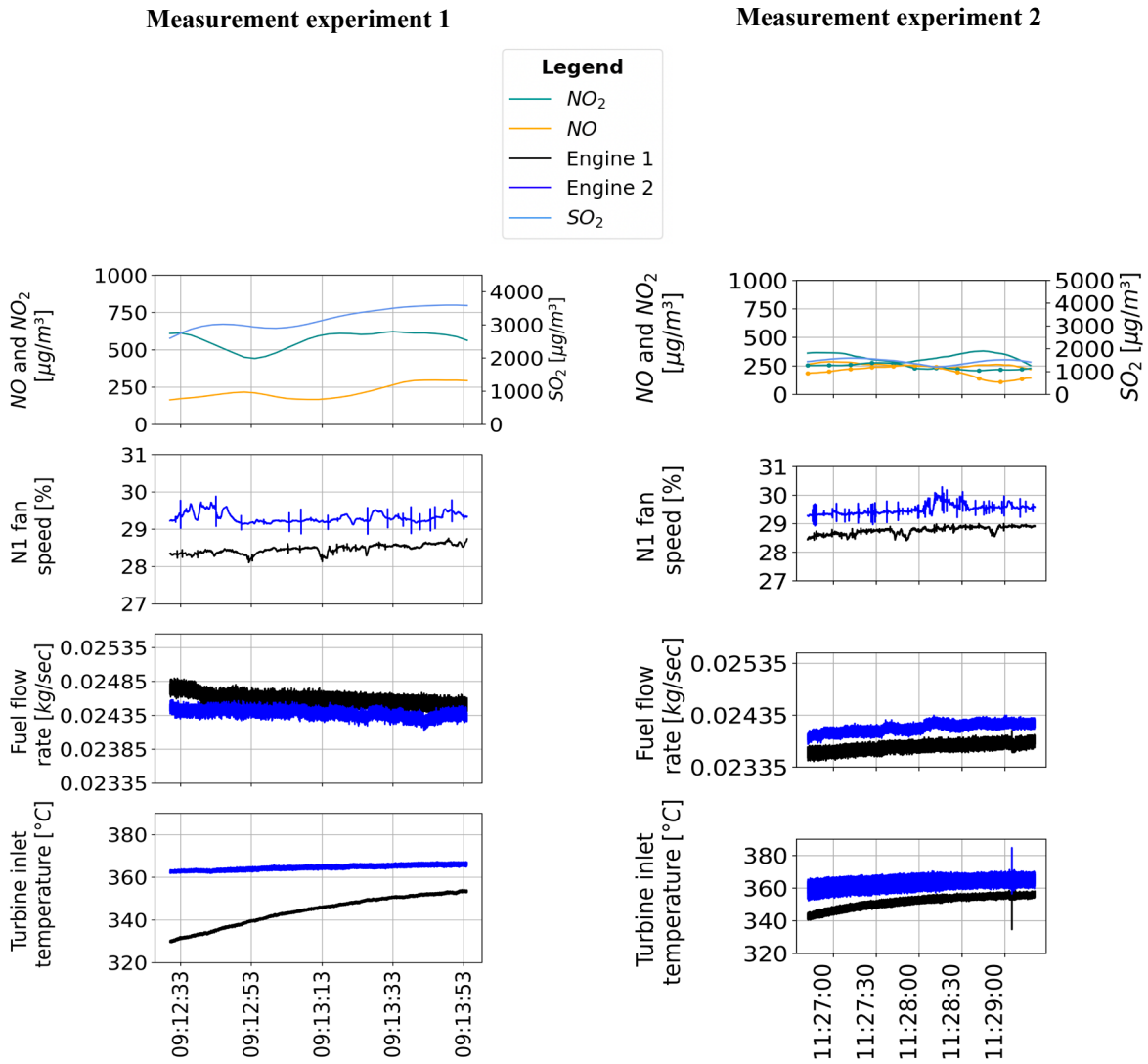

Figure D.27: *Air pollution signals supplemented by engine data for the near-engine exhaust measurement of the first measurement (left) and second measurement (right)*

Figure D.28 indicates by the shaded region the time interval during which engine data of the Flight Test Instrumentation System (FTIS) as discussed in Chapter 3 was available. Subsequent analysis of the results is solely based upon the signals within this time interval.

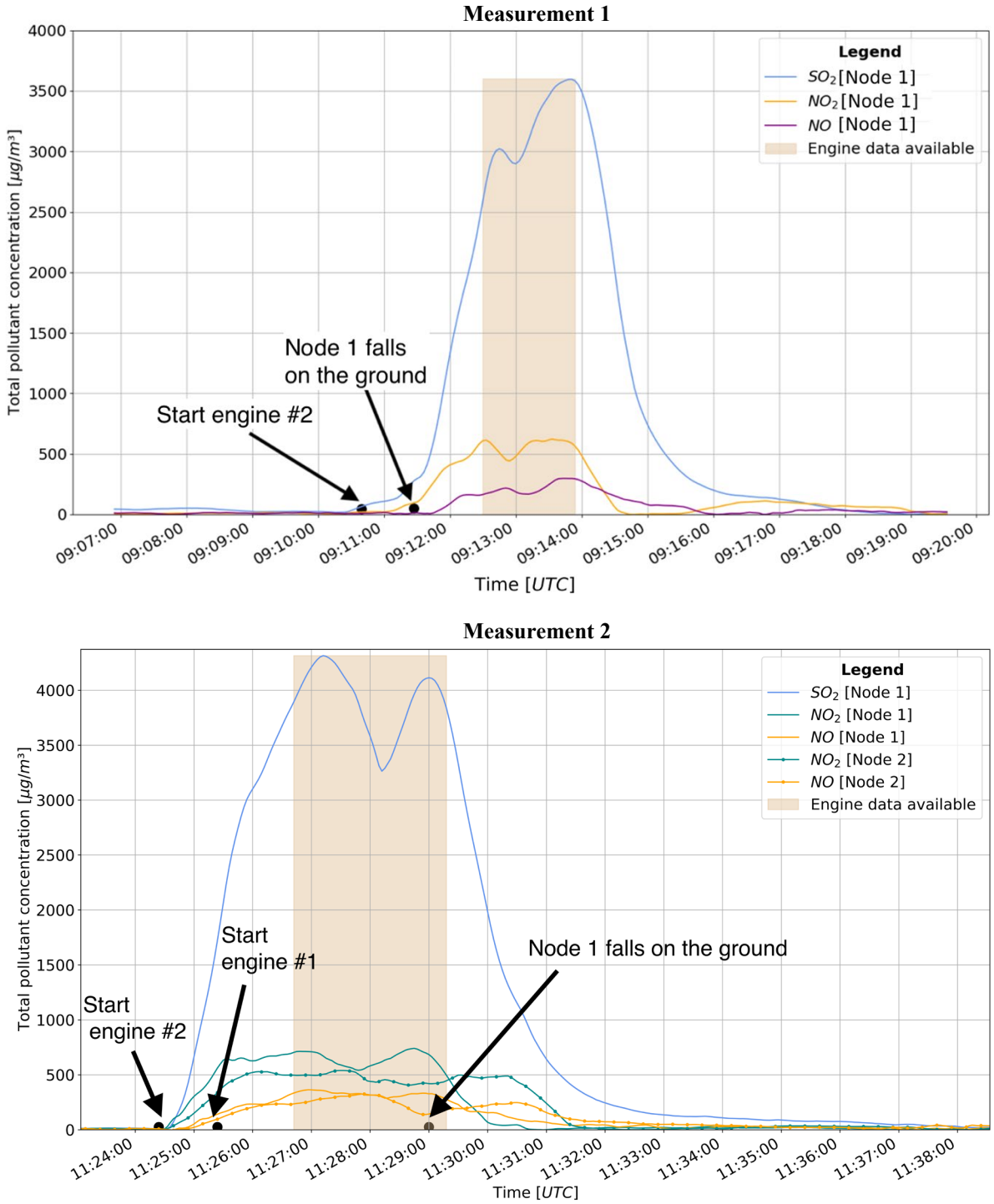

Figure D.28: *Resulting air pollution signals of the near-engine exhaust measurement of the first measurement (top) and second measurement (bottom)*

A rough estimation of the NO_x emission index is obtained by first computing the area under the NO curve for which engine data was available (see the shaded region in Figure D.28) and dividing this by the duration of the NO curve. The same steps are performed for NO_2. Herafter, the NO_x in micrograms per m^3 is retrieved through Equation D.1 with A_{NO} and A_{NO_2} the area over the width of NO and NO2 respectively. The result is multiplied by 10^{-6} to convert the NO_x from micrograms per m^3 to grams per m^3.

$$A_{NO_x} = \frac{46.0055}{30.0061} \times \mathrm{A_{NO}} + A_{NO_2} \quad \text{(D.1)}$$

Delaney et al. [336] and Zaporozhets and Synlo [337] stated that turbulent-free jets can be divided into three stages:

- The initial stage: in this stage the plume dispersion is solely determined by the characteristics of the emitted jet
- The transition stage: in this stage the plume starts to spread under the influence of the ambient wind and plume buoyancy
- The final phase: in this stage atmospheric effects become dominant for plume dispersion

The streamwise distance between the jet-engine exhaust nozzle till the end of the initial stage is denoted as S_I whereby S_I can be expressed relative to the exhaust nozzle diameter R_0 using Equation D.2.

$$\overline{S_I} = \frac{S_I}{R_0} \quad \text{(D.2)}$$

Similarly, the radius of the plume at the end of the initial stage is denoted as R_I and can be expressed relative to the exhaust nozzle diameter using Equation D.3.

$$\overline{R_I} = \frac{R_I}{R_0} \quad \text{(D.2)}$$

According to Zaporozhets and Synlo [337] the radius of the plume at the end of the initial stage relative to the exhaust nozzle radius can be computed using Equation D.3:

$$\overline{R_I} = 0.27\,\overline{S_I} \quad \text{(D.3)}$$

Delaney et al. [336] pointed out that S_I is approximately equal to 7 times the exhaust nozzle diameter D_0, whereby D_0 equals ~1.55 m for the engine on which the near engine exhaust nozzle experiment was performed. This results in S_I ~10 m, which is approximately equal to the distance between the aircraft and the sensor node. Using this value for S_I, the plume radius at the sensor node can be estimated using Equation D.2, D.3 and D.3, which gives R ~ 2.7.

The volume of the exhaust plume can be approximated as a truncated cone with Equation D.4. This results in V ~ 105 m^3.

$$V = \frac{1}{3}\pi S_I({R_I}^2 + R_I R_0 + {R_0}^2) \quad \text{(D.4)}$$

Multiplying the concentration of NO_x in gram/m^3 by V results in 0.06 gram NO_x. The total amount of fuel burned (in kg) can be found by computing the area under the curve of the fuel flow rate (in kg/sec). As the emission index is the amount of pollutant (in gram) per kg of fuel burnt, the emission index can be estimated from which leads to a NO_x emission index of ~0.02 g/kg fuel. However, it should be noted that this merely serves to get a rough approximation of the NO_x emission index. More research is needed to investigate whether this method should be refined. Furthermore, the measurements were conducted during non-ideal conditions, which may have influenced the NO_x emission index.

D.5 Dispersion model results

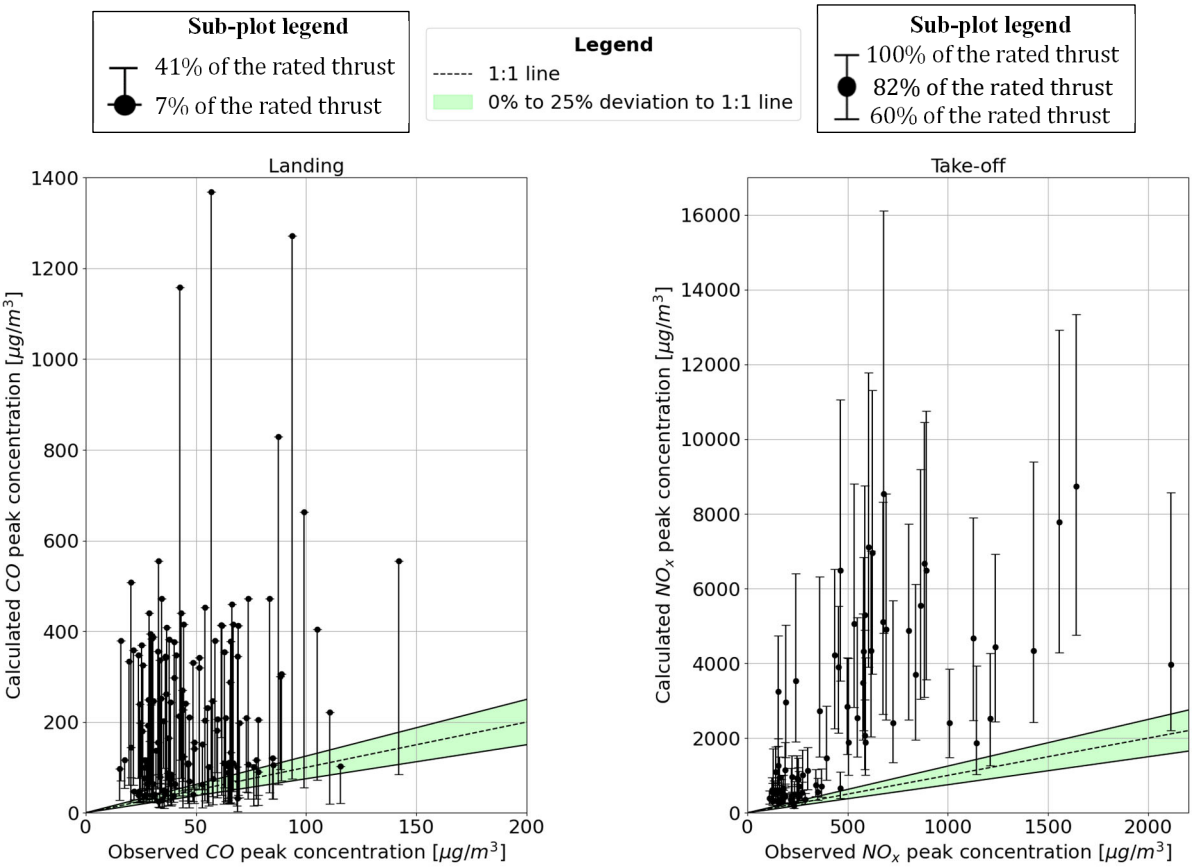

Figure D.29: *Comparison to estimated certified pollutant concentrations for different thrust settings assuming urban conditions*

It was stated in Chapter 6 that the formulas to compute the dispersion parameters are published for urban and open country conditions, whereby urban conditions were assumed for this research. Figure D.30 displays the results if open country conditions would have been assumed instead. It can be observed that this increases pollutant concentrations, whereby mean modelled concentrations are ~137% higher for open country conditions compared to urban conditions. More research is needed to investigate which conditions are most applicable.

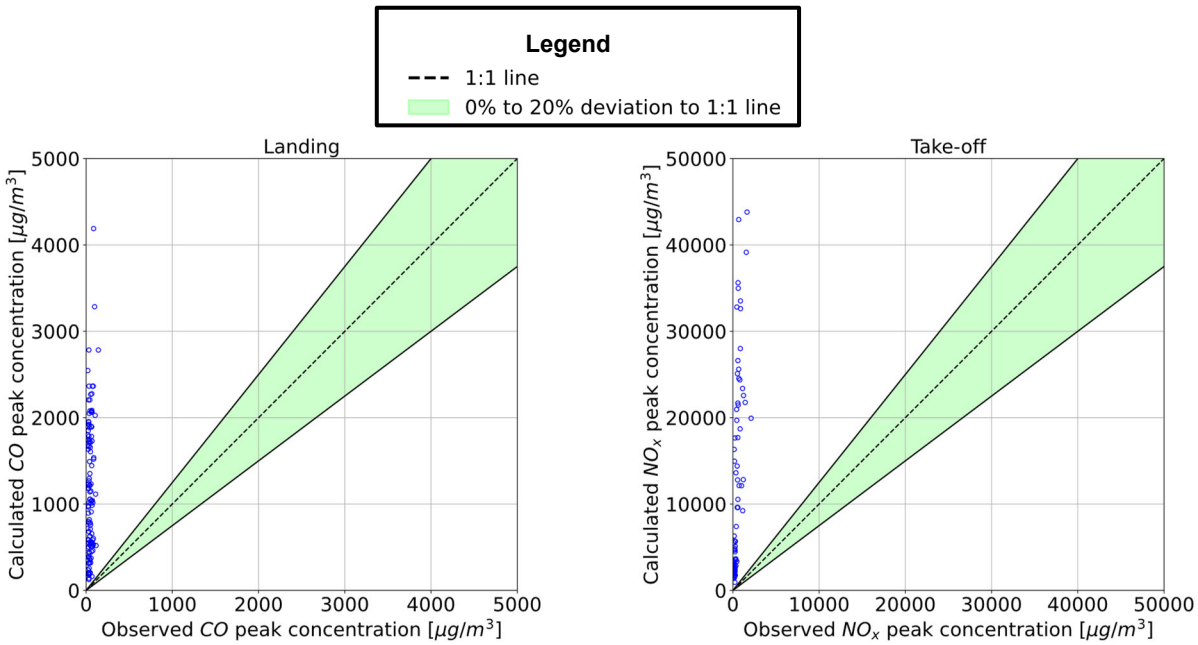

Figure D.30: *Comparison between modelled- and observed peak pollutant concentrations with open country conditions assumed for the plume dispersion coefficients*